Department of Physics and Astronomy
Faculty of Science, University of Aarhus

PhD thesis by
Michael Weidinger

Lyman-α as a tool

Environments of high-redshift quasars

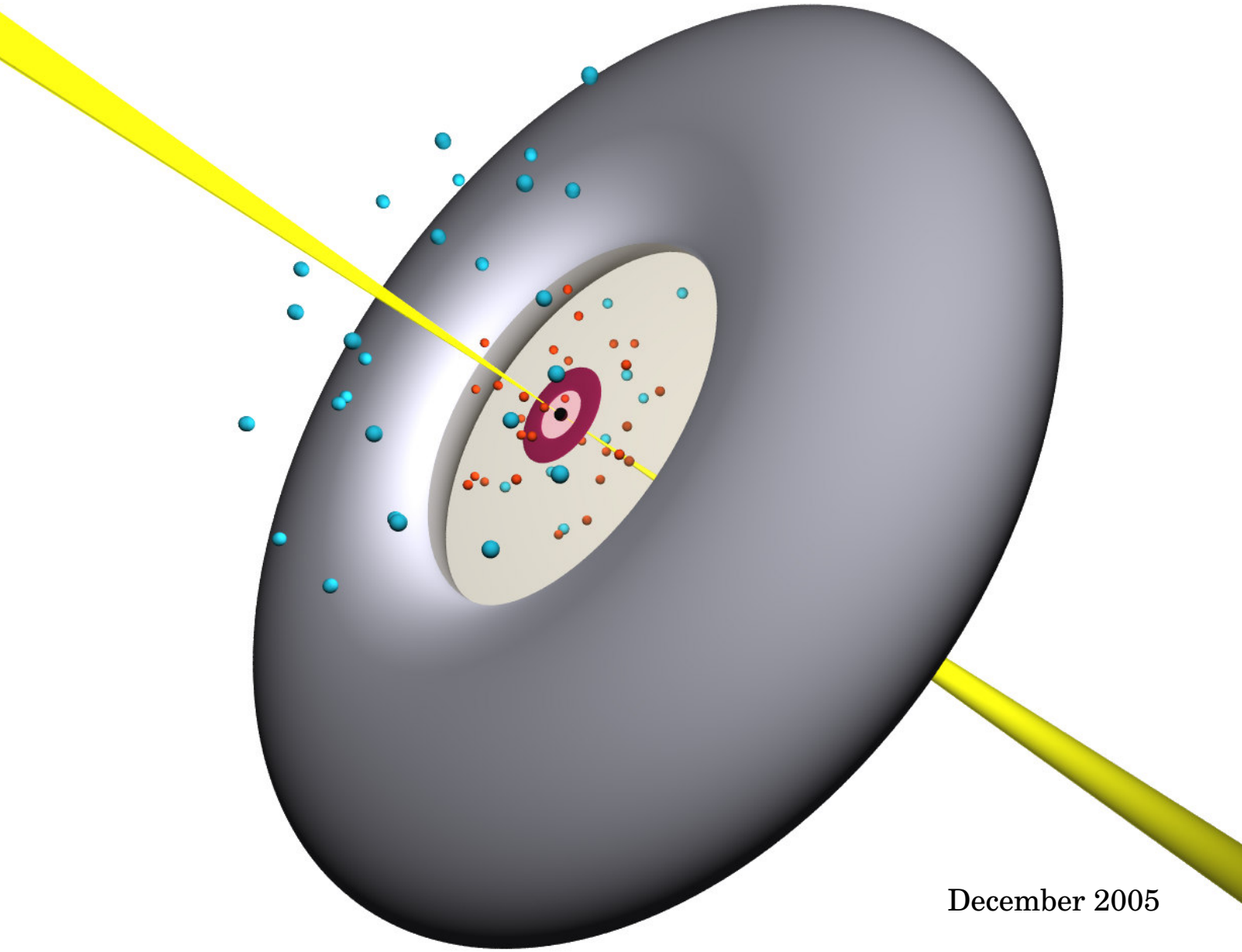

December 2005

Department of Physics and Astronomy
Faculty of Science, University of Aarhus

PhD thesis by
Michael Weidinger

Lyman-α as a tool

Environments of high-redshift quasars

December 2005

This thesis is submitted to the Faculty of Science at the University of Aarhus, Denmark, in order to fulfill the requirements for obtaining the PhD degree in Astronomy.
The studies have been carried out under the supervision of Dr. Bjarne Thomsen at the Department of Physics and Astronomy, University of Aarhus (August 2001 to December 2005), and Dr. Palle Møller at the European Southern Observatory, Garching bei München, Germany (August 2003 to August 2004).

Printed in Denmark by the Reprocenter at the Faculty of Science, University of Aarhus.
This document was typeset in LaTeX by the author.

Contents

Preface

EVEN if it isn't, it seems like a long time ago that my fellow student Mathias tipped me off about two crazy Danes at the European Southern Observatory (ESO) looking for students to spend a few months working with them. I went to visit them (as did Mathias), and during the stay we cooked up an application for admission to the PhD programme, and I was fortunate enough to actually be enrolled.

I have had the privilege to carry out my PhD studies both locally at the Department of Physics and Astronomy and in the stimulating environment at ESO. The time spent at ESO has been an extremely rewarding experience both professionally and personally, and I would not have been without it.

The work carried out during my PhD studies falls in two related, but nonetheless distinct, categories. However, in one way or another the different parts take their starting points in observations of the Lyα line of high-redshift quasars and Lyα emitting galaxies surrounding the quasars. The structure of the thesis is as follows. Chapter 1 is a general introduction to the field of active galactic nuclei (AGN) and the current status of our understanding, and (to a minor degree) the status of narrow-band imaging studies. In Chapter 2 are presented various concepts and strategies of data reduction, which are used extensively throughout, but only briefly discussed. Chapter 3 explores the idea of what one could with a sample of filaments discovered by Lyα narrow-band imaging of quasars and their surroundings. This is a theoretical study standing somewhat apart from the rest of my work. In Chapter 4 we put a dataset mapping out such a filament to an alternative use. We do this by studying Lyα emission from around the quasar itself, interpreting the observations through a simple model. The details of the observations are presented in Chapter 5. In Chapter 6 a similar study is performed, but now the dataset contains observations of 14 high-redshift quasars, enabling conclusions of a more statistical nature to be drawn. Finally, a summary and an outlook to future directions for this type of research are presented in Chapter 7.

Three chapters are essentially reprints of published papers. Chapter 3 is from Weidinger et al. (2002), Chapter 4 is from Weidinger et al.

(2004), and Chapter 5 is from Weidinger et al. (2005).

This work was funded by the Faculty of Science, University of Aarhus, and by the European Southern Observatory through the ESO Studentship programme and the Director General Discretionary Fund.

Acknowledgements

Well, Palle and Johan got me started on all this, so I guess that makes them responsible... Still, I am indebted to them for taking me under their wings. My deepest gratitude goes to Palle Møller for always sparing a moment to discuss a problem (or a movie), showing me the optimal way of attacking it, and for *always* being right. (I know I'll regret writing it, but there it is). My warmest thanks go to Johan Fynbo for his extremely friendly and helpful attitude, and for sharing his experience with me. Without his help I'm sure I would still be searching for the right articles to cite. I am grateful to Bjarne Thomsen for supervising me and for numerous discussions on everything from the latest Linux kernel to the holographic principle. The value of such discussions is greatly underestimated. I would like to thank Mathias Egholm for his friendship and for spending an entire year in Garching just to entertain Tina and me (and Palle, on occasion). Without his gentle care for our general education we would still be ignorant of the joys of "Need for Speed" and "Tekken". Many thanks go to the Spell Weaver Assembly of Dietersheim (SWAD) and the Garching gamers (Antonello, Jonas, Margrethe, Marina, Markus, and Palle) for turning many long days (and nights) into fun, well-spent hours.

I wish to extend my deepest gratitude to my family and family-in-law for their patience and their immense help during this final tour de force, and to Frederik for ensuring that I did not get too much sleep. But most importantly, I am forever grateful to Tina for her unwavering love and support.

Finally, my appreciation and admiration go to the GNU/Linux and the free and open source communities for developing fantastic software. The vast majority of this work was performed on GNU/Linux machines (no MS here).

This work is dedicated to my dear wife Tina, through whom I continue to grow and learn in all aspects of Life.

Michael Weidinger
Århus, December 19, 2005.

A number of minor corrections have been made in the text for this second edition. I wish to stress that no results or conclusions have been changed.

Michael Weidinger
Århus, February 17, 2006.

Abstract

UNDERSTANDING how galaxies in the Universe around us have come to be is one of the major challenges in modern Astronomy. One way to ascertain pieces of information that may add to this puzzle is to observe very distant galaxies. These galaxies emitted their light at a time when the galaxies and the Universe itself were young, and they may therefore help us understand how galaxies have evolved. One approach to finding these distant galaxies is to search around the brightest beacons in the early Universe: Quasars. A quasar is thought to be a supermassive black hole in the centre of a galaxy, swallowing matter at a high rate and converting gravitational energy into the intense radiation we observe with our telescopes. Quasars are expected to be located in regions of the Universe containing the highest densities compared to the surroundings, and due to energy feedback from quasars to their host galaxies and environments, there is a intimate link between the evolution of quasars and galaxies.

In this thesis is presented a method to constrain parameters that go into the cosmological model of the geometry of the Universe. This method uses observations of distant, faint galaxies aligned in long, thin strings ("filaments"), the directions of which are assumed to be distributed evenly in three dimensions. The efficiency of the method is analyzed, meaning how tight constraints may be placed on the cosmological parameters for reasonable numbers of filaments.

Deep spectroscopic observations of a number of very distant quasars are also presented in this thesis. The spectra are analyzed, searching in particular for faint, extended emission from hydrogen gas associated with the quasar. The observed extended emission around one quasar is interpreted in a simple model of cosmological infall of gas which is illuminated by the radiation from the quasar. Drawing on previously published detections of this type of extended emission from distant quasars, a statistical comparison is presented, resulting in tentative evidence for a difference in luminosity between extended emission around quasars from two different subclasses. The extended emission is explained as infalling hydrogen illuminated by the quasar, although outflowing gas expelled and illuminated by radiation from star formation is not ruled out.

Dansk resumé. *Forståelsen af hvordan galakser i Universet omkring os er opstået er en af de største udfordringer i moderne astronomi. En måde hvorpå man kan tilvejebringe information, der kan bidrage med brikker til dette puslespil, er ved at observere meget fjerne galakser. Disse galakser udsendte deres lys på et tidpunkt, hvor galakserne og Universet selv var unge, og de kan derfor hjælpe os til at forstå hvordan galakserne har udviklet sig. En metode til at finde disse fjerne galakser er at lede i nærheden af Universets kraftigste fyrtårne: Kvasarer. En kvasar tænkes at være et meget tungt sort hul, der befinder sig i centret af en galakse, og som sluger stof med stor hast, og derved omdanner gravitationel energi til den intense stråling, vi observerer med vores teleskoper. Kvasarer forventes at befinde sig i områder af Universet med den højeste tæthed sammenlignet med omgivelserne, og på grund af tilbagekobling af energi fra kvasaren til galaksen og omgivelserne er der en nær forbindelse mellem dannelsen af kvasarer og galakser.*

I denne afhandling bliver en metode til at begrænse de tilladte værdier for parametre, der indgår i den kosmologiske model af Universets geometri, præsenteret. Denne metode gør brug af observationer af fjerne, svagt lysende galakser, der er arrangeret i lange, tynde strenge ("filamenter"), hvis retninger antages at være jævnt fordelte i tre dimensioner. Effektiviteten af denne metode bliver analyseret med henblik på at finde ud af hvor snævre grænser, der kan blive sat for de kosmologiske parametre med et rimeligt antal filamenter.

Dybe spektroskopiske observationer af et antal meget fjerne kvasarer bliver også præsenteret i denne afhandling. Spektrene bliver analyseret med henblik på at finde svagt, udstrakt lys fra brintgas knyttet til kvasaren. Det observerede udstrakte lys omkring en af kvasarerne bliver fortolket i en simpel model med kosmologisk indfaldende gas, der bliver oplyst af kvasarens stråling. Ved at trække på tidligere offentliggjorte fund af denne type udstrakt lys omkring fjerne kvasarer bliver en statistisk sammenligning præsenteret. Sammenligningen resulterer i den forsigtige konklusion, at der sandsynligvis er forskel på styrken af det udstrakte lys fra to forskellige underinddelinger af kvasarer. Det udstrakte lys bliver forklaret som indfaldende brintgas, der bliver oplyst af kvasaren, selvom udstrømmende gas, der bliver drevet ud og oplyst af stråling fra stjernedannelse, ikke er udelukket.

Chapter I

Introduction

THE Universe is a magnificent place. Containing a multitude of baryons and dark matter weaving a fine cosmic web over truly vast distances, it is hardly comprehensible. Still, we try to find order in the chaos. One of the most important undertakings in modern Astronomy is to understand how the Milky Way and the galaxies we observe around us came to be. A fraction of the galaxies are known to contain a very bright nucleus; these are known as active galactic nuclei (AGN). The study of galaxy formation is closely coupled to the study of AGN, because probably all galaxies go through a stage of an active nucleus. Quasars are the brightest members of the AGN family, where the active nucleus completely outshines the combined light of the entire galaxy, and as such they are interesting for the study of galaxy formation in the distant, early Universe.

This thesis concerns itself with the environments of quasars studied by use of the Lyman-α (Lyα) emission line of hydrogen at a wavelength of 1215.67 Å. Since quasars are one of the main topics, we shall first give an introduction to AGN in general and quasars in particular. We shall then proceed to describing the observed properties of AGN, followed by a discussion of how these observables may be understood in terms of physical parameters. Subsequently we turn to discussing radio-loud and radio-quiet quasars in particular. Lastly, we briefly address the topic of Lyα emitting galaxies, and how narrow-band selection may be useful for a number of studies.

1.1 Some history and background

History serves as a useful reminder of how far we have reached in a relatively short timespan. After all, only 85 years ago we were still debating the "scale of the Universe" in the 1920 Great Debate (Trimble 1995). In this introduction we shall therefore seek to include brief reminders of

some aspects of the historical background.

1.1.1 The AGN zoo

AGN researchers have over the years employed a great variety of classifications and definitions. In this section we will go through the most commonly used definitions, their discoveries and basic characteristics. The intention is not to give the complete picture of all AGN related discoveries, but rather to present a broad overview of the field.

Seyfert galaxies

Galaxies with rather unusual spectra containing high-excitation nuclear emission lines on top of an ordinary galaxy spectrum were first studied in the early 20th century (Fath 1909; Slipher 1917; Hubble 1926). In a systematic study of 6 spiral galaxies Seyfert (1943) recognized that the objects formed a distinct class. The emission lines typical of objects in this class were either all broad (~ 3000 km s^{-1}), or all forbidden lines were narrow and permitted lines broad ($\gtrsim 4000$ km s^{-1}). This is markedly different from H II regions (at that time called "diffuse nebulae") that all exhibited narrow emission lines. Objects with these characteristics were commonly referred to as Seyfert galaxies. Later, this classification was split into two subclasses, Seyfert 1s and Seyfert 2s, where a Seyfert 1 galaxy has broad lines and a Seyfert 2 galaxy has narrow lines (Khachikian & Weedman 1974).

Radio galaxies

Early radio astronomy (in the 1940's) suffered severely from lack of astrometric precision, making it impossible to link positions of powerful radio sources to known optical sources. However, evidence for the identification of radio emission from otherwise normal galaxies was conclusively established during the first half of the 1950's (Baade & Minkowski 1954). During the next decade, following the advance of radio technology and observational techniques, a large number of optical counterparts to known radio sources were identified, and many new radio sources were discovered. Still, a simple classification scheme was difficult to construct due to the relative poorness of the spatial resolution in radio observations, and the large variation in optical morphology (but see Matthews et al. 1964). Fanaroff & Riley (1974) suggested a morphological classification of radio galaxies displaying two or more bright components ("hotspots" or jets). They noticed that radio galaxies with hotspots close to the nucleus (called FR I galaxies) had systematically fainter radio emission than radio galaxies with hotspots further away

(called FR II galaxies). The FR I galaxies have extended radio lobes that become fainter with increasing distance to the centre with no clear termination of the jet, in contrast to FR II galaxies where the radio lobes are collimated and increasingly bright, ending in luminous "hotspots" (see Fig. 1.1). Later it has become clear that FR II galaxies appear to be otherwise normal giant elliptical galaxies, whereas FR I galaxies apparently are larger, brighter and display flatter surface brightness profiles than normal ellipticals (Owen & Laing 1989). FR II galaxies have more luminous optical emission lines (Zirbel & Baum 1995) and are found in less rich environments compared to FR I galaxies (Prestage & Peacock 1988).

Another typical definition follows the Seyfert galaxies by dividing radio galaxies into narrow-line (narrow-line radio galaxy, NLRG) and broad-line (broad-line radio galaxy, BLRG) ones.

Radio-loud quasars

The third Cambridge (3C) survey of a part of the northern radio sky (Edge 1959; Bennett 1962) provided precise positions of many radio sources, and its large catalogue of objects was a breakthrough in radio astronomy. Based on this catalogue still more accurate positions were determined for a number of point-like objects which were thought of as "radio stars" (also called quasi-stellar radio sources or quasars). The subsequent optical identifications yielded point-like objects, some surrounded by faint extended emission. The optical spectra turned out to contain broad emission lines at peculiar wavelengths. However, Schmidt (1963) noticed that the unusual optical emission lines in 3C 273 corresponded to the Balmer lines Hβ, Hγ, Hδ, and Hε at a redshift of $z = 0.16$. This realization spurred a large number of other redshift discoveries. The large redshifts were best explained as cosmological redshifting (Greenstein & Matthews 1963; Gunn 1971), indicating vast distances and astounding luminosities. Many radio-loud quasars (RLQs) were seen to be surrounded by faint "wisps", later recognized as host galaxies or jets.

Radio-quiet quasars

It was rather early clear that the radio selected quasars displayed an excess of UV emission compared to normal stars (Matthews & Sandage 1963). Sandage (1965) used this discovery for an optical search for quasars, and the result was remarkable. Apart from the quasi-stellar radio sources, there was a whole population of quasi-stellar objects with the same UV excess, but lacking the radio emission. The radio-quiet

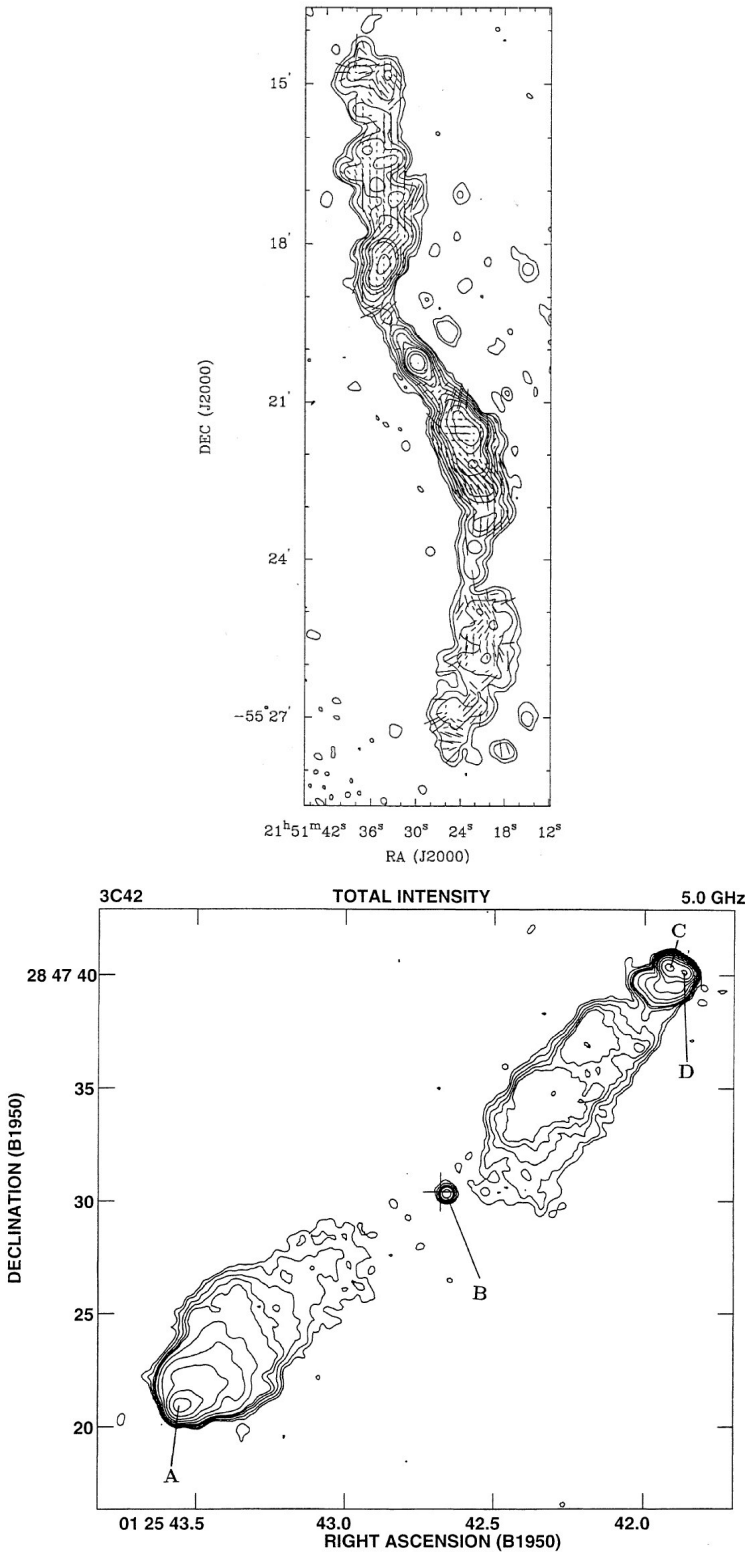

Figure 1.1 Examples of FR I (top) and FR II (bottom) radio galaxies. **Top:** 5.82 GHz radio contours of the FR I galaxy B2148-555 with a resolution of 16 arcsec. The lines are magnetic field direction and fractional polarization, where a length of 1 arcsec represents 2.5% polarization. Taken from Lloyd & Jones (2002). **Bottom:** 5 GHz radio contours of the FR II galaxy 3C 42 with a resolution of 0.41 arcsec. Taken from Fernini et al. (1997).

quasars (RQQs[1]) found in this way outnumber the RLQs by a large factor; ~ 500 according to Sandage (1965), but a more recent estimate is ~ 10 (e.g. Cirasuolo et al. 2003a). The optical spectra of both radio-loud and radio-quiet quasars are well described by broken power-laws (Oke 1963; Vanden Berk et al. 2001), indicating a non-thermal source of energy. Furthermore, the optical flux was observed to vary on a timescale of days to years (Matthews & Sandage 1963), setting an upper limit to the extent of the central engine powering the quasar of several of parsecs (Smith & Hoffleit 1963). For a more modern review of variability in AGN, see Ulrich et al. (1997).

Blazars

Virtually all highly polarized AGN have remarkably similar characteristics: Violent variability, a compact, strong, flat-spectrum radio source, and a smooth continuum extending from the optical far into the infrared. This was noted by Angel & Stockman (1980) who (based on a suggestion from Ed Spiegel) adopted the name "Blazar" for this class of objects. This very small class consists of BL Lacertae objects with a non-thermal spectrum and weak or absent emission lines and quasars that display a very high level of variability. The variability of blazars can provide a wealth of information about the inner working of the central engine, and this makes it an important class to study.

Low-ionization nuclear emission region galaxies

Heckman (1980) identified low-ionization emission regions in the nuclei of a number of otherwise normal galaxies. He defined the class of low-ionization nuclear emission regions (LINERs) as galaxy nuclei with line flux ratios [O II] $\lambda 3727$/[O III] $\lambda 5007] \geq 1$ and [O I] $\lambda 6300$/[O II] $\lambda 5007 \geq 1/3$, although other definitions exist. Heckman (1980) concluded that these narrow-line regions are powered by the same type of source as Seyferts, which was later supported by Keel (1983). Given the observed similarities between Seyfert galaxies and quasars, indicating a common source of power, if indeed LINERs were a low-luminosity equivalent of Seyferts this would suggest that the central engine of quasars were able to scale in power from the brightest quasars down to very faint AGN.

[1]Radio-quiet quasars have earlier been referred to as QSOs, although this term now is used for both the radio-quiet and radio-loud types. In this thesis we shall use the terms quasar and QSO interchangeably.

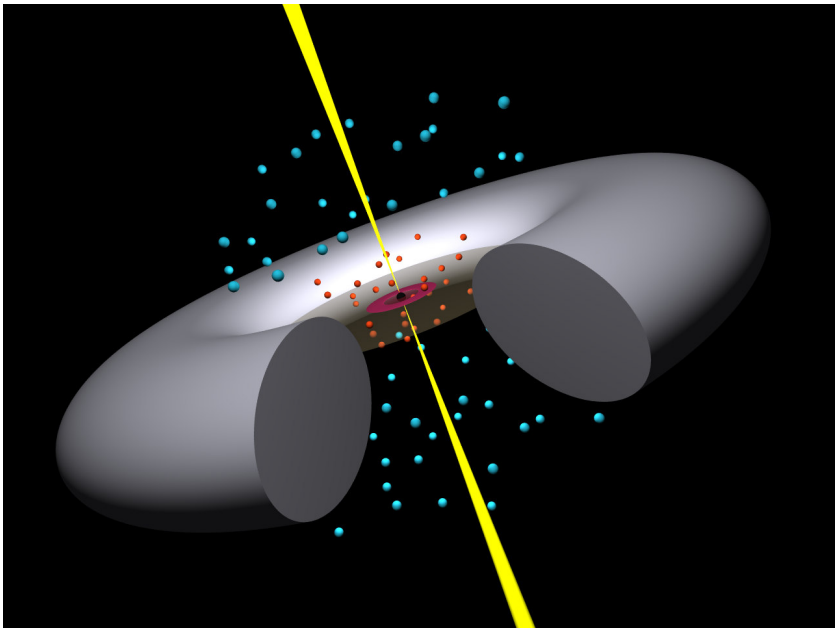

Figure 1.2 Schematic cross-section of the AGN standard model.

1.1.2 Combining the pieces...

Efforts have been made to unify all the different members of the AGN family in a single theory. The goal of such a unified theory is to present a model in which a small number of parameters are sufficient to account for all observed properties. The observed properties of AGN fall along three parameters: Luminosity, radio-loudness and emission line widths. The current paradigm for AGN unification is as follows.

The central engine of an AGN is thought of as a supermassive black hole (SMBH) surrounded by a luminous accretion disk (purple disk in Fig. 1.2) which feeds gas to the black hole (BH). The gravitational energy extracted by this process is radiated away as highly energetic photons or escapes in a jet. Broad emission lines are produced in clouds moving fast (red spheres in Fig. 1.2) in the gravitational potential close above and below the accretion disk. Further away from the BH a thick torus of gas and dust (grey torus in Fig. 1.2) is located, efficiently blocking direct optical and UV sightlines to the broad-line region (BLR) and the BH at high inclination angles. Narrow emission lines are produced in slower moving clouds (light blue spheres in Fig. 1.2) even further out. In case of a radio-loud source, energetic particles stream out along the poles of the obscuring torus at relativistic speeds, resulting in a collimated radio jet (yellow cones in Fig. 1.2) extending from the BH.

In this picture three parameters are needed to explain most of the observed properties (see Table 1.1). One parameter is a simple geo-

Radio–loudness	Optical emission line properties: Type 2 (narrow line)	Type 1 (broad line)	Type 0 (unusual)	
Radio–quiet	Sy 2 NELG IR quasar?	Sy 1 QSO	BAL QSO	Black hole spin or mass?
Radio–loud	FR I, FR II } NLRG	BLRG SSRQ	BL Lac, FSRQ } Blazars	

Decreasing angle to line of sight

Table 1.1 Overview of the AGN taxonomy in the unified model. Within each of the groups the objects are listed by increasing luminosity. Adapted from Urry & Padovani (1995).

metrical effect, the inclination angle. Changing the inclination angle affects which regions are visible to the observer (due to the obscuring torus), and if a powerful radio jet is present the observed spectral energy distribution alters shape. Viewing the obscuring torus close to edge-on reveals a narrow line galaxy (Seyfert 2 or NLRG; see Fig. 1.2), while decreasing the angle to the line of sight changes the identification to a broad line galaxy (Seyfert 1 or BLRG), a radio-quiet quasar (abbreviated QSO in Table 1.1), or a radio-loud quasar (steep-spectrum radio-quasar; SSRQ). Decreasing the angle even further, so that the system is seen close to face-on causes the emission to be dominated by the relativistically beamed jet (in case of a radio-loud source), and only a strong, rapidly varying continuum (Blazar) or a flat-spectrum radio-loud quasar (FSRQ) is visible. In case of a radio-quiet source the object appears to be a radio-quiet quasar with broad absorption lines (BAL QSO; Aldcroft & Green 2003).

The nature of the second parameter which controls the radio-loudness is more unclear. It has been suggested that the radio-loudness was powered by the BH spin (Blandford 1990; Wilson & Colbert 1995), but since all BHs are predicted to rotate rapidly at all epochs this does not seem to be a viable controlling parameter (Madau 2005). It has been suggested that the observed radio-loudness could be coupled to the BH mass (Laor 2000), and indeed it seems that there exists a threshold BH mass which triggers the onset of radio activity (see also Sect. 1.4.4; Magliocchetti et al. 2004; Metcalf & Magliocchetti 2005).

The third parameter which governs the intrinsic luminosity probably finds it physical origin in the process of accreting matter onto the central BH. It could be the accretion rate (Lawrence 2005), the radiative efficiency (Di Matteo et al. 2000), or something completely different.

Numerous studies exist supporting the unified scheme for AGN, the strongest argument probably being the detection of broad emission lines

(Type I object) in polarized light from otherwise typical narrow-line (Type II) galaxies (e.g. Antonucci 1984; Antonucci & Miller 1985). A detailed account of the evidence supporting the unification scheme is beyond the scope of this introduction; instead we refer the reader to the reviews and papers of Antonucci (1993), Urry & Padovani (1995), and Urry (2004). (Note, however, that we discuss the RLQ - RQQ unification in Sect. 1.4, since it has direct relevance for the work presented in this thesis.) More interesting are possibly the problems faced by the model, since they are indicators of areas inadequately described by the model.

As an example, a number of studies in X-rays and at submillimetre (submm) and radio wavelengths have found evidence for a luminosity dependent fraction of obscured AGN (Ueda et al. 2003; Grimes et al. 2004, 2005; Barger et al. 2005; Bassani et al. 2005), which is not possible within the standard unification scheme (but see Dwelly & Page 2005; Haas et al. 2005 for dissenting views). The "receding torus" model (Lawrence 1991) provides an explanation for these observations. In this model the optical depth of the torus decreases, and the radial distance between the central BH and the obscuring torus increases with AGN luminosity, while other parameters such as the torus height remain constant. The effect is that the opening angle of the torus as seen from the BH, and therefore the fraction of unobscured AGN, increases with luminosity, as observed.

Indications pointing towards the existence of "true" Type II AGN (i.e. AGN with no obscured BLR) has led Laor (2003) to suggest a model with an upper limit to the width of the broad emission lines. For low-luminosity AGN the width of BLR lines should increase dramatically until a certain limit is reached, at which point the BLR region vanishes altogether (Laor 2003). In this model some Type II objects are "true" Type II objects, meaning that the BLR is missing entirely, not just obscured.

The standard model has persisted for many years, and it (or some variant of it) provides a good, but not perfect, basis for understanding various constituents of the AGN class. However, it is inherently a static model of the column density distribution, and no time evolution is taken into account. In semi-analytical models, the time evolution is instead kept in a separate model, as is the case of the "light-bulb" model where the quasar luminosity is either on or off, or the constant Eddington ratio model where the BH grows at a constant Eddington ratio $\varepsilon = \frac{L_{\rm Edd}}{\dot{M}c^2} \approx 0.1$ (here $L_{\rm Edd}$ is the Eddington luminosity[2] and $\dot{M}$ is the mass accretion rate), i.e. exponential growth (e.g. Kauffmann & Haehnelt 2000; Wyithe

[2]The Eddington luminosity is the luminosity needed for the force induced by radiation pressure to balance the gravitational force.

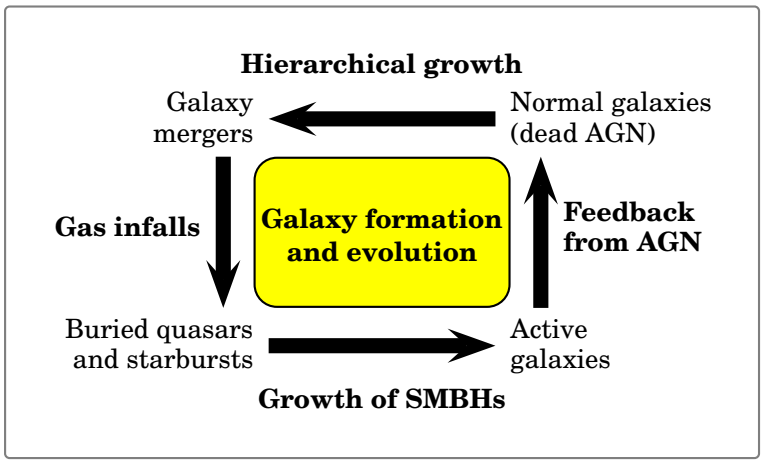

Figure 1.3 Illustration of the "cosmic cycle" for galaxy formation and evolution. Adapted from Hopkins et al. (2005a).

& Loeb 2002; Begelman & Nath 2005). Since a full numerical treatment of the problem is not feasible with present-day computing power, semi-analytical models for e.g. BH accretion and AGN feedback have been employed (e.g. Kauffmann & Haehnelt 2000; Ciotti & Ostriker 2001; Croton et al. 2005), in order to reproduce specific observables. We refer to Hopkins et al. (2005a) for a nice introduction to the various models.

Recently, numerical models of galaxy mergers have been reported which incorporate BH growth and feedback (Springel et al. 2005a), star formation and supernovae (Springel & Hernquist 2003). These are still rather crude approximations compared to solving the full problem, but the dramatic impact they have on the simulations (Di Matteo et al. 2005; Springel et al. 2005a,b) has made it clear that these mechanisms cannot be ignored. Especially the presence of a SMBH has profound effects on the merger remnant by creating large-scale blowouts of gas, leaving behind a gas-poor galaxy with low star formation rate (Di Matteo et al. 2005). These models have provided a nice basis for elucidating aspects of galaxy and quasar formation. Examples include the quasar lightcurve which instead of the simple light-bulb or constant Eddington ratio models is a rapidly varying function of time (Hopkins et al. 2005b), and the column density distribution which is not due a static configuration but rather a spatially and temporally varying phenomenon due to strong gas inflows that bury the central SMBH (Hopkins et al. 2005c). How other members of the AGN family fit into this general picture is not yet clear.

Summarizing the current paradigm for coupled galaxy and quasar formation in a single illustration (Fig. 1.3), Hopkins et al. (2005a) present a nice overview of the general understanding of galaxy formation today,

which we will recapitulate here. In the hierarchical build-up of galaxies mergers are expected be very common, and mergers of two gas-rich systems will cause strong inflows of gas which triggers bursts of star formation and fuel the SMBH growth. The strong inflows leave the SMBH buried for long periods of time, resulting in an obscured quasar. The feedback from the violent growth of the SMBH in turn causes most of the gas and dust to be expelled, leaving behind a visible quasar. The luminous quasar phase is brief, because most of the gas fuelling the quasar has been expelled, and as the quasar activity no longer can be maintained, the merger remnant settles down to a normal galaxy. This normal galaxy may later be involved in yet another merger event, repeating this scenario. How long this picture will last is yet to be seen.

1.2 What do we actually see?

It is not possible directly to probe the physical parameters going into the model. Instead the model must be used to predict observables. This section concerns itself with observable properties of AGN as a class.

1.2.1 Luminosity function and space density

The luminosity function holds important information about the demographics of the AGN population, providing hard constraints on any model of their evolution; e.g. the quasar lifetime and luminosity evolution. With the arrival of large optical surveys such as the Sloan Digital Sky Survey (SDSS; Gunn & Knapp 1993) and the 2-degree Field (2dF) QSO redshift survey (Smith et al. 1997), a detailed study of the AGN optical luminosity function has become possible.

One of the most detailed mappings of the AGN optical luminosity function has been carried out using the 2dF-SDSS luminous red galaxy and QSO (2SLAQ) survey, which in a sense is a merger of the 2dF and SDSS quasar surveys (but see also Fan et al. 2001; Croom et al. 2004). It is based on observations of more than 5600 quasars at $z < 3$ carefully selected to constrain the faint-end slope. The resulting optical luminosity function is shown in Fig. 1.4 (Richards et al. 2005), and it is seen to agree well with 2dF luminosity function (solid line, Croom et al. 2004) at the bright end. However, Richards et al. (2005) find a steeper slope at the faint end, and this could be an effect of incompletion in the 2dF survey.

Combining the optical luminosity function with observed luminosity functions in other wavebands makes it possible to constrain evolutionary models even further. The X-ray luminosity function has been determined by Ueda et al. (2003) and Barger et al. (2005), and their fits –

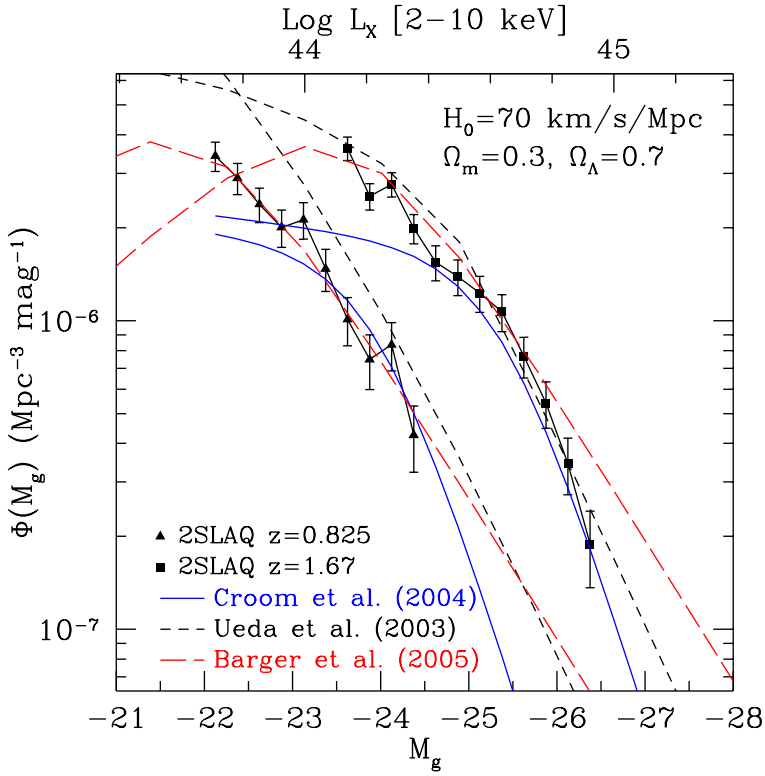

Figure 1.4 Comparison of the 2SLAQ optical quasar luminosity function with X-ray quasar luminosity functions from the literature. Shown are the $z = 0.825$ (triangles) and $z = 1.67$ (squares) quasar luminosity function from 2SLAQ and the best-fitting models for those redshifts from three other papers. The models are from Croom et al. (2004, solid line; optical data), Ueda et al. (2003, dashed line; X-ray data), and Barger et al. (2005, long-dashed line; X-ray data). Taken from Richards et al. (2005).

normalized and converted to M_g as described in Richards et al. (2005) – are also shown in Fig. 1.4 (dashed line and long-dashed line, respectively). The close agreement between the X-ray luminosity function and the optical luminosity function determined from the 2SLAQ survey suggests that there indeed could be a problem with the faint end of the 2dF luminosity function.

Another important and directly observable property of AGN is the space density and its evolution with redshift. The space density is in principle easily determined as the number of objects detected divided by the size of the surveyed volume. In practise one has to carefully consider incompleteness effects, detection limits, and obscuration.

Hasinger et al. (2005) have used a selection of ~ 1000 AGN from various ROSAT, XMM-Newton and Chandra surveys to calculate the space density of unabsorbed AGN. Their results are compared to optical

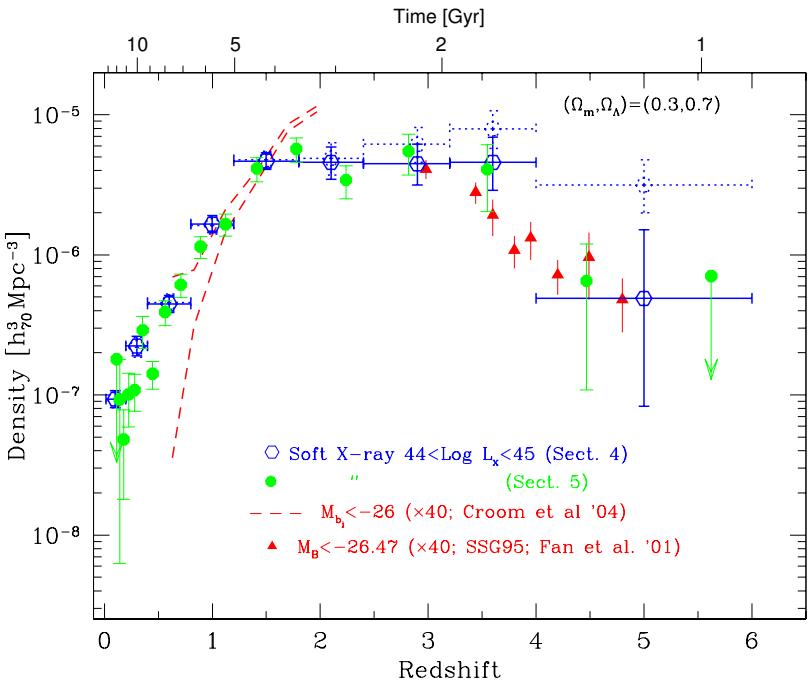

Figure 1.5 Comparison of the space density of luminous QSOs between optically selected and soft X-ray selected samples. The data marked by a dashed line and by triangles have been scaled by a factor of 40 to match the soft X-ray density at $z = 2.7$. Adapted from Hasinger et al. (2005).

surveys in Fig. 1.5. We note that there is a broad peak in the redshift evolution of the space density of AGN. The space density increases dramatically by almost two orders of magnitude between $z = 0$ and the peak at $z \approx 2$. Beyond $z \approx 2$ the space density decreases at a less dramatic pace. However, the effect is even more spectacular plotted against time instead of redshift (note the time axis at the top of Fig. 1.5). At $z = 4$ the Universe is close to 1.5 Gyr old, in which time many AGN are already fully formed. The space density is within an order of magnitude of its peak value between redshifts $z \approx 4$ and $z \approx 1$; the time between $z = 4$ and $z = 1$ is around 4 Gyr. The remaining time from $z = 1$ to $z = 0$ is around 8 Gyr. So the AGN population rises very quickly after the big bang, peaks after ~ 3 Gyr, and then falls off rapidly. It is intriguing to note that the AGN space density peak coincides with the peak in the global star-formation rate (e.g. Somerville et al. 2001), suggesting that the formation of galaxies and AGN are closely linked.

Splitting the space density evolution according to luminosity as presented in Fig. 1.6 a very interesting effect becomes evident: The most luminous AGN peaked at higher redshifts (Ueda et al. 2003; Hasinger

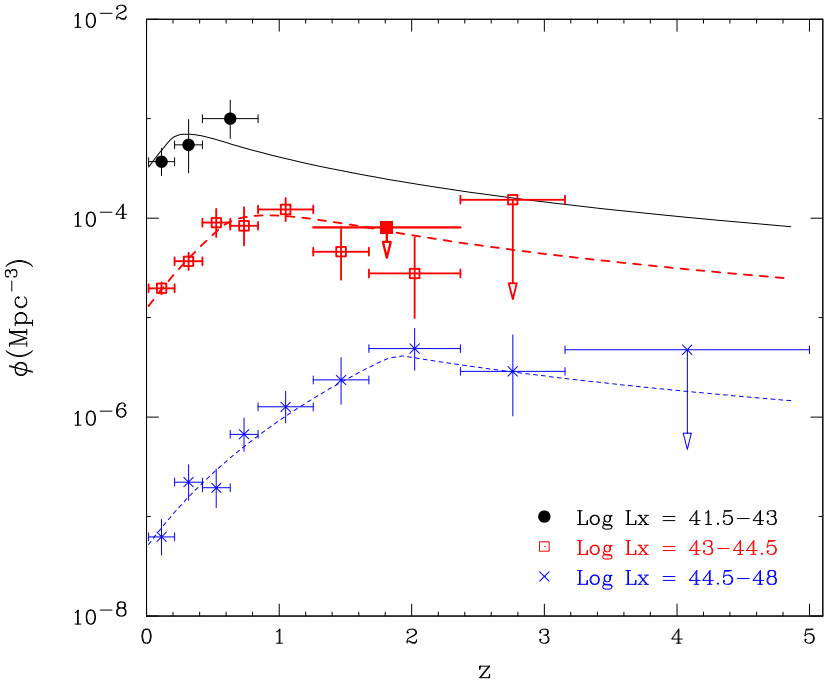

Figure 1.6 Comoving space density of AGN as a function of redshift in three luminosity ranges, $\log L_{\mathrm{X}} = 41.5 - 43$ (solid line), $\log L_{\mathrm{X}} = 43 - 44.5$ (dashed line), and $\log L_{\mathrm{X}} = 44.5 - 48$ (dotted line). Taken from Ueda et al. (2003).

et al. 2005)! In these observations the most luminous AGN peak close to $z = 2$, while the less luminous AGN peak lower than $z = 1$. In other words the most luminous AGN seem to have formed first, apparently at odds with the standard hierarchical formation scenario, in which small substructures merge to form larger bodies. However, if smaller structures (less luminous) took longer to form than their larger (more luminous) siblings, the apparent contradiction could vanish. By way of an aside we note that this effect of downsizing has also been observed in galaxy formation (Cowie et al. 1996; Treu et al. 2005).

Finally, a very powerful constraint on the models is provided by the following simple fact: Currently seven quasars are known at $z \approx 6$ (Fan et al. 2003), at which time the Universe was merely 900 Myr old. This is indeed a great challenge to most modellers, because forming a SMBH of $> 10^9 M_\odot$ (Willott et al. 2003) in less than a Gyr is non-trivial. Growth by gas accretion would imply super-Eddington rates unless the BH is able to grow undisturbed for the age of Universe at $z = 6$ (Shapiro 2005). Growth by mergers depends critically on the mass and space density of the seed BHs[3]. If the seed mass is too low a higher density (resulting in

[3]The seed BH is typically thought to be the end product of the first generation (population III) stars.

a higher merger rate) is required. However, if the density is too high, the rate of three-body interactions rises. A merger of three BHs invariably leads to the ejection of one of the BHs and thus resulting in a population of massive BHs wandering in galaxy halos and the intergalactic matter (Volonteri et al. 2003).

1.2.2 Clustering

The spatial distribution of AGN represents the underlying distribution of matter fluctuations distorted by the complex feedback from BH formation. By statistical comparison of clustering studies and numerical simulations of cold dark matter it is possible to infer physical properties such as AGN lifetime and mass of the parent dark matter (DM) halo (see Sect. 1.3.1 and 1.3.2). Following the first detection of AGN-AGN clustering (Shaver 1984) samples have increased in size, improving the precision (e.g. Croom & Shanks 1996; La Franca et al. 1998). Surveys have now been extended to X-ray wavelengths (Mullis et al. 2004; Gilli et al. 2005; Basilakos et al. 2005), and the search for evolution in the clustering signal has begun (Porciani et al. 2004; Croom et al. 2005).

In terms of the two-point correlation function, which measures the excess probability of finding two objects at a given distance from each other, the clustering follows a power-law with a scale length of $r_0 = 5 - 8h^{-1}$ Mpc and a slope of $\gamma = 1.2 - 1.8$. Modern surveys (both optical and X-ray) seem to favour a slope lower than the classical value $\gamma = 1.8$, whereas the value for the scale length appears to remain in the neighbourhood of $r_0 = 6h^{-1}$ Mpc (Gilli et al. 2005; Croom et al. 2005; Porciani et al. 2004). Furthermore the clustering strength is seen to increase with redshift, meaning that AGN were more strongly clustered in the past.

On a related note, we shall now turn to the topic of clustering between galaxies and AGN – i.e. the environments of AGN. We shall defer the treatment of quasar environments a while (see Sect. 1.4.2), and start out with the low and moderate luminosity AGN.

A number of studies of low-luminosity AGN (mostly Seyferts) have been performed, and consensus has been reached that they are generally found in environments indistinguishable from that of inactive galaxies (Miller et al. 2003; Wake et al. 2004; Waskett et al. 2005). Note, however, that Kaufffmann et al. (2004) in a study of SDSS data find that AGN are twice as often found in low density environments as in high density ones. The discrepancy is ascribed to their AGN classification based on the [O III] emission line, which misses many objects that would have been considered AGN in other surveys (Waskett et al. 2005). Furthermore, it is noticed that the fraction of active galaxies remains $\approx 20\%$ over a large range of environment densities (Miller et al.

2003; Wake et al. 2004). This high and constant fraction means that the fuelling of low-luminosity AGN occurs commonly, and is unlikely to be related to major-mergers. It has been suggested that the fuelling of low-luminosity AGN could be due to the more common minor-mergers of small satellite galaxies or primordial gas clouds which leaves the host galaxy more or less undisturbed (Waskett et al. 2005; Ballantyne et al. 2005).

Surprisingly, it seems that Seyfert 1s tend to be located in slightly poorer environments compared to inactive galaxies, while Seyfert 2s are in significantly richer environments (Laurikainen & Salo 1995; de Robertis et al. 1998; Dultzin-Hacyan et al. 1999; Koulouridis et al. 2005). This difference between Seyfert 1s and 2s is difficult to explain within the AGN standard model and remains a puzzle.

1.3 Welcome to the real world

The properties discussed in the previous section are simply the observable manifestations of the underlying physical parameters. This section is devoted to the presentation of the most important of these parameters.

1.3.1 Lifetime

The briefness of the AGN epoch in the history of the Universe (discussed in Sect. 1.2.1) suggests that nuclear activity in a galaxy is a passing phenomenon. This suspicion is strengthened by the facts that all spheroids (i.e. all elliptical galaxies and bulges of spirals) host a SMBH (Magorrian et al. 1998; Gebhardt et al. 2000a; Merritt & Ferrarese 2001; Tremaine et al. 2002), while only a small fraction of galaxies display nuclear activity. An excellent review of quasar lifetimes is given in Martini (2004).

A strict upper limit of $\sim 10^9$ yr is set to the AGN lifetime (i.e. the total integrated time of nuclear activity) by the rise and fall of the space density (Fig. 1.5; see e.g. Osmer 2004). A lower limit of 10^5 yr may be obtained based upon the requirement that the quasar should survive long enough to emit sufficient radiation to cause the observed enhancement of the ionization fraction in Lyα clouds close to the quasar (the "proximity effect"; see e.g. Bajtlik et al. 1988).

The AGN lifetime could be calculated if one knew the fraction of "dead" to "living" AGN. One way of estimating this fraction for quasars is to compare the QSO two-point correlation function described in Sect. 1.2.2 to one calculated in a numerical simulation of the underlying DM distribution. Assuming that luminous quasars reside in the most mas-

sive DM halos, quasars with long lifetimes but occurring only in a tiny fraction of all galaxies will be strongly clustered. On the other hand, if most galaxies experience a brief quasar phase, the quasars will be less strongly clustered (Martini & Weinberg 2001). This clustering argument was used by Porciani et al. (2004) on quasars in the 2dF QSO Redshift Survey to estimate a lifetime of a few times 10^7 yr at $z \sim 1$ and nearing 10^8 yr at higher redshifts. The existence of a large population of obscured quasars (Type II) will mean that the value is underestimated.

An alternative approach – using demographics of the local BH population – has been considered (e.g. Haehnelt et al. 1998; Salucci et al. 1999; Yu & Tremaine 2002). The basic idea is that, assuming a model for luminosity evolution and BH growth, the quasar space density at a given redshift may be compared to the local density of SMBHs. Various studies obtain values between $\sim 10^6 - 10^8$ yr.

A more theoretically based estimate is found by building a suitable model of quasar evolution, and calculating the lifetime within this model. Kauffmann & Haehnelt (2000) construct a semi-analytical model of quasar and galaxy formation on the assumption that SMBHs are formed and fuelled during major mergers of galaxies. They predict that the lifetime evolves as $(1+z)^{-1.5}$ (apparently contradicting the findings of Porciani et al. (2004)) and with a normalization constant of $\sim 2.5 \times 10^7$ yr, which incidentally is the value at $z = 0$. Of a more recent date is the work of Hopkins et al. (2005c,d) who use a hydrodynamical N-body simulation and a set of prescriptions for calculating the more detailed gas and accretion physics to follow the quasar evolution. They find a typical lifetime of $1 - 2 \times 10^7$ yr, and predict that the lifetime increases with increasing final BH mass.

The lifetime estimates covered until now were all total, integrated lifetimes. The episodic lifetime (if the AGN phase was in fact composed of many smaller episodes of activity) can be constrained using observed sizes of various phenomena owing to the nearby presence of a luminous quasar. Among these are e.g. the (radial and transverse) proximity effect (Bajtlik et al. 1988; Adelberger 2004), Strömgren spheres around a high redshift ($z > 6$) quasars where the intergalactic matter is expected to be neutral (Haiman & Cen 2002; Haiman & Loeb 2001), jets (Blundell et al. 1999), and narrow-line regions (Bennert et al. 2002).

1.3.2 Black hole mass

As one of the fundamental parameters of a BH, its mass is dominating the physics of the central engine. The importance of this parameter is clearly demonstrated when reading this section, since a virtual industry has developed for finding observable parameters possibly correlating with the BH mass $M_{\rm BH}$.

Direct measurements

Using high spatial resolution spectroscopy, the dynamics of stars or gas in the nuclear region of a galaxy have been determined (e.g. Kormendy & Richstone 1995; Richstone et al. 1998; Kormendy & Gebhardt 2001), yielding direct measurements of the central BH by assuming that the motion is dominated by gravity (this assumption is well-justified, see e.g. Wandel et al. 1999). The high spatial resolution is essential, making this method best suitable for nearby sources. Furthermore, targets should be inactive galaxies or low-luminosity AGN to avoid contamination from the otherwise bright central point source. A variation on this method is to use megamasers instead of gas or stars. Only a few close-by objects are known to contain water-vapour maser (microwave laser) emission. Megamasers in the circumnuclear disk in NGC 4258 display rotation curves consistent with Kepplerian motion around the central BH (Miyoshi et al. 1995). The inferred BH mass is $3.6 \times 10^6 M_\odot$, with the highest precision yet (a few percent).

An entirely different and very successful technique has been the study of light echos, or reverberation mapping (Blandford & McKee 1982). It builds on the observations that the variability of broad emission lines in AGN follow the variability of the continuum source, albeit with a small time delay. This delay corresponds to the light travel-time within the BLR out to the region where the relevant emission line is formed, allowing measurements of the distance to the central BH. Furthermore the width of the emission lines is due to bulk motion of the gas, not thermal or pressure broadening (Blandford & McKee 1982), so assuming a virialized gas it is possible to determine the mass from $M_{\rm BH} \propto v^2_{\rm FWHM} R_{\rm BLR}$. This approach does not require high spatial resolution, nor is it affected by a bright central point source, making it widely applicable. It is, however, not practical for distant quasars due to their long variability timescale and the time dilation as a result of the cosmological redshifting. However, reverberation mapping provides an effective zero-point calibration for indirect measurements of BH masses, some of which may be extended to higher redshifts.

Indirect measurements

Indirect measurements are typically based on correlations between $M_{\rm BH}$ and some observable quantity. Studies of galaxies measuring stellar velocity dispersion in the bulge and using reverberation mapping to determine the BH mass have found a tight correlation (see Fig. 1.7) between the mass of the BH and the velocity dispersion, $M_{\rm BH} \propto \sigma^4$ (both for active and inactive galaxies; Gebhardt et al. 2000a,b; Ferrarese & Merritt 2000; Ferrarese et al. 2001; Tremaine et al. 2002). BH masses ranging

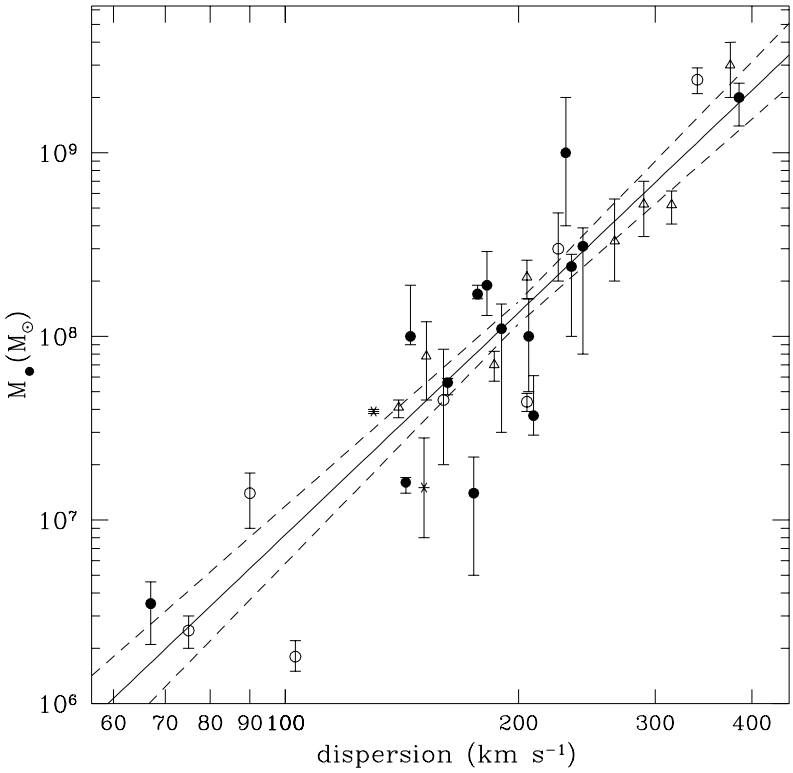

Figure 1.7 BH masses and velocity dispersions. Mass measurements based on stellar dynamics are presented by circles, on gas dynamics by triangles, and on maser dynamics by asterisks; filled circles are measurements by Gebhardt et al. (2000a). The solid line represents the best-fit correlation $M_{\rm BH} \propto \sigma^{4.02\pm0.32}$, the dashed lines are the corresponding 1σ limits. Taken from Tremaine et al. (2002).

from $10^5 M_\odot$ to $10^8 M_\odot$ has been shown to follow the same $M_{\rm BH} - \sigma$ relation (Barth et al. 2005, and references therein). We note that the rather surprising $M_{\rm BH} - \sigma$ correlation makes it clear that there must exist a tight link between the formation of galaxies and BHs.

Analogous to the $M_{\rm BH} - \sigma$ relation, a correlation between the bulge luminosity and BH mass has been found (e.g. Magorrian et al. 1998; Laor 1998; Wandel 1999). In a reverberation mapping study of 17 quasars Kaspi et al. (2000) found that the size of the BLR scales with the rest-frame 5100 Å quasar luminosity, $R({\rm H}\,\beta) \propto L_\lambda^{0.7}$, although the theoretical scaling law predicts $R \propto L_\lambda^{0.5}$. This was used to obtain a scaling relation between the BH mass and the rest-frame 5100 Å luminosity. Since $M_{\rm BH} \propto v_{\rm FWHM}^2 R$ for virialized systems, we expect $M_{\rm BH} \propto v_{\rm FWHM}^2 L_\lambda^\alpha$. Vestergaard (2002) finds $\alpha = 0.7$ for the H β and C IV lines,

while McLure & Jarvis (2002) find $\alpha = 0.47$ when using the Mg II line. Since the line width and continuum luminosities are readily measurable even at high redshifts, the scaling between $M_{\rm BH}$, $v_{\rm FWHM}$, and $L_{\rm bulge}$ offers a great opportunity to estimate the BH masses for very early quasars. McLure & Dunlop (2004) have performed this analysis on a sample of SDSS quasars between redshifts 0.1 and 2.1, and they recover BH masses in the range $10^7 M_\odot \lesssim M_{\rm BH} \lesssim 3 \times 10^9 M_\odot$, consistent with the largest BHs in the local Universe.

Other parameters correlating with BH mass

It has been found that $M_{\rm BH}$ correlates well with the bulge mass $M_{\rm bulge}$, and that $\langle M_{\rm BH}/M_{\rm bulge}\rangle \sim 0.002$ locally (Marconi & Hunt 2003; Häring & Rix 2004). Other studies have investigated the redshift evolution of the BH-bulge mass ratio (Treu et al. 2004; Peng et al. 2005), and McLure et al. (2005) find that $M_{\rm BH}/M_{\rm bulge} \propto (1+z)^{2.07\pm0.76}$. This is inconsistent with both the result of Shields et al. (2003), who find no deviation from the local $M_{\rm BH} - \sigma$ relation in a sample of high redshift quasars, as well as the theoretical prediction that BH growth and spheroid formation occurs together (Hopkins et al. 2005a; Begelman & Nath 2005; Robertson et al. 2005).

In a fashion similar to the calculation of quasar lifetimes (Sect. 1.3.1) from the observed clustering of AGN (Sect. 1.2.2), the mass of the parent DM halo may be estimated by matching observed and simulated two-point correlation functions. In this way Porciani et al. (2004) find in a $z \sim 1$ study of 2dF quasars that all are located in DM halos more massive than $10^{12} M_\odot$, having a characteristic mass of $\sim 10^{13} M_\odot$. A closely related study finds that quasars sit in DM halos with $M_{\rm DM} \approx 3 \times 10^{12} h^{-1} M_\odot$, independent of redshift (Croom et al. 2005), in broad agreement with the work of Adelberger & Steidel (2005). Ferrarese (2002) studied a number of local galaxies, measuring stellar velocity dispersion σ and circular velocity v_c in order to obtain estimates of $M_{\rm BH}$ and $M_{\rm DM}$. Assuming that v_c indeed is a good proxy for $M_{\rm DM}$, she found a (possibly broken power-law) correlation between the BH and DM halo masses (see also Baes et al. 2003).

Finally, McLure & Jarvis (2004) have detected a strong correlation between the BH mass and both the 5 GHz radio luminosity as well as the radio-to-optical flux density ratio $R_{5\ \rm GHz}$ in an SDSS quasar sample. Still, for a given $M_{\rm BH}$ there is a large scatter of several orders of magnitude in radio power and $R_{5\ \rm GHz}$ (see also Sect. 1.4.4).

1.3.3 Obscuration

An important prediction of the AGN standard model is the existence of obscured AGN (Type II), and much observation time has gone into finding these elusive objects. Besides being observable at infrared (IR) and radio wavelengths, the Type II AGN should be detectable in X-rays, unless the obscuring material is Compton-thick (neutral hydrogen column density $N_{\rm H\,I} \gtrsim 10^{24}$ cm^{-2}). By now, Type II AGN have been detected in X-rays, and in optical, IR, submm, and radio bands (Norman et al. 2002; Stern et al. 2002; Della Ceca et al. 2003; Hines et al. 1995; Dawson et al. 2001; Schmidt et al. 2002, 2005; Kleinmann et al. 1988; Rowan-Robinson et al. 1991; Smith et al. 2003; Armus et al. 2005; Martínez-Sansigre et al. 2005; Mainieri et al. 2005; Haas et al. 2005; McCarthy 1993).

A wealth of information has been obtained through X-ray studies of AGN. The soft ($0.5-2$ keV) and hard ($2-10$ keV) X-ray backgrounds have been almost completely resolved into discrete sources (e.g. Hasinger et al. 1998; Hornschemeier et al. 2000; Mushotzky et al. 2000; Giacconi et al. 2002; Moretti et al. 2003), most of which are low-luminosity AGN (Hasinger et al. 2005). This has lead to the conclusion that a significant fraction (75%?) of all AGN are obscured (Urry & Treister 2005). The obscuration is due to a very large column density $N_{\rm H} > 10^{23}$ cm^{-2} (e.g. Ueda et al. 2003).

A number of X-ray observations are apparently at odds with the standard unification model. In order to explain an observed evolution in the fraction of obscured AGN Ballantyne et al. (2005) have suggested that the obscuration could be due to star formation instead of a static torus (but see Dwelly & Page 2005 for a dissenting view). The static torus model is also conflicting with observations of rapid X-ray absorption variability in a selection of Seyfert 2 galaxies (Risaliti 2002; Risaliti et al. 2005). Others have found evidence for Type I and Type II AGN following different evolutionary paths (e.g. Franceschini et al. 2002, and references therein), indicating that the two types are intrinsically different objects.

Some peculiar cases has been seen where low intrinsic absorption ($N_{\rm H} < 10^{21-22}$ cm^{-2}) in X-ray observations are reported for AGN optically classified as Type II objects (e.g. Risaliti 2002; Panessa & Bassani 2002; Wolter et al. 2005; Gallo et al. 2005). As an example Wolter et al. (2005) analyze X-ray spectra of three narrow-line quasars, i.e. Type II quasars where the BLR is expected to be obscured. However, the X-ray spectra only show evidence for weak absorption, meaning that the inner part of the central engine producing the X-rays is not obscured, whereas the outer parts producing the broad lines are. This possibly new class of unobscured Type II AGN poses a challenge to the AGN

unification scheme, but attempts have been made to explain the phenomenon within the frame work of the model, e.g. that the BLR is weak or absent (for a nice discussion see e.g. Wolter et al. 2005). These objects and their interpretations are not yet fully understood.

The opposite situation has also been reported. Page et al. (2005) present observations of a sample of $z \sim 2$ Type I quasars with heavily absorbed X-ray spectra (see also Alexander et al. 2005). Based on submm observations it is suggested that these objects are caught in the brief transitional phase between an ultraluminous infrared galaxy (ULIRG) and a normal quasar (e.g. Page et al. 2005; Stevens et al. 2005).

1.4 Radio-loud – radio-quiet unification?

Having treated AGN in general we now turn to quasars in particular, since they are of direct relevance for this thesis. We shall pay special attention to the apparent radio-loud – radio-quiet dichotomy of quasars.

1.4.1 Radio-loudness

Before it makes sense to discuss any aspect of radio-loudness a definition is called for. Unfortunately, a variety of definitions exist, and a unique classification is difficult, if not impossible.

The conventional definition employs either the radio power at 5 GHz $P_{5\ \mathrm{GHz}}$ or the radio-to-optical flux density ratio R. Classically, R is defined as the ratio 5 GHz radio flux density to 2500 Å optical flux density, $R_{5\ \mathrm{GHz}} = \frac{S_{5\ \mathrm{GHz}}}{S_{2500}}$ (Sramek & Weedman 1980). Another common definition of the radio-loudness parameter R uses the 5 GHz to B-band flux ratio. It was quickly recognized that the quasar population fell in two distinct subgroups, the "radio-quiet" and the "radio-loud" quasars, the radio-loud population usually being catagorized by $R > 10$ (Kellermann et al. 1989) or $P_{5\ \mathrm{GHz}} > 10^{24}$ W Hz^{-1} sr^{-1} (Miller et al. 1990), or both (Falcke et al. 1996; Wold et al. 2001). The radio-loudness distribution was found to be bimodal, and this result has persisted for a number of years (e.g. Sramek & Weedman 1980; Strittmatter et al. 1980; Kellermann et al. 1989; Miller et al. 1990; Stocke et al. 1992; Ivezić et al. 2002). Some studies have found quasars seemingly belonging to a "radio-intermediate" population (Miller et al. 1993), suggested to be relativistically beamed radio-quiet (or radio-weak) quasars (Falcke et al. 1996). However, other studies have weakened or even challenged the claims of bimodality in the radio-loudness distribution (Hooper et al. 1995; Goldschmidt et al. 1999; White et al. 2000; Cirasuolo et al. 2003b), and the dispute continues (Cirasuolo et al. 2003a; Ivezić et al. 2004; Barvainis et al. 2005). An example of the radio-loudness distribution is

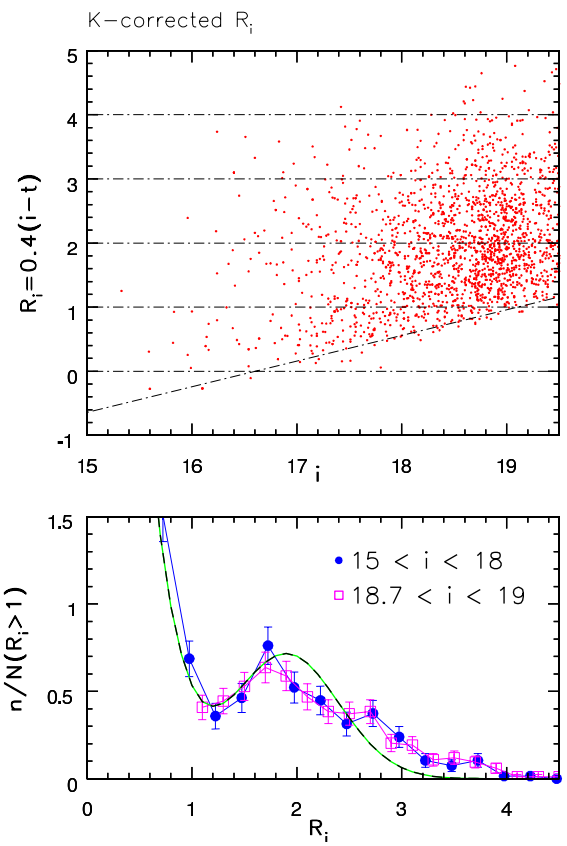

Figure 1.8 Plot of the (K-corrected) radio-loudness parameter $R_i = \log S_{1.4\ \mathrm{GHz}}/S_i$ versus i-band magnitude (top panel) and the distribution of radio-loudness (bottom panel) for quasars in the interval $0.5 < z < 2.5$. The thick line is the best-fit double Gaussian. Taken from Ivezić et al. (2004).

shown in Fig. 1.8, along with the radio-loudness versus i-band magnitude. Irrespective of whether the distribution is bimodal or more continuous, the fundamental observation that otherwise apparently identical objects differ in radio luminosity by several orders of magnitude remains unexplained.

The difference in radio-loudness does not extend to other wavelength bands, where the spectral energy distribution is broadly similar. There is some disagreement as to whether the radio-loud fraction of quasars increases with optical luminosity (Padovani 1993; La Franca et al. 1994; Hooper et al. 1995; Goldschmidt et al. 1999; Impey & Petry 2001) or not (Stern et al. 2000; Ivezić et al. 2002). On a related note, Cirasuolo et al. (2003a) have found no apparent correlation between radio and optical luminosities. These correlations or lack thereof could indicate whether or not the difference between RLQs and RQQs might be due to different evolutionary scenarios, differences in luminosity functions

or underlying physical parameters. Ultimately, this may provide some (circumstantial) evidence for how fundamental any possible bimodality in radio-loudness really is; i.e. how fundamentally different the various quasar populations are.

1.4.2 Environment

Quasars are generally believed to be found in the largest overdensities of the Universe, as a result of quasars being formed during major mergers of galaxies (e.g. Efstathiou & Rees 1988; Carlberg 1990). Quasars located in large DM halos should be surrounded by an overdensity of associated galaxies; an overdensity which may be identified using the angular correlation function.

RLQs are unambiguously found in overdense environments (Wold et al. 2000; McLure & Dunlop 2001; Barr et al. 2003; Zheng et al. 2005), and associated with groups or clusters (Yee & Green 1987; Ellingson et al. 1991), but for RQQs the situation has been less clear. There have been claims that RQQs are found in underdense regions, or at least regions less dense than RLQs (Ellingson et al. 1991; Smith et al. 2000), but recent studies find the environments of RQQs to be consistent with that of RLQs when examining the galaxy-quasar correlation function (Wold et al. 2001; McLure & Dunlop 2001) and the overdensity of $z_{\rm abs} \approx z_{\rm em}$ damped Lyα absorbers (Russel et al. 2005). Thus the environment alone cannot provide the mechanism triggering radio activity.

Still, the close environment of RLQs is dramatically different from that of RQQs: RLQs predominately display tremendous jets emanating from the central engine, ending in bright hotspots. This is not the case for RQQs having at most weak radio emission. In a variability study Barvainis et al. (2005) found that for the majority of radio detected RQQs, the radio signal is emitted from a compact structure intimately associated with the active nucleus (and not due to a starburst), but in a few cases jets are seen. Jets associated with RQQs have also been observed earlier (Blundell et al. 1996; Blundell & Beasley 1998; Ulvestad et al. 2005), but with bulk kinetic powers three orders of magnitude lower than for RLQs (Miller et al. 1993). It has been suggested that the difference in jet appearances may be analogous to the difference between FR I and FR II radio galaxies (Barvainis et al. 2005), since lower power jets are more likely to disrupt and dissipate. Blundell et al. (2003) has voiced concern that the lack of jet detections associated with RQQs could simply be due to lack of radio observations deep enough.

1.4.3 Host galaxy

Early works on quasar host galaxies found the apparent division that RLQs were hosted exclusively by luminous elliptical galaxies, while RQQs were found only in less bright spiral galaxies (Malkan 1984; Smith et al. 1986). Later studies have shown that indeed RLQs are associated with luminous ellipticals, but RQQs are found in both spiral and elliptical galaxies, and RQQs at the bright end of the luminosity function are almost solely hosted by massive ellipticals (e.g. Dunlop et al. 1993; McLure et al. 1999; Schade et al. 2000). One way to understand the early results is to note the difficulties in distinguishing between low-luminosity RQQs and Seyfert galaxies. Since all Seyferts are spirals, a contamination of the quasar sample could lead to a spuriously high level of spiral hosts. At higher redshifts ($1 < z < 2$) a morphological classification is more challenging, but RLQ hosts remain $1 - 2$ magnitudes brighter than hosts associated with RQQ of equal luminosity (Dunlop et al. 2003; Falomo et al. 2001; Kukula et al. 2001). At still higher redshifts the picture is less clear due to the increasing difficulties in detecting a faint host suffering the $(1 + z)^4$ cosmological surface brightness dimming against the glare of a bright quasar. Investigations have mostly concentrated on RLQs (Heckman et al. 1991a,b; Steidel et al. 1991; Lehnert et al. 1992, 1999; Wilman et al. 2000), but a few detections of RQQ hosts have been reported (Bremer et al. 1992; Lowenthal et al. 1995; Fynbo et al. 2000a; Møller et al. 2000; Ridgway et al. 2001; Bunker et al. 2003).

Using radio observations molecular gas has been detected for a number of high-redshift quasars. Both ro-vibrational lines as well as continuum emission are reported (e.g. Guilloteau et al. 1999), making it possible to estimate dust content, gas and virial masses. Typical molecular masses are of the order $10^{10} M_\odot$ for quasars at $z > 4.4$ (Carilli et al. 2002; Iwata et al. 2001; Bertoldi et al. 2003a), while the dust masses are a factor 10 lower (Bertoldi et al. 2003b). Large submm luminosities indicate immense star formation rates of $> 2000 M_\odot$ yr^{-1} for these quasar hosts (Bertoldi et al. 2003b), which is large even compared to the $200 - 300 M_\odot$ yr^{-1} of ultraluminous infrared galaxies (ULIRGs; e.g. Daddi et al. 2005). If these enormous star formation rates hold true, the supply of molecular gas runs out in $< 10^7$ yr (Bertoldi et al. 2003a). Still, it is not yet clear that the emission indeed is powered by star formation; AGN powering remains a viable alternative (Carilli et al. 2002), in which case the quoted star formation rates are invalid.

1.4.4 BH mass

Just as for the general population of AGN the mass of the central BH is a fundamental parameter in the understanding of quasars. The discovery of the correlation between the BH mass and stellar velocity dispersion (or rather the related scaling laws, see Sect. 1.3.2) has spurred many investigations into connections between quasar BH masses and parameters describing the level of radio emission. Correlations or lack thereof could potentially provide insights into the physical parameter(s) governing the radio-loudness.

A collection of such investigations has concluded that on average the BH mass of RLQs is a factor ~ 1.4 more massive than that of RQQs (McLure & Dunlop 2001; McLure & Jarvis 2002; Dunlop et al. 2003; McLure & Jarvis 2004; Laor 2000; Metcalf & Magliocchetti 2005; Marziani et al. 2003). A number of authors have reported finding a correlation between BH mass and radio luminosity or radio-loudness (Nelson 2000; Laor 2000; Lacy et al. 2001; McLure & Jarvis 2004; McLure & Dunlop 2004), although for a given BH mass the radio luminosity has a scatter of several orders of magnitude (McLure & Jarvis 2004). This separation in BH mass with radio power is supported theoretically by the Principal Component analysis (Boroson 2002). On the other hand, Snellen et al. (2003) find that their sample of inactive galaxies shows a correlation between BH mass and radio luminosity, but they also note that this is not the case for their AGN sample, and this view is supported by other studies (Oshlack et al. 2002; Woo & Urry 2002a,b; Ho 2002; Urry 2003; Metcalf & Magliocchetti 2005). Oshlack et al. (2002) and Woo & Urry (2002a,b) argue that the RLQ BH masses found in the interval $10^6 M_\odot < M_{\rm BH} < 10^8 M_\odot$ rule out any correlation between radio power and BH mass. So it appears that BH mass alone cannot explain the radio-loudness dichotomy. However, these findings suggest that exists a threshold in BH mass which controls the onset of radio-loudness (Laor 2000; Magliocchetti et al. 2004; Metcalf & Magliocchetti 2005).

1.5 Lyα emission at high redshift

Since most of the work presented in this thesis revolves around the Lyα emission line, we will dwell for a moment on the question of why this line is useful for studying the distant Universe.

1.5.1 Lyα emitting galaxies

During most of the last decade observations of Lyα emission were considered to be an inefficient way of studying galaxies in the high-redshift Universe. This was in part due to the predicted severe attenuation of

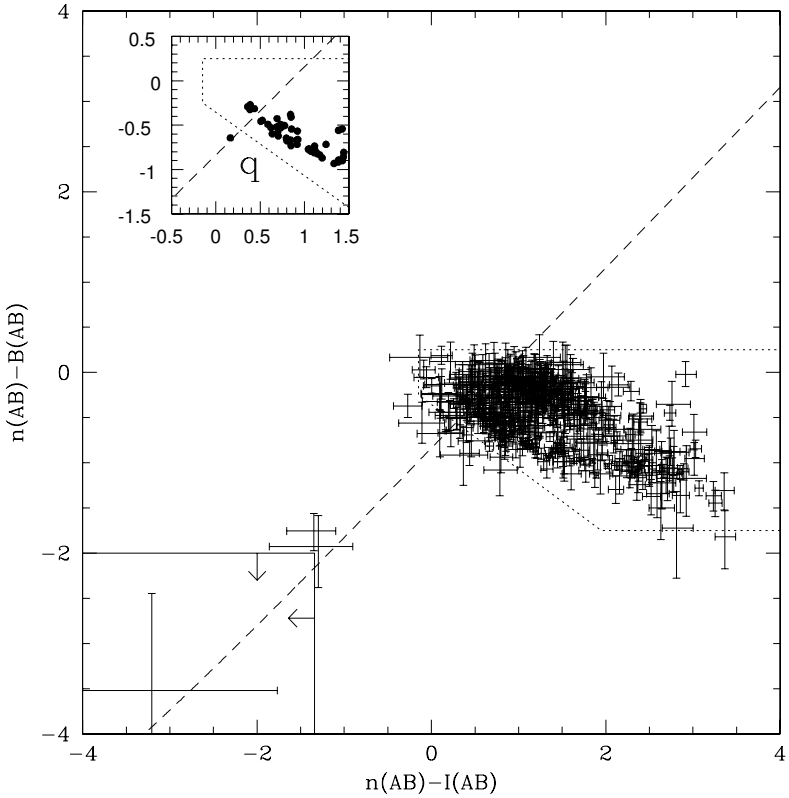

Figure 1.9 Colour-colour diagram. Narrow minus B-band versus Narrow minus I-band for the field of quasar Q 1205-30 at $z = 3.041$. The dashed line is a line of constant $B - I$, but with a spectral feature in the narrow filter ranging from a strong absorption line in the upper right corner to a strong emission line in the lower left corner. The dotted lines confine the expected region of objects with no spectral features in the narrow filter. The insert shows the region of the plot containing Q 1205-30 (marked q) and objects with $S/N > 30$. Taken from Fynbo et al. (2000b).

Lyα photons in the presence of even modest amounts of dust (Ferland & Netzer 1979; Charlot & Fall 1993), and in part due to a number of unsuccessful surveys (e.g. Pritchet 1994, and references therein). Later surveys have made it clear that the lacking success in the earlier surveys was due to too shallow detection limits (e.g. Rhoads et al. 2000; Fynbo et al. 2003a; Ouchi et al. 2003), and now surface densities of Lyα emitting sources as high as 10 arcmin^{-2} per unit redshift are routinely found, the majority of which are much fainter than galaxies selected by other methods (Fynbo et al. 2003a).

For detecting Lyα emitting galaxies a narrow-band technique is usually employed. The idea is to detect a strong emission line on top of a continuum by using a very narrow filter, typically $20 - 80$ Å wide, tuned

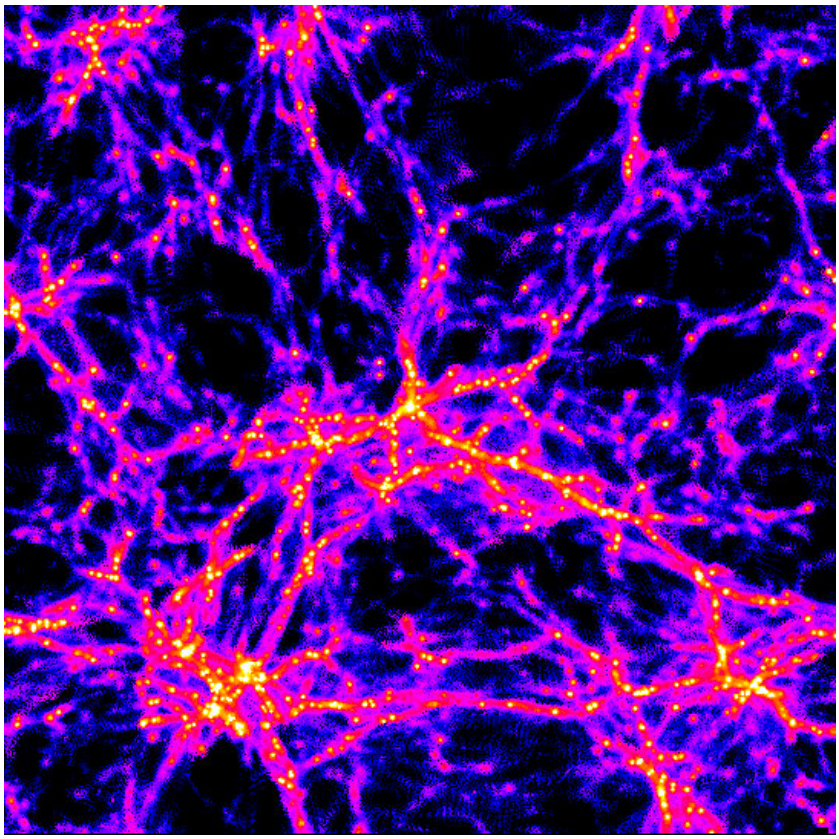

Figure 1.10 Snapshot from a hydrodynamical N-body simulation at $z = 3$. The size of the box is $12.5 \times 12.5 \times 1.6h^{-3}$ Mpc^{-3}. The image shows the density distribution. The white regions correspond to overdensities above 100, and they appear to follow filamentary structures. (Courtesy of Tom Theuns, Institute for Computational Cosmology, Durham).

to the wavelength of an emission line (in this case Lyα) at a given redshift. In order to identify the emission line sources the narrow-band magnitudes, n, are compared to a broad filter, which contains the wavelength region of the narrow-band (on-band-broad, $B_{\rm on}$), and another broad filter, which does not contain the narrow-band (off-band-broad, $B_{\rm off}$). The off-band-broad filter gives a measure of the continuum, while the on-band-broad filter gives a measure of the continuum plus emission line. Emission-line objects plotted in a $(n - B_{\rm off}, n - B_{\rm on})$ colour-colour diagram fall in the lower left region due to the excess emission in n (see Fig. 1.9), while absorption-line objects fall in the upper right region due to the deficit of flux in n.

Unlike other techniques for detecting high-redshift galaxies, which require a detectable continuum, the narrow-band technique probes the very faint galaxy population (Fynbo et al. 2001, 2003a). Because the

technique is sensitive to faint galaxies, the space density of potential targets can be very high. On the other hand, due to the very narrow filter, the volume probed by this method is small. Numerical simulations predict that objects at high redshift are highly clustered in "walls" or "filaments" (Klypin & Shandarin 1983; Rauch et al. 1997; Efstathiou et al. 2000, see also Fig. 1.10), so in order to optimize a survey for Lyα emitters one can select a volume known to contain other objects, such as quasars. Still, it is not yet clear if there actually is an overdensity of Lyα emitters near bright objects (Monaco et al. 2005).

The high-redshift Lyα emitters detected with the narrow-band technique are typically faint, compact galaxies with luminosities in the range $0.3 - 60 \times 10^{42}$ erg s^{-1} (Ouchi et al. 2003; Fynbo et al. 2003a; Palunas et al. 2004).

1.5.2 Filaments?

The high space density of Lyα emitters has some fascinating consequences. Since numerical simulations of cold dark matter predict that voids and filaments are the first structures to form (Klypin & Shandarin 1983; White et al. 1987; Rauch et al. 1997), it could be possible map out such structures, given a selection technique that probes the least massive (faintest) galaxies. In principle this could be done through studies of absorption lines of the galaxy-class absorption systems like damped Lyα absorbers in the spectra of background quasars or gamma-ray bursts. This technique selects by absorption cross-section instead of luminosity, and it is therefore very useful for studying high-redshift gas. However, the lack of a tight mesh of background quasars renders it impossible to utilize this method for mapping high-redshift structures. Another option is offered by Lyα emitters. By spectroscopically mapping out a sample of faint Lyα emitters found using the narrow-band technique, one may reconstruct the three-dimensional distribution of these faint galaxies (Møller & Fynbo 2001; Francis et al. 2004; Matsuda et al. 2005).

Given detections of a number of high-redshift filaments, there are three test using different assumptions that may constrain the allowed space for the cosmological parameters $\Omega_{\rm m}$ and Ω_Λ (Møller & Fynbo 2001). In essence these tests are extensions of the original Alcock & Paczyński (1979) test, which makes use of the fact that a non-zero cosmological constant Ω_Λ would appear to stretch or squeeze an observed volume along the line of sight, thus changing the apparent geometry of an object anchored in the Hubble-flow contained in the volume. The assumption for the first "filament test" is that of isotropy, i. e. the number of filaments pointing in a given direction is the same as for any other direction. The assumption for the second test is that the length-to-radius

ratio is equal for all filaments. For the third test the assumption is that all filaments have circular cross-sections. The first test, based on a very fundamental assumption and therefore the most promising, is further explored in Chapter 3.

1.5.3 Lyα "blobs"

One unusual type of Lyα emitter is commonly referred to as Lyα "blobs" (Steidel et al. 2000), a most descriptive name. Lyα blobs are radically different from the ordinary Lyα emitters (which we shall refer to simply as Lyα emitters) discussed in Sect. 1.5.1. Lyα emitters are compact galaxies, contrary to the enormous Lyα blobs that extend up to 100 kpc. Lyα blobs typically have luminosities of a few times 10^{43} erg s^{-1}, roughly similar to the Lyα emitters (Matsuda et al. 2004; Ouchi et al. 2003; Fynbo et al. 2003a; Palunas et al. 2004).

The exact nature of the Lyα blobs is uncertain, but photoionization by stars or AGN, cooling radiation from gravitationally heated gas, and shock heating by a supernova-driven superwind have been suggested as possible scenarios (Matsuda et al. 2004). It appears that Lyα blobs are somehow related to high-density environments such as in clusters (Matsuda et al. 2004), and bubble-like features which could be explained by the combined effect of many supernovae (Mori et al. 2004) have been identified (Matsuda et al. 2004).

In summary, narrow-band imaging and spectroscopic follow-up observations is a powerful mixture for studying a wide range of astrophysical topics at the frontier of Science. This method not only samples the faint end of the galaxy luminosity function and is a powerful tool for studying host galaxies of quasars, the most luminous objects in the Universe, it may also be used to map out large-scale structures in 3D, and potentially provide an independent check on the cosmological parameters.

Motivated in this fashion, we plunge into the next chapter, which presents the basic methods of data reduction used in this thesis.

Chapter II

Methods

A great variety of tools, concepts and procedures are used throughout the present work. This chapter introduces the most important ones.

First we outline the basic procedure of coming from raw data directly out of the scientific instrument to calibrated science-grade data. This is followed by a description of the algorithm utilized in the spectral extraction. The wavelength and flux calibration of the extracted spectra are then sketched, and we end the chapter with a brief discussion of noise calculations and equivalent width measurements.

2.1 Basic reductions

Astronomical observations at optical wavelengths are today almost exclusively collected with instruments based on charged-coupled devices (CCDs). The characteristics of a CCD may heavily affect the raw data, so in order to arrive at a dataset independent of the instrument in question, the raw data requires processing. This data reduction takes it starting point in the physical properties of CCDs.

A CCD is basically a semiconductor chip capable of collecting and storing charge produced through the photoelectric effect of incident photons. The chip is divided into grid with a number of picture elements (pixels), each separately detecting photons. Today, a grid of 2048×2048 pixels or more is not unusual. The charge stored in a pixel is amplified and converted to a digital number (analogue-to-digital unit; ADU), which is a measure of the number of photons detected.

The main problems with CCD images are due to the following effects. The amplifier generates an offset, a bias, increasing the original signal, and performing the read-out of the CCD adds noise (read-out noise, RON) to the signal. Furthermore, the individual pixels on the CCD are not equally sensitive to photons, resulting in a non-uniform response

across the CCD, and thermal excitation of electrons within the semiconductor (dark current) may spuriously increase the stored charge. The digitally recorded signal $c(i,j)$ (the counts) in a pixel at position (i,j) on the CCD may be written out as

$$c(i,j) = \frac{1}{g}\int_{\Delta t}\left(\int_{\Delta\lambda}\varepsilon_{\mathrm{QE}}(i,j,\lambda)\dot{n}_{\gamma}(i,j,\lambda)\mathrm{d}\lambda + \dot{n}_{\mathrm{DC}}(i,j)\right)\mathrm{d}t + b(i,j) + c_{\mathrm{RON}}(i,j), \tag{2.1}$$

where g is the amplification (the gain) measured in e^- per ADU, $\varepsilon_{\mathrm{QE}}(i,j,\lambda)$ is the quantum efficiency[1] of pixel (i,j), $\dot{n}_{\gamma}(i,j,\lambda)\mathrm{d}\lambda = \frac{\mathrm{d}n_{\gamma}(i,j,\lambda)}{\mathrm{d}t}\mathrm{d}\lambda$ is the rate of photons with wavelengths between λ and $\lambda + \mathrm{d}\lambda$ arriving at the pixel, $\dot{n}_{\mathrm{DC}}(i,j) = \frac{\mathrm{d}n_{\mathrm{DC}}(i,j)}{\mathrm{d}t}$ is the rate of electrons from the dark current in the given pixel, and $b(i,j)$ is the bias. The read-out noise $c_{\mathrm{RON}}(i,j)$ is the result of a stochastic process and it cannot be removed. We have ignored the time-dependence of these quantities, since they are expected to be constant over short periods of time (i.e. during a few nights of observations).

In order to determine the rate of photons at each pixel, the remaining quantities need to be determined. The bias is found by exposing for $\Delta t = 0$ sec, the dark current image (the dark frame) is obtained by mimicing an exposure, but without actually opening the shutter, ensuring that $\dot{n}_{\gamma}(i,j,\lambda) = 0$. The pixel-to-pixel variation of the quantum efficiency is determined by observing a uniformly illuminated field; for imaging data this could be the twilight sky. Then $\dot{n}_{\gamma}(i,j,\lambda) = \dot{n}_{\gamma}(\lambda)$, independent of i and j. For spectroscopic data there is the additional complication that the wavelength in fact is a function of the position on the CCD, $\lambda = \lambda(i)$. Since it quite difficult to obtain a truely flat spectrum, it is correspondingly difficult to obtain a uniform illumination of the CCD in spectroscopic mode. Instead one uses for the illumination a flat field[2] lamp void of spectral features. Assuming a constant flux across the length of the slit, and that all pixels have the same sensitivity dependence on wavelength, we may write

$$\dot{n}_{\gamma}(i,j,\lambda) = \dot{n}_{\gamma,1}(i,\lambda), \tag{2.2}$$

$$\varepsilon_{\mathrm{QE}}(i,j,\lambda) = \varepsilon_{\mathrm{QE},1}(i,j)\varepsilon_{\mathrm{QE},2}(\lambda). \tag{2.3}$$

Letting $\langle\varepsilon_{\mathrm{QE}}n_{\gamma}(i,\lambda)\rangle$ denote the observed, bias-subtracted flat field av-

[1]The ratio of detected photons to total number of photons that hit the pixel.

[2]An image containing only the pixel-to-pixel variation is known as a flat field; the process of removing this variation is known as flat fielding.

eraged along the spatial direction,

$$\begin{aligned}\langle \varepsilon_{\rm QE}\dot{n}_\gamma(i,\lambda)\rangle &\equiv \frac{1}{M}\sum_{j=1}^{M}\varepsilon_{\rm QE}(i,j,\lambda)\dot{n}_\gamma(i,j,\lambda)\\ &= \varepsilon_{\rm QE,2}(\lambda)\dot{n}_{\gamma,1}(i,\lambda)\frac{1}{M}\sum_{j=1}^{M}\varepsilon_{\rm QE,1}(i,j),\end{aligned} \tag{2.4}$$

we can isolate the pixel-to-pixel variation of $\varepsilon_{\rm QE}$ in the reduced flat field, $c_{\rm FF}$:

$$\begin{aligned}c_{\rm FF}(i,j) &= \frac{\varepsilon_{\rm QE}(i,j,\lambda)\dot{n}_\gamma(i,j,\lambda)}{\langle \varepsilon_{\rm QE}\dot{n}_\gamma(i,\lambda)\rangle}\\ &= \frac{\varepsilon_{\rm QE,1}(i,j)}{\frac{1}{M}\sum_{j=1}^{M}\varepsilon_{\rm QE,1}(i,j)}.\end{aligned} \tag{2.5}$$

If no structure along the spatial direction is present in $\varepsilon(i,j,\lambda)$, marginalizing out j will simply yield a constant, $\frac{1}{M}\sum_{j=1}^{M}\varepsilon_{\rm QE,1}(i,j) = \text{constant}$. Otherwise one can use a low-order polynomial fit to $\langle \varepsilon_{\rm QE}\dot{n}_\gamma(i,\lambda)\rangle$ instead of the average itself for the normalization of $c_{\rm FF}$, assuming that any feature in $\langle \varepsilon_{\rm QE}\dot{n}_\gamma(i,\lambda)\rangle$ is due to $\frac{1}{M}\sum_{j=1}^{M}\varepsilon_{\rm QE,1}(i,j)$. The overall normalization of $\varepsilon_{\rm QE}(i,j,\lambda)$ is not relevant at this stage, because an unknown fraction of photons is lost in the optical system of the telescope before arriving at the CCD. Note that the wavelength dependence of the efficiency, $\varepsilon_{\rm QE,2}(\lambda)$, is not removed by the flat fielding. This is intentional for reasons which will become clear when we perform the flux calibration in Sect. 2.3.2. In order to minimize the read-out noise in bias image, dark frame and flat field, a "master" bias image, dark frame, or flat field is calculated as the average of many single images.

Summarizing, the road towards a science-grade image consists of the following steps:

- Obtain and subtract the "master" bias image, $b(i,j)$.
- Obtain and subtract the "master" dark frame, $\frac{1}{g}\int_{\Delta t}\dot{n}_{\rm DC}(i,j){\rm d}t$, scaled to match the exposure time of the science image.
- Obtain and divide by the "master" flat field, $c_{\rm FF}(i,j)$.

Now we have cleaned the raw data of the unwanted effects from the CCD, and we are ready to extract the spectrum.

2.2 Spectral extraction

Extracting a one-dimensional spectrum from a two-dimensional one is a crucial step in our data reduction. Great care is needed when modelling

the quasar spectrum, because the quasar is very bright compared to the faint extended emission. In this section we will discuss the procedure employed in this work. It is based on code originally developed by Møller (2000), and expanded to cover the needs of the work presented in this thesis.

In the following the spectral point-spread function (SPFS) is a one-dimensional (1D) continuous function along the slit. A "realization" of the SPSF is a pixelized edition of the underlying continuous function. There are infinitely many "realizations" obtainable by shifting the SPSF by a fraction of a pixel. This is not unlike the two-dimensional (2D) PSFs known from imaging. However, a few facts complicate the SPSF in ways not applicable to the imaging PSFs. These facts are: The SPSF is wavelength dependent, the telescope focus is wavelength dependent, and the spectrum is not perfectly aligned with the detector rows. These complications need to be considered when performing an optimal extraction.

2.2.1 2D optimal extraction

One of the main objectives of the Møller (2000) code is to optimally extract a 1D spectrum from a 2D spectral image. The basic philosophy of the algorithm is to find a good trace[3] of the spectrum, use the entire spectrum to build a high-resolution realization of the SPSF, which then in each wavelength bin is scaled in width and height to provide the best χ^2-fit to the data. In other words, the SPSF is assumed to be constant with wavelength apart from a simple scaling in width. The noise in the image is assumed to originate from photon statistics and read-out noise only, and is as such a known quantity.

The code takes as input (among other things) the 2D spectrum of the object, a 1D spectrum of the background sky, the gain, and the read-out noise in ADU.

The basic procedure

The basic procedure is a number of user-controlled sequences alternating freely between obtaining the trace, building the high-resolution SPSF and fitting the width – we will use the term "sequence" meaning one of these three. The total χ^2 per degree of freedom (DOF) is written to the screen at the end of each sequence.

Since each sequence uses the information obtained via the other sequences a kind of bootstrapping is called for. This is done by assuming as a first guess that the width is unity for all wavelength bins and that the realization of the SPSF is zero in all points except the three central ones, where it resembles a sawtooth function. Using this and a

[3]The trace is the position of the centroid as a function of wavelength bin

user input of the approximate position of the spectrum in the image a first trace is obtained, and this trace is used to obtain a better high-resolution SPSF. Having completed a few iterations of obtaining trace and high-resolution SPSF the bootstrapping is complete, and a good first approximation to both trace and SPSF is available.

Finding the trace

The position of the centroid of the spectrum is found in each wavelength bin by cross-correlating the obtained high-resolution SPSF with the real spectrum and fitting both a parabola to the five central points and a Gaussian to the three central points. The centre of choice is whichever of the two that is closest to the value obtained in the previous wavelength bin. When all wavelength bins have been treated in this way, a Chebyshev polynomial of a user-specified order is fitted to the centroid as a function of wavelength bin. This fit is accepted as the best estimate of the trace.

Building the SPSF

Obtaining the high-resolution SPSF is a crucial step in the extraction. There are infinitely many ways to pixelize a continuous SPSF onto a CCD by shifting the SPSF by an arbitrary fraction of a pixel relative to the CCD pixels. In order to compensate for this a number of subpixels is used. The subpixels are stored in a 2D look-up table (LUT, see Fig. 2.1). Each entry in the LUT (each column in Fig. 2.1) corresponds to a realization of the SPSF centred on a certain fraction of a pixel. Thus the only difference between the LUT and the high-resolution SPSF is the ordering of the numbers (see Fig. 2.2). The entries in the LUT range from a realization of the SPSF centred on the delimiter between two pixels to a realization of the SPSF centred on the neighbouring delimiter (see Fig. 2.1). In this way the first and the last entry are shifted relative to each other by exactly one full pixel, and the middle entry is (nearly) symmetric around the central pixel.

In the procedure of building the high-resolution SPSF it is assumed that the trace and the width are known as a function of the wavelength bin. In each wavelength bin, the code picks out the requested number of pixels around the centroid of the spectrum. We will refer to this as the "data profile". The fractional position of the centroid is used to select the relevant entry of the LUT. If no cosmic ray hits were found in the previous iteration within the specified rejection limit, then the current data profile is added to relevant entry of the new LUT, corrected for the known width. For each subpixel in the LUT the code keeps a separate

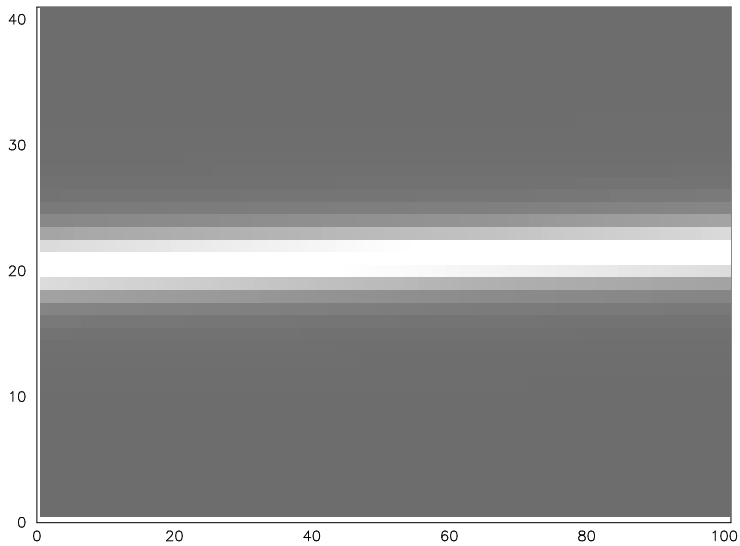

Figure 2.1 LUT of a SPSF which has a width of 41 pixels and contains 101 subpixels. The high-resolution SPSF corresponding to this LUT is shown in Fig. 2.2

account of the normalization. The reason for doing this will become clear shortly.

When all wavelength bins have been treated in this way, the new LUT is normalized and copied to the current LUT. If some entries in the new LUT are not updated with data profiles (this could happen if the spectrum is very highly aligned with the detector rows) the values from the previous LUT are used instead. The LUT is now smoothed according to the user's wishes and normalized to unity.

Ordinarily, one would think that it would be more correct to interpolate between the updated entries in the new LUT instead of reusing entries from old one, but this makes the SPSF building unstable in some cases: If at some point a bad estimate of the real LUT is obtained, the next trace to be obtained will also be rather bad. This in turn will make the next estimate of the LUT even worse, and so the solution diverges. Using the old LUT in the entries that are not updated in the new LUT introduces a kind of latency, which stabilizes the code.

Finding the width

Since the SPSF as well as the telescope focus are wavelength dependent, the width of the SPSF may vary along the spectrum. It is assumed that a simple linear scaling of the SPSF width is sufficient.

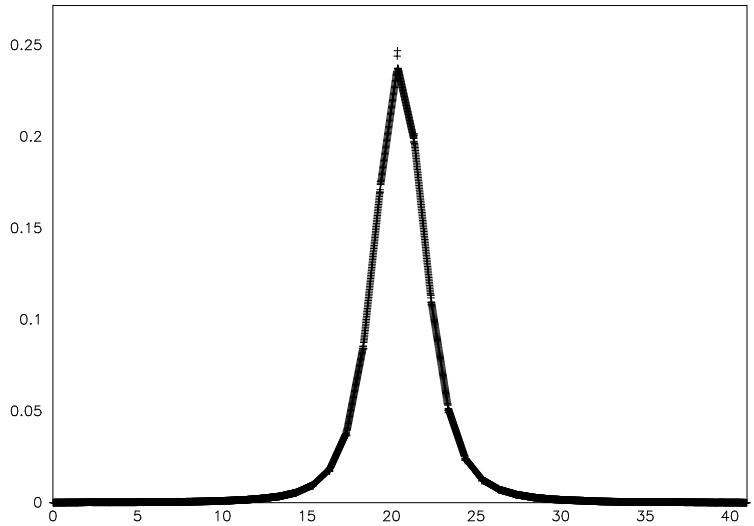

Figure 2.2 The high-resolution SPSF constructed from the LUT in Fig. 2.1.

In each wavelength bin the width scaling of the profile is done as follows. Let $N_{\text{subpixels}}$ be the number of subpixels in each LUT entry. Instead of selecting values in the high-resolution SPSF separated by $N_{\text{subpixels}}$ subpixels, a small correction is applied such that, counting from the central subpixel, all distances to the selected subpixels are multiplied by a factor (the "width", w). So counting from the subpixel in the high-resolution SPSF that corresponds to the centre of the current profile, the subpixel which in the profile is d positions away from the middle is given the value of the subpixel in the high-resolution SPSF which is $d \times w$ (rounded off the nearest integer) positions away from the centre subpixel. In the LUT representation this leads to a mixing of different entries, and it is therefore necessary to keep account of the normalization for each subpixel separately.

The new width in a given wavelength bin is found by picking five test-widths, w_j, $j = 1, \ldots, 5$, distributed evenly around the current width, and for each test-width calculating

$$D_j^2 = \sum_{i=1}^{N} \left(d_i - S_i\left(w_j\right)\right)^2 ,$$

where d_i is pixel i in the data profile, $S_i(w_j)$ is the realization of the SPSF with width w_j, and N is the number of pixels in the data profile and the realization of the SPSF. The new width is found by fitting a parabola to the five sets of (w_j, D_j^2) and calculating the position of the

minimum. This is assumed to be a good estimate of the width.

When all wavelength bins have been treated in this way a Chebyshev polynomial of a user-specified order is fitted to the width as a function of wavelength bin. This fit is accepted as the best estimate of the width.

Calculating the 1D spectrum

One of the outputs of the code is the extracted 1D spectrum. In each wavelength bin the amplitude that yields the minimum χ^2 is calculated in the following way:

Let d_i, $\sigma^2(d_i)$ and S_i, $i = 1, \ldots, N$, be the data profile, the variance of the data profile and the relevant realization of the SPSF (taken from the LUT and normalized to unity) with the correct width, respectively, and let N be the number of pixels in the data profile. The variance $\sigma^2(d_i)$ of the data profile is the quadratic sum of the noise due to photon statistics (Poisson distribution) and read-out noise. We will assume that the amplitude $F_i = \frac{d_i}{S_i}$. Then $\sigma^2(F_i) = \frac{\sigma^2(d_i)}{S_i^2}$ and

$$\chi^2(F) = \sum_{i=1}^{N} \frac{(F - F_i)^2}{\sigma^2(F_i)} = \sum_{i=1}^{N} \frac{S_i^2 (F - \frac{d_i}{S_i})^2}{\sigma^2(d_i)}. \tag{2.6}$$

It is straightforward to show that the condition of extremum $\frac{\partial \chi^2(F)}{\partial F} = 0$ leads to

$$F = \frac{\sum_{i=1}^{N} \frac{d_i S_i}{\sigma^2(d_i)}}{\sum_{i=1}^{N} \frac{S_i^2}{\sigma^2(d_i)}}, \tag{2.7}$$

which will be a minimum if and only if $\sum_{i=1}^{N} \frac{d_i S_i}{\sigma^2(d_i)} > 0$. Since we will always expect F to be positive, the same is true for the sum $\sum_{i=1}^{N} \frac{d_i S_i}{\sigma^2(d_i)}$. If the estimates of the trace, the width and the SPSF are good, F is the flux in this wavelength bin with the optimal signal-to-noise ratio. Note that the normalization of the realization of the SPSF to unity ensures that F in fact is the total number of counts in the spectrum in each wavelength bin. The variance $\sigma^2(F)$ of F is easily found to be

$$\sigma^2(F) = \left(\sum_{i=1}^{N} \frac{S_i^2}{\sigma^2(d_i)} \right)^{-1}. \tag{2.8}$$

2.2.2 Extended emission

The extraction procedure of the previous section will be incorrect if extended emission is present in the spectral image. In this case the code

will assign as much flux as possible to the point source, and thereby end up with a wrong estimate of the SPSF, which will cause over-subtraction in the spectrum away from the extended emission. In order to properly deal with extended emission near a point source spectrum the original code was expanded to include an option to avoid a wavelength region when building of the high-resolution SPSF. This region will have to be dealt with separately.

It is not possible to separate extended flux from the flux of a point source without additional assumptions. Two different assumptions are typically employed.

- Minimum extended flux: The extended emission is assigned as little flux as possible.
- Sérsic profile: The combined extended plus point source spectrum is a Sérsic profile and a Dirac δ-function convolved with the SPSF.

Both these assumptions are built into the code.

Minimum extended flux

When the minimum extended flux assumption is invoked only the innermost pixels are used in the minimum χ^2-fit discussed in Sect. 2.2.1. The precise number of pixels to use in the calculation is left to the user's discretion, but as few pixels as possible should be used in order to ensure that the contribution from any extended flux is negligible compared to the point source flux. The resulting 2D spectrum is subtracted from the full width of the data profile, in order to reveal any underlying emission.

This assumption ensures that the minimum amount of flux is assigned to the extended emission, or equivalently that a maximum amount of flux is assigned to the point source. This gives a conservative flux limit on any extended emission.

Sérsic profile

The four free parameters of the Sérsic profile plus point source are the amplitude, A, the effective radius, r_e, and the shape parameter, n, of the Sérsic profile, as well as the amplitude (or, strictly speaking, the area), P, of the Dirac δ-function. The model profile, $m(r)$, where r is the distance to the centroid, is given by

$$m(r) = \left(A \exp\left[-\left(\frac{r}{r_e} \right)^{1/n} \right] + P\delta(r) \right) * S(r), \quad r > 0. \tag{2.9}$$

Here $S(r)$ is the continuous SPSF, and $*$ indicates convolution. Eq. (2.9) is easily modified to treat pixelized functions. It is implicitly assumed

that the centre of the Sérsic profile and the position of the point source coincide, although this might not always be the case.

Ideally, one should fit to all wavelength bins simultaneously with a single r_e and n, that are then independent of wavelength. The minimization would then occur in a $2N_{\rm ext}+2$ dimensional space (A and C for each wavelength bin, and r_e and n independent of wavelength), where $N_{\rm ext}$ is the number of wavelength bins in the excluded region, typical values ranging from 30 to 80 bins. That is a computational task exceeding the time frame of this work. Instead we fit the profile in each wavelength bin separately. In each bin the four parameters which yield the smallest χ^2 of $m(r_i)$ fitted to d_i are found by using the Downhill Simplex Method (the "amoeba") in four dimensions (Press et al. 1989). One danger connected with the numerical method is the possibility of local minima. The "amoeba" may encounter a local minimum in which case the stopping criterium is fulfilled, and the local minimum is treated as the global minimum. In order to prevent this situation the routine is started a number of times with random initial values close to the original guesses. The lowest minimum found after starting the routine 10^4 times is accepted as global. We limit the parameter space to non-negative values.

We include the option to allow for an asymmetric profile, where the shape parameters r and n may vary on one side of the centroid independently of the other side. Since the amplitude A is assumed to the same on either side, we have 6 free parameters in the asymmetric case. However, in most cases the signal-to-noise ratio is too low to allow for a meaningful fit for the general Sérsic profile. Instead we consider two special cases, namely the exponential profile ($n = 1$) and the de Vaucouleurs profile ($n = 4$), each with 3 free parameters. In the asymmetric cases each profile has 4 free parameters.

In some cases the obtained high-resolution SPSF and the actual observed profile could be slightly different, resulting in a best-fit model with an extremely narrow (before convolution) extended profile and only a very small point source contribution. In this way the extended profile mimics the effect of a point source while compensating for slight difference in SPSF and observed profile. To prevent this, we allowed for a lower bound on the FWHM of the extended profile before convolution. The lower bound should be chosen to be less than half the seeing FWHM, to ensure that it would not artificially push the fit to larger effective radii. For asymmetric profiles the lower bound applies only to the larger of the two effective radii, so that the extended emission may effectively be one-sided.

2.3 Calibrations

Having completed the spectral extraction, we now wish to calibrate the spectra to physical units. Two types of calibrations are of interest to us: Wavelength and flux calibration.

2.3.1 Wavelength calibration

The main purpose of a spectrograph is to disperse the light, but without knowledge of which wavelengths went where, the spectrum is virtually useless. To forestall such a situation, an exposure of an arc lamp (an arc spectrum) is taken immediately before or after the science observation, using the exact same optical setup. The spectrum of the arc lamp is rich in emission lines whose precise wavelengths are known, thus providing a way to map pixel numbers to physical wavelengths.

When studying faint sources it is vital to maximize the signal-to-noise. Any resampling of the original data will degrade the S/N and should be avoided, or at least deferred as long as possible. We have therefore delayed the wavelength calibration until after the crucial spectral extraction (Sect. 2.2).

The observations going into this thesis are all carried out using grisms as dispersive elements. The dispersion relation for grisms is close to linear, so only a slight resampling of the wavelength bins is necessary in order to obtain a constant step size in the wavelength direction. The wavelength solution is found by calculating the optimal linear relation, and fitting a fourth order Chebyshev polynomial to the residuals. The wavelength solution may be checked using emission lines in the sky background.

2.3.2 Flux calibration

Flux calibration of spectroscopic data can be a very tricky task, and it is not made any easier by the fact that we here completely lack observations of spectrophotometric standard stars. Slightly different flux calibration methods have been employed in this work, always seeking to use as much of the available information as possible in order to gain precision. However, the basic idea remains the same.

First it is important to note that the quantum efficiency and the efficiency of the optical system of instrument and telescope are strong functions of the photon wavelength. We recall that the quantum efficiency dependence on the wavelength is not removed by the flat fielding. So after the basic reductions in Sect. 2.1 different wavelength bins are on different flux normalizations. In order to be able to compare count levels at different wavelengths this needs to be corrected for.

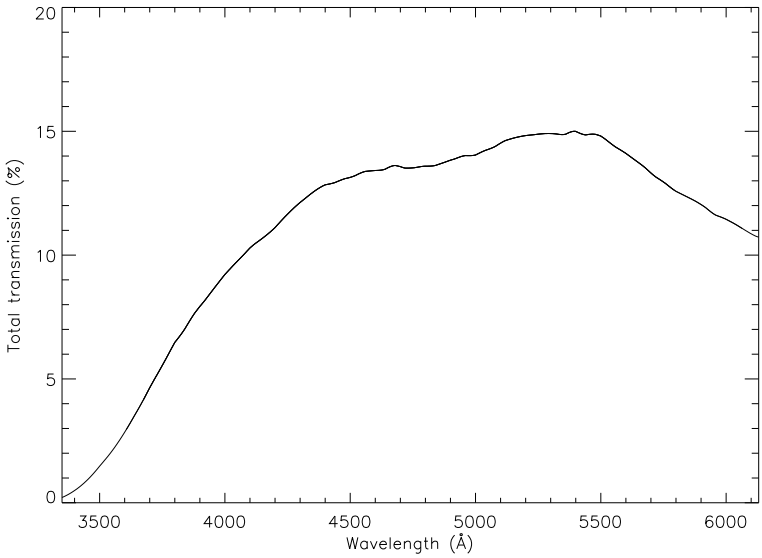

Figure 2.3 Total system transmission for FORS1 using grism 600B.

The common strategy of all the methods is to use the total system transmission curve, which has been measured out reasonably well as a function of wavelength for the instrument setups we are dealing with here (see Fig. 2.3). Dividing the spectrum by the total system transmission curve as a function of wavelength yields the correct relative flux. The absolute flux scale is recovered by convolving the observed quasar spectrum (on correct relative flux) with a filter transmission curve and compare the integrated flux to the observed magnitude in this filter. This may be written out as follows. The average wavelength specific flux in the filter is given by

$$\langle f_\lambda \rangle = C \frac{\int c_\lambda T(\lambda) \mathrm{d}\lambda}{\int T(\lambda) \mathrm{d}\lambda}, \tag{2.10}$$

where c_λ is the count level as a function of the wavelength λ, and $T(\lambda)$ is the filter transmission curve. Here C is the convertion from counts to physical flux units that we are seeking. The AB-magnitude system is defined as (Oke & Gunn 1983)

$$\begin{aligned} m(AB) &\equiv -2.5 \log f_\nu - 48.60 \\ &= -2.5 \log C - 2.5 \log \left(\frac{\lambda^2}{c} \frac{\int c_\lambda T(\lambda) \mathrm{d}\lambda}{\int T(\lambda)} \right) - 48.60, \end{aligned} \tag{2.11}$$

and Fukugita et al. (1996) give the transformations to the standard Johnson-Morgan-Cousins filter set ($UBVR_cI_c$). Knowing the magnitude

in one of these standard filters enables us to determine C, and thus provides the absolute flux calibration.

We note that the method described here is not the optimal one for flux calibration in general, but it is the best we can do with the data at hand.

A few more details about the different methods are given in the individual chapters.

2.4 Data analysis

Once the data have been calibrated to physical units we are able to perform our analysis. Two important aspects of the analysis are mentioned here: Noise calculations and equivalent widths.

2.4.1 Noise calculation

The noise inherent to all observations sets the limit of how faint objects we are able to detect, and it is therefore essential to quantity the noise level.

First we note that the number rate of photons with wavelengths between λ_i and $\lambda_i + \Delta\lambda_i$ incident on the pixel at position (i, j) may be calculated as

$$\dot{n}_\gamma(i, j, \lambda_i)\Delta\lambda_i = \int_{\lambda_i}^{\lambda_i+\Delta\lambda_i} \int_{x_j}^{x_j+\Delta x_j} \frac{\lambda f_\lambda(x, \lambda)}{hc} \varepsilon(x, \lambda) * I(\lambda) S(x, \lambda) \mathrm{d}x \mathrm{d}\lambda, \tag{2.12}$$

where $\Delta\lambda_i \times \Delta x_j$ is the size of a pixel, $f_\lambda(x, \lambda)$ is the monochromatic flux, $\varepsilon(x, \lambda)$ is the fraction of photons reaching the CCD from outside the atmosphere. $I(\lambda)$ is the spectral instrument profile, and $S(x, \lambda)$ is the SPSF; the monochromatic flux is convolved by their product. A photon can be lost in many ways along the optical path from just outside the atmosphere to just before the CCD is reached. It can be absorbed or scattered in the atmosphere, absorped or transmitted in the telescope mirrors, or absorbed or reflected in the instrument. We may write this out as

$$\varepsilon = \varepsilon_{\mathrm{atm}} \varepsilon_{\mathrm{mirrors}} \varepsilon_{\mathrm{inst}}. \tag{2.13}$$

The noise on the number of photons detected in a pixel is Poisson distributed, in which case the variance is $\sigma^2(n_\gamma(i, j, \lambda_i)\Delta\lambda_i) = n_\gamma(i, j, \lambda_i)\Delta\lambda_i$. Denoting the error associated with the readout-noise σ_{RON} and using the law of error propagation the theoretical noise on the flux in a pixel,

$\sigma(f_\lambda(i,j))$, is given by

$$\begin{aligned}\sigma^2(f_\lambda(i,j)) &= \frac{C^2}{g^2}\sigma^2(n_\gamma(i,j,\lambda_i)\Delta\lambda_i) + C^2\sigma^2_{\mathrm{RON}} \\ &= \frac{C^2}{g^2}n_\gamma(i,j,\lambda_i)\Delta\lambda_i + C^2\sigma^2_{\mathrm{RON}} \\ &= \frac{C^2}{g}c_{\mathrm{red}}(i,j) + C^2\sigma^2_{\mathrm{RON}} \\ &= \frac{C}{g}f_\lambda(i,j) + C^2\sigma^2_{\mathrm{RON}}. \end{aligned} \tag{2.14}$$

The actual observed noise may be estimated directly from the spectral image by calculating the standard deviation of the flux over all pixels in a region appearing to be flat. The observed noise in a region should in principle always be greater than the theoretical one, since additional noise may be added, but not removed, so this provides a nice consistency check on the theoretically calculated noise. There is, however, a problem if the selected region is far from being flat. This could happen close the centroid of the quasar spectrum, resulting in an overestimated noise level away from the SPSF and an underestimated noise level within the SPSF. In such a case we have to rely on the theoretical calculation.

The variance spectrum corresponding to the extracted 1D quasar spectrum was calculated in Eq. (2.8).

2.4.2 Equivalent width

The equivalent width is a very useful tool for characterizing spectral lines. The definition is

$$W \equiv \int_0^\infty \frac{f_c(\lambda) - f_\lambda}{f_c(\lambda)}\mathrm{d}\lambda, \tag{2.15}$$

where $f_c(\lambda)$ is the continuum flux, i.e. the monochromatic flux had the line not been present. According to this definition absorption lines have $W > 0$, and emission lines have $W < 0$. Throughout this work we will disregard the sign of W, since it will always be clear from the context if we are dealing with one or the other.

Due to the cosmological redshifting of wavelengths observed equivalent widths are a factor $(1+z)$ larger than in the rest-frame. So given a spectral line with observed equivalent width W_{obs}, the rest-frame equivalent width W_{rest} is found by $W_{\mathrm{rest}} = \frac{W_{\mathrm{obs}}}{1+z}$.

One simple fact about QSO spectra complicates the process of measuring equivalent widths considerably: The emission lines are blended

(see e.g. Fig. 5.3 on p. 72). As a first consequence this makes it difficult to determine how much equivalent width each line is responsible for. This is remedied by fitting a number of Voigt to the line profiles. A second and more severe consequence is that determining the continuum flux level is made hard. An error in the placement of the continuum will introduce a systematic error in the measured equivalent widths. In an effort to quantify this effect we performed the continuum fitting by hand a number of times, each time deblending and measuring out the emission lines. The associated uncertainty is included in the error estimate of W.

Chapter III

Constraints on $(\Omega_{\rm m}, \Omega_\Lambda)$ using distributions of inclination angles for high redshift filaments

Weidinger, M., Møller, P., Fynbo, J. P. U., Thomsen, B., & Egholm, M. P. (2002). *A&A*, **391**, 13

3.1 Introduction

RECENT studies have successfully narrowed down the permitted parameter space for the cosmological parameters $\Omega_{\rm m}$ and Ω_Λ. Confidence intervals defined by observations of distant supernovae (Riess et al. 1998; Perlmutter et al. 1999) and those resulting from the high-resolution observations of the cosmic microwave background radiation (CMB) (Jaffe et al. 2001) meet almost orthogonally, and as a result they combine to bracket a domain of high probability. There remains, however, the question of possible systematic effects which may produce significant errors (e.g. Simonsen & Hannestad 1999; Rowan-Robinson 2002). It is therefore important that new and independent methods to determine $\Omega_{\rm m}$ and Ω_Λ should be sought and exploited.

The simplest and cleanest cosmological tests one might imagine would be a purely geometric test not involving measurements of standard candles or standard rods as it is the case with the classical cosmological tests (Sandage 1961). The first purely geometrical test was proposed by Alcock & Paczyński (1979), who considered an idealized set of objects distributed spherically symmetric and on average following the Hubble flow. The idea is beautiful in its simplicity, but the requirement of spherical symmetry of the distribution (requiring a length scale to be the same in all directions) is in reality an indirect use of a standard rod, even if at a single point in redshift space. The hypothetical spherical

distribution might as well be ellipsoidal, which would then invalidate the result. The question is if it is at all possible to devise a geometrical test not requiring any length scale at all.

Numerical simulations of early structure formation based on the Cold Dark Matter scenario (Klypin & Shandarin 1983; White et al. 1987; Rauch et al. 1997) show that high redshift star-forming regions tend to align themselves in long filaments with a higher-than-average matter density. This has recently been confirmed observationally by Møller & Fynbo (2001), who also pointed out that such structures offered three independent cosmological tests, all of which were purely geometric, and none of which required the early structure formation to have a preferred length scale. The only requirement is that of global isotropy. The first of those three tests concerns the distribution of filament inclination angles which, in an isotropic Universe, must be random. In this paper we present a detailed analysis, based on Monte Carlo simulations, of this first filament test.

3.2 F($\Omega_{\rm m}$, Ω_Λ, z): The line of sight scale factor

The cosmological principle tells us that any class of elongated objects or structures will, at all redshifts, display a random distribution of orientations of their major axes. The basis of the cosmological test described here is to determine the sets of ($\Omega_{\rm m}$, Ω_Λ) which, at any given redshift, will make the observed distribution of orientations anchored in the Hubble flow conform to this requirement of isotropy.

As a simple example let us first consider an area on the sky in the form of a square with sides of angular size ϕ. At any given redshift z this will correspond to a square in the plane of the sky with sides of proper size

$$W_{\rm true} = \frac{\phi}{H_0} f_{\rm W}(\Omega_{\rm m}, \Omega_\Lambda, z) \tag{3.1}$$

where prescriptions for calculation of $f_{\rm W}$ (as well as of $f_{\rm L}$ below) are provided in an appendix (Sect. 3.6). If we further consider a redshift interval δz centered on z, we have defined a box of proper length

$$L_{\rm true} = \frac{\delta z}{H_0} f_{\rm L}(\Omega_{\rm m}, \Omega_\Lambda, z). \tag{3.2}$$

Let the box be filled with a large number of filaments, and let their distribution of orientations be isotropic. If one were to either stretch or squeeze the box along the line of sight (along the redshift direction), the angular distribution of the filaments would (because they are anchored in the Hubble-flow) no longer remain isotropic.

Because the actual length and width of the box is irrelevant for our test, the only numerical value of interest is the "change of scale" between the two directions (along the line of sight and perpendicular to the line of sight). What we are interested in is therefore the ratio between the length and the width

$$\frac{L}{W} = \frac{\delta z}{\phi} \frac{f_{\rm L}(\Omega_{\rm m}, \Omega_\Lambda, z)}{f_{\rm W}(\Omega_{\rm m}, \Omega_\Lambda, z)} \tag{3.3}$$

and how the *apparent* value of that ratio relates to its *true* value

$$F(\Omega_{\rm m}, \Omega_\Lambda, z) = \frac{(L/W)_{\rm app}}{(L/W)_{\rm true}}. \tag{3.4}$$

Note that H_0, ϕ, and δz have cancelled out of the ratio $F(\Omega_{\rm m}, \Omega_\Lambda, z)$. In what follows we shall refer to this ratio as the *"line of sight scale factor"*.

Returning briefly to the example above, for a given triple of observables $(\phi, z, \delta z)$ and an assumed cosmology $(\Omega_{\rm m}, \Omega_\Lambda)$, the box is fully defined. If one now assumes a different cosmology, the inferred size of the box will change. For most choices of cosmology, the change in length and width of the box will be different (hence the value of F will change), but it is always possible to find sets of $(\Omega_{\rm m}, \Omega_\Lambda)$ with the combined effect of changing both length and width by the same factor, thereby keeping F constant. Our test can now be formulated simply: "Determine the sets of $(\Omega_{\rm m}, \Omega_\Lambda)$ for which $F = 1$". The remainder of this paper is concerned with the formulation of how this is done in practice. In addition we use Monte Carlo simulated data to determine what level of accuracy may be reached with current telescopes and instrumentation.

3.3 Limits on F from Monte Carlo simulations

Consider a large number of idealized, randomly aligned, linear and thin filaments. Let the inclination angle θ of a filament be the angle between the filament major axis and our line of sight to the filament. A filament pointing towards us will hence have inclination angle zero, and the cumulative distribution of isotropically distributed inclination angles can be shown to be

$$P(x) = 1 - \frac{1}{\sqrt{1 + \tan^2 x}}. \tag{3.5}$$

where $x \in [0, \pi/2]$ and $P(x)$ is the probability of observing an inclination angle $\theta < x$. If we now use a wrong set of values $(\Omega_{\rm m}, \Omega_\Lambda)$, then the *apparent* distribution is no longer isotropic and the accumulated distribution of inclination angles is instead given by the general expression

$$P(x, F) = 1 - \frac{1}{\sqrt{1 + F^2 \tan^2 x}}. \tag{3.6}$$

Table 3.1 The $n\sigma$ errors fitted with $F(N) = ae^{bN} + c$.

$n\sigma$	a	b	c
$+3\sigma$	2.67	-0.0650	1.45
$+2\sigma$	1.25	-0.0560	1.27
$+1\sigma$	0.482	-0.0507	1.13
-1σ	-0.313	-0.0451	0.887
-2σ	-0.498	-0.0396	0.791
-3σ	-0.671	-0.0417	0.694

where F is the line of sight scale factor (Eq. (3.4)).

Given a set of observed inclination angles, a K-S test (Press et al. 1989) against $P(x, F)$, can be used to determine the value of F which best fits the observed distribution. At present there is no data set available large enough to place useful constraints on the cosmological parameters. Instead we have created Monte Carlo data in order to determine how large a data set we shall need to be able to set interesting limits. The K-S test is only valid for fairly large samples, so in addition we have tested a number of alternative estimators all based on the comparison of cumulative distributions. For small samples we found that the scatter of the fit was smaller when we minimized the sum of the square of the difference at *each* entry in the sample, while for large samples the two methods gave identical scatter.

It is now interesting to ask how many filaments one would need to observe, to be able to place cosmologically interesting limits on the observed value of F. To address this question we repeated the simulations for the range 10 to 100 filaments in steps of 10, and in each case running 2×10^4 simulations. The results are shown in Fig. 3.1. The one-sided 1, 2 and 3σ curves were found as the 15.9%, 2.28% and 0.13% quantiles. The 1, 2, and 3σ curves are fitted well by the exponential functions given in Table 3.1. The median is consistent with a straight line with intercept 1.00 and slope 0.000.

Each value of F represents, at a given redshift, a curve in the $(\Omega_{\rm m}, \Omega_\Lambda)$ diagram. Using the cosmological relations given in the appendix, Sect. 3.6, we can therefore transform our limits on F (Fig. 3.1) into a set of curves confining the permitted cosmologies (Fig. 3.2).

The contours of F in Fig. 3.2 are calculated for $z = 3$, for 20 and 50 filaments, and are normalized to $F = 1$ for an $\Omega_{\rm m} = 0.3$, $\Omega_\Lambda = 0.7$ Universe. For easy comparison, the confidence regions obtained by supernovae observations (Riess et al. 1998) are also plotted. Two interesting points are immediately obvious from Fig. 3.2. First it is seen that the isoscale curves are mostly horizontal, and that they place tight upper limits on Ω_Λ almost independently of $\Omega_{\rm m}$. This is contrary to the cor-

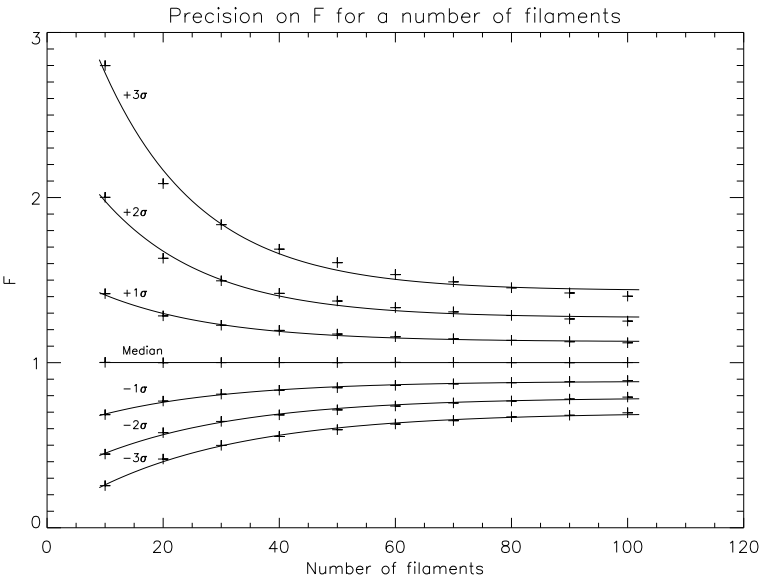

Figure 3.1 Plot of the uncertainty with which we can determine the stretching factor F as a function of how many filaments are in our sample. This is the result of 2×10^4 simulations for each number of filaments. The upper and lower 1, 2 and 3σ uncertainties are fitted with exponentials. The result is given in table 3.1.

responding confidence limits from the supernovae observations which span diagonal regions in the diagram. Secondly it is seen that already with a sample of 20 filaments one would set upper limits on the value of Ω_Λ intersecting those currently set by the high z SN studies. Such a limited study would therefore not only provide a new and independent way to determine Ω_Λ, it would already serve to further constrain the parameter space allowed by the SN studies. For 50 filaments the intersections would be such that they would reduce the area of the 1σ upper confidence limit set by the SN studies by 30%.

3.4 Observational implementation of the test

3.4.1 The optimal redshift range

For the planning of an observing campaign to carry out the proposed test, it is useful first to consider at which redshifts the test is most sensitive to realistic values of Ω_Λ, and how one may best identify filaments at those redshifts. In Fig. 3.3 we plot F as a function of redshift for several different cosmological models, also here normalized so that $F = 1$ corresponds to the $\Omega_\mathrm{m} = 0.3$, $\Omega_\Lambda = 0.7$ model. The dotted and dashed

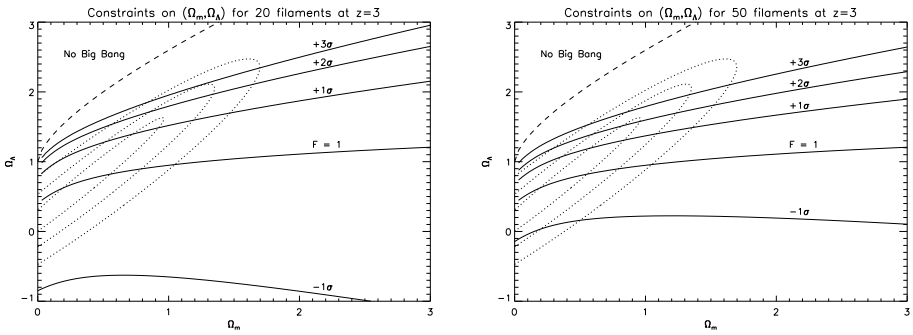

Figure 3.2 Solid: Confidence limits on F for observations of 20 (left plot) and 50 (right plot) filaments at $z = 3$, normalized to $\Omega_{\rm m} = 0.3$, $\Omega_\Lambda = 0.7$. Dotted: The 68.3% (smallest), 95.4% and 99.7% (largest) confidence regions obtained by supernovae observations (Riess et al. 1998).

curves below the $F = 1$ line correspond to $\Omega_\Lambda = 0$ models with $\Omega_{\rm m} = 1$ and $\Omega_{\rm m} = 0.3$ respectively. The dot-dashed curves above the $F = 1$ line correspond to models with $\Omega_\Lambda > 0.7$ (see caption for details). All curves converge at $F = 1$ in the limit of zero redshift. It is seen that for all models with $\Omega_\Lambda < 1$, F is almost independent of redshift in the redshift range $z \approx 1.5 - 4$, while F grows monotonically with redshift for models with $\Omega_\Lambda > 1$. Hence, in order to test against any cosmology with $\Omega_\Lambda < 1$ one should select the redshift in the range $1.5 - 4$ where filaments are most easily detected.

3.4.2 Filament identification and sparse sampling errors

Lyα narrow band imaging has proven an efficient technique for identification of high redshift filaments (Møller et al. 1998; Møller & Fynbo 2001). Confirming spectroscopy then maps out filaments as strings of separate star forming regions, each glowing in Lyα. In what follows we shall refer to those Lyα emitting regions using the shorter name 'LEGOs' (Lyα Emitting Galaxy-building Objects). Since each filament in this way is mapped by a finite number of objects, the accuracy with which one may determine its inclination angle will be a function of the number of LEGOs defining it.

As for the optimal redshift range and number of filaments, it is useful to consider what may be the minimum number of LEGOs needed per filament for an adequate determination of its inclination angle. To address this question we ran a series of simulations in which we randomly placed N LEGOs inside filaments defined as cylinders of length L and diameter D. We then determined the "observed" orientation vector of each filament, (defined as the best fitting straight line through the

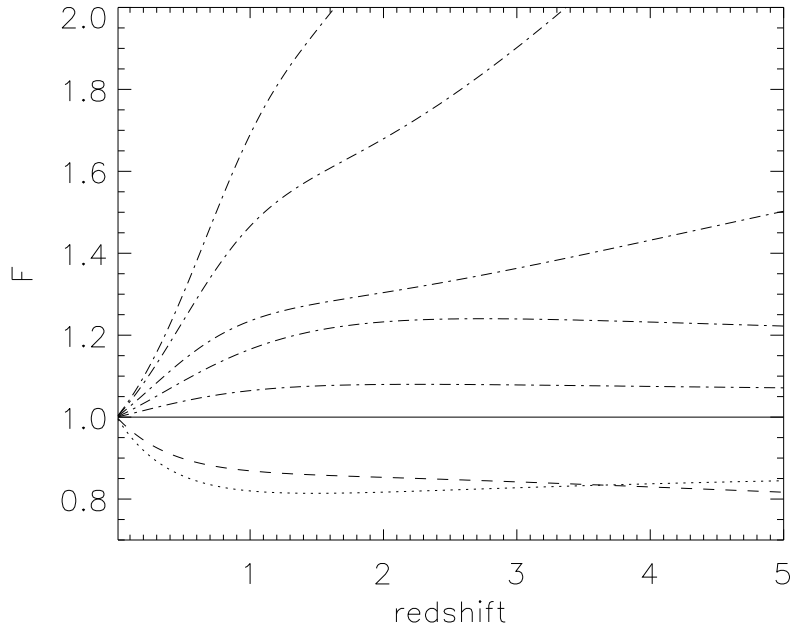

Figure 3.3 We plot F as a function of redshift for a range of cosmological models. $F = 1$ corresponds to the $\Omega_{\rm m} = 0.3$, $\Omega_\Lambda = 0.7$ model. The dotted and dashed curves below the $F = 1$ line correspond to $\Omega_\Lambda = 0$ models with $\Omega_{\rm m} = 1$ and $\Omega_{\rm m} = 0.3$ respectively. The dot-dashed curves above the $F = 1$ line correspond to models with ($\Omega_{\rm m}$,Ω_Λ) = (0.2,0.8), (0.1,0.9), (0.3,1.2), (0.3,1.4), (0.3,1.5).

N points), and the "observed" length-to-diameter ratio, $L_{\rm obs}/D_{\rm obs}$.[1] The observed set of orientation vectors define a solid angle centered on the true orientation vector, from which the sparse sampling error ($\sigma_{\rm sp}$) may be determined directly as the RMS of the 2D distribution of the observed set of intersections between the orientation vectors and the surface of the unit sphere. In Fig. 3.4 we show contours of constant $\sigma_{\rm sp}$ as a function of N and the $L_{\rm obs}/D_{\rm obs}$ ratio. As one would expect $\sigma_{\rm sp}$ is small for long/thin filaments but larger for short/wide filaments. It is also seen that for filaments defined by fewer than four LEGOs $\sigma_{\rm sp}$ grows rapidly. Møller & Fynbo (2001) reported the detection of a filament at $z = 3.04$ defined by eight LEGOs. Assuming ($\Omega_{\rm m}$,Ω_Λ) $= (0.3, 0.7)$ and using the procedure outlined above, we find $L_{\rm obs} = 20.2$ Mpc and $D_{\rm obs} = 3.2$ Mpc (comoving) for the $z = 3.04$ filament, and an inclination angle of $25.5°$. Its position is marked in Fig. 3.4 and it is seen that the sparse sampling error on its orientation is $\approx 1.9°$.

[1]The length of the cylinder is found as $L_{\rm obs} \equiv \sqrt{12}\,{\rm RMS}(z)$, and the diameter $D_{\rm obs} \equiv \sqrt{8}\,{\rm RMS}(r)$, where z is the position of a point projected onto the axis of symmetry, and r is the distance of a point to the axis of symmetry.

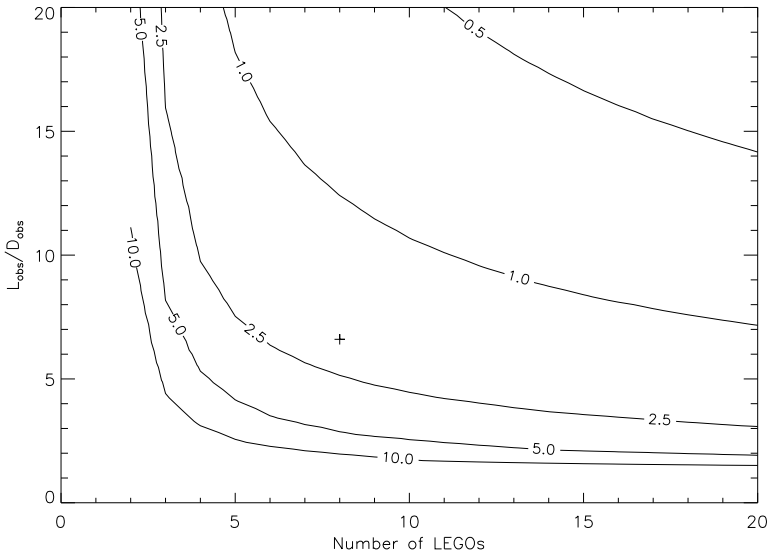

Figure 3.4 Contours of constant sparse sampling error on filament orientation as a function of the number of LEGOs defining the filament and the length-to-diameter ratio $L_{\rm obs}/D_{\rm obs}$. The contours are $\sigma_{\rm sp} = 0.5°$, $1°$, $2.5°$, $5°$ and $10°$, and the cross marks the filament detected by Møller & Fynbo (2001). The contours are based on 10^6 runs at each point.

In order to propagate the sparse sampling errors shown in Fig. 3.4 to errors on the determination of the line of sight scale factor F, we repeated the Monte Carlo simulations of Sect. 3.3, now including random errors on filament orientations as described above. The goal was to determine how large intrinsic errors on the filament orientations we could tolerate before the error analysis summarized in Fig. 3.1 would be seriously compromised. The Monte Carlo simulations were repeated for 20, 50, and 80 filaments, and for $\sigma_{\rm sp}$ in the range $0°$ to $10°$. The results are summarized in Table 3.2 where we list errors on F from Fig. 3.1, and from the full analysis including sparse sampling errors. It is seen that even for $\sigma_{\rm sp}$ as large as $10°$ the additional errors are insignificant. From Fig. 3.4 we see that $\sigma_{\rm sp} < 10°$ always is achieved for filaments with $L_{\rm obs}/D_{\rm obs} > 3$ defined by four LEGOs or more.

In conclusion of this section, a first rough determination of $(\Omega_{\rm m}, \Omega_\Lambda)$ can be obtained with the discovery of 20 filaments each defined by four LEGOs, or 80 LEGOs in all. With 50 filaments, or 200 LEGOs total, the errors are such that they will place significant new constraints on the values of $\Omega_{\rm m}$ and Ω_Λ permitted by the current supernova observations.

Table 3.2 Errors (1σ) on determination of the line of sight scale factor F (Fig. 3.1) including sparse sampling of individual filaments. The results are based on 2×10^5 runs.

	Filaments		
$\sigma_{\rm sp}$	20	50	80
$0.0°$	0.259	0.162	0.128
$5.0°$	0.265	0.166	0.131
$10.0°$	0.283	0.179	0.140

3.5 Summary and conclusions

A significant number of $8-10$ meter class telescopes became operational during the past decade, thereby moving several cosmological tests from the domain of speculation into the domain of observation. The currently most successful test relies heavily upon the assumption that supernovae of type Ia are standard candles. Other proposed tests, based on e.g. distances between Lyman Break galaxies, seek to exploit an expected standard rod.

In this paper we have presented a detailed discussion of a test which relies on neither standard candles nor standard rods. The test makes use of only the requirement of isotropy, and of the prediction from numerical simulations of the high redshift Universe that it has a filamentary structure. Direct observational evidence that such filaments may indeed be found was presented by Møller & Fynbo (2001) who also proposed three cosmological tests based on the existence of such filaments. Here we have in detail investigated and described the implementation of the first of these tests. We have used Monte Carlo simulations to determine the accuracy with which one may obtain values of $\Omega_{\rm m}$ and Ω_Λ, and we have described how additional statistical errors and observational effects will affect the results.

We find that the constraints this test can set are mostly on Ω_Λ, or in other words the limiting curves in the usual ($\Omega_{\rm m}$, Ω_Λ) diagram are mostly horizontal. This means that they intersect the probability curves from the $z < 1$ SN Ia projects. Already with a sample of only 20 filaments the SN Ia results will be intersected, but with a sample of 50 filaments the area of allowed values in the ($\Omega_{\rm m}$, Ω_Λ) diagram will be significantly reduced. The optimal redshift range for the test is found to be $z = 1.5-4$. In the range $z = 2-4$ filaments can conveniently be detected using deep searches for faint Lyα emitters (LEGOs). Each filament to be used in this test must have an observed length-to-diameter ratio of no less than 3, and must be defined by no less than four objects.

Three surveys are currently underway which should produce data useful for this test: *i)* the Large Area Lyman Alpha (LALA) survey

(Rhoads et al. 2000) that targets Lyα emitters at redshift 4.5 and 5.7, *ii)* a survey conducted with the SUBARU telescope which has resulted in a large sample of candidate Lyα emitters at $z = 4.86$ (Ouchi et al. 2003), and *iii)* in the opposite end of the optimal redshift window there is a survey on the Nordic Optical Telescope (NOT) to map out a slice of the $z = 2$ Universe in Lyα emission (Møller et al. in prep). The NOT survey started in 2001 and takes advantage of the excellent UV capabilities of the NOT instrumentation which was demonstrated in similar observations of fields containing $z = 2$ host galaxies of Gamma Ray Bursters (Fynbo et al. 2002). Currently there are no large area Lyα surveys targeting $z = 3$, and there are no large area Lyα surveys conducted on the ESO VLT. Smaller targeted programmes aimed at $z = 3$ fields have been successfully conducted on the VLT (Fynbo et al. 2003a), confirming that the necessary volume density of Lyα emitters will indeed be found.

Acknowledgements

We are grateful to H.-J. Gerber for interesting discussions, and for helpful comments on an earlier version of this manuscript. MPE and MW acknowledge support from the ESO Directors Discretionary Fund.

3.6 Appendix: Cosmology with $\Lambda \neq 0$

We follow the treatment given in Longair (1998), which uses the metric in the form:

$$ds^2 = c^2 dt^2 - R^2(t)[dr^2 + \mathcal{R}^2 \sin(r/\mathcal{R})^2 (d\theta^2 + \sin(\theta)^2 d\phi^2)],$$

where $\mathcal{R}$ is the radius of curvature of the Universe, and R is the scale factor normalized to 1 at the present epoch. The radial coordinate r is the metric distance at time t, and it can be found as a function of z by integrating the differential equation

$$\frac{dr}{dz} = \frac{c}{H_0} \left((1+z)^2 (\Omega_{\rm m} z + 1) - \Omega_\Lambda z (z+2) \right)^{-1/2}, \tag{3.7}$$

where $\Omega_{\rm m}$ and Ω_Λ are given by the present mean density ρ_0 and the cosmological constant Λ, respectively:

$$\Omega_{\rm m} = \frac{8\pi G \rho_0 c^2}{3H_0^2}, \quad \Omega_\Lambda = \frac{\Lambda c^2}{3H_0^2}. \tag{3.8}$$

The radius of curvature $\mathcal{R}$ can be determined from the relation

$$\frac{1}{\mathcal{R}^2} = \frac{\Omega_{\rm m} + \Omega_\Lambda - 1}{c^2/H_0^2}. \tag{3.9}$$

Longair defines the distance measure

$$D = \begin{cases} \mathcal{R}\sin(r/\mathcal{R}) & \text{if } 1/\mathcal{R}^2 > 0 \\ r & \text{if } 1/\mathcal{R}^2 = 0 \\ \mathcal{R}\sinh(r/\mathcal{R}) & \text{if } 1/\mathcal{R}^2 < 0 \end{cases} \tag{3.10}$$

from which the angular diameter distance D_{A} can be derived as $D_{\mathrm{A}} = D/(1+z)$. The proper radial distance is determined from the differential $\left(\frac{dr}{dz}\right)_{\mathrm{prop}} = \frac{dr}{dz}/(1+z)$.

We can now finally derive the two functions f_L and f_W introduced in Sect. 3.2. As $W_{\mathrm{true}} = \phi D_A$ the function f_W is simply given by $H_0 D_A$. Similarly, the proper length L_{true} of a box defined by two redshifts z_{min} and z_{max} ($\delta z = z_{\mathrm{max}} - z_{\mathrm{min}} \ll (z_{\mathrm{max}} + z_{\mathrm{min}})/2$) is given by $\left(\frac{dr}{dz}\right)_{\mathrm{prop}} \delta z$, hence $f_L = H_0 \left(\frac{dr}{dz}\right)_{\mathrm{prop}}$.

Chapter IV

The Lyman-α glow of gas falling into the dark matter halo of a $z = 3$ galaxy

Weidinger, M., Møller, P., Fynbo, J. P. U., & Thomsen, B. (2004). *Nature*, **430**, 999

QUASARS are the visible signatures of supermassive black holes in the centres of distant galaxies. It has been suggested (e.g. Carlberg 1990) that quasars are formed during "major merger events" when two massive galaxies collide and merge, leading to the prediction that quasars should be found in the centres of the regions of largest overdensity in the early Universe. In dark matter (DM)-dominated models of the early Universe, massive DM halos are predicted to attract the surrounding gas, which falls towards its centre. The neutral gas is not detectable in emission by itself, but gas falling into the ionizing cone of such a quasar will glow in the Lyman-α line of hydrogen, effectively imaging the DM halo (Haiman & Rees 2001). Here we present a Lyα image of a DM halo at redshift 3, along with a two-dimensional spectrum of the gaseous halo. Our observations are best understood in the context of the standard model for DM halos (Navarro et al. 1997); we infer a mass of $(2-7)\times 10^{12}$ solar masses ($M_\odot$) for the halo.

Using radiative transfer calculations, Haiman & Rees (2001) predicted that gas falling into a DM halo between redshifts 3 and 8 that was harbouring a quasar should be detectable in Lyα-emission at flux levels accessible to present day telescopes, owing to the reprocessing of quasar ultraviolet photons. Recently, Barkana & Loeb (2003) found absorption features in quasar spectra, which they interpreted as a signature of neutral hydrogen (HI) falling into the DM halos surrounding two quasars. Such absorption features can be used to study the gas in one

dimension (1D) along the line of sight, whereas detection of extended Lyα-emission can be used in a 2D study, providing more constraints on the interplay between gas, quasar radiation and DM halo.

4.1 Observations

In a deep Lyα narrow-band image we detected asymmetric extended emission North-East of the $z = 3$ radio-quiet quasar Q 1205-30, making this quasar a prime candidate for a study of its DM halo. The extended Lyα emission was first thought to be related to a foreground absorber (Fynbo et al. 2000b), but deep follow-up spectroscopy obtained with the FORS1 instrument on the ESO Very Large Telescope allowed us to measure precise redshifts of quasar, absorber, and extended emission, clearly linking the extended emission to the quasar, not the absorber. The 2D spectrum is presented in Fig. 4.1 (details of the data reduction will be presented elsewhere). In the 2D spectrum the wavelength increases along the abscissa, and the position on the sky changes along the ordinate. In order to reveal the underlying extended emission we have optimally extracted the 2D quasar spectrum by fitting and removing the quasar spectral point-spread function (Møller 2000). Spectroscopic detection of kinematically resolved extended Lyα-emission is not uncommon (Møller et al. 2000; Bunker et al. 2003), but it does not provide sufficient information to distinguish between scenarios of – for example – nearly edge-on disks and gaseous halos. For this, morphological information is needed. In Fig. 4.2a we present a 10×10 arcsec^2 narrow-band image of the extended emission.

4.2 Photoionizing model

A quasar emits its radiation in an ionizing cone with an opening angle of Ψ, while we observe the whole system under an inclination angle of θ (see Fig. 4.3). The surface brightness at each point in the vicinity of the quasar is calculated by integration of the volume emission along the line of sight (Gould & Weinberg 1996). We take the gas density profile to be a power-law, $n_{\rm HI}(r) = n_{\rm HI,1}\,(r/1\ {\rm kpc})^{-\alpha}$, with a slope α and a neutral hydrogen density at a distance of 1 kpc $n_{\rm HI,1}$, because this appears in numerical simulations of DM halos to be a good approximation at small radii (Barkana 2004). If we assume a mass of the DM halo, we may calculate the observed infall velocity in the model. At a given projected distance from the quasar the observed velocity is the average projected velocity weighted with the emissivity of the gas along the line of sight.

Applying this model to Q 1205-30, our calculation shows that the Lyα halo should be detectable with 8-m class telescopes up to several

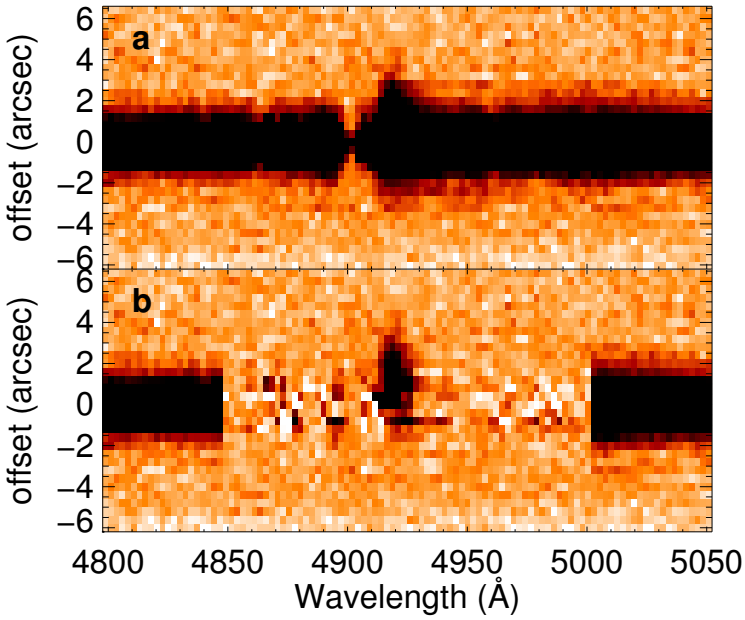

Figure 4.1 Two-dimensional spectrum of Q 1205-30 and the extended Lyα emission. The wavelength increases along the abscissa, the position on the sky changes along the ordinate. The spectroscopy was performed with a slit position angle of 7.9° east of north (see Fig. 4.2a). **a**, The 2D quasar spectrum. The extended Lyα emission is faintly visible at 4920 Å. **b**, The quasar spectrum has been subtracted between the wavelengths $4850 - 5000$ Å, clearly revealing the underlying extended emission.

arcsec from the quasar, assuming a modest amount of neutral hydrogen infall. Considering – for now – the case where only one cone is visible, the extended emission may be symmetric (if $\theta \approx 0$, that is, the cone is seen close to end-on) or highly asymmetric (if $\theta \approx \Psi/2$). By fitting the calculated surface brightness maps to the observed narrow-band image we establish a relation between the opening angle and the best-fitting inclination angle. Thus, we are left with the opening angle, Ψ, the slope, α, and the neutral hydrogen density at 1 kpc, $n_{\rm HI,1}$, as the only free parameters of the model. In Fig. 4.2, we compare our observed narrow-band image to calculated Lyα surface brightness maps with an opening angle $\Psi = 110^\circ$ and three different inclination angles: the best-fit and two others. For the expected large opening angles ($\Psi \approx 90^\circ - 120^\circ$) (Lawrence 1991; Elvis 2000), varying the opening angle primarily affects the shape of the surface brightness profile seen on the side where the emission is weakest (in Fig. 4.3, that would be on side A of the sightline), and only has a minor effect on the shape of the main emission profile (on side B). The gas density scale, $n_{\rm HI,1}$, determines the normalization of the surface brightness profile, but not the shape, which is set

by the slope α. The results are not dependent on the choice of a power-law gas density profile. An exponential gas density profile provides an equally good fit to the data.

The extended emission is spatially resolved, so we can measure its surface brightness profile and velocity profile (see Fig. 4.4). The surface brightness profile is measured by integrating the flux from 4900 Å to 4947 Å in each spatial bin. The velocity in each spatial bin is measured by fitting a gaussian to the line profile. The infall velocity is calculated relative to the redshift $z = 3.041$ of the quasar.

4.3 Results

We find that the model describes the observations well. The opening angle is the only parameter which remains unconstrained, so we plot the surface brightness profile for a range of opening angles (Fig. 4.4a). The best-fit values for the neutral hydrogen density at 1 kpc vary less than a factor two between $\Psi = 90°$ and $170°$, while the slope varies between 0.02 and 0.09. The velocity profile of the extended emission (Fig. 4.4b) arises as a projection effect, and fitting velocity curves of canonical DM halo profiles (Navarro et al. 1997) to the observed velocities, we infer a virial mass of $(2-7) \times 10^{12} M_\odot$ for the DM halo. An identical mass estimate is obtained when using an exponential gas density profile. The HI density from our best fitting model allows us to calculate an accretion rate of $\sim 0.1 M_\odot \mathrm{yr}^{-1}$ in neutral hydrogen. The total accretion rate will be higher as the gas is highly ionized.

Where studies based only on spectra are unable to provide evidence to distinguish between several different scenarios, the combination of deep imaging and deep spectroscopy allows us to rule out alternative explanations of the extended emission. Jets are generally believed to be present in radio-quiet quasars and are predicted to extend out to ~ 0.1 kpc (Blundell et al. 2003), where the extended Lyα emission around Q 1205-30 extends out to ~ 30 kpc. Outflowing galactic winds are believed to be triggered by supernovae going off inside the galaxy, and are therefore expected to be metal-enriched. Our detection limit of 4×10^{-18} erg s^{-1} cm^{-2} arcsec^{-2} (3σ) ensures that we are able to detect the CIV and HeII lines typical in extended emission around radio-loud quasars (Heckman et al. 1991a). We did not detect any of these lines, so the gas appears not to have been enriched by supernovae.

Acknowledgements

Based on observations made with ESO Telescopes at the Paranal Observatory.

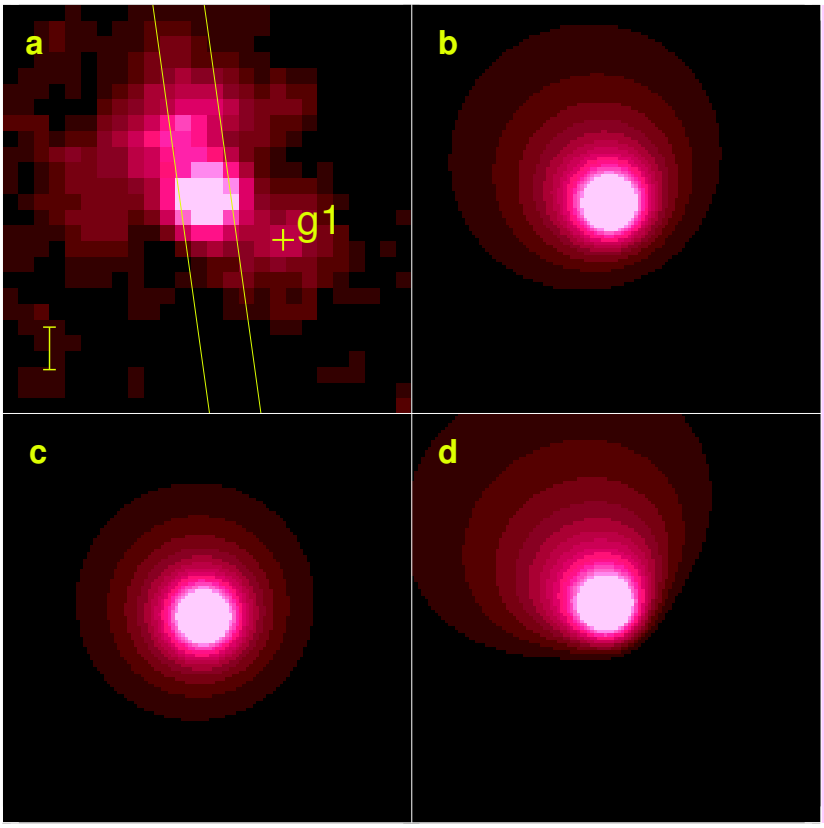

Figure 4.2 Narrow-band image of the extended Lyα emission compared to models. **a**, Image of the 10×10 arcsec^2 region around Q 1205-30 seen in Lyα. The quasar has been subtracted from this image to reveal the underlying extended emission. A 1.2-arcsec-wide slit is overplotted at a position angle of $7.9°$ east of north, and the position of an unrelated foreground galaxy[5] is marked g1. The vertical bar on the lower left is 1 arcsec high. **b – d**, Calculated 10×10 arcsec^2 surface brightness maps for an opening angle of $\Psi = 110°$ and three inclination angles. The best fitting inclination angle ($\theta = 27°$) is shown in **b**, two other inclination angles are shown in **c** ($\theta = 10°$, excluded at 3.5σ) and **d** ($\theta = 50°$, excluded at 3σ) for comparison. Given an opening angle, the best-fit inclination angle is determined in the following way. An average surface brightness profile, parallel and perpendicular to the apparent major axis of the extended emission, is fitted to the same average calculated from the models. For each opening angle Ψ the best-fitting inclination angle is found.

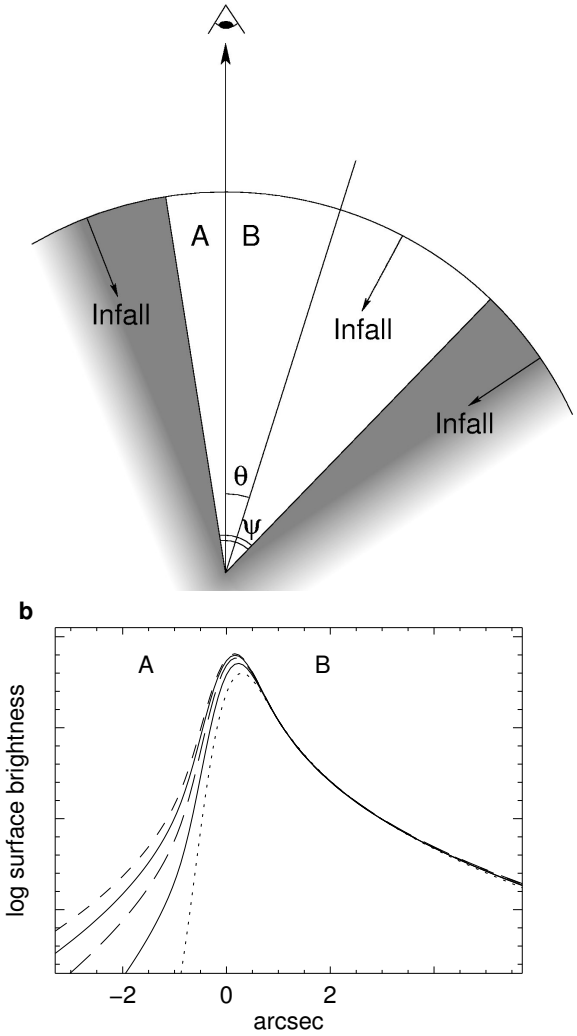

Figure 4.3 Schematic presentation of the model. **a**, A quasar is located in the centre of a DM halo into which neutral hydrogen is falling. The ionizing photons from the quasar are emitted in a cone of opening angle Ψ, and they cause the infalling HI to glow in Lyα. The observer views the system inclined at an angle θ. The surface brightness at each point is calculated by integration of the volume emission along the line of sight (Gould & Weinberg 1996): $\Sigma_{\rm Ly\alpha} = \frac{\int E_{\rm Ly\alpha}\dot{n}_{\rm Ly\alpha}(r)dl}{4\pi D_L^2}\frac{D_A^2}{d\Omega}$, where $E_{\rm Ly\alpha} = 10.4$ eV is the energy of a Lyα photon, $\dot{n}_{\rm Ly\alpha}(r)$ is the production rate of Lyα photons at a distance r from the quasar, D_L is the quasar luminosity distance, and D_A is the angular distance, such that $\frac{d\Omega}{D_A^2}$ is the conversion from cm^2 to arcsec^2. The Lyα production rate is $\dot{n}_{\rm Ly\alpha}(r) = \eta_{\rm thin} n_{\rm HI}(r)\Gamma(r)$, and $\eta_{\rm thin} = 0.42$ is the probability for an ionizing photon to result in a Lyα photon in the optically thin case, $n_{\rm HI}(r)$ is the volume density of neutral hydrogen atoms, and $\Gamma(r)$ is the ionization rate of hydrogen atoms. **b**, A schematic illustration of the predicted surface brightness profile for various opening angles $\Psi = 90°$ (dotted), $110°$ (solid), $130°$ (long-dashed), $150°$ (solid), and $170°$ (short-dashed), and a fixed inclination angle $\theta = 40°$. The profiles are presented as they would appear when observed with a seeing of 0.7 arcsec through a slit aligned with the line between the sightline l and the symmetry axis of the cone. Negative angular distances correspond to emission seen from side A, and positive angular distances correspond to emission seen from side B.

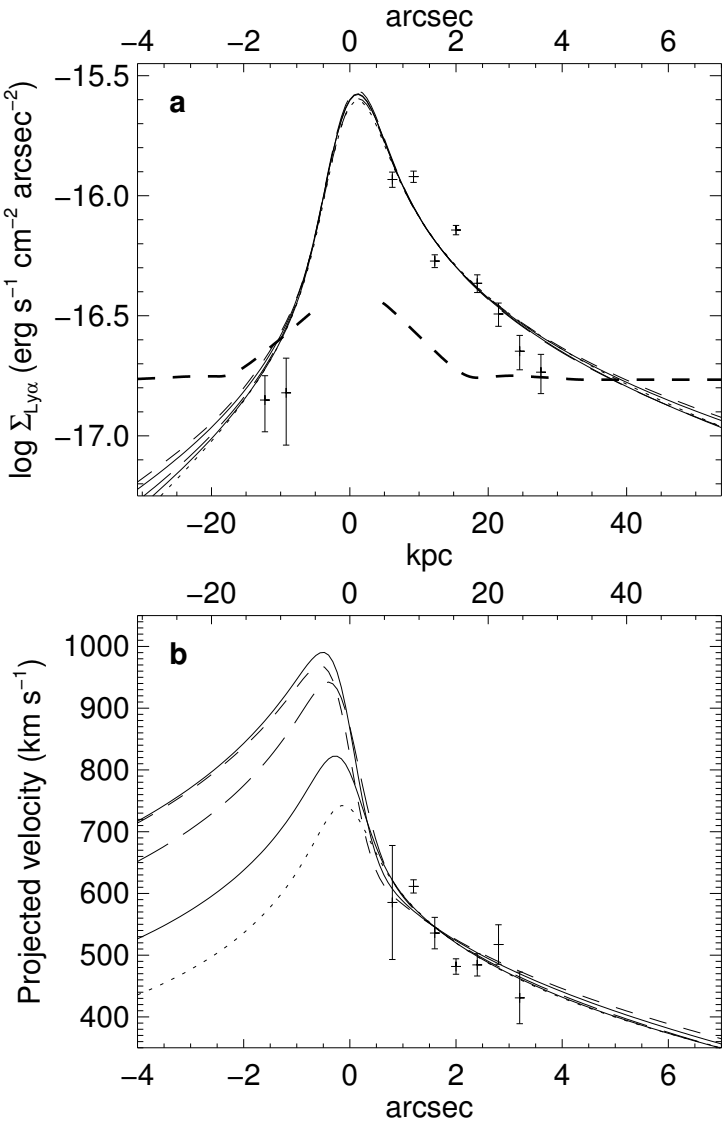

Figure 4.4 Calculated surface brightness profile and projected velocity. **a**, Comparison of the calculated and observed surface brightness profile. Thin lines are the calculated profile for various opening angles, and data points are our observations of the extended Lyα-emission around Q 1205-30. The calculations were performed for opening angles and inclination angles of $\Psi = 90°$, $\theta = 22.5°$ (dotted), $\Psi = 110°$, $\theta = 27.2°$ (solid), $\Psi = 130°$, $\theta = 31.8°$ (long-dashed), $\Psi = 150°$, $\theta = 36.5°$ (solid), and $\Psi = 170°$, $\theta = 41.1°$ (short-dashed). The thick dashed line shows our 5σ detection limit. **b**, Comparison of calculated and observed projected velocity relative to the quasar redshift. Lines are the calculated best-fit velocity profiles for opening angles and inclination angles of $\Psi = 90°$, $\theta = 22.5°$ (dotted), $\Psi = 110°$, $\theta = 27.2°$ (solid), $\Psi = 130°$, $\theta = 31.8°$ (long-dashed), $\Psi = 150°$, $\theta = 36.5°$ (solid), and $\Psi = 170°$, $\theta = 41.1°$ (short-dashed). Three of the measurements in panel **a** were too faint to allow a secure velocity determination. In both panels the angular distance was converted to physical distance assuming a flat $\Omega_\Lambda = 0.7$ Universe with a Hubble constant $H_0 = 70$ km s^{-1}Mpc^{-1}. Error bars are 1σ.

Chapter V

The extended Lyman-α emission surrounding the $z = 3.04$ radio-quiet QSO1205-30: Primordial infalling gas illuminated by the quasar?

Weidinger, M., Møller, P., Fynbo, J. P. U., & Thomsen, B. (2005). *A&A*, **436**, 825

5.1 Introduction

QUASAR host galaxies are visible tracers of the close environment of this powerful type of active galactic nuclei (AGN). The feeding of the central engine from the host galaxy, and the feedback of the quasar to the host are important unknown factors in current numerical models, which need to be understood. The study of quasar host galaxies is difficult, because of the high contrast between the bright point source quasar and the faint, extended host galaxy. Surveys of AGN host galaxies have primarily targeted radio-loud quasars (RLQs) and radio galaxies (RGs) (e.g. Lehnert et al. 1992, 1999; Reuland et al. 2003; Sánchez & González-Serrano 2003), despite the fact that the majority of quasars are radio-weak or radio-quiet. In such surveys it has been found that RLQs and RGs at low z (here taken to mean $z < 1$) reside in luminous elliptical galaxies, while radio-quiet quasars (RQQs) are found in both elliptical and early spiral galaxies. At intermediate redshifts ($1lz \lesssim 2$) galaxies in general appear to have more disturbed morphologies, making it difficult to apply the simple classification of "ellipticals" and "spirals". Studies have found that host galaxies of RQQs are $1 - 2$ mag fainter than hosts of RLQs with similar luminosity (Falomo et al. 2001;

Kukula et al. 2001). Similarly, in a study of quasars out to $z = 2.1$ the black holes of RLQs are typically found to be 45% more massive than their radio-quiet counterparts (McLure & Jarvis 2004). At $z > 2$ the cosmological surface brightness dimming makes it increasingly difficult to make secure detections of the host galaxies. For RLQs some 20 examples of $z > 2$ hosts are seen (Hu et al. 1991; Heckman et al. 1991a,b; Steidel et al. 1991; Lehnert et al. 1992, 1999; Wilman et al. 2000), but only few surveys have targeted RQQs and with limited success (Bremer et al. 1992; Lowenthal et al. 1995; Fynbo et al. 2000a; Møller et al. 2000; Ridgway et al. 2001; Bunker et al. 2003). The relatively faint hosts of RQQs compared to RLQs makes them more difficult to detect. A promising method is narrow-band imaging tuned to the Lyα line at the quasar redshift (Hu & Cowie 1987; Hu et al. 1996). Haiman & Rees (2001) predict that gas enshrouding a quasar between redshifts 3 and 8 would be photoionized by the quasar UV emission and should be detectable at a surface brightness of 10^{-18} to 10^{-17} erg s^{-1} cm^{-2} arcsec^{-2} in the Lyα line. These limits have only been reached for very few surveys.

In this paper we report on a spectroscopic study of the sightline towards the radio-quiet quasar Q 1205-30 at $z = 3.04$ and its associated extended Lyα emission detected by Fynbo et al. (2000b) (hereafter Paper I).

The paper is organized as follows: In Sect. 5.2 we present the observations and data reductions. We continue in Sect. 5.3 with the results of our analysis. In Sect. 5.4 we discuss the foreground galaxies, and we present a simple model for the extended Lyα emission in Sect. 5.5. We end in Sect. 5.6 with a discussion of the origin of the extended emission. Unless stated otherwise we will use $\Omega_{\rm m} = 0.3$, $\Omega_\Lambda = 0.7$, $H_0 = 100h$ km s^{-1}Mpc^{-1} $= 70$ km s^{-1}Mpc^{-1}. In this model a redshift of 3.04 corresponds to a luminosity distance $D_L = 25.8$ Gpc and a distance modulus of 47.1. One arcsec on the sky corresponds to a projected distance of 7.67 proper kpc and the lookback time is 11.4 Gyr (84.5% of the time since Big Bang).

5.2 Observations and data reduction

The observations were carried out with the Unit Telescope 1 (Antu) of the ESO Very Large Telescope (VLT) on March 4–5, 2000, under photometric and good seeing conditions. The data were acquired with the FOcal Reducer/low dispersion Spectrograph (FORS1) instrument in Multi Object Spectroscopy (MOS) mode with the red G600R and blue G600B grisms as a part of a larger campaign (see Fynbo et al. 2001). The slitlet used was 1.2 arcsec wide and 20 arcsec long, and the positions on the CCD resulted in a wavelength coverage of approximately $4000 - 6000$ Å

Table 5.1 Observation log.

	PA	Grism	Seeing	Exp-time
PA1	$67.20°$	G600B	$0\farcs91$	4×1800 s
PA1	$67.20°$	G600R	$0\farcs69$	2×1800 s
PA2	$7.90°$	G600B	$0\farcs69$	4×1800 s
PA2	$7.90°$	G600R	$0\farcs73$	3×1800 s

(G600B) and $5800 - 7800$ Å (G600R). The slitlets had position angles of $67.20°$ (PA1) and $7.90°$ (PA2) East of North centred on the quasar (see below). For the observations we used the standard resolution collimator. During observations with the G600B grism the CCD was binned 2×2, and resulting in a pixel size of 0.4 arcsec by 2.4 Å for G600B and 0.2 arcsec by 1.2 Å for G600R. The seeing in the combined science frames was measured to be 0.9 arcsec (PA1) and 0.7 arcsec (PA2) at a wavelength of ~ 5100 Å, leading to spectral resolutions of 5 Å (PA1) and 4 Å (PA2). The exposure times are given in Table 5.1.

Contour plots of the 18×18 arcsec^2 field of Q 1205-30 imaged in I and Lyα narrow band is shown in Fig. 5.1 taken from Paper I. We shall here follow the naming convention of that paper, i.e. g1 is the blue galaxy SW of the quasar, g2 is the red galaxy NE of the quasar, and S6 is the extended Lyα emission N and NE of the quasar. The projected distances from the QSO are 2.12 ± 0.04 arcsec for g1 and 2.77 ± 0.07 arcsec for g2. For PA1 the slitlet covers g1, g2, the QSO and a part of S6, whereas for PA2 the slitlet covers the central part of S6 and the QSO.

5.2.1 Basic reductions

The individual science frames were bias subtracted using standard techniques. The flat fielding was done by first filtering the flat fields along the dispersion axis with a 61×1 pixels (146 Å long) median filter for the G600B grism, and a 121×1 pixels (145 Å long) median filter for the G600R grism. Then the flat fields were normalized by dividing the unfiltered flat fields by the filtered ones, and finally we divided the science frames by these normalized flat fields. In order to obtain a mean sky spectrum spatial bins on both sides of the quasar spectrum were filtered using a 1×13 pixels median filter (i.e. only filtering along the spatial axis) to remove cosmic ray hits and averaged. Regions used for determining the sky spectrum were never closer than 5 arcsec to the QSO on the side of the extended emission and 4 arcsec on the opposite side. The mean sky spectrum was expanded to a two dimensional spectrum by duplicating the 1D spectrum and subtracted from the unfiltered science frame.

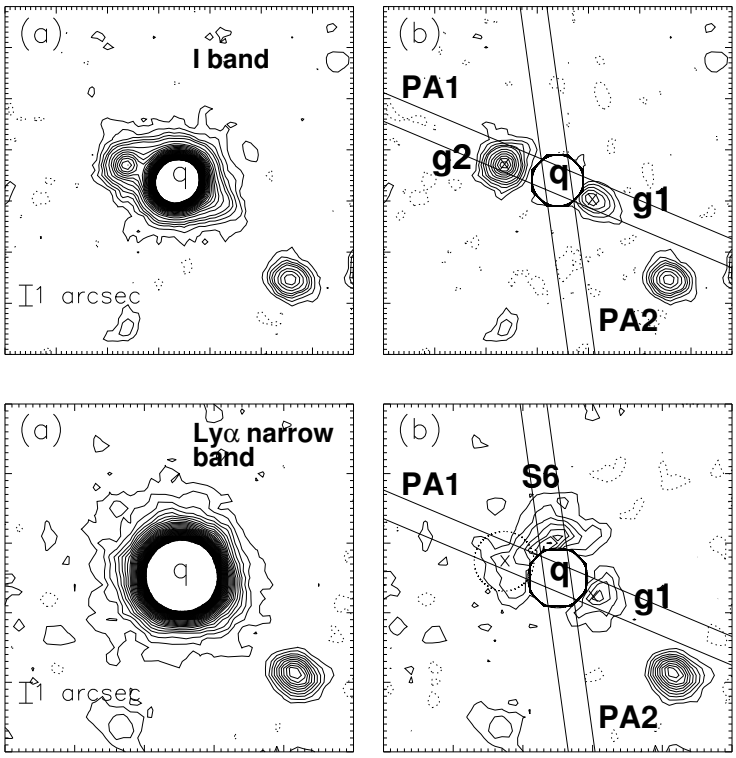

Figure 5.1 The 18×18 arcsec^2 field of Q 1205-30. *Upper panels:* Contour plot of the I-band image before (a) and after (b) PSF subtraction of the quasar. North is up and East is left. *Lower panels:* Contour plot of the narrow band image before (a) and after (b) PSF subtraction of the quasar. North is up and East is left. Taken from Paper I.

5.2.2 Spectral extractions

The science frames were coadded and the quasar spectrum was optimally extracted using the code described in Møller (2000). After spectral point-spread-function (SPSF) fitting and removal of the QSO, the extended Lyα emission of S6 was clearly visible at both PA1 and PA2 (see Fig. 5.2).

PA1 was aligned with the two galaxies g1 and g2 (see Fig. 5.1) and centred on the QSO, so in this case we had to decompose the spectrum into its individual components. We employed an iterative procedure to separate the contributions from g1 and S6 to the total quasar flux: *i)* Extract and remove the QSO spectrum. *ii)* Extract and remove the spectrum of g1 and S6. The procedure converged to a stable solution after three iterations. For the PA1 observations using grism G600R the seeing conditions were slightly better than for those using G600B (see Table 5.1), so the projected distances of g1 and g2 were enough to bring

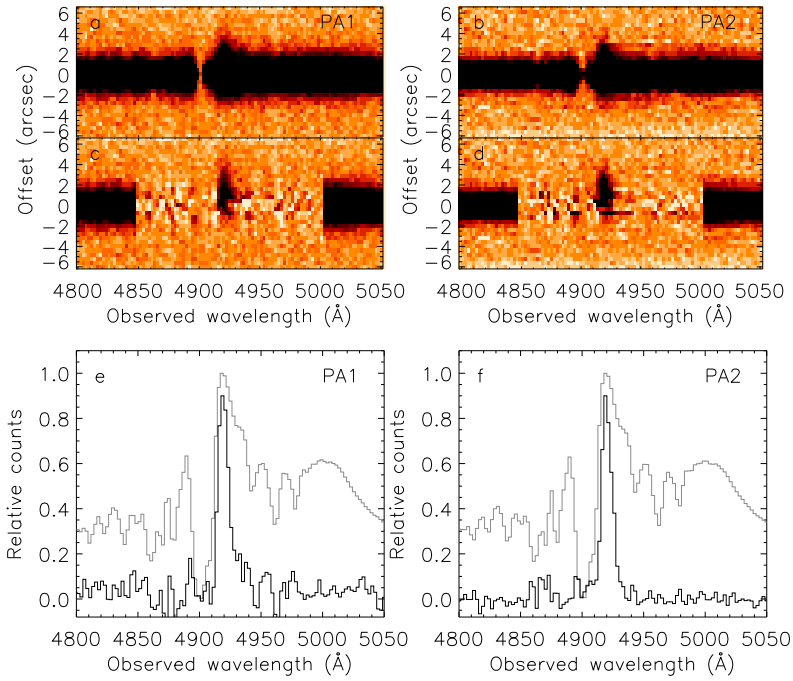

Figure 5.2 Spectra at PA1 (*left column*) and PA2 (*right column*). **a) – b)** The 2D quasar spectrum. **c) – d)** The 2D quasar spectrum has been subtracted between 4850 Å and 5000 Å revealing the extended Lyα emission. The zero point of the spatial axis is set to the centroid of the QSO. Note the large residuals from the quasar SPSF subtraction, which are due to the large shot noise near the centroid. **e) – f)** The spectrum of the QSO Lyα emission line (*light grey curve*) and the spatially averaged spectrum of the extended Lyα emission (*black curve*). The maximum flux of the extended Lyα emission is scaled to 90% of the maximum QSO flux. The total line flux in extended Lyα is around 1% of the flux from the QSO Lyα line. The overall flux scale in this plot is arbitrary.

them outside the QSO point-spread function (PSF) and we could make a normal extraction of the quasar spectrum.

In the PA2 spectra we had only the QSO and S6 on the slit. In order to make sure that the extended flux of S6 was not modifying the quasar SPSF, we here used an option in the code which allowed us to exclude a wavelength region from the construction of the quasar SPSF. In the region from 4902 Å to 4987 Å the code therefore only fitted and extracted the QSO spectrum, it did not update the SPSF lookup table (for details see Møller 2000). For the general problem of decomposing a 2D spectrum of two superimposed objects there is a certain degeneracy of solutions. One may choose to assign the maximum amount of flux to one object, to the other object, or to aim for somewhere in between. In this case we decided to opt for a solution in between, which avoids digging a hole in the extended Lyα emission near the QSO centroid.

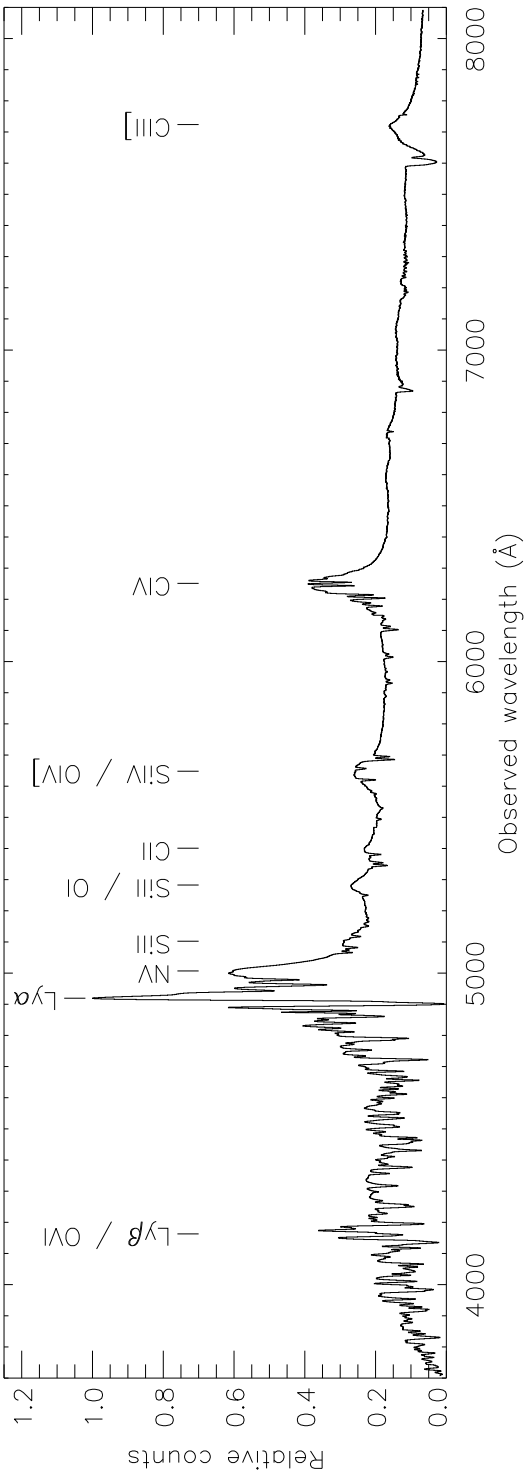

Figure 5.3 Extracted spectrum of Q 1205-30. The most prominent emission lines are indicated. The spectrum has not been extinction corrected nor flux calibrated.

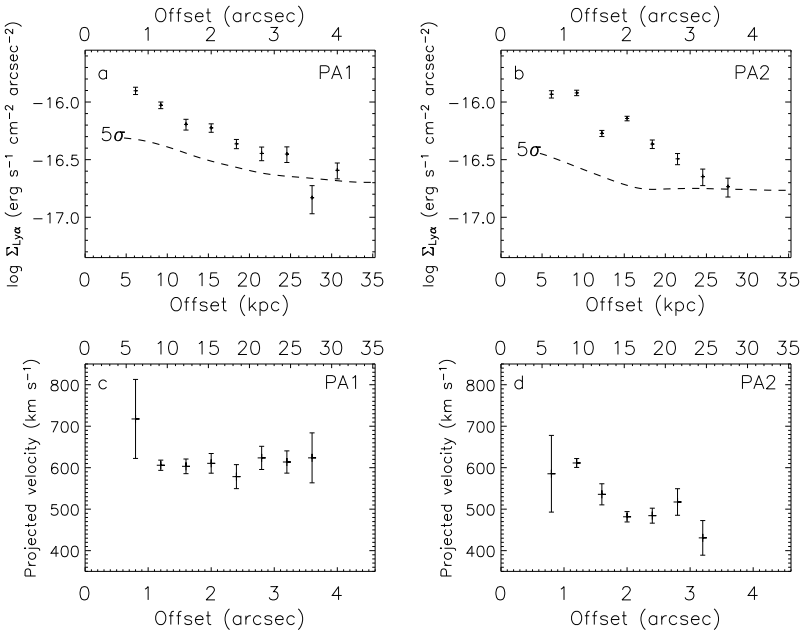

Figure 5.4 Surface brightness and velocity profiles of the extended Lyα emission based on spectra at PA1 (*left column*) and PA2 (*right column*). **a) – b)** Surface brightness profile. The error bars are based on photon statistics only. Systematic errors due to the flux calibration are not considered. The thick dashed line shows our 5σ detection limit. **c) – d)** Velocity profile of the extended Lyα emission measured relative to the systemic redshift of the quasar (see Sect. 5.3.2). The uncertainties are statistical uncertainties on the position of the maximum of a fitted Gauss curve (Landman et al. 1982). In both PAs the most distant detection was too faint to allow a secure determination of the velocity. A rest-frame velocity of 600 km s^{-1} relative to the systemic quasar redshift (see Sect. 5.3.2) corresponds to a redshift $z = 3.049$.

The degeneracy has no consequence at distances larger than 1 arcsec from the QSO, but closer to the QSO the Lyα surface brightness of S6 is very uncertain.

The output from the code is the optimally extracted 1D and 2D spectrum of the QSO as well as the 2D spectrum of the extended Lyα emission. The 2D spectrum of the extended Lyα emission and the 1D spectrum of the QSO (with cosmic ray hits removed) are shown in Fig. 5.2a-5.2d and Fig. 5.3, respectively. For comparison we show a zoom of the Lyα emission of the quasar and the spatially averaged extended Lyα emission in Fig. 5.2e-5.2f.

5.2.3 Wavelength and flux calibrations

The spectra in Fig. 5.2 were wavelength calibrated using the *dispcor* task in IRAF[1]. The RMS of the deviations from a 4.$^{\rm th}$ order Chebyshev polynomial fit to 12-19 lines were 0.6 Å for the G600B spectra and $0.08-0.16$ Å for 28-33 lines in the G600R spectra.

The flux calibration was done as follows. First we estimated the continuum of the QSO away from the emission lines. We divided the spectrum by the continuum, obtaining a flat spectrum, and forced it onto an arbitrary power-law. Measuring the Bessel $B-I$ colour on the resulting spectrum and comparing to the observed $B-I$ colour (Paper I) we calculated the slope of the power-law which would bring the two in agreement ($\alpha = 0.65$). We then forced the spectrum onto this power and normalized it to agree with our photometric measurements. The advantage of this procedure is that to the first several orders all absolute and differential slit losses as well as atmospheric absorption are automatically taken into account for all point source objects on the slit. We estimate the absolute flux calibration to be correct to within 10% while the relative is better. This applies to point sources, but not to extended sources for which there are additional slit losses. We present surface brightness profiles and rest-frame velocity curves of the extended Lyα emission (relative to the systemic redshift of the quasar, see Sect. 5.3.2) in Fig. 5.4.

5.3 Results

5.3.1 Redshifts of the galaxies g1 and g2

The primary purpose of this study is to clarify the nature of the extended Lyα emission at $z \approx 3.04$. As pointed out in Paper I the galaxies g1 and in particular g2 may have a lensing effect, enhancing and stretching the Lyα patch. Therefore we first set out to determine their redshifts.

We identify four emission lines in the spectrum of the blue galaxy g1. The AB-magnitudes of g1 are $B(AB) = 24.8$, $I(AB) = 23.3$, $n(AB) = 24.1$ (Paper I). Disregarding the weak and noisy O III $\lambda 4960$ line, we derive a mean redshift of $z = 0.4732 \pm 0.00011$ (Table 5.2). In the 2D spectrum (Fig. 5.5) we see along the slit a tilt of the emission lines caused by the rotation of g1. The $\lambda 4960$ line is too weak, but for the three remaining lines O II $\lambda 3727$, Hβ, and O III $\lambda 5007$, we mapped out their rotation profiles. The three profiles are identical within the errors, so we combined

[1]IRAF is distributed by the National Optical Astronomy Observatories, which are operated by the Association of Universities for Research in Astronomy, Inc., under cooperative agreement with the National Science Foundation.

Table 5.2 Emission lines of g1.

Line	$\lambda_{\rm vac}$ (Å)	$z_{\rm em}$
O II λ3727	5492.21	0.4733(5)
Hβ λ4862	7163.67	0.4731(9)
O III λ4960	7308.07	0.4733(2)
O III λ5007	7377.66	0.4731(1)

the profiles and performed a joint fit (see Fig. 5.6). From linear extrapolation of the rotation profile down to the position of the QSO ($b = 0$ kpc), we find that g1 would cross the QSO spectrum at -212 ± 20 km s^{-1} corresponding to $z = 0.4722 \pm 0.0001$. Assuming instead a flattened rotation curve after the observed point closest to the QSO, we find that g1 would cross the QSO spectrum at -100 ± 10 km s^{-1} corresponding to $z = 0.4727 \pm 0.0001$. We shall return to a search for absorption at this redshift in Sect. 5.4.

The red galaxy g2 has no emission but absorption lines (see Fig. 5.7). The AB-magnitudes of g2 are $B(AB) > 26.5$, $I(AB) = 22.22$, $n(AB) > 24.8$ (Paper I). It was suggested in Paper I that g2 most likely is a normal elliptical galaxy at $z \gtrsim 0.5$. Minimum-χ^2 fitting to redshifted template elliptical galaxy spectra (Kinney et al. 1996) gave a best fit redshift of $z = 0.865 \pm 0.003$, confirming the prediction of Paper I. The observed spectrum and the best-fit template are shown in Fig. 5.7. The observed I-band magnitude of g2 corresponds roughly to an absolute B-band magnitude of $M_B = -22.1$, which is 0.7 mag brighter than M_B^* for field galaxies in the redshift interval $0.75 < z < 1.0$ (Cross et al. 2004).

5.3.2 The systemic redshift of the QSO

The quasar spectrum contains a Lyman-limit system (LLS) very close to the redshift of the quasar (Lanzetta et al. 1991). In order to establish the relation between the QSO, the LLS and the extended Lyα emission we need to determine the precise redshifts of all three. For QSOs this is not entirely straight forward. It is well known that high-ionization lines are blueshifted with respect to the QSO systemic redshift by typically several hundred km s^{-1} (e.g. Tytler & Fan 1992). For low-ionization lines the blueshifts are known to be small or zero.

We measure equivalent widths, line fluxes and vacuum-corrected wavelengths for eight both high- and low-ionization emission lines in the quasar spectrum after removing absorption lines from intervening systems. The results are presented in Table 5.3. Because the LLS redshift is very close to the QSO redshift, the quasar Lyα emission line is heavily absorbed, so the observed centre wavelength is dependent on

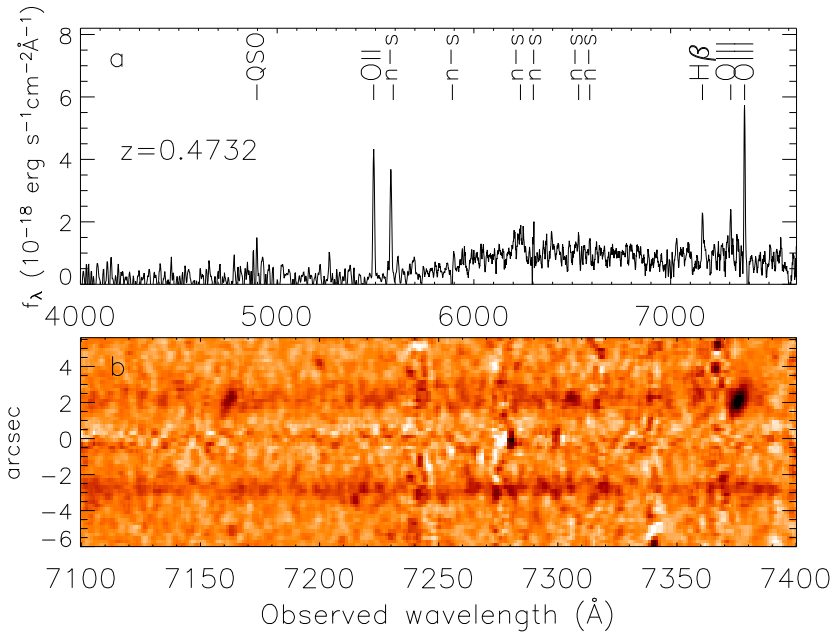

Figure 5.5 **a)** Spectrum of the blue galaxy g1 smoothed with a 7 Å wide boxcar filter. The identified lines are indicated, and strong residuals from night sky lines are marked "n–s". **b)** 2D spectrum of the QSO residuals (at 0 arcsec), the blue galaxy g1 (at 2.12 arcsec), and the red galaxy g2 (at −2.77 arcsec). The rotation profile of g1 is clearly visible in the emission lines Hβ at 7162 Å and O III at 7376 Å.

how the line is reconstructed, resulting in an uncertainty of 20 Å. We calculate the systemic redshift of the quasar using the subset of the lines listed in Table 5.3 which also appear with blueshift-adjusted rest-frame wavelengths in Tytler & Fan (1992). The five lines used are N V, Si II / O I, Si IV / O IV], C IV, and C III]. The inverse-variance weighted average of these lines provides a final $z_{\rm QSO} = 3.041 \pm 0.001$.

5.3.3 Absorption line systems

In the quasar spectrum we identify 12 C IV absorption systems between the Lyα and C IV emission lines. In Fig. 5.8 we plot this section of the QSO spectrum normalized to the continuum. The line identifications are presented in Table 5.4, and the redshifts and identified lines for the 12 systems are summarized in Table 5.5. We expect to detect 5.2 ± 1 C IV absorbers per unit redshift (Fig. 5 in Sargent et al. 1988). We find 13.9 systems per unit redshift between the Lyα ($z = 2.17$) and C IV ($z = 3.04$) lines of the QSO. Applying the same selection criteria as the S2 sample of Sargent et al., namely rest equivalent widths $W_{\rm rest} > 0.15$ Å for both lines in the C IV doublet, a rest-frame velocity relative to the QSO $v < -5000$ km s^{-1} (in this case corresponding to $z_{\rm abs} < 2.974$), and grouping

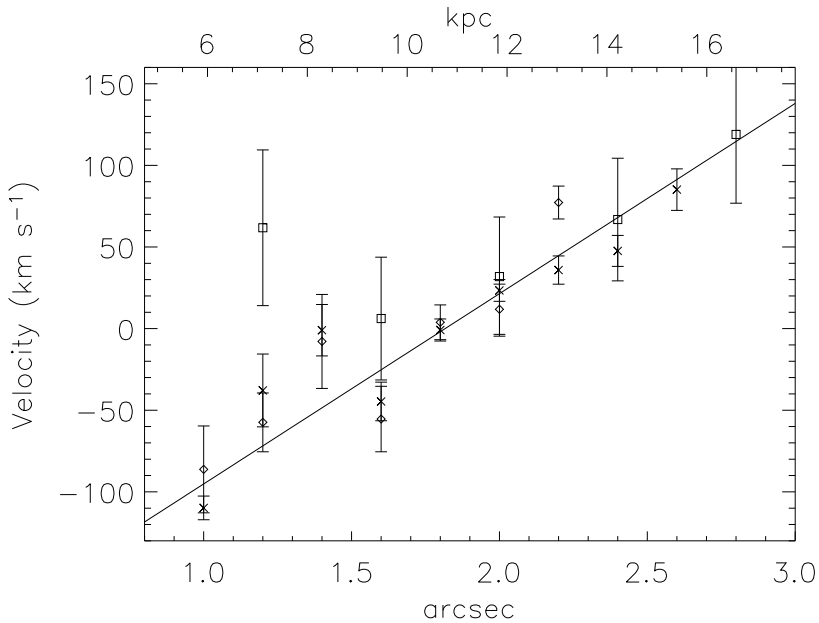

Figure 5.6 Rotation profile of galaxy g1 mapped out from the O II $\lambda 3727$ (□), Hβ $\lambda 4862$ (◇) and O III $\lambda 5007$ (×) lines. The straight line is the best combined fit to all velocity profiles. The x-axis denotes the distance from the QSO in arcsec (bottom) and kpc (top), whereas the y-axis is the velocity relative to the redshift of O III $\lambda 5007$ ($z = 0.47311$).

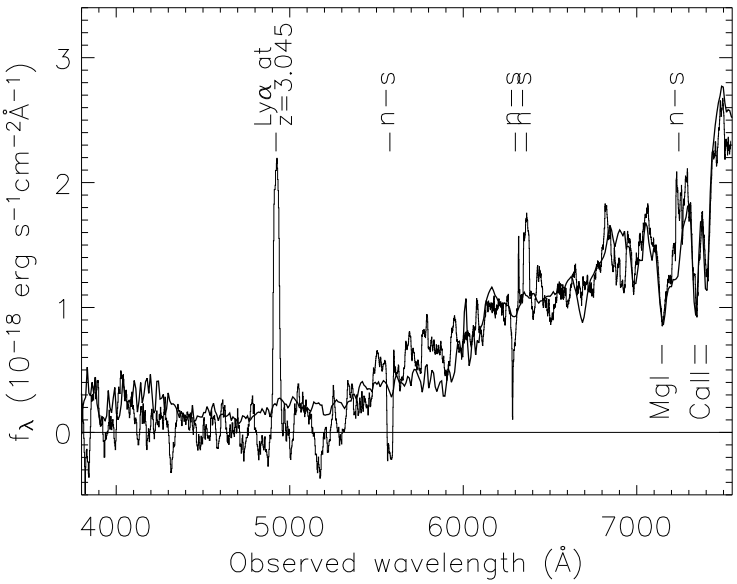

Figure 5.7 Spectrum of g2 (thin line) smoothed with a 35 Å wide boxcar filter, and template of an elliptical galaxy (thick line) at $z = 0.865$ (Kinney et al. 1996). Strong residuals from night sky lines are marked "n–s".

Table 5.3 Measured characteristics of eight QSO emission lines. The columns show the line identification, the observed wavelength in vacuum, the equivalent widths in observers frame and rest frame, the line flux, the blueshift-adjusted rest wavelengths from Tytler & Fan (1992), and the corresponding redshift. The error associated with the placement of the continuum is included in the errors on $W_{\rm obs}$, $W_{\rm rest}$ and the line flux. The Lyα line is heavily absorbed, so the redshift derived from this line (shown in square brackets) is not used in the calculation of the systemic QSO redshift.

Line	$\lambda_{\rm rest}$ [a] (Å)	$\lambda_{\rm vac}$ (Å)	$W_{\rm obs}$ (Å)	$W_{\rm rest}$ (Å)	Line flux (10^{-16} erg s^{-1} cm^{-2})	$\lambda_{\rm TF}$ (Å)	$z_{\rm TF}$
Lyα	1215.67	4918 ± 20	281 ± 15	69 ± 4	541 ± 33	1214.97 ± 0.07	$[3.048 \pm 0.016]$
N V	1240.15	5005 ± 5	96 ± 4	24 ± 1.0	183 ± 27	1239.16 ± 0.28	3.039 ± 0.004
Si II	1263.31	5101 ± 7	6 ± 2	1.5 ± 0.5	10 ± 3	—	—
Si II / O I	1305.57	5281 ± 7	15 ± 2	3.8 ± 0.6	22.7 ± 1.5	1304.24 ± 0.30	3.049 ± 0.005
C II	1335.31	5400 ± 3	9 ± 2	2.2 ± 0.5	11 ± 2	—	—
Si IV / O IV]	1399.55	5647 ± 3	62 ± 9	15 ± 2	81 ± 4	1398.62 ± 0.19	3.037 ± 0.002
C IV	1549.05	6249 ± 5	180 ± 15	44 ± 4	195 ± 11	1547.46 ± 0.04	3.038 ± 0.003
C III]	1908.73	7722 ± 7	100 ± 12	25 ± 3	94 ± 9	1906.53 ± 0.09	3.050 ± 0.004

[a] Taken from Wilkes (2000).

systems separated by less than 1000 km s^{-1}, we are left with 5.8 ± 2.4 systems per unit redshift. Using these criteria Sargent et al. find $2.2^{+0.7}_{-0.5}$ systems per unit redshift at $z = 2-3$ (Fig. 6 in Sargent et al. 1988). Our result is higher than normally observed, but still marginally consistent with the Sargent et al. study.

Table 5.4 Identified absorption lines redwards of Lyα. The columns show the line number, the observed wavelength in vacuum, the observed equivalent width, the inferred redshift and the absorption line and system identification. The error bars are 1σ errors due to read-out noise and photon statistics only. The error associated with the position of the continuum is not considered. The line numbers refer to the numbering in Fig. 5.8.

#	$\lambda_{\rm vac}$ (Å)	$W_{\rm obs}$ (Å)	$z_{\rm abs}$	Identification	
1	4945.0	1.92 ± 0.02	2.9917	N V	I
2	4963.0	3.82 ± 0.02	2.9934/3.0063	N V	I / J
3	4979.4	2.16 ± 0.02	3.0066	N V	J
4	4989.6	0.18 ± 0.02	2.8318	O I	E
5	4996.8	0.03 ± 0.02	2.8308	Si II	E
6	5067.6	0.83 ± 0.03	2.2732	C IV	A
7	5075.7	0.57 ± 0.02	2.2730	C IV	A
8	5083.5	1.02 ± 0.03	3.0332	Si II	K
9	5110.4	0.20 ± 0.02	2.8293	C II	E
10	5118.5	0.73 ± 0.03	2.6725	Si IV	D
11	5134.1	0.20 ± 0.03	2.9427	O I	G
12	5142.2	0.10 ± 0.02	2.9423	Si II	G
13	5152.5	0.50 ± 0.04	2.6731	Si IV	D
14	5187.2	0.07 ± 0.03	2.8869	C II	F
15	5195.0	0.04 ± 0.02	2.9895	O I	I
16	5201.9	0.01 ± 0.02	2.9880	Si II	I
17	5215.3	0.06 ± 0.03	3.0051	O I	J
18	5251.8	0.40 ± 0.03	3.0331	O I	K
19	5261.6	0.05 ± 0.03	2.9426 / 3.0338	C II / Si II	G / K
20	5338.7	0.23 ± 0.03	2.8305	Si IV	E
21	5347.0	1.48 ± 0.03	2.4537	C IV	B
22	5356.1	0.97 ± 0.03	2.4538	C IV	B
23	5373.3	0.13 ± 0.03	2.8305	Si IV	E
24	5382.5	0.97 ± 0.03	3.0332	C II	K
25	5414.5	0.04 ± 0.02	2.8848	Si IV	F
26	5448.5	0.07 ± 0.03	2.8841	Si IV	F
27	5495.2	0.34 ± 0.03	2.9427	Si IV	G
28	5531.5	0.29 ± 0.03	2.9433	Si IV	G
29	5563.2	0.22 ± 0.03	2.9915	Si IV	I

Continued on next page

#	$\lambda_{\rm vac}$ (Å)	$W_{\rm obs}$ (Å)	$z_{\rm abs}$	Identification	
30	5577.1	0.28 ± 0.05	2.6023	C IV	C
31	5587.2	0.13 ± 0.02	2.6028	C IV	C
32	5621.7	1.05 ± 0.03	3.0335	Si IV	K
33	5657.9	0.63 ± 0.02	3.0334	Si IV	K
34	5686.9	2.29 ± 0.02	2.6732	C IV	D
35	5696.4	1.41 ± 0.02	2.6732	C IV	D
36	5932.1	0.58 ± 0.02	2.8316	C IV	E
37	5942.5	0.43 ± 0.03	2.8320	C IV	E
38	6015.8	0.92 ± 0.02	2.8857	C IV	F
39	6025.8	0.49 ± 0.02	2.8857	C IV	F
40	6103.9	1.69 ± 0.02	2.9425	C IV	G
41	6114.8	1.12 ± 0.02	2.9430	C IV	G
42	6137.3	1.19 ± 0.02	2.9641	C IV	H
43	6146.9	1.01 ± 0.33	2.9637	C IV	H
44	6159.3	0.36 ± 0.02	3.0344	Si II	K
45	6165.9	0.10 ± 0.02	2.8334	Fe II	E
46	6180.0	1.41 ± 0.02	2.9918	C IV	I
47	6190.2	0.97 ± 0.02	2.9917	C IV	I
48	6205.3	2.52 ± 0.02	3.0081	C IV	J
49	6215.7	2.20 ± 0.02	3.0081	C IV	J
50	6245.2	1.55 ± 0.01	3.0338	C IV	K
51	6256.0	1.47 ± 0.01	3.0341	C IV	K
52	6267.3	0.29 ± 0.01	3.0481	C IV	L
53	6278.8	0.08 ± 0.01	3.0488	C IV	L

The LLS at $z \approx 3.034$, which was the original target (Paper I), is identical to the absorption system K, for which both low- and high-ionization lines are detected. This is in agreement with the findings for other $z_{\rm abs} \approx z_{\rm em}$ absorbers (Savaglio et al. 1994; Hamann 1997; Møller et al. 1998). By fitting line profiles to the Lyα and Lyβ lines we find the H I column density to be in the interval $17 \leq \log N_{\rm H\,I} \leq 19.9$. The best fit gives $\log N_{\rm H\,I} = 19.5$. In Fig. 5.9 we plot the absorption lines originating from system K in velocity space relative to the redshift obtained from the O I absorption line, $z_{\rm OI} = 3.0331 \pm 0.0002$. We notice that high-ionization lines have systematically higher redshifts than low-ionization lines. We use the redshift from the O I line as the redshift of the low-ionization region, and we take the redshift obtained from the C IV doublet, $z_{\rm CIV} = 3.0340 \pm 0.0002$, to be the redshift of the high-ionization region. We find that the region of highly ionized elements moves with a velocity of ~ 60 km s^{-1} relative to the low-ionization region. Furthermore, we notice an H I absorption system in the red wing

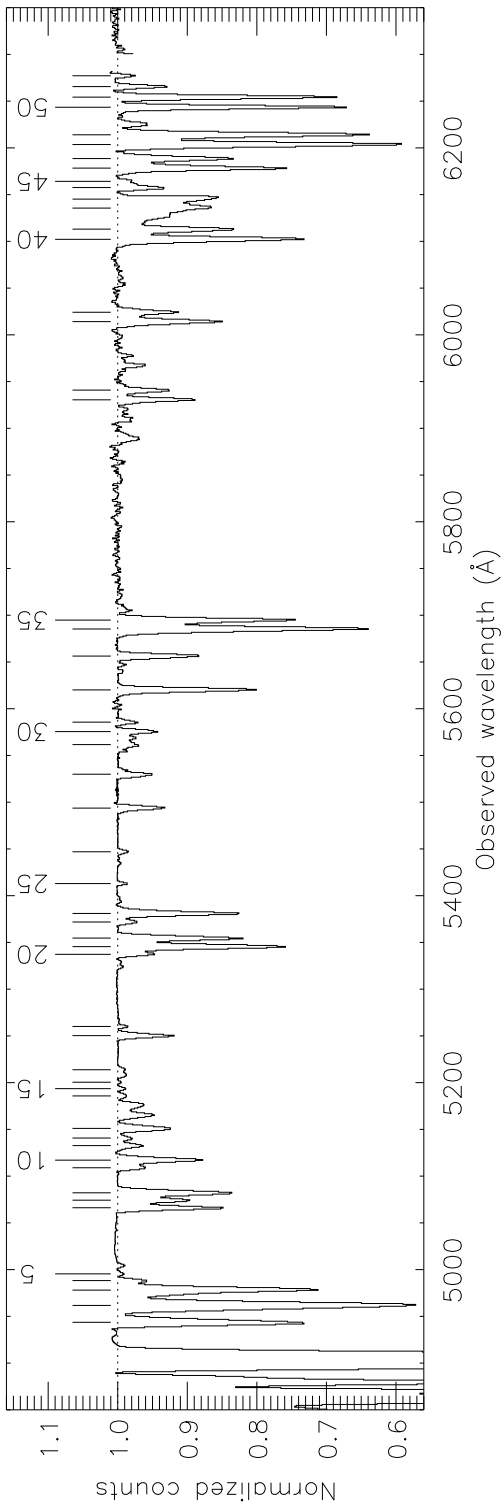

Figure 5.8 Zoom on the normalized spectrum of Q 1205-30 between the Lyα and C IV QSO emission lines. The numbering of the absorption lines correspond to the numbering in Table 5.4.

Table 5.5 Overview of the absorption systems in the spectrum of Q 1205-30.

System	Detected lines	$z_{\rm abs}$
A	C IV $\lambda\lambda$1548, 1550	2.2731 ± 0.0001
B	C IV $\lambda\lambda$1548, 1550	2.4538 ± 0.0001
C	C IV $\lambda\lambda$1548, 1550	2.6026 ± 0.0004
D	Si IV $\lambda\lambda$1393, 1402, C IV $\lambda\lambda$1548, 1550	2.6730 ± 0.0004
E	O I λ1302, Si II λ1304, C II λ1334, Si IV $\lambda\lambda$1393, 1402, C IV $\lambda\lambda$1548, 1550, Fe II λ1608	2.8309 ± 0.0009
F	C II λ1334, Si IV $\lambda\lambda$1393, 1402, C IV $\lambda\lambda$1548, 1550	2.885 ± 0.001
G	O I λ1302, Si II λ1304, C II λ1334, Si IV $\lambda\lambda$1393, 1402, C IV $\lambda\lambda$1548, 1550	2.9427 ± 0.0003
H	C IV $\lambda\lambda$1548, 1550	2.9639 ± 0.0003
I	N V $\lambda\lambda$1238, 1242, O I λ1302, Si II λ1304, Si IV λ1393[a], C IV $\lambda\lambda$1548, 1550	2.991 ± 0.002
J	O I λ1302, N V $\lambda\lambda$1238, 1242, C IV $\lambda\lambda$1548, 1550	3.007 ± 0.001
K	Si II $\lambda\lambda$1260, 1304, 1526, O I λ1302, C II λ1334, Si IV $\lambda\lambda$1393, 1402, C IV $\lambda\lambda$1548, 1550	3.0336 ± 0.0004
L	C IV $\lambda\lambda$1548, 1550	3.0485 ± 0.0005

[a] Si IV λ1403 was too weak to be detected.

of both the Lyα and Lyβ lines of the LLS (see Fig. 5.9). This system, which we will call system K1, has a redshift of 3.039 ± 0.002, and we find no associated metal-lines.

We detect high-ionization N V absorption for the systems I and J. If the high degree of ionization is caused by the high UV flux from the quasar, the systems must be located between the QSO and the LLS at $z \approx 3.034$, since no UV photons pass through the LLS. The redshifts of systems I and J are lower than that of the LLS (system K), which suggests that systems I and J are high-velocity clouds. Furthermore, the high degree of ionization suggests that they are associated with the QSO. The apparent line-locking between N V λ1242 of system I and N V λ1238 of system J strengthens this hypothesis. The line-locking effect is thought to occur in clouds driven by radiation pressure and accelerated via absorption until the wavelength of the feature falls in the shadow of

another line in a neighbouring cloud (Vilkoviskij et al. 1999; Strianand et al. 2002). The velocities of the absorption systems are -4050 km s^{-1} (system I) and -2850 km s^{-1} (system J) relative to the systemic redshift of the quasar.

5.4 Foreground galaxies

A classical way to search for galaxies at intermediate or high redshifts has been to look for absorption systems in the spectra of background QSOs (e.g. Weymann et al. 1979). Studies of the galaxy counterparts of Mg II absorption systems have concluded that the galaxies responsible for the absorption are bright galaxies which can be found at impact parameters of ~ 100 kpc (Bergeron & Boissé 1991; Guillemin & Bergeron 1997). Using a sample of damped Lyα absorbers (DLAs) Lanzetta et al. (1995) found that most galaxy counterparts of DLAs at $z \lesssim 1$ have gaseous halos extending over ~ 230 kpc. This is in contrast to studies at high redshift ($z = 2 - 3.5$), where Møller et al. (2002) have found that galaxy counterparts of DLAs reside at impact parameters ~ 10 kpc. The large impact parameters have been used to advocate a picture of galaxies surrounded by a large, homogeneous gaseous envelope which is responsible for the absorption, but doubt has arisen whether the galaxies at large projected distances are the true absorbers (Yanny & York 1992; Vreeswijk et al. 2003; Jakobsson et al. 2004).

We have looked for absorption lines in the QSO spectrum due to the foreground galaxies g1 and g2 located at impact parameters 12.6 kpc and 21.3 kpc, respectively. Considering the redshifts of g1 and g2, the only lines covered by our spectrum are Ca II H and K, Mg II $\lambda\lambda 2796$, 2804, Mg I $\lambda 2853$ for both galaxies, as well as Fe II $\lambda\lambda 2344$, 2374, 2383, 2587, 2600 for g2. Lines in the Lyman-forest are not well-constrained due to the large number of Lyα lines. We fitted and removed lines corresponding to Lyα, Lyβ and O VI absorption from the C IV systems listed in Table 5.5. In the residuals we identify two absorption lines (see Fig. 5.10) which may be due to Mg II at $z = 0.4722$. Alternatively, they could be two Lyman-forest lines. In Table 5.6 we list the 2σ upper limits on the equivalent widths of the other lines.

We find no absorption lines in the QSO spectrum outside the Lyman-forest due to the two foreground galaxies g1 and g2 down to a 2σ upper limit on the equivalent widths of ~ 90 mÅ (rest frame), but we cannot exclude that g1 is a Mg II absorber with equivalent width less than $\sim$ 1 Å, as the lines would fall in the Lyman forest. Assuming that the g1 Mg II doublet candidate is correctly identified, we cannot exclude that g1 is a DLA (see Fig. 24 in Rao & Turnshek 2000). Conversely, it is unlikely that g2 is a DLA system (Fig. 25 and 26 in Rao & Turnshek

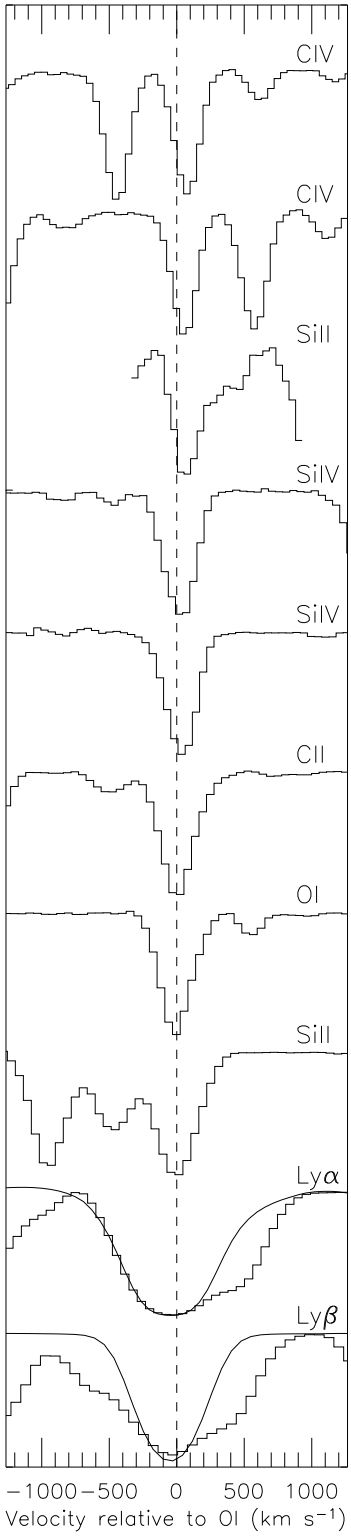

Figure 5.9 Velocities of lines originating from absorption system K (the LLS) relative to $z_{\rm OI} = 3.0331$. The model plotted for Lyα and Lyβ has an H I column density of $\log N_{\rm H\,I} = 19.5$. The Si II $\lambda1304$ transition is not included here due to the probable blend with C II $\lambda1334$ at $z = 2.9426$ (see Table 5.4).

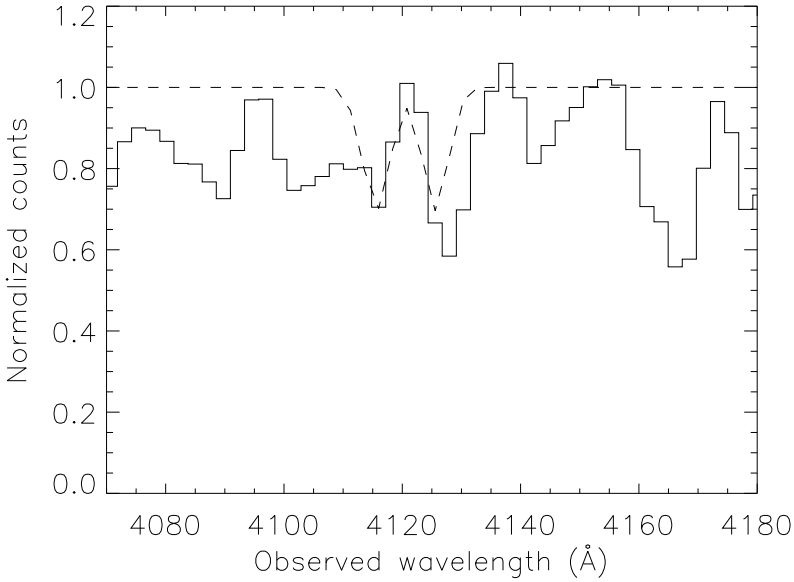

Figure 5.10 Spectrum of Q 1205-30 normalized to the continuum. In the spectrum we have subtracted lines corresponding to Lyα, Lyβ and O VI absorption from the systems listed in Table 5.5. The dashed line shows the model of a possible Mg II doublet from g1.

2000).

Old elliptical galaxies have recently been found up to a redshift $z = 1.9$ (Cimatti et al. 2004), but not much is known about the gas content in elliptical galaxies at these early times. The combination of a small impact parameter (corresponding to 21.3 kpc) and strict upper limits on absorption for the elliptical galaxy g2 indicates that it has no significant gas column density at these radii. The redshift $z = 0.865$ of g2 corresponds to a lookback time of 7.1 Gyr.

5.4.1 Gravitational lensing

The position of g2 could introduce a lensing effect on S6. Knowing the true redshift of g2, we can repeat the calculation in Paper I of the radius of its Einstein ring. For easy comparison to Paper I we assume that g2 has a singular isothermal mass distribution with a velocity dispersion $\sigma = 300$ km s^{-1}, in which case the radius of the Einstein ring is

$$\theta_E = 4\pi \left(\frac{\sigma}{c}\right)^2 \frac{d_{LS}}{d_S} = 1.4 \text{ arcsec} \tag{5.1}$$

(from the equation following Eq. 4.14 in Peacock 1999), where d_{LS} is the lens-source angular distance and d_S is the observer-source angular

Table 5.6 Absorption line search in the QSO spectrum due to g1 and g2. The quoted upper limits are 2σ limits on the equivalent widths. The error associated with the placement of the continuum is taken into account for lines not in the Lyman-forest ($\lambda_{\rm obs} > 4900$ Å).

	Ion	$\lambda_{\rm rest}$ (Å)	$\lambda_{\rm expected}$ (Å)	$W_{\rm rest}$ (Å)
g1	Mg II	2796.4	4116.8	1.2^a
	Mg II	2803.5	4127.4	1.1^a
	Mg I	2853.0	4200.1	< 0.20
	Ca II	3934.7	5792.8	< 0.095
	Ca II	3969.6	5844.0	< 0.068
g2	Fe II	2344.2	4372.0	< 0.4
	Fe II	2374.4	4428.4	< 0.4
	Fe II	2382.8	4443.9	< 0.5
	Fe II	2586.6	4824.1	< 0.5
	Fe II	2600.2	4849.3	< 0.6
	Mg II	2796.4	5215.2	< 0.097
	Mg II	2803.5	5228.6	< 0.107
	Mg I	2853.0	5320.8	< 0.059
	Ca II	3934.7	7338.4	< 0.089
	Ca II	3969.6	7403.3	< 0.073

[a] The line is in the Lyman-forest, so it may be Lyα at an intermediate redshift. The identification is therefore not secure.

distance. Gravitational lensing will introduce stretching and distortion perpendicular to the radius vector from g2, most notably at a distance of one Einstein radius. Emission appearing within one Einstein radius of the centre of g2 (roughly corresponding to the dotted circle in the lower right part of Fig. 5.1) is expected to originate from the same small region. This stretching effect would result in a flat velocity profile along PA1, which is seen in Fig. 5.4c over a distance of up to 4 arcsec from the QSO centre towards g2.

The fact that we only detect one lensed image of the quasar constrains the mass of g2 within a projected distance corresponding to the g2 – quasar angular distance (2.77 arcsec). Following the calculations of Le Brun et al. (2000), we may calculate a model independent upper limit on the projected mass $M^{\Sigma}_{\rm max}(< r_{\rm I})$ enclosed within a radius $r_{\rm I} = d_L\theta_{\rm I} = 21.3$ kpc:

$$M^{\Sigma}_{\rm max}(< r_{\rm I}) = \pi r_{\rm I}^2 \Sigma_{\rm crit} = 2.8 \times 10^{12} M_{\odot}, \tag{5.2}$$

where $\Sigma_{\rm crit} = \frac{c^2}{4\pi G}\frac{d_S}{d_L d_{LS}}$ is the critical surface density. This corresponds to an upper limit to the radius of the Einstein ring of $\theta_E < 2.77$ arcsec.

Conversely, the following lower limit to the size of the Einstein ring

allows us to constrain from below the projected mass. From Fig. 5.4c it is evident that the Einstein radius is at least 0.8 arcsec (the constant part of the velocity profile between galaxy g2 at ~ 2.8 arcsec and out to the most distant measurement at 3.6 arcsec). Thus $\theta_E > \theta_{\rm min} = 0.8$ arcsec, and

$$M(< r_{\rm I}) > M(< d_L\theta_E) > \frac{\theta_{\rm min}^2 c^2}{4G}\frac{d_S d_L}{d_{LS}} = 2.3 \times 10^{11} M_\odot. \tag{5.3}$$

Thus the projected mass of galaxy g2 is between $2.3 \times 10^{11} M_\odot$ and $2.8 \times 10^{12} M_\odot$ within a radius of 2.77 arcsec (21.3 kpc). This is consistent with the super-M_B^* finding of Sect. 5.3. In terms of velocity dispersion the range is 230 km s$^{-1} < \sigma < 420$ km s^{-1}, assuming a singular isothermal mass distribution.

5.5 A model of the extended Lyα emission

In trying to understand the extended Lyα emission, we have constructed a numerical model, where the quasar lies in the centre of a large, optically thin H I cloud. This model was already prosposed in Weidinger et al. (2004,hereafter Paper II); hereafter Paper II) together with the main conclusions. The details of our calculations were not included in that paper, but they will now be presented here.

The quasar emission is collimated in a cone with a full opening angle Ψ, and the system is seen under an inclination angle θ (see Fig. 3a of Paper II). The H I within the cone is photoionized by the quasar UV photons, causing it to emit Lyα photons when recombining. For the calculation of the extended Lyα-emission, we follow the treatment of the optically thin case given in Gould & Weinberg (1996). The ionization rate of a hydrogen atom at a distance r from the quasar is

$$\Gamma(r) = \int_{\nu_L}^{\infty} \phi(\nu)\sigma(\nu)d\nu, \tag{5.4}$$

where $\phi(\nu)$ is the photon flux density

$$\phi(\nu) = \frac{f_\nu(r)}{h\nu} \tag{5.5}$$

and the H I ionization cross section is

$$\sigma(\nu) \approx 6.3 \times 10^{-18}\ {\rm cm}^2 \left(\frac{\nu}{\nu_L}\right)^{-2.75}. \tag{5.6}$$

Here $h\nu_L = 13.6$ eV is the hydrogen ionization potential, and $f_\nu(r)$ is the frequency-specific flux at a distance r from the QSO. The production rate of Lyα photons per unit volume is

$$\dot{n}_{{\rm Ly}\alpha}(r) = \eta_{\rm thin} n_{\rm H\,I}(r)\Gamma(r), \tag{5.7}$$

where $\eta_{\rm thin} = 0.42$ is the fraction of recombinations that result in a Lyα photon. We assume a power-law hydrogen density profile, $n_{\rm H\,I}(r) = n_{\rm H\,I,1}\left(\frac{r}{1\,\rm kpc}\right)^{-\gamma}$. By integrating along the line of sight, l, we obtain the surface brightness (in erg s^{-1} cm^{-2} arcsec^{-2})

$$\Sigma_{\rm Ly\alpha} = \frac{\int E_{\rm Ly\alpha}\dot{n}_{\rm Ly\alpha}(r)dl}{4\pi D_L^2}\frac{D_A^2}{d\Omega}. \tag{5.8}$$

Here $E_{\rm Ly\alpha} = 10.4$ eV is the energy of a Lyα photon, and D_L the quasar luminosity distance. D_A is the angular distance, such that $\frac{d\Omega}{D_A^2}$ is the conversion from cm^2 to arcsec^2.

The flux emitted from the quasar close to the Lyman-limit frequency, ν_L, is given by

$$f_\nu(r) = \begin{cases} f_{\nu_L,\,\rm obs}\left(\frac{D_L}{r}\right)^2\left(\frac{\nu}{\nu_L}\right)^{-\alpha} & \text{inside the cone,} \\ 0 & \text{outside the cone.} \end{cases} \tag{5.9}$$

We obtain the observed Lyman-limit flux, $f_{\nu_L,\,\rm obs}$, using the slope of the quasar spectrum and an observed flux, $f_{\nu_0,\,\rm obs}$, on the continuum at ν_0, that is

$$f_{\nu_L,\,\rm obs} = f_{\nu_0,\,\rm obs}\left(\frac{\nu_L}{\nu_0}\right)^{-\alpha}. \tag{5.10}$$

The free parameters of the model are the observed flux at ν_0, $f_{\nu_0,\,\rm obs}$, the spectral slope, α, the redshift, z, the angles Ψ and θ, the neutral hydrogen density at a distance of 1 kpc, $n_{\rm H\,I,1}$, and the density slope, γ.

5.5.1 Model parameters

Several free parameters are determined directly via observations. We measure the observed continuum flux at a given point in the spectrum. For the spectral index α we use the value found in the flux calibration in Sect. 5.2.3. The obtained values for these parameters are listed in Table 5.7. In Paper II a method to obtain a relation between the opening angle and the inclination angle is described. The free parameters in our model are now reduced to the opening angle, Ψ, the hydrogen density scale, $n_{\rm H\,I,1}$, and the density slope, γ.

The numerical implementation of the model was carried out by incorporating the cone into a cubic grid inclined at an angle θ. The Lyα production rate was calculated in each grid point within the cone, and the process of integrating along the line of sight was simply to sum along the grid z-axis.

Table 5.7 Input parameters of the model.

Description	Symbol	Value
Observed flux	$f_{\lambda_0,\,\mathrm{obs}}$	1.3×10^{-16} erg s^{-1} cm^{-2} Å^{-1}
Reference wavelength	λ_0	5946 Å
Spectral slope	α	0.65
Redshift	z	3.041

Table 5.8 Best-fit values for θ, $n_{\mathrm{H\,I},1}$, γ, and M_{200} for various opening angles.

Ψ	θ	$n_{\mathrm{H\,I},1}$ (10^{-8} cm^{-3})	γ	M_{200} ($10^{12} M_\odot$)
90°	22.5°	9.8	0.018	**2.6**
110°	27.2°	9.3	0.072	**3.5**
130°	31.8°	8.2	0.093	**5.3**
150°	36.5°	6.4	0.064	**6.5**
170°	41.1°	5.5	0.054	**6.5**

5.5.2 Results of the model

Using the parameters listed in Table 5.7, and assuming a given opening angle and corresponding best-fit inclination angle, we now fit the model to the observed surface brightness profile, leaving the hydrogen density scale, $n_{\mathrm{H\,I},1}$, and slope, γ, as free parameters. The best-fit values for each opening angle are listed in Table 5.8, and the corresponding surface brightness profiles are plotted in Fig. 5.11.

The numerical model described in Paper II and above is purely geometrical. Assuming in addition that the gas is in free fall into a dark matter (DM) halo introduces a velocity field in the gas. In Paper II this was used to fit the virial mass, M_{200}, to the observed velocity profile. The obtained virial masses are also listed in Table 5.8. The conclusions are presented in Paper II.

5.6 Discussion

Returning to the main topic of the origin of the extended Lyα emission, there are several elements of this puzzle that now can to be pieced together. There is a LLS at $z = 3.0336 \pm 0.0004$ (absorber K, see Table 5.5), an additional absorber at $z = 3.039 \pm 0.002$ (K1, see Sect. 5.3.3), the systemic redshift of the quasar is $z = 3.041 \pm 0.001$ (Sect. 5.3.2), the absorber L at $z = 3.0485 \pm 0.0005$ (Table 5.5) and finally the extended Lyα emission S6 at $z \approx 3.049$ (see caption of Fig. 5.4c-d). We assume that the high-ionization, line locked systems I and J are intrinsic to the central engine and will not consider them here.

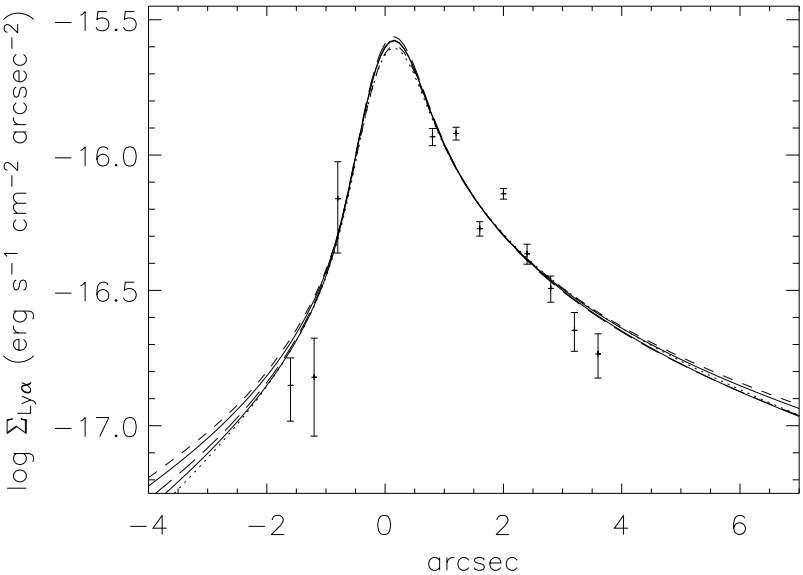

Figure 5.11 Best-fit surface brightness profiles as seen through a 1.2 arcsec wide slit with a seeing of 0.7 arcsec for opening angles of $90°$ (dotted), $110°$ (solid), $130°$ (long dashes), $150°$ (solid), and $170°$ (short dashes). The model parameters are listed in Table 5.8. Overplotted is the measured surface brightness profile of S6 shown in Fig. 5.4b. Note that three marginal measurements at negative offsets are included.

5.6.1 The origin of the extended Lyα emission

The separation of the low- and high-ionization lines in the LLS suggests that it is heated by the quasar UV photons and expanding. However, the large velocity offset between the LLS and the extended Lyα emission (~ 1000 km s^{-1}) makes it very unlikely that the two are physically associated as previously thought (Paper I). Since the LLS absorbs all UV photons, the extended emission must be located between the LLS and the QSO, which makes an association between the extended Lyα emission and the QSO the most likely one. It was suggested by Haiman & Rees (2001) that neutral gas falling into the dark matter halo around a quasar could be photoionized by the quasar UV flux, causing the gas to emit Lyα photons.

Interpreting the observations in the Haiman & Rees (2001) picture as described in the numerical model (Sect. 5.5; Paper II), we identify K1 as absorption due to a large hydrogen cloud around the quasar, in which case the redshift of K1 should be close to that of the quasar. A part of this large cloud is pulled into the DM halo of the QSO where it is photoionized and gives rise to the Lyα emission of S6. S6 therefore lies between us and the quasar, and the higher redshift is due to

infall. The velocity of S6 is ~ 500 km s^{-1} relative to the quasar and the surrounding cloud (K1). The absorption system L is located somewhere between the emitting and the absorbing part of the hydrogen cloud. There are at least two possibilities for placing the LLS. *i)* It is very close to the quasar and moving at high velocity (~ -500 km s^{-1}). In this case the LLS has to be very small in order for the majority of the UV photons to pass by and photoionize the surrounding hydrogen cloud. *ii)* The LLS is sufficiently distant for the Lyα photons produced in the cloud surrounding the quasar to be redshifted out of the resonance wavelength and pass through the LLS unhindered. Because the low- and high-ionization lines in the LLS are only mildly separated in velocity space (~ 60 km s^{-1}) we favour the latter possibility.

Table 5.9 Redshifts, fluxes and luminosities of the Lyα emission from the host galaxies of radio-quiet quasars.

Quasar	z	Lyα flux (10^{-17} erg s^{-1} cm^{-2})	Lyα luminosity (10^{42} erg s^{-1})	Reference
Q 0054-284	3.616	6	7.3	Bremer et al. (1992)
Q 0055-26	3.656	8	10	Bremer et al. (1992)
Q 1548+0917	2.746	47	29	Steidel et al. (1991)
Q 1205-30	3.041	70	56	This work
Q 1202-0725	4.69	26	58	Hu et al. (1996), Petitjean et al. (1996)

The extended Lyα emission could possibly be explained by other scenarios rather than the projected ionization cone. However, the combination of imaging and spectroscopic data enables us to rule out most of these other scenarios (Paper II). *i)* Jets are believed to be present in radio-quiet quasars. They are predicted to extend out to only ~ 0.1 kpc (Blundell et al. 2003), more than two orders of magnitude less than the ~ 30 kpc extent of the emission around Q 1205-30. *ii)* Outflowing galactic winds are generally thought to be triggered by the cumulative effect of many supernovae exploding inside the galaxy, which would metal-enrich the outflowing gas. Around radio-loud quasars this is typically seen as extended C IV emission with strength $7 - 10\%$ of that of the extended Lyα line (Heckman et al. 1991a). Our detection limit at the position of redshifted C IV is 4×10^{-18} erg s^{-1} cm^{-2} arcsec^{-2} (3σ), which would have enabled us to detect the typical C IV line seen around some radio-loud quasars (a strength of 10% of the Lyα line corresponds to 7×10^{-18} erg s^{-1} cm^{-2} arcsec^{-2}). The fact that we do not detect this line makes it unlikely that it is a supernova powered outflow. The most plausible explanation that remains is cosmological infall of hydrogen.

5.6.2 Extending the sample

To date only a handful of detections of extended Lyα emission around RQQs has been reported (Steidel et al. 1991; Bremer et al. 1992; Hu et al. 1996; Petitjean et al. 1996; Bunker et al. 2003). Hu et al. (1991) find no extended Lyα emission in their sample of seven radio-quiet quasars down to a limiting flux of 2×10^{-16} erg s^{-1} cm^{-2}. We have compiled a list of fluxes and luminosities for the detections of extended Lyα emission (see Table 5.9). We measure an average Lyα surface brightness of $\sim 7 \times 10^{-17}$ erg s^{-1} cm^{-2} arcsec^{-2} around Q 1205-30. Assuming a spatial extent of 10 arcsec^2, we infer a Lyα flux of $\sim 7 \times 10^{-16}$ erg s^{-1} cm^{-2}. The luminosity in the Lyα line of S6 is at the high end of the ones listed in Table 5.9.

It is important for the study of the link between galaxy and quasar formation to understand how frequent and under which circumstances extended Lyα emission arises around RQQs. The most efficient method to detect Lyα emission around QSOs is narrow band imaging. The study of extended Lyα emission can successfully be combined with narrow band searches for Lyα emitting (proto)-galaxies around QSOs (e.g. Fynbo et al. 2001, 2003b). The follow-up multi-object spectroscopy needed to confirm candidate Lyα emitters may conveniently be utilized to study any extended Lyα emission associated with the QSO. Alternatively, integral field spectroscopy is a promising method for very detailed studies of extended emission at high redshifts (Bower et al. 2004). The method makes it possible to map out the entire velocity field of the extended emission, strongly constraining any model.

It is imperative for any search for extended Lyα emission around RQQs to go to very deep detection limits. Haiman & Rees (2001) predict that halos of infalling gas around quasars should be seen in Lyα emission with a typical surface brightness around $10^{-18} - 10^{-17}$ erg s^{-1} cm^{-2} arcsec^{-2} and typical angular sizes between $2 - 3$ arcsec, i.e. with typical fluxes around $3 \times 10^{-18} - 7 \times 10^{-17}$ erg s^{-1} cm^{-2}. This limit has only been reached for very few surveys.

A larger sample of QSOs with extended Lyα emission will make it possible to address primary issues like morphology, environment, luminosity function etc. The corresponding DM halo masses obtained in a similar fashion as in Paper II may be compared to black hole masses obtained via the correlation between $M_{\rm BH}$ and quasar emission line widths (Vestergaard 2002; McLure & Jarvis 2002). A $M_{\rm DM} - M_{\rm BH}$ correlation could provide a powerful consistency check of N-body hydrodynamical simulations.

We are currently looking for extended Lyα emission in a small sample of quasars using an analysis similar to what has been employed in this paper.

Acknowledgements

MW acknowledges support from ESO's Director General's Discretionary Fund. We wish to thank Pall Jakobsson for helpful discussions of gravitational lensing, and Henning Jørgensen for useful comments on our manuscript. It is a great pleasure to thank the referee Cedric Ledoux for his large effort and very helpful comments. Based on observations made with ESO Telescopes at the Paranal Observatory under programme ID 64.O-0187

Chapter VI

Lyα blobs around high-redshift quasars

Weidinger, M., Møller, P., Thomsen, B., & Fynbo, J. P. U. (2005). *A&A*, in preparation

6.1 Introduction

ALTHOUGH extensively studied, quasars remain in many ways mysterious objects. Many of the most fundamental physical aspects, such as how gas is accreted onto the central supermassive black hole, and why some quasars show a high level of radio activity and others little or none, are yet to be understood.

Historically, quasars have been divided into radio-loud and radio-quiet subclasses, but recently there has been some controversy about a claimed bimodality in the quasar radio-loudness distribution (e.g. Cirasuolo et al. 2003a; Ivezić et al. 2004). In any case it is clear that a number of quasars fall between the typical definitions of radio-loud quasars (RLQs) and radio-quiet quasars (RQQs; Falcke et al. 1996).

In order to better understand the differences between RLQs and RQQs, and determine how well the unification scheme of active galactic nuclei (AGN) applies to the unification of quasars, it is imperative to perform comparative studies of as many different aspects of quasars as possible. Environments (within a few Mpc) of RLQs have been targeted by a number of studies, all concluding that RLQs are found in overdense environments (Wold et al. 2000; McLure & Dunlop 2001; Barr et al. 2003; Zheng et al. 2005). For RQQs the situation is less clear, but recent studies have found environments of RQQs similar to those of RLQs (Wold et al. 2001; McLure & Dunlop 2001; Russel et al. 2005).

Closer to the quasar itself, studies of emission lines arising in the broad-line region of the central engine agree that black holes (BHs) in RLQs are $\sim 40\%$ more massive than BHs in RQQs (e.g. McLure & Dun-

lop 2001; McLure & Jarvis 2002; Metcalf & Magliocchetti 2005). A correlation between BH mass and radio-luminosity has been suggested (Nelson 2000; Laor 2000; Lacy et al. 2001; McLure & Jarvis 2004; McLure & Dunlop 2004), but consensus has yet to be reached (Snellen et al. 2003; Oshlack et al. 2002; Woo & Urry 2002a,b; Ho 2002; Urry 2003; Metcalf & Magliocchetti 2005). However, there appears to be a threshold in BH mass which governs the onset of radio-loudness (Laor 2000; Magliocchetti et al. 2004; Metcalf & Magliocchetti 2005).

Studies of quasar host galaxies have concluded that both RLQs and bright RQQs are almost exclusively found in massive ellipticals (Dunlop et al. 1993; McLure et al. 1999; Schade et al. 2000). At higher redshift ($1 < z < 2$) RLQ host galaxies are on average $1 - 2$ magnitudes brighter than hosts of RQQs (Dunlop et al. 2003; Falomo et al. 2001; Kukula et al. 2001). Going to still higher redshifts makes it increasingly difficult to study host galaxies due to the combination of cosmological surface brightness dimming and the proximity of a bright quasar. Some 20 detections of RLQ hosts have been reported (Heckman et al. 1991b,a; Steidel et al. 1991; Lehnert et al. 1992, 1999; Wilman et al. 2000), but only few studies have targeted RQQs, and with limited success (Bremer et al. 1992; Lowenthal et al. 1995; Fynbo et al. 2000a; Møller et al. 2000; Ridgway et al. 2001; Bunker et al. 2003).

In this paper we will reduce the difference in numbers of studied RLQs and RQQs somewhat. We examine a sample of 14 quasars, 3 radio-loud and 11 radio-quiet, searching for extended Lyα emission around the quasars.

This paper is organized in the following way. We introduce the observations and the data reductions in Sect. 6.2, and present our results in Sect. 6.3. In Sect. 6.4 we analyze the radio properties of the quasars in our sample, and in Sect. 6.5 we discuss the implications of our results. Finally, we conclude and summarize in Sect. 6.6. In Appendix 6.7 we present the extracted one-dimensional (1D) quasar spectra and quasar subtracted two-dimensional (2D) spectra, and in Appendix 6.8 we comment on the individual objects.

Throughout, we will use a cosmological model in which $\Omega_{\rm m} = 0.3$, $\Omega_\Lambda = 0.7$, and $H_0 = 100h$ km s^{-1} Mpc^{-1} = 70 km s^{-1} Mpc^{-1}. In this model a redshift $z = 2$ ($z = 4$) corresponds to a luminosity distance of $D_{\rm L} = 15.5$ Gpc ($D_{\rm L} = 35.9$ Gpc) and a distance modulus of 46.0 (47.8). One arcsec on the sky corresponds to a projected distance of 8.37 proper kpc (6.95 proper kpc), and the lookback time is 10.2 Gyr (12.0 Gyr), 76% (89%) of the time since Big Bang.

6.2 Observations and data reduction

The basic data set of 10 quasars was originally taken for a large project searching for spectroscopic confirmation of galaxy counterparts of damped Lyα absorbers (DLAs; Møller & Warren 1998; Warren et al. 2001; Møller et al. 2002, 2004). This basic data set was augmented with archival data of 4 additional quasars. The archival data were selected by searching the ESO science archive facility for FORS1 and FORS2 quasar spectra covering the Lyα emission line with total exposure times longer than 3000 seconds. We shall refer to this combined sample as the FORS sample.

The observations were carried out with the Unit Telescopes 1 (Antu) and 4 (Yepun) of the ESO Very Large Telescope (VLT) during several runs between August 1999 and March 2004. The data were acquired with the FORS1 and FORS2 instruments in Longslit Spectroscopy mode (LSS) and Multi Object Spectroscopy mode (MOS). For all observations the standard resolution collimator was used. A detailed log of the observations is presented in Table 6.1. The quoted seeing is the full width at half maximum (FWHM) of a point source measured around 5500 Å (from $5450 - 5550$ Å).

6.2.1 Basic reductions

The raw science frames were bias subtracted and flat field corrected using standard techniques. Cosmic ray hits were rejected in the individual science frame by sigma-clipping along the spatial axis. Any pixel deviating more than 7σ was replaced with a median value. At this stage no cosmic rejection was performed close to the quasar because of the difficulty in identifying a cosmic ray hit on top of a spectral point-spread function (SPSF).

The cosmic-rejected science frames were coadded, and a 1D sky spectrum was determined by taking spatial averages on either side of the quasar spectrum. Regions used for calculating the sky spectrum were never closer than 4 arcsec to the quasar in order to avoid being affected by any extended emission. The mean sky spectrum was expanded to a 2D spectrum by duplicating the 1D sky spectrum, and it was subtracted from the combined science frame.

6.2.2 Spectral extractions

The quasar spectrum in the coadded science frame was optimally extracted using the code described in Møller (2000). The output from code is the 1D and 2D optimally extracted quasar spectrum as well as the 2D residual spectrum. In the first iteration of the spectral extraction we

Table 6.1 Observing log.

Object	Instrument/ Telescope	Obs-mode[a]	Position angle No.	(E of N)	Grism	Slit width (arcsec)	Exp-time (hours)	Pixel size	Seeing[a] (arcsec)	Resolution (Å)	Observing dates
Q 0049-2820	FORS1 / UT1	LSS	PA1	86.0°	G600B	1.3	2.78	2.35 Å×0.″40	1.00	5.9	Aug 11-12 1999
Q 0056+0125	FORS1 / UT1	LSS	PA1	64.9°	G600B	1.0	1.11	1.19 Å×0.″20	0.64	3.8	Oct 25 2000
	FORS1 / UT1	LSS	PA2	44.4°	G600B	1.0	1.11	1.19 Å×0.″20	0.53	3.1	Oct 25 2000
	FORS1 / UT1	LSS	PA3	−10.0°	G600B	1.0	2.22	1.19 Å×0.″20	0.66	3.9	Oct 25, 27 2000
	FORS1 / UT1	LSS	PA4	116°	G600B	1.0	2.22	1.19 Å×0.″20	0.82	4.9	Oct 26-27 2000
Q 0135-273	FORS2 / UT4	LSS	PA1	0.0°	G600B	1.0	0.83	1.49 Å×0.″25	1.25	5.9	Jan 10 2003
Q 0201+113	FORS1 / UT1	LSS	PA1	−150°	G600B	1.0	1.67	1.19 Å×0.″20	0.64	3.8	Oct 26-27 2000
	FORS1 / UT1	LSS	PA2	108°	G600B	1.0	2.64	1.19 Å×0.″20	0.69	4.1	Oct 25-27 2000
Q 0216+0803	FORS1 / UT1	LSS	PA1	55.0°	G600B	0.7	1.36	1.18 Å×0.″20	0.55	3.2	Aug 13 1999
Q 0458-0203	FORS1 / UT1	LSS	PA1	55.0°	G600B	1.3	2.06	2.35 Å×0.″40	0.92	5.4	Oct 25-26 2000
Q 0528-2505	FORS1 / UT1	LSS	PA1	−151°	G600B	1.0	1.50	1.19 Å×0.″20	0.70	4.2	Oct 27 2000
Q 0841+129	FORS1 / UT1	LSS	PA1	−80.6°	G600B	1.3	2.22	1.18 Å×0.″20	0.97	5.7	Mar 5-6 2000
Q 1202-0725	FORS2 / UT4	MOS	PA1	16.0°	G600RI	1.4	1.67	1.63 Å×0.″25	0.94	6.1	Mar 22-23 2004
Q 1209+0919	FORS2 / UT4	LSS	PA1	0.0°	G600B	1.0	0.83	1.49 Å×0.″25	0.78	4.6	Jan 2 2003
Q 2116-358	FORS1 / UT1	LSS	PA1	−176°	G600B	1.3	2.22	2.35 Å×0.″40	0.77	4.5	Aug 12-13 1999
	FORS1 / UT1	LSS	PA2	−36.0°	G600B	1.3	2.50	1.19 Å×0.″20	0.97	5.8	Aug 11 1999
Q 2138-4427	FORS1 / UT1	LSS	PA1	−46.5°	G600B	1.0	4.67	1.20 Å×0.″20	0.72	4.3	Sept 17-18 2003
Q 2206-1958	FORS1 / UT1	LSS	PA1	26.0°	G600B	1.3	2.22	2.34 Å×0.″40	1.02	6.0	Aug 11 1999
	FORS1 / UT1	LSS	PA2	−12.0°	G600B	1.3	2.22	2.34 Å×0.″40	1.11	6.5	Aug 11-12 1999
	FORS1 / UT1	LSS	PA3	−124°	G600B	0.7	2.22	1.18 Å×0.″20	0.55	3.2	Aug 13 1999
Q 2212-1626	FORS1 / UT1	LSS	PA1	105°	G600R	1.0	2.08	1.06 Å×0.″20	0.94	5.0	Aug 12 1999
	FORS1 / UT1	LSS	PA2	76.1°	G600R	0.7	0.83	1.06 Å×0.″20	0.55	2.9	Aug 13 1999

[a] Long-slit spectroscopy (LSS) or multi-object spectroscopy (MOS).
[b] Average seeing (FWHM) measured around 5500 Å in the combined frames.

ignored any apparent extended emission and performed the extraction as we would on a single point source. Should any extended emission be present it would distort the obtained SPSF and provide a non-optimal extraction. However, this procedure assigns as much flux as possible to the quasar, yielding a conservative estimate of the extended flux.

This "first-fit" 2D residual spectrum was used to detect any faint excess emission using the following initial statistical analysis. Two small regions on either side of the QSO spectrum extending from 0 to 3 arcsec from the quasar and 2000 km s^{-1} (rest-frame) wide was used when calculating the signal-to-noise ratio, S/N. Since the extended emission may be significantly Doppler shifted in the quasar rest-frame, we searched for the largest S/N in the two regions along the spectral direction from $-10,000$ km s^{-1} to $+10,000$ km s^{-1} relative to the quasar systemic redshift in steps of 500 km s^{-1}. In the two regions we disregarded the spatial bins close to the centroid that were heavily affected by large shot noise. In case of a maximum signal-to-noise ratio $S/N > 3$ in either region we mark the spectrum for closer inspection.

Spectra thus marked were re-extracted with a $10,000$ km s^{-1} wide wavelength interval around the quasar Lyα line excluded from the construction of the SPSF, so it would not be affected by the extended emission. Generally, it is not possible to separate an extended profile from a point source without additional assumptions. In the excluded interval we used one of two standard assumptions. *i)* The extended profile is assumed to be exponentially decreasing. *ii)* The extended profile is assumed to follow a de Vaucouleurs law. In both cases, the model profile is the sum of extended profile and point source, which is then convolved with the SPSF.

In some cases the obtained SPSF and the actual observed profile could be slightly different, resulting in a best-fit model with an extremely narrow (before convolution) extended profile and only a very small point source contribution. In this way the extended profile mimics the effect of a point source while compensating for slight difference in SPSF and observed profile. To prevent this, we introduced a lower bound on the FWHM of the extended profile before convolution. The lower bound was never greater than half the seeing FWHM, to ensure that it would not artificially push the fit to a larger effective radius.

Ideally, the best-fitting model of quasar and extended emission should be determined by χ^2-fitting all wavelength bins simultaneously. This, however, is a very computationally demanding task. Instead we performed the fit to each wavelength bin individually. We subtracted the point source contribution of the best-fit model from the science spectrum, resulting in a best-fit residual spectrum. The best-fit residual spectrum was used to measure total Lyα flux and spectral width as well as surface brightness and velocity relative to the quasar systemic red-

shift as a function of impact parameter. All spectra initially marked for a closer inspection turned out to indeed contain extended Lyα emission. This is as expected, because the initial spectral extraction gives a conservative estimate on any extended flux.

6.2.3 Wavelength and flux calibrations

The spectra were wavelength calibrated with the *dispcor* task in IRAF[1]. A fourth order Chebyshev polynomial was fitted to a number reference lines in an arc-spectrum. For G600B spectra the RMS (root-mean-square) of the fit was around 0.08 Å for 10-14 lines, for G600R spectra it was around 0.07 Å for 27-31 lines, and for the G600RI spectrum it was 0.1 Å for 44 lines.

In order to establish a rough flux calibration we proceeded in the following way. We obtained an estimate of the total system transmission as a function of wavelength using the ESO exposure time calculator. Dividing the observed spectra by the transmission function gives us the spectra on a relative flux scale. The absolute flux scale was reached by normalizing the spectra to agree with photometric measurements in the literature. This procedure takes into account atmospheric absorption and absolute slit losses, but not differential slit losses. We estimate the absolute flux calibration to be correct within 30%, while the relative is better. This holds true for point sources, but for extended sources there are additional slit losses.

6.3 Results

6.3.1 Quasar systemic redshifts

When searching for extended Lyα emission associated with the central quasar we need to determine the systemic redshift of the quasar to the highest possible precision. This is not a straightforward task, since high-ionization lines are blueshifted relative to the quasar systemic redshift by up to more than 450 km s^{-1} (Tytler & Fan 1992). For low-ionization lines the blueshifts are known to be small or zero. The blueshift-adjusted rest-frame wavelengths from Tytler & Fan (1992) are given in Table 6.2 for easy reference.

[1]IRAF is distributed by the National Optical Astronomy Observatories, which are operated by the Association of Universities for Research in Astronomy, Inc., under cooperative agreement with the National Science Foundation.

Table 6.2 Blueshift-adjusted rest wavelengths from Tytler & Fan (1992).

Line	$\lambda_{\rm TF}$ (Å)
Lyα	1214.97 ± 0.07
N V	1239.16 ± 0.28
Si II	—
Si II/O I	1304.24 ± 0.30
C II	—
Si IV/O IV]	1398.62 ± 0.19
C IV	1547.46 ± 0.04

Table 6.3 Measured properties of quasar emission lines. The shown columns are the quasar, the line identification, the vacuum-corrected observed wavelength, the rest-frame equivalent width, the line flux, and the blueshift-adjusted redshift (see Table 6.2). The errors on $W_{\rm rest}$ and the line flux include errors arising from the placement of the continuum.

Quasar Line	$\lambda_{\rm vac}$ (Å)	$W_{\rm rest}$ (Å)	Line flux (10^{-15} erg s^{-1} cm^{-2})	$z_{\rm TF}$
Q 0049-2820				
Lyα	3972 ± 8	77 ± 11	59 ± 9	2.269 ± 0.007
N V	4047 ± 6	21 ± 3	15 ± 5	2.266 ± 0.005
Si II	4137 ± 5	2.6 ± 0.8	1.3 ± 0.4	—
Si II/O I	4274 ± 6	2.1 ± 0.4	1.3 ± 0.3	2.277 ± 0.005
C II	4374 ± 4	1.3 ± 0.3	0.8 ± 0.2	—
Si IVO IV]	4566 ± 5	8.9 ± 1.7	6.0 ± 1.1	2.265 ± 0.004
C IV	5042 ± 5	31 ± 5	20 ± 3	2.258 ± 0.003
Q 0056+0125				
Lyα	5060 ± 3	84 ± 6	33 ± 2	3.165 ± 0.003
N V	5160 ± 3	34 ± 3	12.2 ± 1.0	3.164 ± 0.002
Si II	5256 ± 4	9.7 ± 1.5	3.7 ± 0.5	—
Si II/O I	5437 ± 2	4.9 ± 0.4	1.65 ± 0.17	3.1688 ± 0.0015
C II	5555 ± 3	3.5 ± 0.4	1.17 ± 0.13	—
Si IV/O IV]^a	5826 ± 4	—	—	3.166 ± 0.003
Q 0135-273				
Lyα	5122 ± 5	106 ± 12	153 ± 11	3.215 ± 0.004
N V	5219 ± 10	14 ± 4	31 ± 11	3.211 ± 0.008
Si II	5314 ± 20	0.5 ± 0.3	0.7 ± 0.4	—
Si II/O I	5498 ± 4	2.8 ± 0.5	4.7 ± 0.6	3.215 ± 0.003
C II	5625 ± 8	0.5 ± 0.2	0.9 ± 0.2	—
Si IV/O IV]	5892 ± 6	9.8 ± 1.7	16.8 ± 1.2	3.213 ± 0.004
Q 0201+113				

Continued on next page

Quasar Line	$\lambda_{\rm vac}$ (Å)	$W_{\rm rest}$ (Å)	Line flux (10^{-15} erg s^{-1} cm^{-2})	$z_{\rm TF}$
Lyα	5642 ± 11	27.0 ± 1.7	7.2 ± 0.6	3.644 ± 0.009
N V	5721 ± 18	13.5 ± 0.9	4.4 ± 0.4	3.617 ± 0.014
Si II	5853 ± 14	2.3 ± 0.4	0.65 ± 0.13	—
Q 0216+0803				
Lyα	4853 ± 3	95 ± 5	73 ± 5	2.995 ± 0.002
N V	4946 ± 6	20 ± 3	17 ± 3	2.991 ± 0.005
Si II	5028 ± 8	4.2 ± 1.3	2.3 ± 0.6	—
Si II/O I	5208 ± 4	4.9 ± 0.3	2.8 ± 0.3	2.993 ± 0.003
C II	5332 ± 5	1.17 ± 0.13	0.63 ± 0.10	—
Si IV/O IV]	5590 ± 8	4.8 ± 0.7	3.3 ± 0.6	2.997 ± 0.006
Q 0458-0203[b]				
Lyα	3992 ± 10	61 ± 50	16.9 ± 1.3	2.286 ± 0.008
N V	4067 ± 10	27 ± 6	12 ± 3	2.282 ± 0.008
Si II	4157 ± 15	1.3 ± 0.6	0.21 ± 0.11	—
Si II/O I	4289 ± 15	1.6 ± 0.4	0.44 ± 0.13	2.289 ± 0.012
Si IV/O IV]	4605 ± 20	9.6 ± 1.7	3.2 ± 0.5	2.292 ± 0.014
C IV	5087 ± 10	44 ± 7	19 ± 2	2.287 ± 0.006
Q 0528-2505				
Si II	4790 ± 15	1.33 ± 0.19	1.6 ± 0.3	—
Si II/O I	4954 ± 20	1.3 ± 0.3	1.7 ± 0.4	2.798 ± 0.015
C II	5064 ± 15	0.91 ± 0.14	1.5 ± 0.2	—
Si IV/O IV]	5281 ± 10	4.5 ± 0.3	4.7 ± 0.4	2.776 ± 0.007
C IV	5847 ± 15	9.2 ± 0.7	9.9 ± 0.7	2.778 ± 0.010
Q 1202-0725				
Lyα	6928 ± 15	41 ± 4	158 ± 17	4.702 ± 0.012
N V	7119 ± 35	12 ± 4	51 ± 15	4.74 ± 0.03
Si II	7200 ± 50	0.23 ± 0.18	0.6 ± 0.5	—
Si II/O I	7382 ± 30	5.3 ± 1.1	22 ± 4	4.66 ± 0.02
C II	7576 ± 35	3.0 ± 1.1	8 ± 3	—
Si IV/O IV]	7870 ± 30	17 ± 3	69 ± 13	4.63 ± 0.02
Q 1209+0919				
Lyα	5222 ± 8	57 ± 5	27 ± 2	3.298 ± 0.007
N V	5318 ± 8	6.7 ± 1.9	3.9 ± 1.1	3.292 ± 0.007
Si II	5401 ± 12	2.9 ± 0.8	1.3 ± 0.4	—
Si II/O I	5600 ± 8	1.9 ± 0.7	0.8 ± 0.2	3.293 ± 0.006
C II	5724 ± 8	1.0 ± 0.4	0.68 ± 0.15	—
Si IV/O IV]	5982 ± 15	17.2 ± 1.9	8.5 ± 0.7	3.277 ± 0.011
Q 2116-358				
Lyα	4058 ± 7	114 ± 3	152 ± 4	2.340 ± 0.006
N V	4149 ± 6	20.1 ± 1.4	19.8 ± 1.3	2.349 ± 0.005
Si II	4213 ± 20	1.5 ± 0.4	3.7 ± 1.1	—

Continued on next page

Quasar Line	$\lambda_{\rm vac}$ (Å)	$W_{\rm rest}$ (Å)	Line flux (10^{-15} erg s^{-1} cm^{-2})	$z_{\rm TF}$
Si II/O I	4357 ± 3	3.3 ± 0.2	3.7 ± 0.3	2.341 ± 0.002
C II	4460 ± 6	0.8 ± 0.2	1.8 ± 0.4	—
Si IV/O IV]	4667 ± 4	10.8 ± 1.2	10.7 ± 1.1	2.337 ± 0.003
C IV	5174 ± 3	36 ± 2	46 ± 2	2.3435 ± 0.0018
Q 2138-4427[c]				
Lyα	5036 ± 35	54 ± 4	38 ± 3	3.14 ± 0.03
N V	5202 ± 25	3.5 ± 0.7	2.4 ± 0.5	3.20 ± 0.02
Si II/O I	5369 ± 15	3.3 ± 0.3	1.94 ± 0.15	3.117 ± 0.012
C II	5501 ± 5	0.93 ± 0.14	0.65 ± 0.10	—
Si IV/O IV]	5732 ± 5	9.3 ± 1.2	5.1 ± 0.7	3.098 ± 0.004
Q 2206-1958				
Lyα	4335 ± 9	64 ± 3	84 ± 4	2.568 ± 0.007
N V	4415 ± 6	12.3 ± 1.5	22 ± 2	2.563 ± 0.005
Si II	4500 ± 17	1.8 ± 0.3	3.4 ± 0.3	—
Si II/O I	4654 ± 6	4.1 ± 0.4	4.2 ± 0.4	2.568 ± 0.005
C II	4773 ± 10	3.9 ± 0.4	6.6 ± 0.9	—
Si IV/O IV]	4978 ± 7	27 ± 2	31.1 ± 1.6	2.559 ± 0.005
C IV	5501 ± 6	25.7 ± 1.4	28.9 ± 1.6	2.555 ± 0.004
Q 2212-1626				
Lyα	6073 ± 7	158 ± 14	62 ± 2	3.998 ± 0.006
N V	6204 ± 7	14.2 ± 1.8	3.6 ± 0.5	4.006 ± 0.006
Si II	6278 ± 14	2.2 ± 0.6	0.7 ± 0.2	—
Si II/O I	6514 ± 4	6.2 ± 0.4	1.88 ± 0.13	3.994 ± 0.003
C II	6670 ± 15	0.43 ± 0.14	0.12 ± 0.03	—
Si IV/O IV]	6999 ± 11	6.3 ± 0.4	1.65 ± 0.12	4.004 ± 0.008

[a] The Si IV/O IV] line was only partly covered by our spectrum. We were able to reliably measure the position, but not the flux or the equivalent width.

[b] The C II $\lambda 1335$ line was too faint to be detected.

[c] The Si II $\lambda 1264$ line was too faint to be detected.

After removing absorption lines due to intervening systems, we measured equivalent widths, line fluxes and vacuum-corrected wavelengths for the QSO emission lines covered by our spectra. The results are presented in Table 6.3. We determined the systemic redshift of the quasars as the inverse-variance weighted average of the redshifts calculated in Table 6.3. The obtained systemic redshifts are presented in Table 6.4.

6.3.2 Extended Lyα emission

During the spectral extraction (Sect. 6.2.2) we used both exponential and de Vaucouleurs profiles (symmetric and asymmetric) for modelling

Table 6.4 Systemic redshifts of quasars in the FORS sample based on blueshift-adjusted rest-frame wavelengths.

Quasar	$z_{\rm em}$
Q 0049-2820	2.265 ± 0.002
Q 0056+0125	3.1667 ± 0.0011
Q 0135-273	3.215 ± 0.002
Q 0201+113	3.636 ± 0.007
Q 0216+0803	2.9938 ± 0.0017
Q 0458-0203	2.286 ± 0.004
Q 0528-2505	2.779 ± 0.005
Q 1202-0725	4.686 ± 0.009
Q 1209+0919	3.293 ± 0.003
Q 2116-358	2.3419 ± 0.0012
Q 2138-4427	3.103 ± 0.003
Q 2206-1958	2.561 ± 0.002
Q 2212-1626	3.998 ± 0.002

the extended emission. The best-fitting profile was in all cases an asymmetric exponential profile, although in terms of χ^2 an exponential profile in a few cases provided only a marginally better fit than an asymmetric de Vaucouleurs profile. The resulting extended flux profiles from either fit differ only inside a radius of 1 arcsec, where the de Vaucouleurs profiles have high and extremely narrow peaks. Such a high and narrow peak indicates that the de Vaucouleurs fit seeks to mimic the effect of a point source, rendering it useless for our purpose of separating extended and point source. Note that the preference of the exponential profile not necessarily means that the extended emission is disk-like, but merely that the de Vaucouleurs profile is not suitable for separating extended emission from point source contributions. We shall in the following only consider the fits using an exponential profile.

After subtracting the quasar spectra, we analyze the residual spectra. We calculate the spatially averaged extended spectrum (left column of Fig. 6.1), the surface brightness profile of the Lyα line (middle column of Fig. 6.1), and the velocity profile relative to the quasar systemic redshift (right column of Fig. 6.1). We use the surface brightness profile to measure the average effective radius of the exponential profile, letting a profile be described by

$$\Sigma_{\rm Ly\alpha}(r) = \begin{cases} Ae^{r/r_1} & \text{for } r < 0, \\ Ae^{-r/r_2} & \text{for } r \geq 0. \end{cases} \tag{6.1}$$

Here we have taken $r = 0$ to be the position of the point source. The surface brightness profile is fitted by an exponential convolved with the

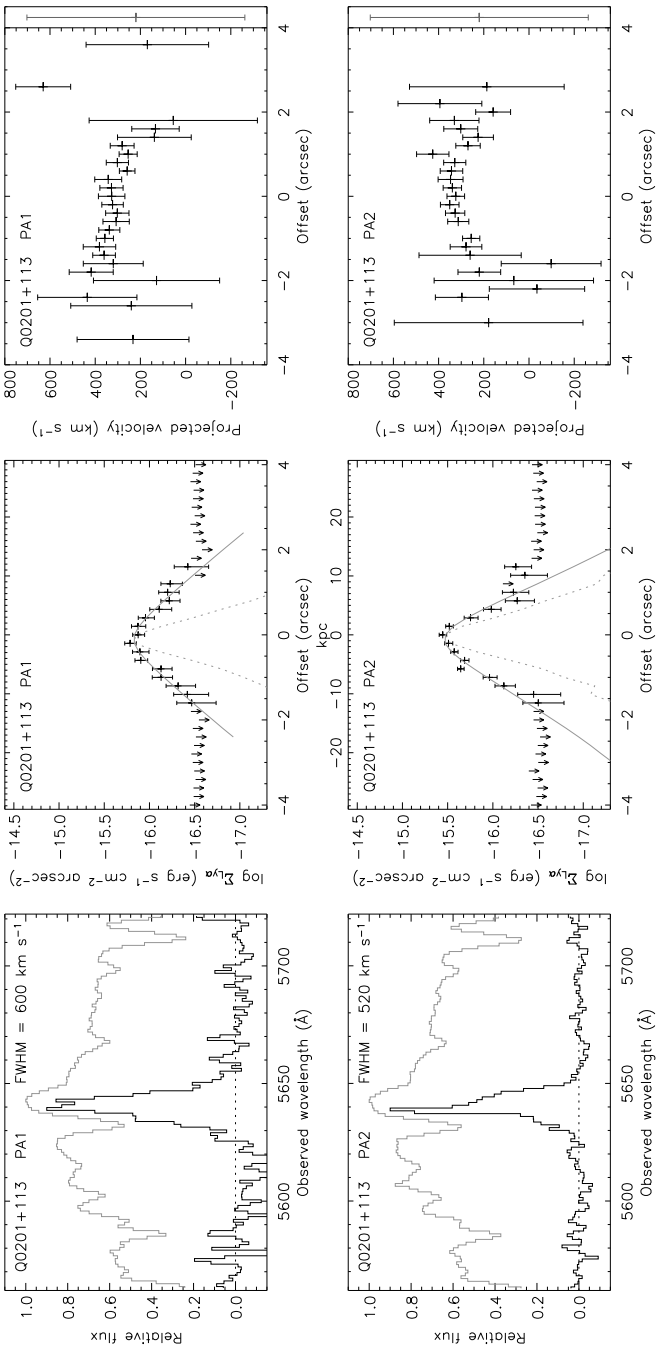

Figure 6.1 Spectrum, surface brightness and velocity profiles of the extended emission. Quasar identification and position angle are shown in the upper-left corner of all plots. *Left column:* Spectrum of the QSO around its Lyα emission line (*grey curve*) and the spatially averaged spectrum of the extended emission (*black curve*). The extended spectrum has been normalized to 90% of the maximum quasar flux. The spectral width (FWHM) of the extended Lyα line corrected for the instrumental broadening is given in the upper right corner. *Middle column:* Surface brightness profile of the Lyα line. The errors are estimated from the residuals present in the spectrum after subtraction of the quasar spectrum. Systematic errors due to errors in the flux calibration are not included. Arrows illustrate 2σ upper limits. Overplotted are the best-fit surface brightness profiles (solid grey curve) and the SPSF (dotted grey curve). The best-fit parameters are given in Table 6.5. *Right column:* Velocity profiles of the extended Lyα emission. Velocities are measured relative to the systemic redshift of the quasar, such that positive velocities correspond to higher wavelengths. The errorbars are uncertainties on the position of the maximum of a fitted Gauss curve. Cases where the fitting procedure did not provide a meaningful result are excluded from the plot. The systematic error arising from the uncertainty on the quasar redshift is shown as a grey errorbar in a box to the right of the plot.

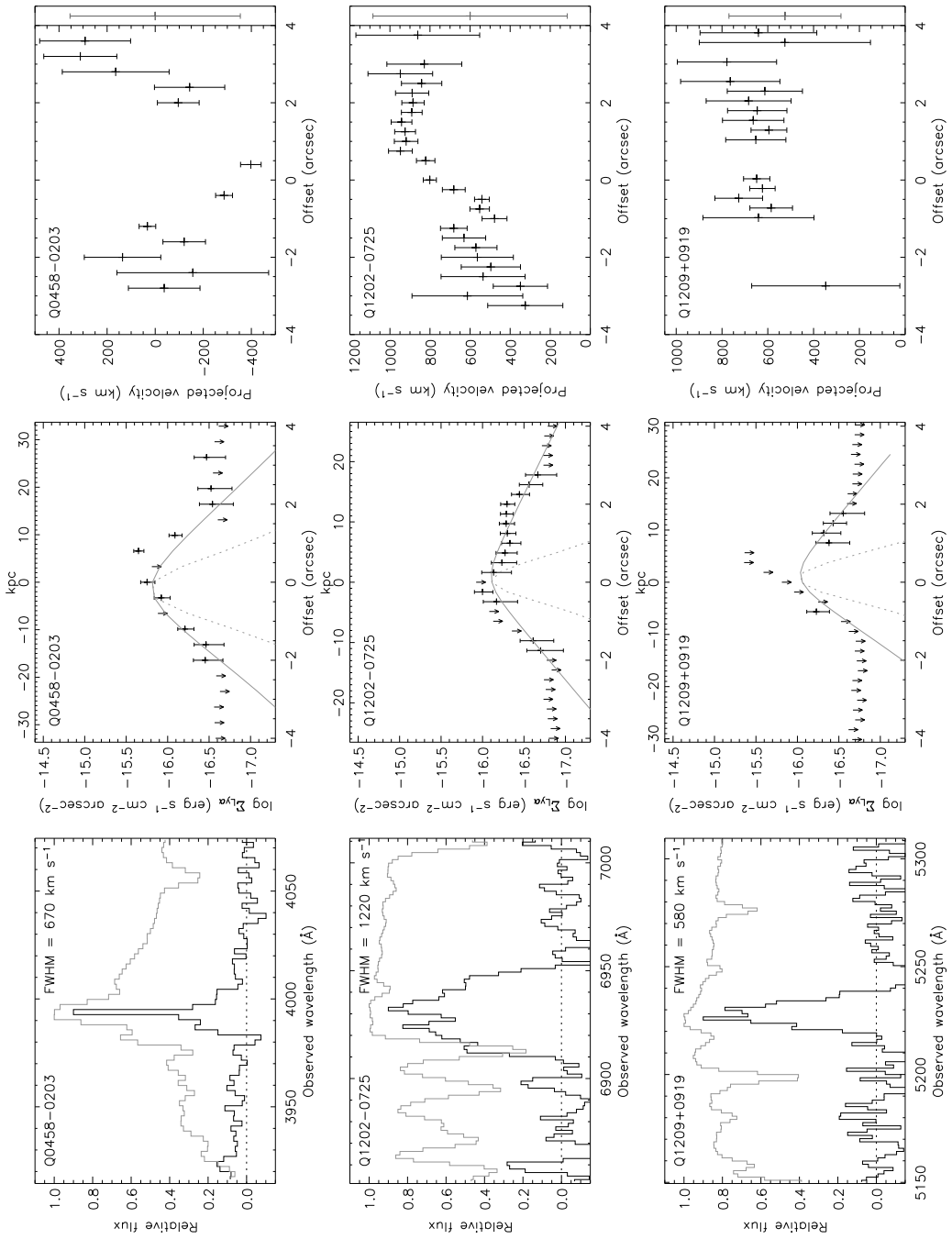

Fig. 6.1. (continued)

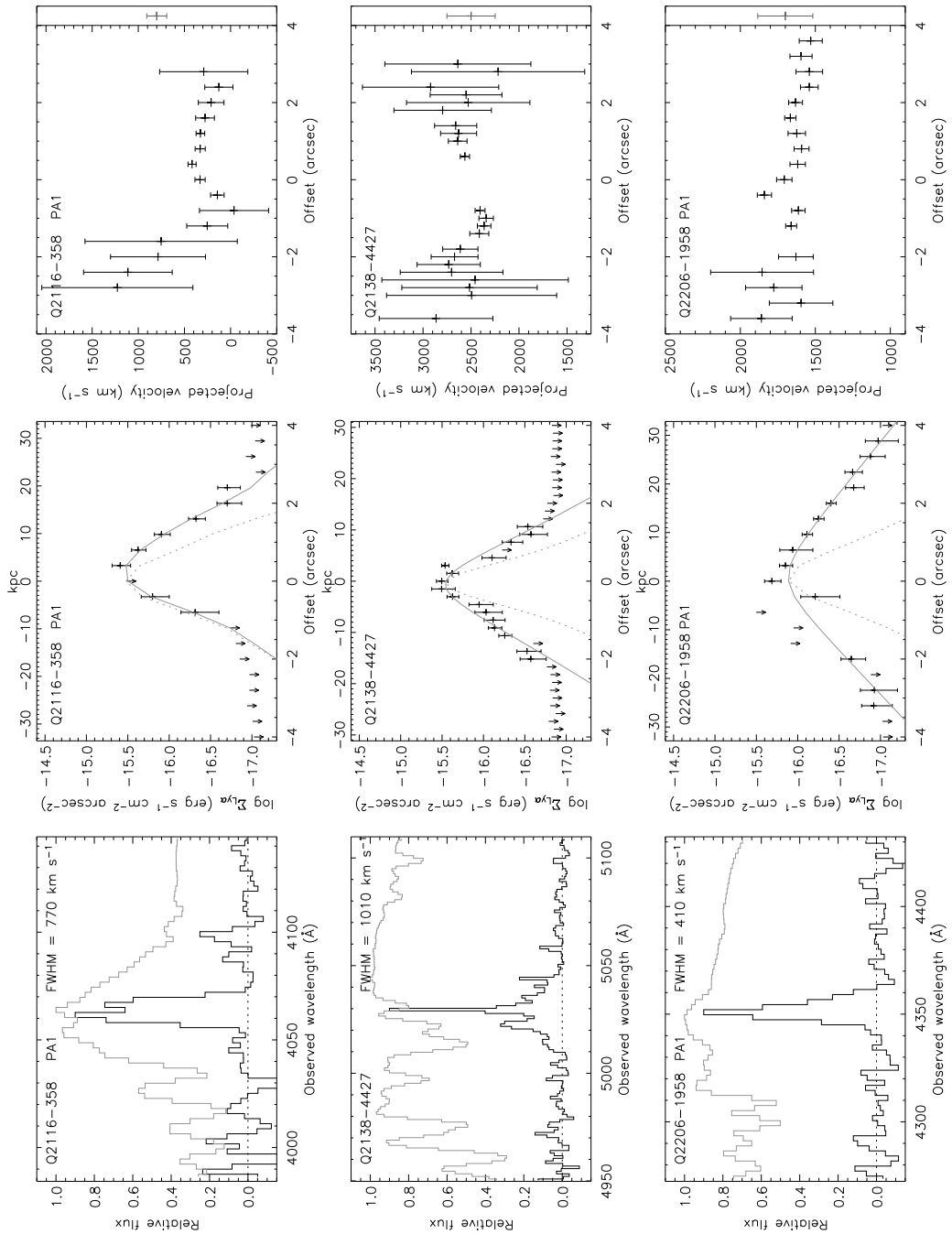

Fig. 6.1. (continued)

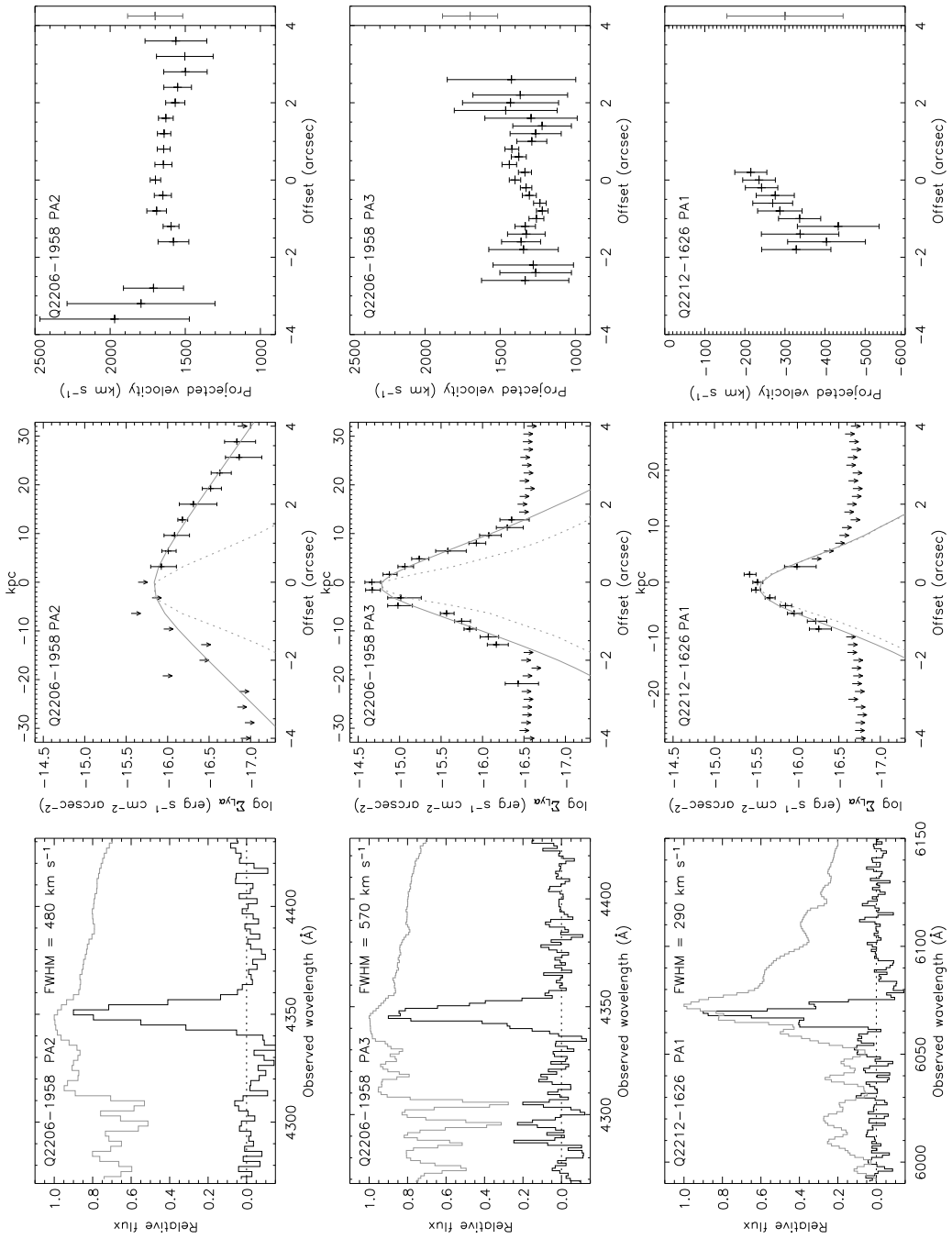

Fig. 6.1. (continued)

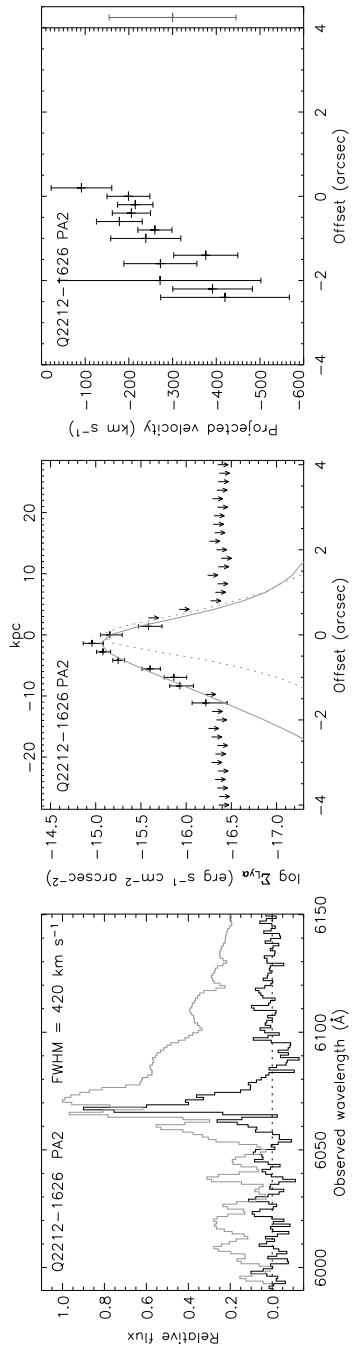

Fig. 6.1. (continued)

Table 6.5 Characteristics of the best-fit extended profiles. In all cases the best-fitting profile was an asymmetric exponential. The effective radii (before convolution with the seeing-profile) of the profiles, r_1 and r_2, are given in kpc measured at the redshift of the quasar. The best-fit profiles are shown in the middle column of Fig. 6.1.

Quasar	#PA	Profile	r_1 (kpc)	r_2 (kpc)
Q 0201+113	PA1	Exp	5.3	5.4
	PA2	Exp	3.7	2.4
Q 0458-0203	PA1	Exp	5.6	6.8
Q 1202-0725	PA1	Exp	6.7	12.1
Q 1209+0919	PA1	Exp	4.4	8.1
Q 2116-358	PA1	Exp	0.2	3.1
Q 2138-4427	PA1	Exp	3.7	2.9
Q 2206-1958	PA1	Exp	7.2	8.6
	PA2	Exp	6.8	10.4
	PA3	Exp	2.2	2.5
Q 2212-1626	PA1	Exp	1.2	0.66
	PA2	Exp	2.4	0.019

seeing-profile. The results are presented in Table 6.5, where effective radii are given in kpc at the redshift of the corresponding quasar. The fits are shown as solid grey curves in the middle panels of Fig. 6.1.

In order to compare our findings to other studies, we need to compute the total flux in the Lyα line. However, not knowing the spatial distribution of surface brightness poses a serious problem. Instead we consider two extreme models. The first model assumes that the slit completely covers the extended emission, i.e. the observed flux is all there is. This gives a minimum estimate of the total extended flux. The second model assumes that the extended emission is rotationally symmetric around the quasar and follows the observed surface brightness profile at any position angle. This can be considered a maximum flux model, giving an upper limit to the total extended flux. On either side of the quasar we define the extent of the emission to be between the least and most distant (relative to the QSO centroid) spatial bins with $S/N > 2$. For the spectra with no detectable Lyα fuzz we calculate the upper limits in the interval $1 < b < 3$ arcsec on either side of the quasar. The inferred fluxes and the corresponding luminosities are presented in Table 6.6. The maximum flux model yields a flux between a factor 2 and 10 higher than that in the minimum flux model.

Table 6.6 Observed Lyα fluxes, luminosities, and velocities. The minimum flux model assumes that extended emission is completely covered by the slit. The maximum flux model assumes that the extended emission is rotationally symmetric around the quasar and follows the surface brightness profile measured along the slit. The error bars do not include systematic errors due to the flux calibration. The upper limits are 3σ. $v_{\mathrm{Ly}\alpha}$ is the rest-frame velocity relative to the systemic quasar redshift (Table 6.4), and $\langle\mathrm{FWHM}\rangle$ denotes the spatially averaged rest-frame full width at half maximum of the extended Lyα line corrected for the instrumental broadening. The error includes the uncertainty arising from the error on the quasar redshift. The velocities are obtained from the spatially averaged extended Lyα line presented in the left column of Fig. 6.1.

Quasar	#PA	Minimum flux model		Maximum flux model			
		$f_{\mathrm{Ly}\alpha}$ (10^{-17} erg s^{-1} cm^{-2})	$L_{\mathrm{Ly}\alpha}$ (10^{42} erg s^{-1})	$f_{\mathrm{Ly}\alpha}$ (10^{-17} erg s^{-1} cm^{-2})	$L_{\mathrm{Ly}\alpha}$ (10^{42} erg s^{-1})	$v_{\mathrm{Ly}\alpha}$ (km s^{-1})	$\langle\mathrm{FWHM}\rangle$ (km s^{-1})
Q 0049-2820	PA1	< 8.1	< 3.2	< 27	< 11	—	—
Q 0056+0125	PA1	< 5.5	< 4.9	< 36	< 31	—	—
	PA2	< 5.5	< 4.8	< 35	< 31	—	—
	PA3	< 4.2	< 3.7	< 26	< 23	—	—
	PA4	< 5.1	< 4.5	< 40	< 26	—	—
Q 0135-273	PA1	< 94	< 86	< 500	< 460	—	—
Q 0201+113	PA1	27.7 ± 1.7	34.0 ± 2.1	54.0 ± 4.6	66.2 ± 5.7	300 ± 484	600
	PA2	49.5 ± 2.2	60.7 ± 2.7	82.2 ± 5.9	100.8 ± 7.3	297 ± 483	520
Q 0216+0803	PA1	< 7.5	< 5.7	< 68	< 53	—	—
Q 0458-0203	PA1	51.5 ± 7.0	20.6 ± 2.8	110 ± 15	44.0 ± 6.0	-33 ± 386	670
Q 0528-2505	PA1	< 9.1	< 5.9	< 44	< 29	—	—
Q 0841+129	PA1	< 12	< 27	< 58	< 130	—	—
Q 1202-0725	PA1	31.6 ± 3.4	70.7 ± 7.6	81.0 ± 8.0	181 ± 18	819 ± 489	1220
Q 1209+0919	PA1	4.22 ± 0.98	4.08 ± 0.95	16.2 ± 3.7	15.7 ± 3.6	638 ± 367	580
Q 2116-358	PA1	56.5 ± 7.5	23.9 ± 3.2	104 ± 11	44.0 ± 4.6	127 ± 156	770
	PA2	< 11	< 4.7	< 62	< 26	—	—
Q 2138-4427	PA1	43.1 ± 3.3	36.2 ± 2.8	70.7 ± 5.4	59.3 ± 4.5	2483 ± 261	1010
Q 2206-1958	PA1	56 ± 12	29.7 ± 6.5	140 ± 29	74 ± 15	1599 ± 212	410
	PA2	52 ± 11	27.3 ± 5.7	157 ± 30	83 ± 16	1545 ± 296	480
	PA3	149 ± 14	78.8 ± 7.5	281 ± 24	148 ± 13	1303 ± 244	570
Q 2212-1626	PA1	35.1 ± 2.6	54.0 ± 3.9	40.2 ± 3.9	61.8 ± 6.0	-293 ± 166	290
	PA2	58.2 ± 6.4	89.4 ± 9.9	99.4 ± 9.9	153 ± 15	-286 ± 197	420

Table 6.7 Upper limits on extended N V, Si IV/O IV], C IV, and He II flux relative to the extended Lyα flux. The bounds are 3σ upper limits in the minimum flux model. The absolute values for $f_{\mathrm{Ly}\alpha}$ are given in Table 6.6.

Quasar	#PA	$f_{\mathrm{N\,V}}$ (%)	$f_{\mathrm{Si\,IV/O\,IV]}}$ (%)	$f_{\mathrm{C\,IV}}$ (%)	$f_{\mathrm{He\,II}}$ (%)
Q 0201+113	PA1	< 20	—	—	—
	PA2	< 13	—	—	—
Q 0458-0203	PA1	< 12	< 21	< 12	< 12
Q 1202-0725	PA1	< 24	< 27	—	—
Q 1209+0919	PA1	< 100	< 130	—	—
Q 2116-358	PA1	< 9.3	< 7.1	< 7.2	< 6.0
Q 2138-4427	PA1	< 6.7	< 8.2	—	—
Q 2206-1958	PA1	< 7.5	< 10	< 13	—
	PA2	< 6.8	< 13	< 15	—
	PA3	< 2.6	< 2.6	< 3.0	—
Q 2212-1626	PA1	< 3.5	< 12	—	—
	PA2	< 8.5	< 8.0	—	—

6.3.3 Other extended emission lines

We also searched the residual spectra for traces of extended emission from the N V $\lambda1240$, Si IV/O IV] $\lambda1400$, C IV $\lambda1549$, and He II $\lambda1640$ lines seen accompanying extended Lyα emission around radio galaxies and RLQs (Heckman et al. 1991a; Villar-Martín et al. 2003).

No extended emission lines other than Lyα appear to be present, so where covered by our spectrum we compute upper limits for these lines using the redshift and width of the observed extended Lyα line between ±1 arcsec and ±3 arcsec. The result is presented in Table 6.7 as relative strengths compared to the extended Lyα line.

6.4 Radio properties

We wish to determine the radio properties of the quasars in our sample. Since various definitions of "radio-loud" and "radio-quiet" exist, it is virtually impossible to make a unique classification. Indeed, it has been shown that radio-loudness of quasars form a continuous distribution (White et al. 2000; Cirasuolo et al. 2003b), but it is debated whether or not this continuous distribution contains a signature of bimodality (Cirasuolo et al. 2003a; Ivezić et al. 2004).

In order to quantify the radio properties of our quasar sample, we searched the 1.4-GHz NRAO/VLA Sky Survey (NVSS) online catalogue (Condon et al. 1998) for sources at the positions of the quasars. The result is presented in Table 6.8. Radio-flux is detected for 5 of the quasars,

and for the rest we use a detection limit of 3σ, 1σ being 0.5 mJy beam^{-1}.

Table 6.8 Radio properties of quasars in the FORS sample. The observed radio flux at 1.4 GHz, $S_{1.4\ \mathrm{GHz}}$, is taken from NVSS (Condon et al. 1998). $S_{5\ \mathrm{GHz}}$ is the 5 GHz rest frame flux density calculated on the basis of $S_{1.4\ \mathrm{GHz}}$ (except for Q 2138-4427, see Sect. 6.8), $P_{5\ \mathrm{GHz}}$ is the 5 GHz radio power, and α is the assumed spectral index. The optical rest frame flux density at 2500 Å, S_{2500}, is calculated using the B-band magnitude. The quoted upper limits on 1.4 GHz radio flux are 3σ limits.

Quasar	α	m_B	S_{2500} (mJy)	$S_{1.4\ \mathrm{GHz}}$ (mJy)	$S_{5\ \mathrm{GHz}}$ (mJy)	$R_{5\ \mathrm{GHz}}$	$P_{5\ \mathrm{GHz}}$ (10^{25} W Hz^{-1})
Q 0049-2820	1.7^a	18.1	0.022	< 1.5	< 0.39	< 1.8	< 1.5
Q 0056+0125	0.5	19.6	0.024	5.5	1.4	60	13
Q 0135-273	0.5	19.2	0.034	< 1.5	< 0.39	< 11	< 3.5
Q 0201+113	-0.3^b	19.5	0.011	780.8	156	13700	1910
Q 0216+0803	0.5	18.9	0.046	< 1.5	< 0.40	< 8.6	< 3.1
Q 0458-0203	-0.48^c	20.0	0.010	2264.3	717	71600	2870
Q 0528-2505	0.5	18.17	0.093	1161.9	316	3400	2060
Q 0841+129	0.5	18.6	0.051	3.1	0.69	13	15
Q 1202-0725	0.5	18.4	0.061	< 1.5	< 0.33	< 5.4	< 7.4
Q 1209+0919	0.5	20.4	0.011	< 1.5	< 0.38	< 34	< 3.7
Q 2116-358	0.5	17.2	0.24	< 1.5	< 0.43	< 1.8	< 1.8
Q 2138-4427	0.5	19.17	0.035	No map	< 0.91	< 26	< 7.7
Q 2206-1958	1.0^a	17.49	0.25	< 1.5	< 0.42	< 1.7	< 2.2
Q 2212-1626	0.5	20.6	0.0086	< 1.5	< 0.36	< 41	< 5.5

[a] Spectral index measured by Forster et al. (2001).
[b] Spectral index measured by Becker et al. (1991).
[c] Spectral index measured by Barthel et al. (2000).

Commonly, either the radio-to-optical flux density ratio, R, or the radio power, P, has been used to distinguish between the two classes. Here we will define the R-parameter as the ratio between rest frame flux densities measured at 5 GHz and 2500 Å (Sramek & Weedman 1980), $R_{5\ \mathrm{GHz}} = S_{5\ \mathrm{GHz}}/S_{2500}$, and use the radio power measured at 5 GHz, $P_{5\ \mathrm{GHz}}$. In order to calculate these two quantities, we proceed in the following way. We convert the 1.4 GHz flux densities obtained from the NVSS database to 5 GHz rest frame flux densities using the relation

$$S_{5\ \mathrm{GHz}} = S_{1.4\ \mathrm{GHz}} \left(\frac{5}{1.4}\right)^{-\alpha} (1+z)^{\alpha-1}, \tag{6.2}$$

where α is the spectral index such that $S_\nu \propto \nu^{-\alpha}$. The radio power is given by

$$P_{5\ \mathrm{GHz}} = 4\pi D_L^2 S_{5\ \mathrm{GHz}}, \tag{6.3}$$

where D_L is the luminosity distance to the quasar. Since all quasars in our sample have B-band magnitude measurements available, we will

use this for calculating the 2500 Å flux density. This is done according to the relation

$$S_{2500} = S_B \left(\frac{4400}{2500}\right)^{-\alpha} (1+z)^{\alpha-1} \,. \tag{6.4}$$

The flux density in the B-band, S_B, is given by $\log S_B = -22.35 - 0.4 m_B$ (Longair 1981). The optical flux densities are also shown in Table 6.8.

The transition between the radio-loud and radio-quiet classes is usually chosen at $R_{5\ \mathrm{GHz}} = 10$ or $P_{5\ \mathrm{GHz}} = 1.3 \times 10^{25}$ W Hz^{-1} (see e.g. Wold et al. 2001). Since all our upper limits on $P_{5\ \mathrm{GHz}}$ are greater than 1.3×10^{25} W Hz^{-1} (Table 6.8), we will use the R-parameter for the classification. However, the $R_{5\ \mathrm{GHz}} = 10$ division has for a population of flat-spectrum ($\alpha < 0.5$) quasars been seen to lead to classifications inconsistent with the general unified model of AGN (Falcke et al. 1996). Instead a division line at $R \approx 25$ for steep-spectrum quasars and at $R \approx 250$ for flat-spectrum quasars was suggested. Furthermore, it has been noted that if the radio-loudness classification was based on the level of extended radio emission radio-intermediate quasars ($25 \lesssim R \lesssim 250$) would fall in the radio-quiet category (Blundell & Beasley 1998). We shall therefore take any radio-intermediate quasar to be radio-quiet (Wold et al. 2001), so that only 3 RLQs are present in our sample. We have checked that our results do not depend critically on the possibly radio-intermediate quasars (Q 0056+0125, Q 1209+0919, Q 2138-4427) being interpreted as radio-loud or radio-quiet.

Only few measurements of spectral indices exist for our sample. Where possible we use the actual measurement of α, but otherwise we assume $\alpha = 0.5$ for both radio and optical spectra. We do not believe that our flux calibration is sufficiently precise to measure the spectral index, since it may be subject to differential slitlosses. The radio-loudness is not dependent on the spectral index; setting $\alpha = 0.3$ or $\alpha = 0.8$ does not significantly change $R_{5\ \mathrm{GHz}}$ or $P_{5\ \mathrm{GHz}}$ for any quasar.

6.5 Discussion

6.5.1 Sizes and shapes

Two radio-quiet quasars at $z \approx 3.6$ studied by Bremer et al. (1992) show extended Lyα emission covering $30 - 40$ kpc. Heckman et al. (1991b) reported 15 RLQs with $2 \lesssim z \lesssim 3$ displaying extended Lyα emission typically between 40 and 110 kpc wide. In their sample the Lyα fuzz is typically asymmetric with a morphological axis aligned with the radio source, while the extended ultraviolet (UV) continuum shows no such alignment.

The sizes of the Lyα fuzz reported here is typically in the range

$20 - 40$ kpc, and the fuzz around the two RLQs does not seem to fall outside the distribution of the radio-quiet fuzz. The sizes are considerably smaller than for the extended emission around RLQs and radiogalaxies. Two of the quasars (Q 2212-1626, Q 2116-358) display asymmetric one-sided extended emission, the rest of the detections appear symmetric. One-sided extended Lyα emission was also reported by Weidinger et al. (2005). The extended emission is in most cases well described by an exponential surface brightness profile with effective radii ranging from 1 to 10 kpc. The most prominent exception is Q 1202-0725, which has an 8 kpc wide plateau at an impact parameter close to 10 kpc.

The fact that the extended profiles are best fitted by exponentials should not be taken as an indication of disk-like structures, but rather that an exponential function does a better job separating extended from point source flux. For this purpose the de Vaucouleurs profile is too centrally peaked, resulting in a degeneracy between flux of point source and amplitude of extended emission. In any case, the flux outside a 1 arcsec radius is not affected by changing the fitting profile.

6.5.2 Dynamics

The interesting dynamics that may be inferred from spectroscopic observations of extended Lyα emission divide into three parts: The velocity width (FWHM) of the extended line, the relative velocity as a function of impact parameter, and the velocity offset between the extended Lyα emission and the quasar systemic redshift.

Heckman et al. (1991a) find widths in the range $1000 - 1500$ km s^{-1} for a selection of five RLQs, and relatively little variation (< 500 km s^{-1}) across the slit. Bremer et al. (1992) measure velocity widths for the detections of Lyα fuzz around two RQQs of $600 - 1000$ km s^{-1}. Lehnert & Becker (1998) find widths > 1000 km s^{-1} for two RLQs (including one from the Heckman et al. (1991a) sample). In our present sample we measure velocity width typically in the range $400 - 600$ km s^{-1}, although FWHMs as low as 290 km s^{-1} and as high as 1220 km s^{-1} are seen. In terms of velocity width the two RLQs in our sample do not seem to deviate from the rest of the sample, which has widths similar to the radio-quiet sample from Bremer et al. (1992). The velocity widths in the radio-loud sample from Heckman et al. (1991a) are as large and larger than the radio-quiet sample. In this study we observe variations in velocity along the slit of typically $200 - 400$ km s^{-1}, which is less than the typical velocity width, and similar to the ~ 200 km s^{-1} variation reported by Weidinger et al. (2005). Incidentally, this similar to quiescent halos around $z \sim 2.5$ radio galaxies (Villar-Martín et al. 2003), although the physical sizes of these halos are larger by a factor of $2 - 10$.

Velocity offsets between the nuclear and extended emission are zero

(within the errors) for the Heckman et al. (1991a) sample when comparing to the redshift derived from the QSO Lyα line, but when comparing to the C IV redshift there may be velocity offsets of up to 2000 km s^{-1}. On the other hand, Bremer et al. (1992) find a difference of 1000 km s^{-1} between the nuclear and extended Lyα lines, the extended emission having the higher redshift. For our sample the velocity offsets relative to the QSO Lyα line are zero to within the errors for all objects except Q 2206-1958 which has an offset of ≈ 1000 km s^{-1}. When comparing to the systemic QSO redshift, the picture changes somewhat (see Table 6.6). In this case the velocity offsets range from slightly negative (Q 2212-1626) or zero to substantial (~ 1000 km s^{-1}) or extreme (2500 km s^{-1} for Q 2138-4427). Given the problems inherent in obtaining the systemic redshift of a quasar, it is uncertain how much information is contained in the velocity offsets of the extended Lyα line relative to the QSO systemic redshift.

Finally, we note that a few of the velocity profiles appear symmetrically inverted around zero impact parameter (e.g. Q 1202-0725). This could be taken as evidence for rotation (Møller et al. 2000).

6.5.3 Other extended emission lines

Although Lyα is the most powerful line, other extended emission lines are seen around high-redshift RQQs, RLQs and radio galaxies. Bremer et al. (1992) find indications of extended N V $\lambda 1240$ associated with a RQQ, while Heckman et al. (1991a) find evidence for extended C IV $\lambda 1549$ and He II $\lambda 1640$ and place upper limits to the strength of N V and Si IV/O IV] $\lambda 1400$. The strengths of C IV and He II are $7-10\%$ of the Lyα line in extended emission around RLQs, and for N V and Si IV/O IV] it is $\lesssim 10\%$ (Heckman et al. 1991a).

As argued in Villar-Martín et al. (2003), extended lines of highly ionized metals require an ionizing continuum harder than the one producible by stars, and thus the presence of such extended lines is a clear indication of photoionization by a central AGN. The absence of such extended lines may imply that the gas is not sufficiently metal enriched or that a hard ionizing continuum is lacking.

Due to the undeniable presence of a hard ionizing continuum from the central quasar, the presence or absence of extended metal lines should in our case probably be taken as an indication of the state of metal enrichment in the gas, rather than an indication of the nature of the power source for the extended emission.

In this study we detect no extended lines other than Lyα down to the 3σ upper limits given in Table 6.7. In most cases the upper limits are too large to contain much information. However, for a couple of quasars (Q 2116-358 and possibly Q 2206-1958) we would have seen other ex-

tended lines, had they been present with the expected strengths. For quasars with multiple PAs combining the results from the different PAs yields somewhat lower bounds; for Q 0201+113 we find $f_{\mathrm{N\,V}}/f_{\mathrm{Ly}\alpha} < 11\%$, for Q 2206-1958 we find $f_{\mathrm{N\,V}}/f_{\mathrm{Ly}\alpha} < 2.6\%$, $f_{\mathrm{Si\,IV/O\,IV]}}/f_{\mathrm{Ly}\alpha} < 3.6\%$, and $f_{\mathrm{C\,IV}}/f_{\mathrm{Ly}\alpha} < 4.5\%$, and for Q 2212-1626 we find $f_{\mathrm{N\,V}}/f_{\mathrm{Ly}\alpha} < 5.4\%$ and $f_{\mathrm{Si\,IV/O\,IV]}}/f_{\mathrm{Ly}\alpha} < 6.7\%$. Thus for Q 2116-358 and Q 2206-1958 we may conclude that the C IV and He II (for Q 2116-358) lines are either missing or extraordinarily weak. For the rest of the sample our data are not sufficient to make any statements for or against. This also prevents us from determining whether or not the two RLQs in our sample with extended Lyα emission distinguish themselves from the RQQs.

6.5.4 Differences between RLQs and RQQs?

The apparent differences in sizes and line widths for the extended Lyα emission around RLQs and RQQs suggests that they do not share a common origin. To pursue this idea, we compare the luminosities of Lyα fuzz around the two types of quasars. Seeking to maximize the statistical footing of our analysis, we have searched the literature for detections of extended Lyα emission around high-redshift ($z > 2$) quasar with published fluxes and non-detections with quoted upper flux limits irrespective of radio-loudness. This resulted in 26 quasars (22 detections and 4 upper limits), the majority radio-loud. Treating this literature sample in a fashion similar to our sample of Lyα fuzz detections we calculate the corresponding Lyα luminosity $L_{\mathrm{Ly}\alpha}$, and from the B-band magnitudes and the 1.4 GHz radio flux densities we estimate the radio-loudness $R_{5\ \mathrm{GHz}}$ and radio power $P_{5\ \mathrm{GHz}}$. The details of the literature sample and the resulting estimates are presented in Table 6.9. Upper limits are 3σ. In a few cases we were unable to find measurements of the spectral index α; where possible we instead calculate it using the observed 5 GHz and 1.4 GHz flux densities, but otherwise we assume $\alpha = 0.5$. We note that although the quoted B-band magnitudes fainter than 18.5 are possibly rather uncertain (Flesch & Hardcastle 2004), the radio-loudness R calculated from the V-band magnitude agrees with our B-band based estimates to within a factor of $2-3$ ($0.3-0.5$ dex), and never pushes a quasar past the $R_{5\ \mathrm{GHz}} = 25 - 250$ dividing region.

Merging the literature sample and the FORS sample we plot the radio-loudness versus the Lyα line luminosity in Fig. 6.2a. In the merger of the two samples we have dropped our own Lyα luminosity measurement for Q 1202-0725, since our lack of spatial information makes our estimate more uncertain than the measurement in the literature (Petitjean et al. 1996). Taking quasars with $\log R \lesssim 2$ as belonging to the radio-quiet population (see Sect. 6.4), we compare in Fig. 6.2b the Lyα luminosities of host galaxies in the two classes. In this figure we

Table 6.9 Detections of extended Lyα around $z > 2$ quasars in the literature. The table lists the quasar name, the redshift, the total flux in the extended Lyα line and its reference, the inferred Lyα luminosity, the spectral index α ($f_\nu \propto \nu^{-\alpha}$) and its reference, the quasar B-band magnitude and its reference, the calculated 2500 Å rest-frame flux density S_{2500}, the observed 1.4 GHz radio flux density $S_{1.4\ \mathrm{GHz}}$, the calculated 5 GHz rest-frame flux density $S_{5\ \mathrm{GHz}}$, the radio-to-optical flux density ratio $R_{5\ \mathrm{GHz}}$, and the 5 GHz rest-frame radio power $P_{5\ \mathrm{GHz}}$. All 1.4 GHz radio flux densities are from the NVSS catalogue (Condon et al. 1998). Upper limits are 3σ bounds. S_{2500} is calculated using Eq. (6.4), $S_{5\ \mathrm{GHz}}$ is calculated using Eq. (6.2), and $P_{5\ \mathrm{GHz}}$ is calculated using Eq. (6.3). Where no observations of the spectral index α could be found, we either calculated it based on 5 GHz and 1.4 GHz flux densities (marked with the reference "Calc") or, if that was not possible, assumed $\alpha = 0.5$.

Quasar	z	$F_{\mathrm{Ly}\alpha}$ (10^{-17} erg s^{-1} cm^{-2})	Ref	$L_{\mathrm{Ly}\alpha}$ (10^{42} erg s^{-1})	α	Ref	m_B	Ref	S_{2500} (mJy)	$S_{1.4\ \mathrm{GHz}}$ (mJy)	$S_{5\ \mathrm{GHz}}$ (mJy)	$R_{5\ \mathrm{GHz}}$	$P_{5\ \mathrm{GHz}}$ (10^{25} W Hz^{-1})
Q 0017+154	2.012	398	f	116.72	1.2	a	18.44	g	0.12	2180	590	4992	1730
Q 0054-284	3.616	6.0	b	7.26	0.5		19.55	g	0.024	< 1.5	< 0.37	< 16	< 4.5
Q 0055-26	3.656	8.0	b	9.93	0.47	p	18.8	d	0.045	< 1.5	< 0.36	< 8.0	< 4.5
Q 0109+176	2.157	40	f	13.84	1.0	a	19.1	d	0.058	483	135	2340	470
Q 0225-014	2.037	158	f	47.89	0.8	g	18.0	d	0.14	455	131	921	397
Q 0316-203	2.880	< 20	f	< 13.98	0.72	c	18.9	d	0.056	100	27	492	192
Q 0445+097	2.11	200	f	65.71	0.6	a	20.7	i	0.011	946	280	26560	922
Q 0549-213	2.245	317	j	121.45	0.96	c	18.4	d	0.11	647	182	1689	697
Q 0730+257	2.686	79	f	47.04	1.2	a	19.6	i	0.042	609	172	4060	1017
Q 0751+298	2.106	< 100	f	< 32.78	0.9	a	17.6	m	0.22	407	116	531	379
Q 0758+120	2.66	158	f	91.68	0.9	a	19.35	l	0.043	127	36	833	206
Q 0805+046	2.877	794	f	555.34	0.4	a	18.7	i	0.052	509	136	2608	949
Q 0941+261	2.91	200	f	143.38	0.7	a	16.8	m	0.38	774	211	558	1516
Q 1202-0725	4.69	26	n	58.25	0.5		18.4	m	0.061	< 1.5	< 0.33	< 5.4	< 7.5
Q 1205-30	3.041	70	q	55.93	0.65	q	19.06	e	0.045	< 1.5	< 0.40	< 9.0	< 3.2
Q 1318+113	2.171	631	f	222.78	0.8	a	19.25	k	0.045	2238	642	14342	2266
Q 1345+584	2.039	794	f	240.61	0.8	a	18.9	i	0.062	642	186	2980	562

Continued on next page

Quasar	z	$F_{\mathrm{Ly}\alpha}$ (10^{-17} erg s^{-1} cm^{-2})	Ref	$L_{\mathrm{Ly}\alpha}$ (10^{42} erg s^{-1})	α	Ref	m_B	Ref	S_{2500} (mJy)	$S_{1.4\ \mathrm{GHz}}$ (mJy)	$S_{5\ \mathrm{GHz}}$ (mJy)	$R_{5\ \mathrm{GHz}}$	$P_{5\ \mathrm{GHz}}$ (10^{25} W Hz^{-1})
Q 1354+258	2.032	631	f	189.52	0.9	a	18.3	d	0.11	398	113	990	340
Q 1548+0917	2.746	47	o	29.36	0.5		18.0	d	0.11	< 1.5	< 0.41	< 3.8	< 2.6
Q 1614+051	3.209	110	o	99.68	-0.4	a	20.9	d	0.0032	329	73	22494	664
Q 1658+575	2.173	316	f	111.91	1.1	a	18.4	i	0.12	514	142	1218	503
Q 2000-330	3.777	< 0.94†	b	< 1.26	0.5		18.5	h	0.061	446	108	1771	1449
Q 2150+053	1.979	158	f	44.62	0.9	a	18.0	d	0.15	1187	339	2241	953
Q 2222+051	2.323	158	f	65.99	1.0	a	19.0	d	0.063	882	247	3898	1029
Q 2251+244	2.328	< 20	f	< 8.98	0.4	a	18.1	m	0.10	1889	552	5570	2482
Q 2338+042	2.594	251	f	136.73	1.0	a	20.2	d	0.021	1613	452	21522	2458

† Assuming a circular flux distribution with a radius of 1 arcsec

References: a: Becker et al. (1991), b: Bremer et al. (1992), c: Calculated spectral index, see text, d: Flesch & Hardcastle (2004), e: Fynbo et al. (2000b), f: Heckman et al. (1991a), g: Hewitt & Burbidge (1993), h: Jackson et al. (2002), i: Lehnert et al. (1992), j: Lehnert et al. (1999), k: Lynds & Wills (1972), l: McMahon et al. (2000), m: Monet et al. (1998), n: Petitjean et al. (1996), o: Steidel et al. (1991), p: Warren et al. (1991), q: Weidinger et al. (2005).

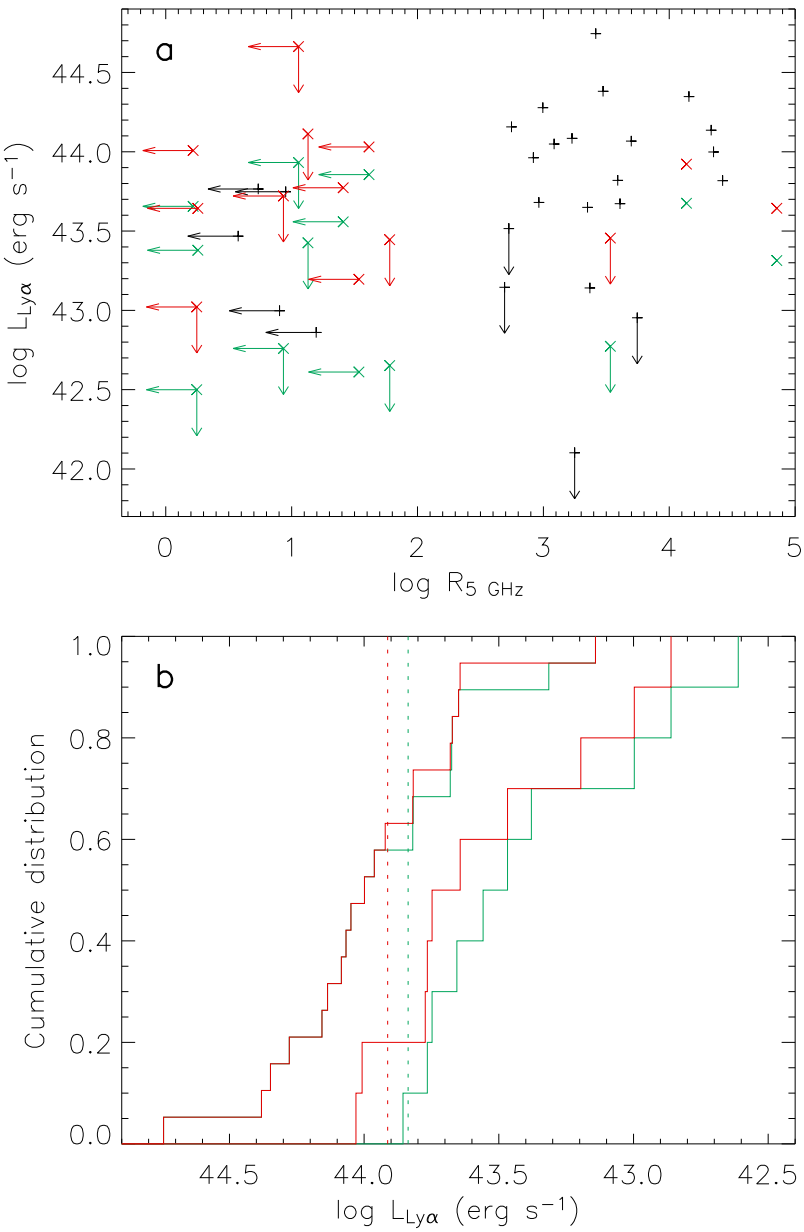

Figure 6.2 Radio-loudness and Lyα luminosity. **a)** Plot of the radio-loudness parameter $R_{5\ \mathrm{GHz}}$ versus Lyα luminosity for the FORS sample ($\times$) and the literature sample (+). For the FORS sample we plot Lyα luminosities from the minimum flux model (green) and from the maximum flux model (red). Arrows indicate upper limits. **b)** Cumulative distribution of Lyα luminosities surrounding radio-loud (left-most set of lines) and radio-quiet (right-most set of lines) quasars. Luminosities from the minimum flux model are drawn in green, from the maximum flux model in red. The vertical lines indicate the position of the maximum distance between the radio-loud and the radio-quiet distributions in the minimum (green) and maximum (red) flux models. We have ignored the upper limits on the Lyα luminosities (see text).

plot the cumulative Lyα luminosity distribution of the detections in Tables 6.6 and 6.9 for both the minimum and the maximum flux model. We compare the two distributions using a Kolmogorov-Smirnov (K-S) test, yielding probabilities of the two distribution being drawn from the same underlying population of 0.033 (minimum flux model) and 0.063 (maximum flux model). This is tentative evidence for the hypothesis that extended emission around RLQs is as luminous as that surrounding RQQs. Shifting the division line between RLQs and and RQQs to $R_{5\ \mathrm{GHz}} = 25$ only changes these numbers slightly (on the level of 3×10^{-3}). Since about a quarter of the merged sample only provides us with upper limits a significant amount of information is potentially wasted when we ignore them. We therefore proceed to applying more sophisticated statistical methods able to handle these upper limits (Feigelson & Nelson 1985, and references therein). The nonparametric tests provided by the Gehan, the Peto & Peto, and the Peto & Prentice statistics all give probabilities around 0.01 (minimum flux model) and 0.04 (maximum flux model), and they remain essentially unchanged if we exclude the very high upper limit from Q 0135-273 ($\log L_{\mathrm{Ly}\alpha} < 44.7$ and $\log R_{5\ \mathrm{GHz}} < 1.1$). If we shift the division line to $R_{5\ \mathrm{GHz}} = 25$ the probabilities increase to around 0.03 and 0.08, respectively. The logrank test gives significantly higher probabilities (0.06 for the minimum model, ~ 0.2 for the maximum model, increasing to ~ 0.2 for the minimum model and 0.3 for the maximum model when $R_{5\ \mathrm{GHz}} = 25$). The deviating logrank test may be attributed to the fact that the extended emission around the RLQs and RQQs in this sample typically are observed very differently (the majority of the RLQs are observed using narrow-band imaging, while the majority of the RQQ observations are spectroscopic). This difference is likely to result in very different distributions of upper limits, in which case the Peto & Prentice statistics is the most precise (Feigelson & Nelson 1985). However, as cautioned by Feigelson & Nelson (1985), the large discrepancy between the logrank and the other tests should serve as a warning that alternative treatments of the data may give alternative conclusions, but given the close agreement of the test probabilities apart from the logrank one, we consider the logrank test probability anomalous. To conclude, we find that extended Lyα emission around RQQs is less luminous than that seen around RLQs with a significance at $92 - 99\%$ level. The difference in the means calculated using the Kaplan-Meier estimator ranges between 0.3 and 0.6 dex corresponding to $0.8 - 1.5$ magnitudes, similar to findings at lower redshifts (Dunlop et al. 2003; Falomo et al. 2001; Kukula et al. 2001).

We have checked if any overall difference in luminosity between the radio-quiet and radio-loud sample could have biased our result. Using the rest-frame flux density at 2500 Å we compute the wavelength specific luminosity L_{2500}. We find that the luminosities of the parent RLQ

and RQQ samples are consistent with being drawn from the same distribution, the RQQs on average being slightly more luminous. In other words, the radio-loud and the radio-quiet samples are consistent with being matched in luminosity, so this is most likely not affecting our result.

One worry is that other selection effects may have influenced our result, but the complex selection function for the merged sample makes an investigation into this matter problematic. Imposing an artificial detection limit by setting all detections and upper limits below $\log L_{\mathrm{Ly}\alpha} = 43.5$ to that value, we find that the statistical tests now all reach similar probabilities of < 0.01 (minimum flux model) and < 0.05 (maximum flux model). This suggests that the flux limit itself does not affect the result, and it strengthens our presumption that the deviating logrank statistic is due to significant differences in the distributions of upper limits. However, one should keep in mind that this is a rather small sample, subject to unknown selection effects.

6.5.5 The origin of the extended Lyα emission

The presence of extended lines of Lyα and highly ionized metals like C IV or He II, all with large velocity widths (~ 1000 km s^{-1}), has been interpreted as high-speed galactic-scale outflows driven by the powerful radio emission from a RLQ (Heckman et al. 1991a). Since no powerful radio emission or jets are present in RQQs (Blundell et al. 2003), we need an alternative explanation. Scenarios typically considered include cooling radiation, stellar photoionization and quasar photoionization (e.g. Villar-Martín et al. 2003).

In two of the cases of extended Lyα emission in our sample occur around RLQs, namely Q 0201+113 and Q 0458-0203, and should be discussed separately. The radio emission of Q 0201+113 displays structure westward at 8.4 GHz extending ≈ 2 milli-arcsec (mas) and diffuse structure SW of the core at 2.3 GHz with a size close to 20 mas (Fey & Charlot 1997), and there appears to be an elongated structure NW of the core at 15 GHz extending about 2 mas (Zensus et al. 2002). As a consequence the extended Lyα emission could possibly be powered by this extended radio emission. Q 0458-0203 is a powerful radio source displaying jet-dominated extended radio emission, a strong knot about 2 arcsec SW of the core, and a straight 0.5 arcsec long jet propagating due W (Punsly 1995). This means that our observations of Q 0458-0203 ($\mathrm{PA} = 55°$ E of N) more or less cover the strong knot, and that the extended Lyα emission probably is powered by the radio jet.

We now proceed to discussing the possible scenarios for the origin of extended Lyα emission around our RQQs.

Cooling radiation

Galaxies in the process of formation are expected to attract surrounding hydrogen, which is heated by conversion of gravitational energy. A fraction of this released energy is radiated away in the Lyα line.

In a model of the gravitational collapse and line cooling, Haiman et al. (2000) predict that the phenomenon should generate Lyα luminosities of typically $10^{43} - 10^{44}$ erg s^{-1} out to the virial radius, i.e. covering angular sizes of $11 - 15$ arcsec at $z = 2 - 3$. The surface brightness profiles in this model are rather flat (the "continuous" models in Dijkstra et al. 2005), and although the predicted luminosity agrees well with the luminosities inferred in our sample, the large sizes (compared to our typical $3 - 5$ arcsec) result in surface brightnesses below our detection limits (Dijkstra et al. 2005), a clear inconsistency.

A similar model proposed by Fardal et al. (2001) predicted the absence of the high-temperature shocks responsible for the Lyα line cooling radiation. Instead a series of small low-temperature shocks would be followed by rapid cooling at small radii. In this model the most luminous objects with $L_{\mathrm{Ly}\alpha} \gtrsim 10^{43}$ erg s^{-1} have sizes < 10 kpc. For most of the examples of extended Lyα emission in our sample this is too small a size, but in a few cases this could explain the observed Lyα fuzz. The lacking high-temperature shock is confirmed by Birnboim & Dekel (2003) in a similar model.

A model of gravitational collapse including effects from the ionizing background radiation predict Lyα surface brightnesses between 10^{-20} and 10^{-17} erg s^{-1} cm^{-2} arcsec^{-2}, and sizes $\lesssim 100$ kpc (Furlanetto et al. 2005). This is fainter than what we observe by more than an order of magnitude, and larger than the $20 - 40$ kpc in our sample.

To conclude, with the current predictions cooling radiation alone is not able to explain the general sizes and surface brightness we observe. A few extreme cases in our sample could be consistent gravitational collapse and line cooling could in the Fardal et al. (2001) model, but the presence of the ionizing flux from a quasar is expected to change dramatically the appearance of any extended Lyα emission (Cantalupo et al. 2005).

Stellar photoionization

Photoionization due to UV photons from hot, young stars and energy injected into the interstellar matter due to supernovae is expected to result in an expanding hot superwind emitting Lyα photons at a luminosity of $\sim 10^{43}$ erg s^{-1} covering ~ 100 kpc (e.g. Taniguchi & Shioya 2000; Mori et al. 2004). The size of the Lyα emitting region is uncertain (Le Delliou et al. (2005) find sizes of ~ 1 kpc), but the Lyα luminosities

are similar to our findings. The FWHM of the extended Lyα line is expected to be ≈ 600 km s^{-1} (Taniguchi & Shioya 2000), also in agreement with the majority of our observations.

The data neither require nor rule out stellar photoionization as the source of the extended Lyα emission. Still, we consider this a less likely source of power, because the presence of a powerful AGN is known to suppress star formation in its host galaxy (Di Matteo et al. 2005; Ho 2005).

Quasar photoionization

Since both the quasar and the hydrogen clearly are present, the most obvious explanation is probably photoionization by the quasar, where the quasar ionizing flux is reprocessed into Lyα flux in the surrounding gas.

The observable properties of a configuration of infalling cold hydrogen around a luminous quasar was investigated by Haiman & Rees (2001). They found that the result is a nebula extending $15-25$ kpc and with a surface brightness between $10^{-18} - 10^{-16}$ erg s^{-1} cm^{-2} arcsec^{-2} in the Lyα line.

The scenario was recently studied by Dijkstra et al. (2005) using a full radiative transfer calculation, assuming a power-law velocity field for the gas dynamics and cooling radiation plus a central quasar for the Lyα emissivity profile. The results of their computations are surface brightness profiles and spectra of the Lyα line. The normalization of the surface brightness depends on the ionizing luminosity of the quasar, but the shape of the profile (in the case of fully ionized gas) is approximately exponentially decreasing with an effective radius $r_2 \approx 7$ kpc (with r_2 defined as in Eq. (6.1)) for the innermost 2 arcsec, comparable to our findings. The spectrum of the extended Lyα line is predicted to be double-peaked, which is seen clearly in a few of our spectra (Q 1202-0725, Q 2138-4427). Still, some inconsistencies exist. The velocity profiles observed in our sample display considerably more kinematic activity (variations of $200 - 400$ km s^{-1} across the slit) compared to the < 100 km s^{-1} reported in Dijkstra et al. (2005). Furthermore, Dijkstra et al. (2005) find that all extended Lyα lines are blueshifted relative to the true line centre, and the extended emission around the brightest quasars shows the smallest net blueshifts. We observe only one example of a net blueshifted Lyα line (Q 2212-1626). This could be due to absorption in the intergalactic matter (IGM), or it could (more likely) be due problems in obtaining the systemic quasar redshift. An interesting prospect presented by Dijkstra et al. (2005) is using the FWHM of the extended Lyα line for measuring the velocity dispersion of the gas. Even though Lyα photons are resonantly scattered, they claim that the

FWHM is a good measure for the velocity distribution.

Concluding, we consider quasar photoionization the most likely interpretation, both due to the consistent sizes and luminosities as well as the lack of viable alternative explanations, although our data do not exclude stellar photoionization.

Infall or outflow?

As demonstrated by Dijkstra et al. (2005) it is tricky by use of spectroscopic observations of the Lyα line to distinguish between bulk infall or outflow of the gas in which the extended Lyα emission is generated. The appearances of the spectra of in- and outflowing material are nearly identical with only a slight velocity shift of the line centre. However, in the presence of a quasar the absence of extended metal lines could indicate that the material is primordial, not metal enriched by star formation, and therefore likely infalling from the IGM on to an assembling host galaxy (Weidinger et al. 2004, 2005). Conversely, the detection of extended metal lines would imply that the gas indeed has been metal enriched by star formation, and therefore likely outflowing from the quasar host galaxy, possibly driven by AGN feedback (Di Matteo et al. 2005). On the other hand, the presence of extended metal lines could also imply inflows of gas, because the quasar phase is expected to be triggered by major mergers, which generate strong inflows (Di Matteo et al. 2005).

To conclude this section, we find that our observations of extended Lyα emission around RQQs may be explained by gas being photoionized either by the central quasar or by young hot stars. Since the presence of a powerful quasar is known to suppress star formation (Di Matteo et al. 2005; Ho 2005), we prefer the quasar photoionization scenario. The nature of the nebular gas (infalling or outflowing) in general is not constrained by our observations, although we in two cases significantly fail to detect extended metal line emission, suggesting that the surrounding gas is primordial, and that it therefore could be cold gas infalling on to an assembling host galaxy.

6.5.6 The relation between Lyα blobs and extended Lyα emission around quasars

High-redshift Lyα emitting galaxies are now routinely detected (e.g. Rhoads et al. 2000; Fynbo et al. 2003a; Ouchi et al. 2003), and they are almost exclusive compact objects (see e.g. Fig. 3 in Palunas et al. 2004) with luminosities between 0.3 and 60×10^{42} erg s^{-1} (Ouchi et al. 2003; Fynbo et al. 2003a; Palunas et al. 2004), in contrast to Lyα "blobs" (Stei-

del et al. 2000) that extend over typically $30 - 100$ kpc (areas ranging from 900 kpc^2 to $13,000$ kpc^2), reaching Lyα luminosities in the range $6 - 80 \times 10^{42}$ erg s^{-1} (Steidel et al. 2000; Matsuda et al. 2004). The Lyα blobs are similar to the extended Lyα emission surrounding radio galaxies at high redshift, but the Lyα blobs are not associated with powerful radio sources (e.g. Steidel et al. 2000), and it is therefore natural to compare them to the extended Lyα emission in our sample.

One clear difference between the two types of objects lies in the size. The largest of our objects are similar in size to the smallest Lyα blobs. This could be due our detection limits, which are bright ($\sim 10^{-17}$ erg s^{-1} cm^{-2} arcsec^{-2}) compared to the $\sim 3 \times 10^{-18}$ erg s^{-1} cm^{-2} arcsec^{-2} of Matsuda et al. (2004). The luminosities appear to be within the same ranges, although on average the Lyα blobs may be slightly less luminous. Comparing the space density, we note that Matsuda et al. (2004) detected 35 Lyα blobs in a survey volume of 1.3×10^5 Mpc^3, i.e. a space density of 2.7×10^{-4} Mpc^{-3}. Note that this estimate probably is too high, as the 35 Lyα blobs are clustered around a large overdensity (Steidel et al. 1998, 2000). The space density of luminous quasars goes from close to 4×10^{-7} Mpc^{-3} at $z = 2$ to around 3×10^{-8} Mpc^{-3} at $z = 4$ (Boyle et al. 2000; Fan et al. 2001), which translates to $\sim 10^{-8}$ Mpc^{-3}, assuming half of the RQQs display the type of extended Lyα emission presented in this paper. So, although a Lyα blob appears to be a very unusual phenomenon, and extended Lyα emission around RQQs seems rather common, the exceeding rareness of quasars makes the extended Lyα emission less common than Lyα blobs by a factor of 10^4. If a significant fraction of the Lyα blobs were shown to be powered by an AGN (possibly obscured), it would imply a space density for AGN a factor of ~ 10 higher than found in X-ray surveys down to $L_{\rm X} = 10^{42}$ erg s^{-1} (Fig. 5a in Hasinger et al. 2005), and therefore that these additional AGN are X-ray faint ($L_{\rm X} < 10^{42}$ erg s^{-1}) or X-ray obscured.

6.6 Summary and conclusion

The main result of this paper is the secure detection of extended Lyα emission in the spectra of 8 high-redshift quasars, 2 radio-loud and 6 radio-quiet, out of a sample of 14 quasars, 11 RQQs and 3 RLQs. The extended Lyα emission has a typical size of $20 - 40$ kpc, and an effective radius ranging from 1 to 10 kpc (see Eq. (6.1) for a definition). These sizes are smaller than the $40 - 100$ kpc Lyα fuzz seen around RLQs and radio-galaxies (Heckman et al. 1991b; Villar-Martín et al. 2003). The widths of the extended Lyα lines in our sample are $400 - 600$ km s^{-1} (rest-frame), smaller than the $1000 - 1500$ km s^{-1} for extended Lyα emission around RLQs (Heckman et al. 1991a). For two quasars our

data are deep enough to rule out the presence of extended C IV (and He II for one of them), probably indicating a lack of metal enrichment.

The significantly smaller sizes and velocity widths for our sample suggests that Lyα fuzz around RQQs and RLQs do not share a common origin. We test this hypothesis by collecting from the literature published detections and upper limits of extended Lyα emission around quasars at $z > 2$. This literature sample of 22 detections (17 RLQs, 5 RQQs) and 4 upper limits (all RLQs) combined with our new sample provides tentative evidence (on the 2σ level) that Lyα fuzz around RLQs is drawn from a luminosity distribution brighter than the fuzz around RQQs. We find that the extended Lyα emission on average is $0.8 - 1.5$ magnitudes brighter around RLQs than around RQQs. The RQQ and RLQ samples are consistent with being matched in luminosity, but we nevertheless warn that the extended emission could be affected by unknown selection effects.

Except for two RLQs with extended emission which are likely powered by jets or extended radio emission, we find that the extended Lyα emission in our sample is consistent with both stellar and quasar photoionization as power sources, although we prefer the latter because quasar activity is known to quench star formation (Di Matteo et al. 2005; Ho 2005). Cooling radiation alone cannot explain the extended emission. One way to settle the question of power source is to obtain near- and far-infrared observations, and analyze the properties of any dust emission present (Chapman et al. 2004; Staguhn et al. 2005).

The flow of the nebular gas (infalling or outflowing) is not constrained by our observations. However, in two cases we significantly fail to detect extended metal line emission, suggesting that the surrounding gas is primordial, and that it therefore could be cold gas infalling on to an assembling host galaxy.

The surprisingly large detection rate ($8/14$) indicates that extended Lyα emission is more common than previously assumed, and we encourage more work in this field.

Acknowledgements

MW wishes to thank Stephen Weatherley for help with the basic data reductions. This research has made use of the SIMBAD database, operated at CDS, Strasbourg, France, and NASA's Astrophysics Data System Bibliographic Services. MW gratefully acknowledges support from the ESO studentship programme.

This research is based on observations made with ESO Telescopes at the Paranal Observatory under programme IDs 63.O-0618, 64.O-0187, 66.A-0386, 70.A-0425, and 072.A-0073.

6.7 Appendix: Spectra

We present in Fig. 6.3 the optimally extracted 1D quasar spectra and in Fig. 6.4 the 2D quasar spectra with a $10,000$ km s^{-1} wide part around the quasar redshift removed, revealing any underlying extended Lyα emission. For clarity the position of the quasar Lyα line has been indicated.

6.8 Appendix: Comments on individual objects

Q 0049-2820

Q 0049-2820 is part of the original Warren et al. (2001) sample, and the spectrum contains a Lyman-limit system (LLS) at $z = 1.8862$ and a DLA at $z = 2.0713$. No clear DLA galaxy candidates were found around the quasar (Warren et al. 2001), but the slit PA was chosen to cover a very weak peak at an impact parameter of $b \approx 0.5$ arcsec. No extended Lyα emission is detected around this quasar.

Q 0056+0125

Q 0056+0125 is part of the original Warren et al. (2001) sample, and the spectrum contains a DLA at $z = 2.7771$. Four DLA galaxy candidates were found with impact parameters in the range $b = 2.3 - 4.8$ arcsec (Warren et al. 2001). At PA3 a faint neighbour is visible at an impact parameter of $b = 9.9$ arcsec. The object is consistent with being an elliptical galaxy at $z = 0.0 \pm 0.2$ (see Fig. 6.5). At PA4 a faint extended source is apparent at an impact parameter of $b = 9.0$ arcsec, extending from 7.8 to 10.2 arcsec from the quasar. The object is consistent with being either an Sb galaxy at $z = 0.2^{+0.4}_{-0.2}$ or an Sc galaxy at $z = 0.9^{+0.5}_{-0.3}$ (see Fig. 6.6). In the fit the former is slightly preferred over the latter. No extended Lyα emission is detected around this quasar.

Q 0135-273

Q 0135-273 was selected in our archive search. The quasar spectrum contains a DLA at $z = 2.80$. No extended Lyα emission is detected around this quasar.

Q 0201+113

Q 0201+113 is part of the original Warren et al. (2001) sample, and the quasar spectrum contains a DLA at $z = 3.3875$. Four candidate DLA galaxies were detected between $b = 1.0$ arcsec and $b = 4.0$ (Warren et

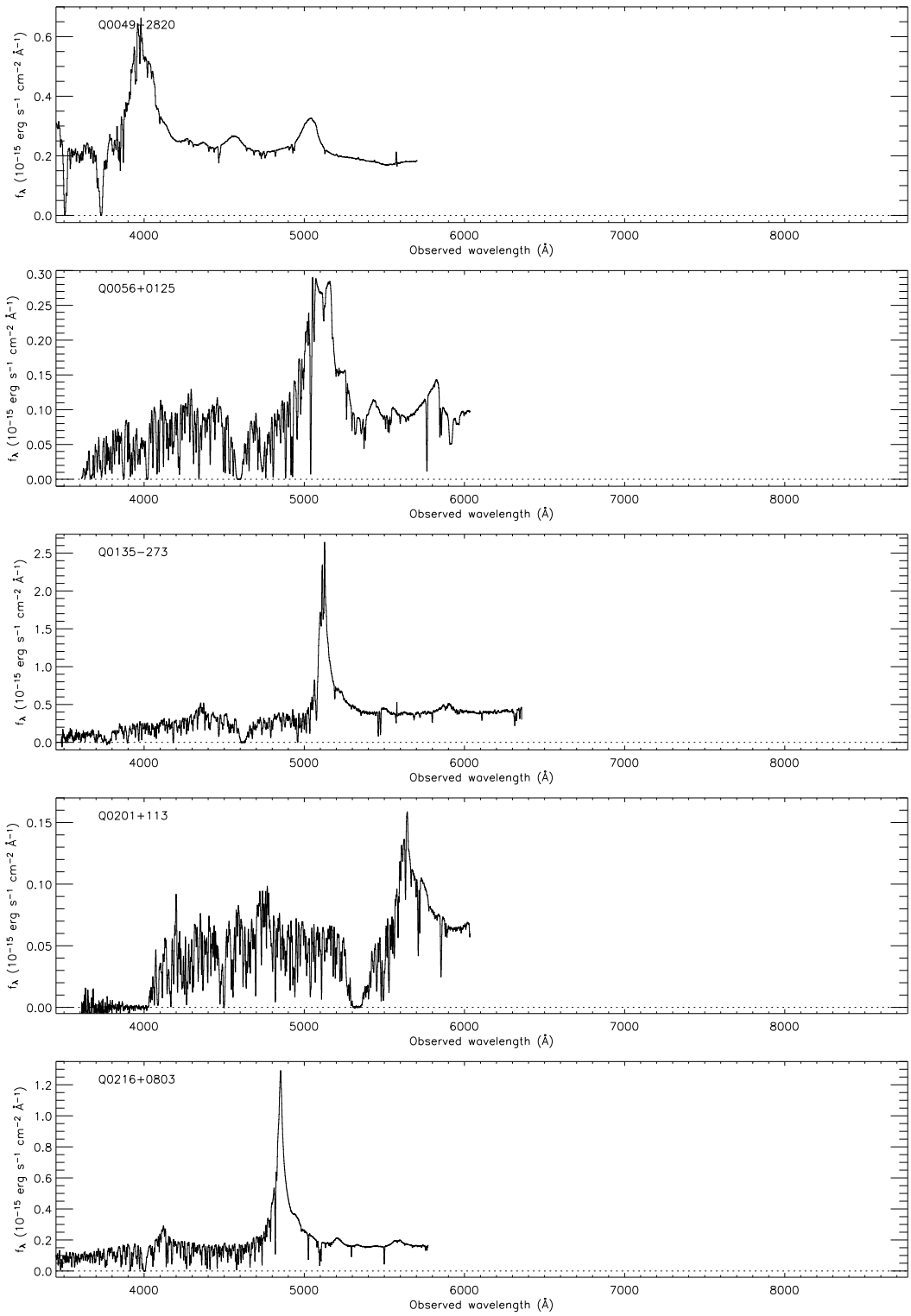

Figure 6.3 Extracted and calibrated quasar spectra.

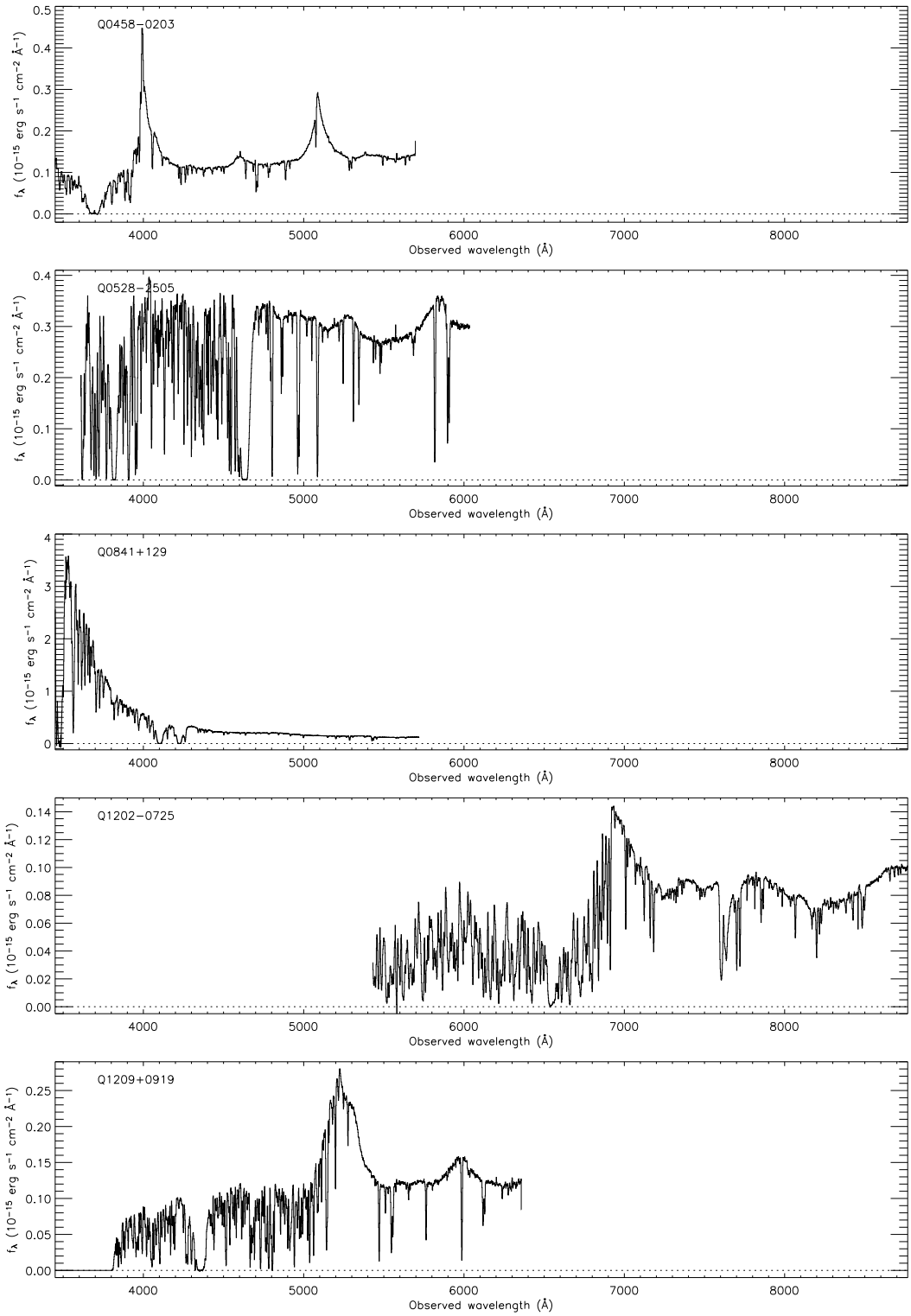

Fig. 6.3. (continued)

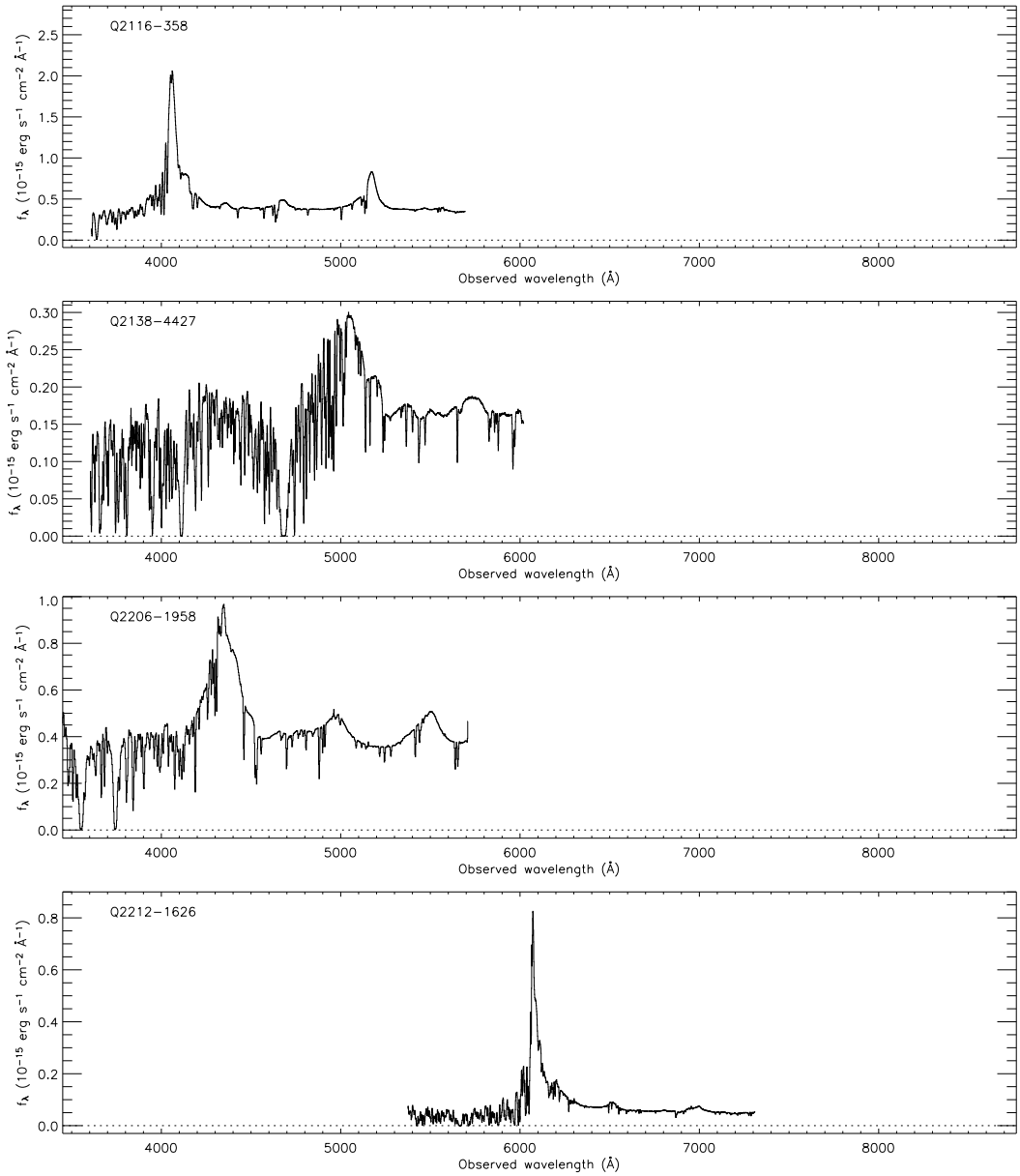

Fig. 6.3. (continued)

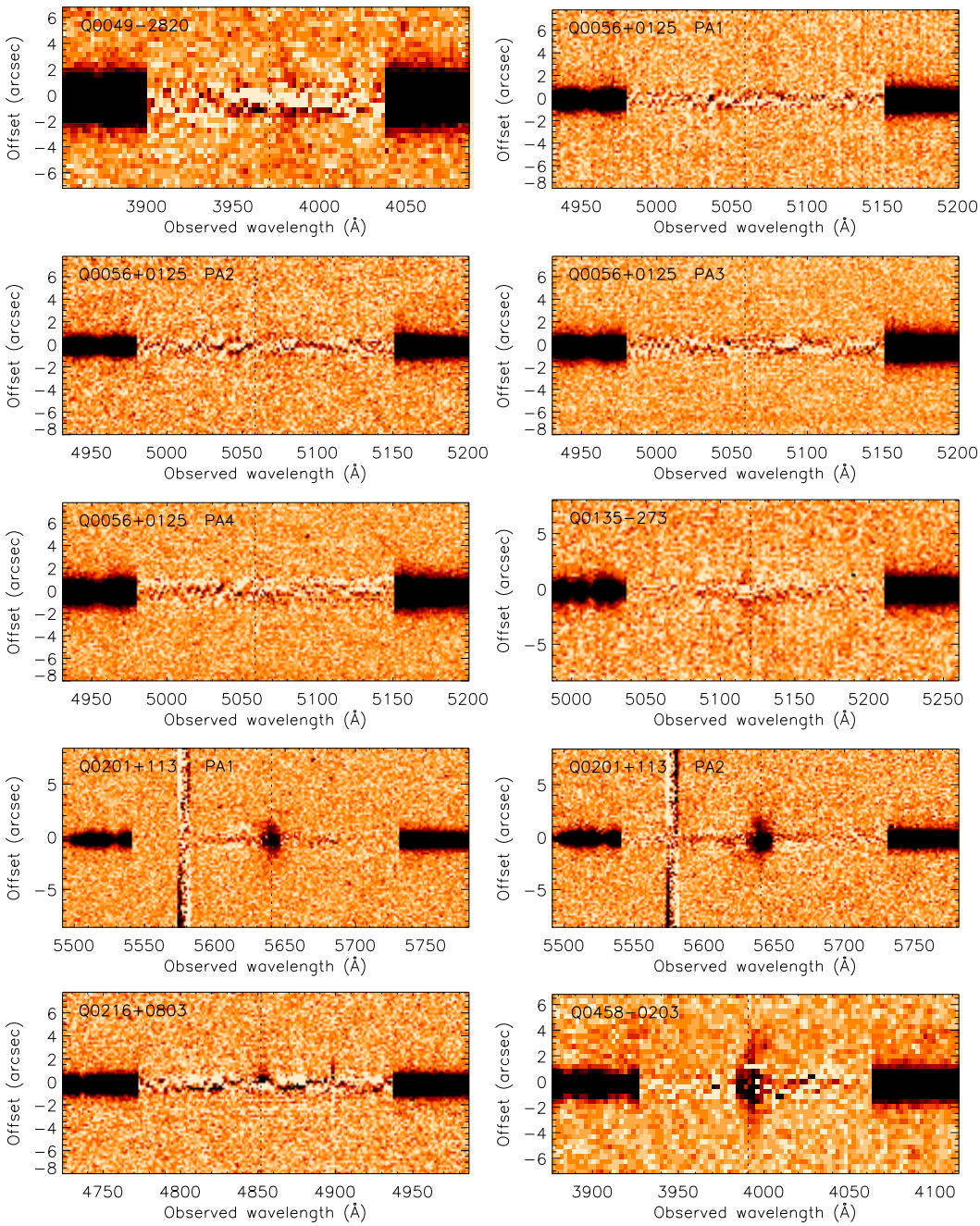

Figure 6.4 Two-dimensional quasar spectra with a $10,000$ km s^{-1} wide part around the quasar redshift removed. The zero point of the spatial axis is set to the centroid of the quasar. The dotted vertical line marks the position of the quasar Lyα emission line, where known. The noise level increases close to the centroid due to the large shot noise from the quasar flux.

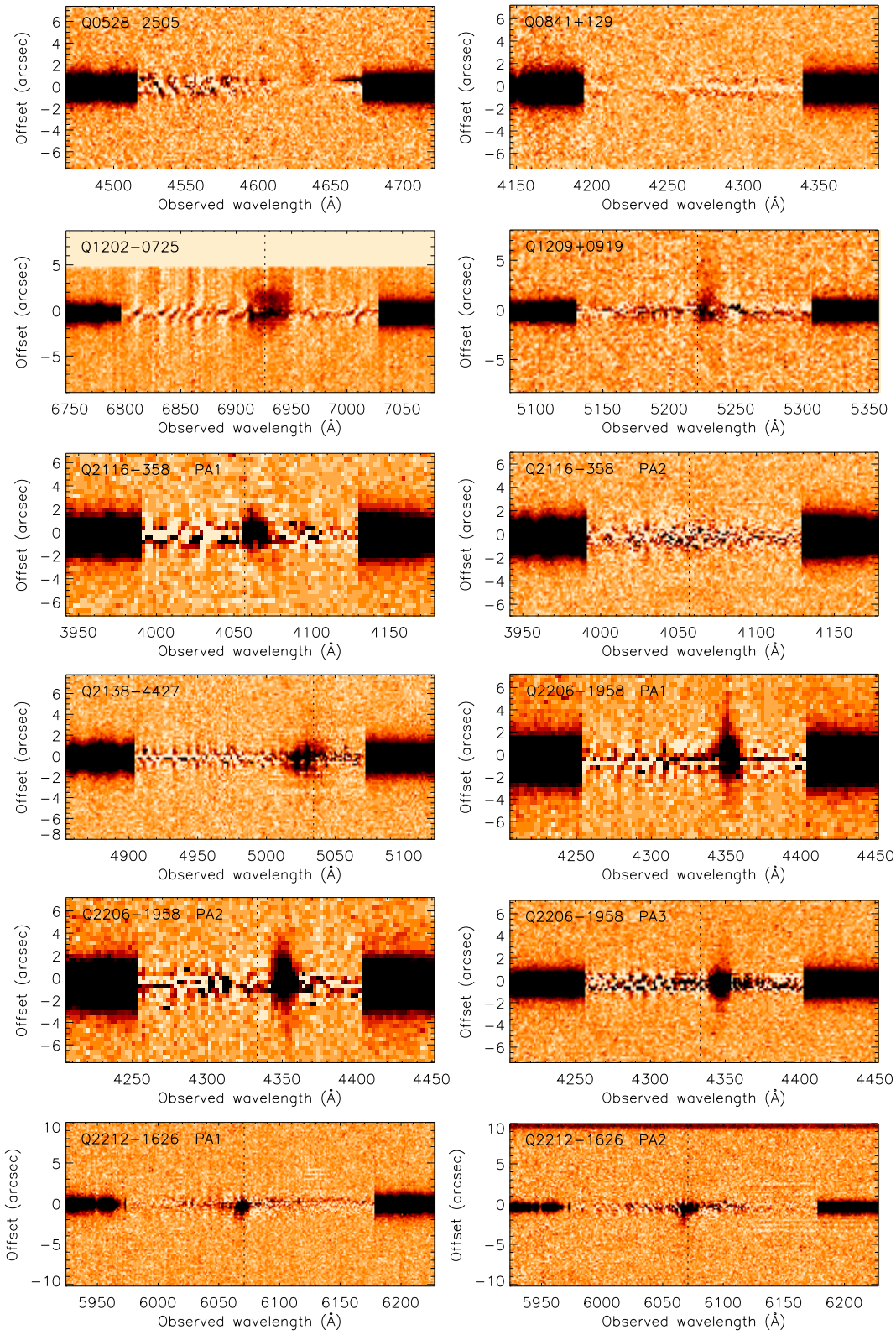

Fig. 6.4. (continued)

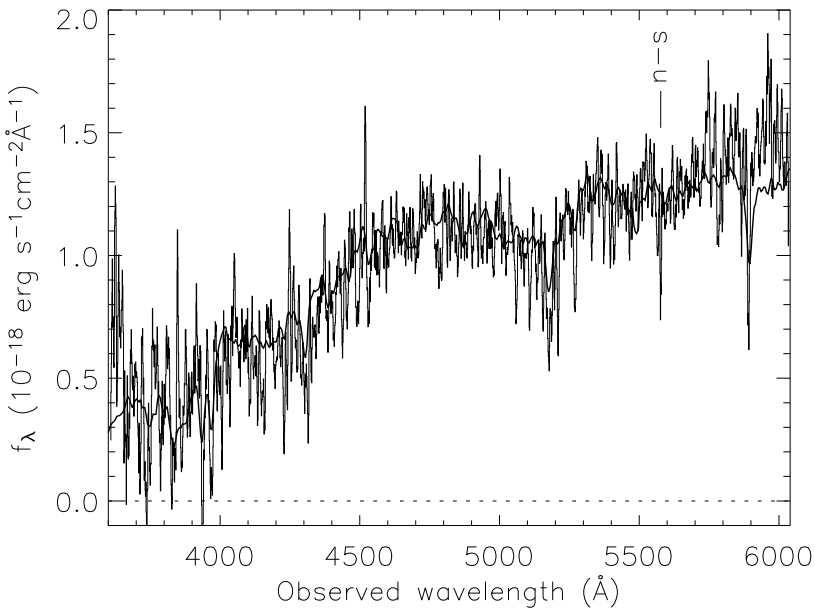

Figure 6.5 Spectrum of the object neighbouring Q 0056+0125 at PA3 (thin line) smoothed with a 6 Å wide boxcar filter, and template of an elliptical galaxy (thick line) at $z = 0$ (Kinney et al. 1996). A strong residual from a night sky line is marked n-s.

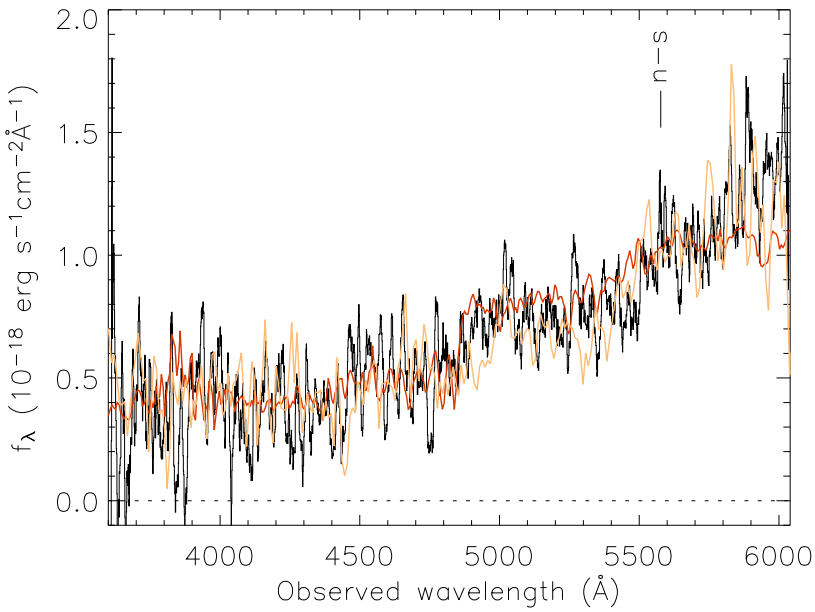

Figure 6.6 Spectrum of the object neighbouring Q 0056+0125 at PA4 (black line) smoothed with a 13 Å wide boxcar filter, a template of an Sb galaxy (red line) at $z = 0.2$, and a template of an Sc galaxy (yellow line) at $z = 0.9$ (Kinney et al. 1996). A strong residual from a night sky line is marked n-s.

al. 2001). Symmetric, extended Lyα emission is clearly detected around the quasar in both PAs, extending out to $b = \pm 2$ arcsec. For both PAs the exponential fit to the extended emission was only marginally better than de Vaucouleurs fit. The quasar is radio-loud, and the radio emission displays structure westward at 8.4 GHz extending ≈ 2 mas and diffuse structure SW of the core at 2.3 GHz with a size close to 20 mas (Fey & Charlot 1997). There appears to be an elongated structure NW of the core at 15 GHz extending about 2 mas (Zensus et al. 2002).

Q 0216+0803

Q 0216+0803 is part of the original Warren et al. (2001) sample, and the quasar spectrum contains a LLS at $z = 1.7688$ and a DLA at $z = 2.2930$. Two DLA galaxy candidates at angular separations of 1.4 arcsec and 3.8 arcsec were found. We detect no extended Lyα emission around Q 0216+0803.

Q 0458-0203

The radio-loud Q 0458-0203 is part of the original Warren et al. (2001) sample, and the quasar spectrum contains a DLA at $z = 2.0395$. Five DLA galaxy candidates were detected at angular separations between 0.9 and 4.2 arcsec. Extended Lyα emission is detected around this quasar between $b = -2$ arcsec and $b = 3$ arcsec. The exponential fit to the extended emission was only marginally better than de Vaucouleurs fit. Extended 5 GHz radio emission is seen to the SW about 2 arcsec from the core with a bridge-like structure almost connecting it to the core (Punsly 1995). Apparently it is a partially resolved image of a double knot, and with straight jet going due W of the core between 0.1 and 0.5 arcsec, so the extended radio emission is jet dominated (Punsly 1995).

Q 0528-2505

The radio-loud Q 0528-2505 is part of the original Warren et al. (2001) sample, and the quasar spectrum contains two DLAs at $z = 2.8110$ and $z = 2.1408$. Two DLA galaxy candidates were detected at impact parameters $b = 1.1$ arcsec and $b = 3.7$ arcsec. The galaxy counterpart of DLA 0528-2505 (Møller et al. 2002) is clearly visible in Lyα emission at $\lambda_{\rm obs} = 4635$ Å and $b \approx 1.6$ arcsec.

Q 0841+129

Q 0841+129 is part of the original Warren et al. (2001) sample, and the spectrum contains two DLAs at $z = 2.3745$ and $z = 2.4764$. Three

candidate DLA galaxies are detected at angular separations between 1.1 arcsec and 3.9 arcsec. Since Q 0841+129 is a BL Lacertae object, no emission lines are present in its spectrum. Therefore Q 0841+129 does not appear in Tables 6.3 and 6.4. We use a systemic redshift $z = 2.51$ for Q 0841+129, although the precise redshift is not known (Aragon-Salamanca et al. 1996; Pettini et al. 1997). Due to the uncertain redshift we widened the scanned interval in the first iteration of searching for extended Lyα emission from $\pm 10,000$ km s^{-1} to cover the range from $-10,000$ km s^{-1} ($z = 2.4$) to $+40,000$ km s^{-1} ($z = 3.0$). We detect no extended Lyα emission around Q 0841+129.

Q 1202-0725

Q 1202-0725 was selected in our archive search. It was observed in MOS mode using a 22 arcsec wide slitlet. The quasar was positioned close to one end of the slitlet, which is apparent in the 2D spectrum (Fig. 6.4). The relatively small slitlet resulted in very small sky regions usable for sky subtraction. The sky-subtracted spectrum was therefore rather noisy, and we optimized the sky subtraction around the position of the quasar Lyα line. The quasar spectrum contains a strong absorption line (probably a LLS) at $z = 4.80$.

We detect extended Lyα emission around Q 1202-0725, which is unusual in many ways. The width of the extended Lyα emission line is extremely large (1200 km s^{-1}) compared to the other RQQs in our sample, and there is evidence of self-absorption in the spatially averaged spectrum. The surface brightness profile shows an 8 kpc wide plateau at an impact parameter close to 10 kpc. The velocity profile shows a shear which could be due to rotation. This structure makes both the exponential and the de Vaucouleurs profiles fit badly, although the exponential fit is the better one.

Extended Lyα emission around this quasar has previously been reported based on narrow-band imaging (Hu et al. 1996) and integral field spectroscopy (Petitjean et al. 1996). Spatially extended CO line emission and thermal continuum emission at 1.35 mm has also been detected (Omont et al. 1996; Ohta et al. 1996) for this quasar, the emission splitting into two components – a northern and a southern source separated by 4 arcsec and 160 km s^{-1} (rest-frame), the northern component having the largest redshift (Carilli et al. 2002). Our PA is not aligned with the extended emission, but our Lyα observations none the less confirm velocity shift, although we find the shift to be around ~ 300 km s^{-1}. The redshift of the CO-emission is on average $z = 4.6932$, which is a reliable estimate of the systemic quasar redshift. Our systemic redshift of $z = 4.686$ is 380 km s^{-1} from this value. The CO line widths are $200-300$ km s^{-1}, smaller than our vast 1220 km s^{-1} for Lyα. This could suggest

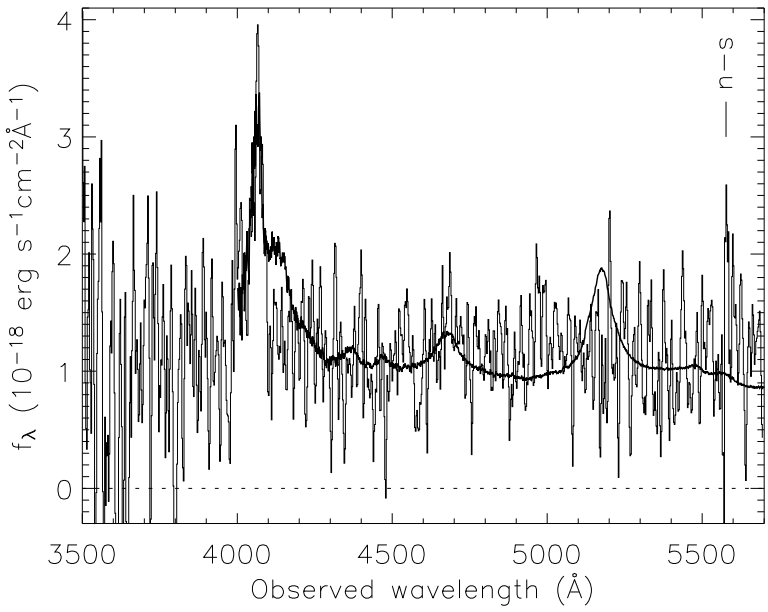

Figure 6.7 Spectrum of the object neighbouring Q 2116-358 at PA1 (thin line) smoothed with a 7 Å wide boxcar filter, and a composite quasar spectrum at $z = 2.345$ (Richards et al. 2003). A strong residual from a night sky line is marked n-s.

that the two types of emission originate in different physical locations.

Q 1209+0919

This quasar was selected in our archive search. The spectrum shows a DLA at $z = 2.58$. We detect extended Lyα emission around Q 1209+0919 between impact parameters $b = -1$ arcsec and $b = 3$ arcsec. The exponential fit to the extended emission was only marginally better than de Vaucouleurs fit.

Q 2116-358

Q 2116-358 is part of the original Warren et al. (2001) sample, and the spectrum contains a LLS at $z = 1.9966$. Three candidate galaxy-counterparts were detected between $b = 1.4$ arcsec and $b = 4.9$ arcsec. We detect extended Lyα emission around the quasar in PA1, but not in PA2. The Lyα emission extends between impact parameters $b = -0.8$ arcsec and $b = 2.4$ arcsec, and the velocity profile shows a shear which could be due to rotation.

A faint neighbour object is visible in PA1 at an impact parameter of 5.2 arcsec. The spectra are slightly overlapping, so we had to employ

an iterative procedure to deconvolve the two spectra. The spectrum of the neighbouring object is shown in Fig. 6.7. The proximity of the quasar makes the most likely interpretation of the broad emission line at 4065 ± 10 Å Lyα emission at a redshift of $z = 2.345 \pm 0.008$, very close to the quasar at $z = 2.3419 \pm 0.0012$. Due to the width of the emission line (FWHM ~ 3000 km s^{-1}) the object is presumably a second quasar at this redshift. At PA2 a faint neighbour object resides at an impact parameter of 7.7 arcsec. At a signal-to-noise around 1 the spectrum is too faint to allow any conclusion to be reached.

Q 2138-4427

This quasar was selected in our archive search. The spectrum contains an absorption system at $z = 2.38$ and another at $z = 2.85$ (Fynbo et al. 2003a). We detect Lyα emission extending from -2 arcsec to 1.5 arcsec. In the spatially averaged spectrum there is evidence of self-absorption. The exponential fit to the extended emission was only marginally better than de Vaucouleurs fit.

Q 2138-4427 is at a position not covered by the NVSS. In order to infer the rest-frame 5 GHz flux density, we instead use the 843-MHz flux from the Sydney University Molonglo Sky Survey (Bock et al. 1999), assuming

$$S_{5\ \mathrm{GHz}} = S_{843\ \mathrm{MHz}} \left(\frac{5}{0.843}\right)^{-\alpha} (1+z)^{\alpha-1}. \tag{6.5}$$

Q 2206-1958

Q 2206-1958 is part of the original Warren et al. (2001) sample, and the spectrum contains two DLAs at $z = 1.9205$ and $z = 2.0762$. Five candidate DLA galaxies were detected between $b = 1.1$ arcsec and $b = 3.5$ arcsec. We detect extended Lyα emission around the quasar at all PAs. The surface brightness profiles in PA1 and PA2 are much broader than that in PA3 (Fig. 6.1), and one could think it is an effect of the larger seeing during the observations at PA1 and PA2. However, by comparing the surface brightness profile to the seeing profile (grey dotted line in Fig. 6.1) it is evident that the wider profiles at PA1 and PA2 compared to PA3 cannot be due to the seeing alone. This is also reflected in the deconvolved effective radii in Table 6.5 that are larger for PA1 and PA2. The exponential fit to the extended emission was only marginally better than de Vaucouleurs fit. The velocity profiles at PA1 and PA2 show very little structure, while the one at PA3 shows shear at $b = 0$ arcsec, which could be a sign of rotation. A neighbour object is present in the 2D spectrum at PA1 at $b = 6.1$ arcsec. It is consistent with being an elliptical

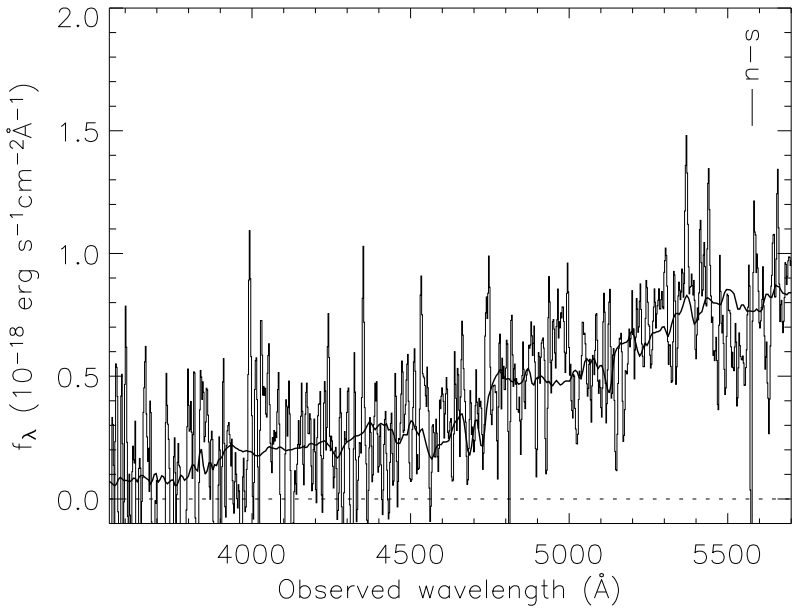

Figure 6.8 Spectrum of the $b = 6.1$ arcsec object neighbouring Q 2206-1958 at PA1 (thin line) smoothed with a 7 Å wide boxcar filter, and a template elliptical galaxy spectrum at $z = 0.2$ (Kinney et al. 1996). A strong residual from night sky line is marked n-s.

galaxy at $z = 0.2^{+0.4}_{-0.2}$ (see Fig. 6.8). The data for PA3 was previously published in Møller et al. (2000).

Q 2212-1626

Q 2212-1626 is part of the original Warren et al. (2001) sample, and the spectrum contains a LLS at $z = 3.6617$. Five candidate DLA galaxies were detected between $b = 1.1$ arcsec and $b = 3.6$ arcsec. We detect extended Lyα emission around the quasar at both PAs between -1.5 arcsec and 0.2 arcsec, so the emission is effectively one-sided. A faint neighbour object is visible in PA2 at an impact parameter of -1.6 arcsec, consistent with being identical to N-15-2C (Warren et al. 2001). We employed an iterative procedure to disentangle the two spectra. Since the extended Lyα emission and the faint neighbour object were at different impact parameters, and thus not associated, we interpolated linearly the neighbour spectrum from 6044 Å to 6098 Å, covering the wavelength of the extended Lyα line. The extracted spectrum of the faint neighbour is presented in Fig. 6.9. We cannot confirm that N-15-2C is a second quasar at $z = 3.99$ as proposed by Warren et al. (2001). We see no obvious emission lines (apart from the extended Lyα line at 6068 Å over which we have interpolated), and there is no evidence for the onset of

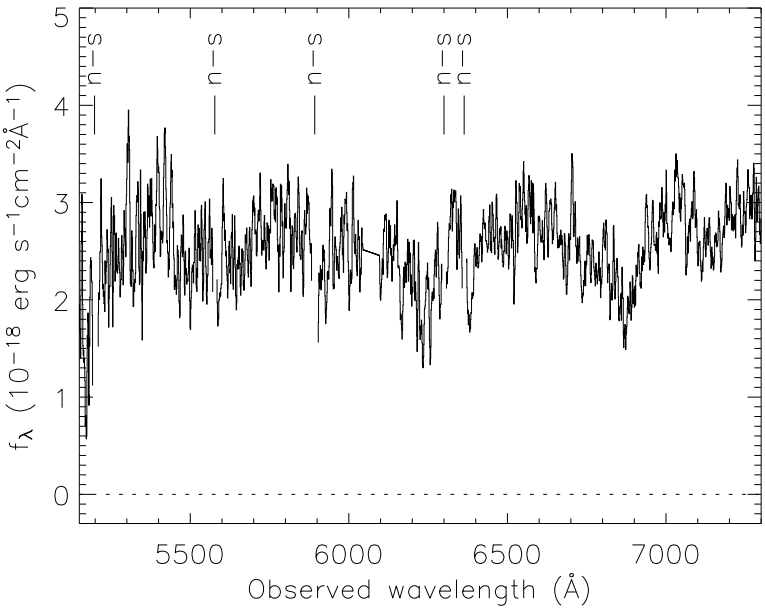

Figure 6.9 Spectrum of the $b = 1.6$ arcsec object neighbouring Q 2212-1626 at PA2 smoothed with a 5 Å wide boxcar filter. Between 6044 Å and 6098 Å we interpolated the spectrum in order to avoid being influenced by the extended Lyα emission (see text for details). Strong residuals from night sky lines are marked n-s.

the Lyα-forest below 6000 Å as is the case for the quasar spectrum. Due to the point source nature of the object, we do not attempt to fit any galaxy templates.

A second neighbour object is visible in PA2 at $b = 10.2$ arcsec. The spectrum is well fitted by Sa, Sb, bulge and elliptical galaxy templates at $z = 0$ (see Fig. 6.10), although the elliptical galaxy template is slightly favoured.

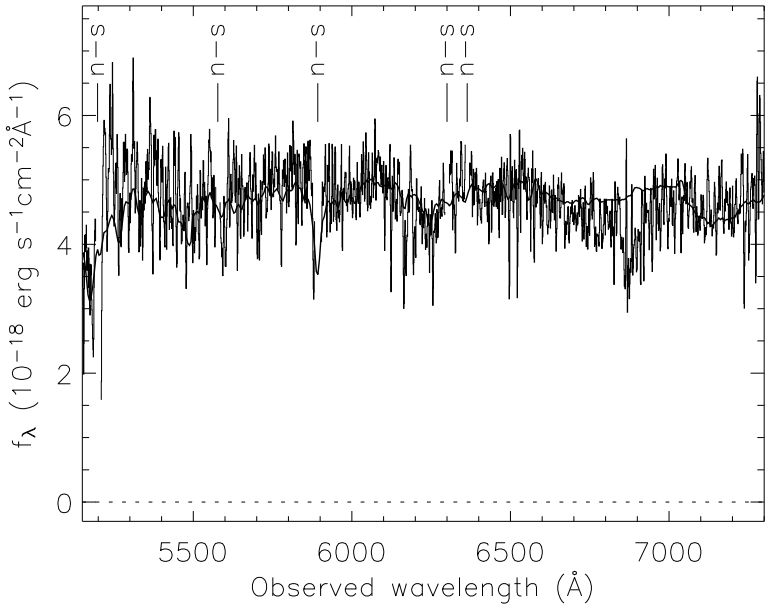

Figure 6.10 Spectrum of the $b = 10.2$ arcsec object neighbouring Q 2212-1626 at PA2 (thin line) smoothed with a 3 Å wide boxcar filter, and a template elliptical galaxy spectrum at $z = 0$ (Kinney et al. 1996). Strong residuals from night sky lines are marked n-s.

Chapter VII

Summary and outlook

THE work presented in this thesis revolves around using the Lyα emission line to study the early Universe. Lyα narrow-band observations of quasar fields and follow-up spectroscopy have multiple uses such as finding and characterizing faint Lyα emitting galaxies at the redshift of the quasar and studying extended Lyα emission around the quasar itself. The population of Lyα emitting galaxies in the field of the quasar may in turn be used to map out in three dimensions the large-scale structure in which they sit.

From numerical simulations matter has been shown to collapse into large walls, long filaments, and vast voids, and examples of high-redshift filaments have been reported. We have proposed an independent test of the cosmological parameters $\Omega_{\rm m}$ and Ω_Λ, based on the original Alcock & Paczyński (1979) test, that makes use of observations of such filaments. The test does not rely on assumptions such as standard candles or standard rods, as is the case with some other cosmological tests. The test is based only on the requirement of isotropy, i.e. that the inclination angle of a filament relative to the line of sight is randomly distributed. Although we have now entered an era of "precision cosmology", such independent sanity checks of the cosmological model remain important, as they ensure that measurements of the cosmological parameters do not suffer from unknown systematic errors.

We have presented a detailed discussion of this filament test, and using Monte Carlo simulations we have determined the precision with which one could obtain values of $\Omega_{\rm m}$ and Ω_Λ. We find that the test mostly constrains Ω_Λ, meaning that the confidence curves are mostly horizontal in the usual $(\Omega_{\rm m}, \Omega_\Lambda)$ diagram. With as few as 20 filaments this test may provide interesting limits on Ω_Λ, and with 50 filaments the confidence regions from SN Ia studies will be reduced.

Follow-up spectroscopic observations of the quasar Q 1205-30 reveal extended Lyα emission surrounding it. We analyzed the extended Lyα

emission in the frame work of a simple model of cosmological infall of optically thin hydrogen photoionized by the hard UV radiation inside the quasar ionization cone. We find that the model describes well the observed surface brightness profile, and assuming a canonical DM halo density profile we calculate the apparent velocity profile. The velocity profile arises as a projection effect, and the calculated apparent velocity profile follows nicely the observed one for a DM halo mass of a several times $10^{12} M_{\odot}$. The rate of infalling gas amounts to $\sim 0.1 M_{\odot}$ yr^{-1} in neutral hydrogen.

The spectroscopy also reveals a complex sight-line towards Q 1205-30. Analyzing the spectra we find two unrelated foreground galaxies at $z = 0.4732$ and $z = 0.865$ at impact parameters of $b \approx 2.5$ arcsec, the higher redshift one acting as a gravitational lens on a part of the extended Lyα emission around the quasar. We conclude that a LLS in the quasar spectrum close to the redshift of the quasar most likely is unrelated to both the quasar and the extended Lyα emission. Due to the absence of extended C IV emission which otherwise indicates metal enrichment by SNe, we consider most likely an interpretation of cosmological infall of pristine hydrogen photoionized inside the quasar ionization cone.

Encouraged by the success of the first quasar study we proceeded to analyzing spectroscopic data for a larger sample of high-redshift quasars. Out of 14 quasars we find extended Lyα emission around 8 (2 radio-loud and 6 radio-quiet), and we put upper limits on the Lyα fuzz around the remaining 6 quasars. We find that the typical sizes of the extended Lyα emission are smaller than what has previously been seen around RLQs and radio galaxies; the same is true for the typical line widths. These differences suggest that the extended emission around RQQs and around RLQs do not share a common origin. This is strengthened by the fact that in the two cases, where our data are deep enough, we can rule out the presence of extended C IV (and He II in one case) at the strengths seen around RLQs. In order to significantly detect any difference between extended emission around RQQs and RLQs, we expand our sample by 22 detections and 4 upper limits of extended Lyα emission around $z > 2$ quasars from the literature. This combined sample enables us to obtain tentative evidence for Lyα fuzz being less luminous around RQQs than around RLQs. The difference in luminosity is around $0.8 - 1.5$ magnitudes. We prefer an explanation where the extended emission around RQQs is due to infalling hydrogen photoionized by the quasar, although outflows and photoionization by star formation are not ruled out.

Concluding, we have presented an independent geometrical test which may be used to narrow down the space allowed for the cosmological parameters. Furthermore, we have presented observations and subse-

quent analysis of a sample of radio-quiet (12) and radio-loud (3) quasars. Two thirds of both the RQQs and the RLQs show extended Lyα emission around the quasar. The extended Lyα emission around RQQs is seemingly different from the Lyα fuzz seen around RLQs in general, and it is consistent with being infalling gas photoionized by the ionizing flux from the quasar.

A variety of future directions are possible for this kind of research. Staying on the course plotted in this thesis, it would be natural to increase the statistics by extending the sample of Lyα emitters (and hence filaments, possibly) and detections of extended Lyα emission around quasars. One way of doing this could be to set up an industry of narrow-band imaging and follow-up spectroscopy of quasar fields. This could be done at $z \approx 2$ with a smaller telescope ($2-3$ m class) with a high through-put in the blue such as the Nordic Optical Telescope. The result of such a study would be to securely establish any differences between extended Lyα emission around RQQs and RLQs, and determine possible correlations between the extended emission and the central quasar. By obtaining DM halo masses (using the method in Chapter 4 or, more reliably, by performing a clustering analysis of Lyα emitters in the field), any correlations between DM halo mass and BH mass (obtained using the $M-\sigma$ relation) could be found. All these findings would be very helpful to distinguish between different models of quasar and galaxy formation, and to identify the parameters regulating the radio-loudness of quasars. Furthermore, a large catalogue of Lyα emitters would be built, from which properties such as luminosity function, space density, and clustering could be inferred. Any detected filaments would add to the constraints on the cosmological parameters.

Another option would be to investigate the nature of the non-detections of extended Lyα emission around quasars; is the extended emission very faint, is its size very small so that it disappears in the quasar PSF, or is there simply no emission? One way to study this could be to perform very deep narrow-band imaging or spectroscopy of a sample of these non-detections. Deep observations of known extended Lyα emission could determine whether the size differences between RQQs and RLQs are real or not, and whether the surface brightness profiles are well-described by those predicted for cooling flows (do they really extend to 100 kpc?) As an alternative one could use adaptive optic facilities such as NACO on the VLT to examine extended emission at very small impact parameters, although the problem of PSF removal should be considered carefully. Yet another alternative could be to use integral field spectroscopy to map out the entire velocity field of the extended emission. However, the data analysis is rather time consuming, so it would only be feasible for a relatively small number of quasars.

A perhaps more innovative approach could be to study the extended Lyα emission at other wavelengths. By studying the Lyα fuzz in the near- or far-infrared it would be possible to distinguish between quasar and stellar photoionization as sources of power. Studying extended molecular lines at radio wavelengths would yield reliable systemic redshifts for the quasar and possibly precise velocity profiles, which may be used to infer dynamical masses and constrain the kinematics of the systems.

As is evident from this outlook, there are still many open questions in need of attention. Hopefully, we can address some of them in the coming years.

Bibliography

Adelberger, K. L. (2004). *ApJ*, **612**, 706.

Adelberger, K. L. & Steidel, C. C. (2005). *ApJ*, **630**, 50.

Alcock, C. & Paczyński, B. (1979). *Nature*, **281**, 358.

Aldcroft, T. L. & Green, P. J. (2003). *ApJ*, **592**, 710.

Alexander, D. M., Smail, I., Bauer, F. E., et al. (2005). *Nature*, **434**, 738.

Angel, J. R. P. & Stockman, H. S. (1980). *ARA&A*, **8**, 321.

Antonucci, R. (1993). *ARA&A*, **31**, 473.

Antonucci, R. R. J. (1984). *ApJ*, **278**, 499.

Antonucci, R. R. J. & Miller, J. S. (1985). *ApJ*, **297**, 621.

Aragon-Salamanca, A., Ellis, R. S., & O'Brien, K. S. (1996). *MNRAS*, **281**, 945.

Armus, L., Bernard-Salas, J., Spoon, H. W. W., et al. (2005). *ApJ*. astro-ph/0511381.

Baade, W. & Minkowski, R. (1954). *ApJ*, **119**, 206.

Baes, M., Buyle, P., Hau, G. K. T., & Dejonghe, H. (2003). *MNRAS*, **341**, L44.

Bajtlik, S., Duncan, R. C., & Ostriker, J. P. (1988). *ApJ*, **327**, 570.

Ballantyne, D. R., Everett, J. E., & Murray, N. (2005). *ApJ*. astro-ph/0509356.

Barger, A. J., Cowie, L. L., Mushotzky, R. F., et al. (2005). *AJ*, **129**, 578.

Barkana, R. (2004). *MNRAS*, **347**, 59.

Barkana, R. & Loeb, A. (2003). *Nature*, **421**, 341.

Barr, J. M., Bremer, M. N., Baker, J. C., & Lehnert, M. D. (2003). *MNRAS*, **346**, 229.

Barth, A. J., Greene, J. E., & Ho, L. C. (2005). In A. Merloni, S. Nayakshin, and R. A. Sunyaev, editors, *Growing Black Holes: Accretion in a Cosmological Context*, ESO Astrophysics Symposia, page 154. Berlin: Springer.

Barthel, P. D., Vestergaard, M., & Lonsdale, C. J. (2000). *A&A*, **354**, 7.

Barvainis, R., Hehár, J., Birkinshaw, M., Falcke, H., & Blundell, K. M. (2005). *ApJ*, **618**, 108.

Basilakos, S., Plionis, M., Georgakakis, A., & Georgantopoulos, I. (2005). *MNRAS*, **356**, 183.

Bassani, L., Molina, M., Malizia, A., et al. (2005). *ApJL*. astro-ph/0512015.

Becker, R. H., White, R. L., & Edwards, A. L. (1991). *ApJS*, **75**, 1.

Begelman, M. C. & Nath, B. B. (2005). *MNRAS*, **361**, 1387.

Bennert, N., Falcke, H., Schulz, H., Wilson, A. S., & Wills, B. J. (2002). *ApJ*, **574**, L105.

Bennett, A. S. (1962). *MmRAS*, **68**, 163.

Bergeron, J. & Boissé, P. (1991). *A&A*, **243**, 344.

Bertoldi, F., Cox, P., Neri, R., et al. (2003a). *A&A*, **409**, L47.

Bertoldi, F., Carilli, C. L., Cox, P., et al. (2003b). *A&A*, **406**, L55.

Birnboim, Y. & Dekel, A. (2003). *MNRAS*, **345**, 349.

Blandford, R. D. (1990). In T. J.-L. Courvoisier and M. Mayor, editors, *Active Galactic Nuclei*, Saas-Fee Advanced Course 20, page 161. Berlin: Springer.

Blandford, R. D. & McKee, C. F. (1982). *ApJ*, **255**, 419.

Blundell, K. M. & Beasley, A. J. (1998). *MNRAS*, **299**, 165.

Blundell, K. M., Beasley, A. J., Lacy, M., & Garrington, S. T. (1996). *ApJ*, **468**, L91.

Blundell, K. M., Rawlings, S., & Willot, C. J. (1999). *AJ*, **117**, 677.

Blundell, K. M., Beasley, A. J., & Bicknell, G. V. (2003). *ApJ*, **591**, L103.

Bock, D. C.-J., Large, M. I., & Sadler, E. M. (1999). *AJ*, **117**, 1578.

Boroson, T. A. (2002). *ApJ*, **565**, 78.

Bower, R. G., Morris, S. L., Bacon, R., et al. (2004). *MNRAS*, **351**, 63.

Boyle, B. J., Shanks, T., Croom, S. M., et al. (2000). *MNRAS*, **317**, 1014.

Bremer, M. N., Fabian, A. C., Sargent, W. L. W., et al. (1992). *MNRAS*, **258**, 23.

Bunker, A., Smith, J., Spinrad, H., Stern, D., & Warren., S. J. (2003). *Ap&SS*, **284**, 357.

Cantalupo, S., Porciani, C., Lilly, S. J., & Miniati, F. (2005). *ApJ*, **628**, 61.

Carilli, C. L., Kohno, K., Kawabe, R., et al. (2002). *AJ*, **123**, 1838.

Carlberg, R. G. (1990). *ApJ*, **350**, 505.

Chapman, S. C., Smail, I., Windhorst, R., Muxlow, T., & Ivison, R. J. (2004). *ApJ*, **614**, 671.

Charlot, S. & Fall, S. M. (1993). *ApJ*, **415**, 580.

Cimatti, A., Daddi, E., Renzini, A., et al. (2004). *Nature*, **430**, 184.

Ciotti, L. & Ostriker, J. P. (2001). *ApJ*, **551**, 131.

Cirasuolo, M., Celotti, A., Magliocchetti, M., & Danese, L. (2003a). *MNRAS*, **346**, 447.

Cirasuolo, M., Magliocchetti, M., Celotti, A., & Danese, L. (2003b). *MNRAS*, **341**, 993.

Condon, J. J., Cotton, W. D., Greisen, E. W., et al. (1998). *AJ*, **115**, 1693.

Cowie, L. L., Songaila, A., & Hu, E. M. (1996). *AJ*, **112**, 839.

Croom, S. M. & Shanks, T. (1996). *MNRAS*, **281**, 893.

Croom, S. M., Smith, R. J., Boyle, B. J., et al. (2004). *MNRAS*, **349**, 1397.

Croom, S. M., Boyle, B. J., Shanks, T., et al. (2005). *MNRAS*, **356**, 415.

Cross, N. J. G., Bouwens, R. J., Benítez, N., et al. (2004). *AJ*, **128**, 1990.

Croton, D. J., Springel, V., White, S. D. M., et al. (2005). *MNRAS*. astro-ph/0508046.

Daddi, E., Dickinson, M., Chary, R., et al. (2005). *ApJ*, **631**, L13.

Dawson, S., Stern, D., Bunker, A. J., Spinrad, H., & Dey, A. (2001). *AJ*, **122**, 598.

de Robertis, M. M., Yee, H. K. C., & Hayhoe, K. (1998). *ApJ*, **496**, 93.

Della Ceca, R., Braito, V., Beckmann, V., et al. (2003). *A&A*, **406**, 555.

Di Matteo, T., Quataert, E., Allen, S. W., Narayan, R., & Fabian, A. C. (2000). *MNRAS*, **311**, 507.

Di Matteo, T., Springel, V., & Hernquist, L. (2005). *Nature*, **433**, 604.

Dijkstra, M., Haiman, Z., & Spaans, M. (2005). *ApJ*. astro-ph/0510407.

Dultzin-Hacyan, D., Krongold, Y., Fuentes-Guridi, I., & Marziani, P. (1999). *ApJ*, **513**, L111.

Dunlop, J. S., Taylor, G. L., Huges, D. H., & Robson, E. I. (1993). *MNRAS*, **264**, 455.

Dunlop, J. S., McLure, R. J., Kukula, M. J., et al. (2003). *MNRAS*, **340**, 1095.

Dwelly, T. & Page, M. J. (2005). In *The X-ray Universe 2005*. astro-ph/0511436.

Edge (1959). *MmRAS*, **68**, 37.

Efstathiou, G. & Rees, M. J. (1988). *MNRAS*, **230**, 5P.

Efstathiou, G., Schaye, J., & Theuns, T. (2000). *Philos. Trans. R. Soc. London A*, **358**, 2049.

Ellingson, E., Yee, H. K. C., & Green, R. F. (1991). *ApJ*, **371**, 49.

Elvis, M. (2000). *ApJ*, **545**, 63.

Falcke, H., Sherwood, W., & Patniak, A. R. (1996). *ApJ*, **471**, 106.

Falomo, R., Kotilainen, J., & Treves, A. (2001). *ApJ*, **547**, 124.

Fan, X., Strauss, M. A., Schneider, D. P., et al. (2001). *AJ*, **121**, 54.

Fan, X., Strauss, M. A., Schneider, D. P., et al. (2003). *AJ*, **125**, 1649.

Fanaroff, B. L. & Riley, J. M. (1974). *MNRAS*, **167**, 31P.

Fardal, M. A., Katz, N., Gardner, J. P., et al. (2001). *ApJ*, **562**, 605.

Fath, E. A. (1909). *Lick Observatory Bulletin*, **5**, 71.

Feigelson, E. D. & Nelson, P. I. (1985). *ApJ*, **293**, 192.

Ferland, G. & Netzer, H. (1979). *ApJ*, **229**, 274.

Fernini, I., Burns, J. O., & Perley, R. A. (1997). *AJ*, **114**, 2292.

Ferrarese, L. (2002). *ApJ*, **578**, 90.

Ferrarese, L. & Merritt, D. (2000). *ApJ*, **539**, L9.

Ferrarese, L., Pogge, R. W., Peterson, B. M., et al. (2001). *ApJ*, **555**, L79.

Fey, A. L. & Charlot, P. (1997). *ApJS*, **111**, 95.

Flesch, E. & Hardcastle, H. J. (2004). *A&A*, **427**, 387.

Forster, K., Green, P. J., Aldcroft, T. L., et al. (2001). *ApJS*, **134**, 35.

Franceschini, A., Braito, V., & Fadda, D. (2002). *MNRAS*, **335**, L51.

Francis, P. J., Palunas, P., Teplitz, H. I., Williger, G. M., & Woodgate, B. E. (2004). *ApJ*, **614**, 75.

Fukugita, M., Ichikawa, T., Gunn, J. E., et al. (1996). *AJ*, **111**, 1748.

Furlanetto, S. R., Schaye, J., Springel, V., & Hernquist, L. (2005). *ApJ*, **622**, 7.

Fynbo, J. P. U., Burud, I., & Møller, P. (2000a). *A&A*, **358**, 88.

Fynbo, J. P. U., Thomsen, B., & Møller, P. (2000b). *A&A*, **353**, 457. (Paper I).

Fynbo, J. P. U., Møller, P., & Thomsen, B. (2001). *A&A*, **374**, 443.

Fynbo, J. P. U., Møller, P., & Thomsen, B. (2002). *A&A*, **388**, 425.

Fynbo, J. P. U., Ledoux, C., Møller, P., Thomsen, B., & Burud, I. (2003a). *A&A*, **407**, 147.

Fynbo, J. P. U., Jakobsson, P., Møller, P., et al. (2003b). *A&A*, **406**, L63.

Gallo, L. C., Lehmann, I., Pietsch, W., et al. (2005). *MNRAS*. astro-ph/0510551.

Gebhardt, K., Bender, R., Bower, G., et al. (2000a). *ApJ*, **539**, L13.

Gebhardt, K., Kormendy, J., Ho, L. C., et al. (2000b). *ApJ*, **543**, L5.

Giacconi, R., Zirm, A., Wand, J., et al. (2002). *ApJS*, **139**, 369.

Gilli, R., Daddi, E., Zamorani, G., et al. (2005). *A&A*, **430**, 811.

Goldschmidt, P., Kukula, M. J., Miller, L., & Dunlop, J. S. (1999). *ApJ*, **511**, 612.

Gould, A. & Weinberg, D. H. (1996). *ApJ*, **468**, 462.

Greenstein, J. L. & Matthews, T. A. (1963). *Nature*, **197**, 1041.

Grimes, J. A., Rawlings, S., & Willott, C. J. (2004). *MNRAS*, **349**, 503.

Grimes, J. A., Rawlings, S., & Willot, C. J. (2005). *MNRAS*, **359**, 1345.

Guillemin, P. & Bergeron, J. (1997). *A&A*, **328**, 499.

Guilloteau, S., Omont, A., Cox, P., McMahon, R. G., & Petitjean, P. (1999). *A&A*, **349**, 363.

Gunn, J. E. (1971). *ApJ*, **164**, L113.

Gunn, J. E. & Knapp, G. R. (1993). In B. T. Soifer, editor, *Sky Surveys. Protostars to Protogalaxies*, volume 43 of *ASP Conf. Ser.*, page 267. San Fransisco: ASP.

Haas, M., Chini, R., Müller, S. A. H., Bertoldi, F., & Albrecht, M. (2005). *A&A*. astro-ph/0509084.

Haehnelt, M., Natarajan, P., & Rees, M. J. (1998). *MNRAS*, **300**, 817.

Haiman, Z. & Cen, R. (2002). *ApJ*, **578**, 702.

Haiman, Z. & Loeb, A. (2001). *ApJ*, **552**, 459.

Haiman, Z. & Rees, M. J. (2001). *ApJ*, **556**, 87.

Haiman, Z., Spaans, M., & Quataert, E. (2000). *ApJ*, **537**, L5.

Hamann, F. (1997). *ApJS*, **109**, 279.

Häring, N. & Rix, H.-W. (2004). *ApJ*, **604**, L89.

Hasinger, G., Burg, R., Giacconi, R., et al. (1998). *A&A*, **329**, 482.

Hasinger, G., Miyaji, T., & Schmidt, M. (2005). *A&A*, **441**, 417.

Heckman, T. M. (1980). *A&A*, **87**, 152.

Heckman, T. M., Lehnert, M. D., Miley, G. K., & van Breugel, W. (1991a). *ApJ*, **381**, 373.

Heckman, T. M., Lehnert, M. D., van Breugel, W., & Miley, G. K. (1991b). *ApJ*, **370**, 78.

Hewitt, A. & Burbidge, G. (1993). *ApJS*, **87**, 451.

Hines, D. C., Schmidt, G. D., Smith, P. S., Cutri, R. M., & Low, F. J. (1995). *ApJ*, **450**, L1.

Ho, L. C. (2002). *ApJ*, **564**, 120.

Ho, L. C. (2005). *ApJ*, **629**, 680.

Hooper, E. J., Impey, C. D., Foltz, C. B., & Hewett, P. C. (1995). *ApJ*, **445**, 62.

Hopkins, P. F., Hernquist, L., Cox, T. J., et al. (2005a). *ApJ*. astro-ph/0506398.

Hopkins, P. F., Hernquist, L., Cox, T. J., et al. (2005b). *ApJ*, **630**, 716.

Hopkins, P. F., Hernquist, L., Cox, T. J., et al. (2005c). *ApJ*, **630**, 705.

Hopkins, P. F., Hernquist, L., Martini, P., et al. (2005d). *ApJ*, **625**, L71.

Hornschemeier, A. E., Brandt, W. N., Garmire, G. P., et al. (2000). *ApJ*, **541**, 49.

Hu, E. M. & Cowie, L. L. (1987). *ApJ*, **317**, L7.

Hu, E. M., Songaila, A., Cowie, L. L., & Stockton, A. (1991). *ApJ*, **368**, 28.

Hu, E. M., McMahon, R. G., & Egami, E. (1996). *ApJ*, **459**, L53.

Hubble, E. (1926). *ApJ*, **64**, 321.

Impey, C. & Petry, C. (2001). *ApJ*, **547**, 117.

Ivezić, Ž., Menou, K., Knapp, G. R., et al. (2002). *AJ*, **124**, 2364.

Ivezić, Ž., Richards, G. T., Hall, P. B., et al. (2004). In G. T. Richards and P. B. Hall, editors, *AGN Physics with the Sloan Digital Sky Survey*, volume 311 of *ASP Conf. Ser.*, page 347. San Fransisco: ASP.

Iwata, I., Ohta, K., Nakanishi, K., Kohno, K., & McMahon, R. G. (2001). *PASJ*, **53**, 871.

Jackson, C. A., Wall, J. V., Shaver, P. A., et al. (2002). *A&A*, **386**, 97.

Jaffe, A. H., Ade, P. A. R., Balbi, A., et al. (2001). *Phys. Rev. Let.*, **86**, 3475.

Jakobsson, P., Hjort, J., Fynbo, J. P. U., et al. (2004). *A&A*, **427**, 785.

Kaspi, S., Smith, P. S., Netzer, H., et al. (2000). *ApJ*, **533**, 631.

Kaufffmann, G., White, S. D. M., Heckman, T. M., et al. (2004). *MNRAS*, **353**, 713.

Kauffmann, G. & Haehnelt, M. (2000). *MNRAS*, **311**, 576.

Keel, W. C. (1983). *ApJ*, **269**, 466.

Kellermann, K. I., Sramek, R. A., Schmidt, M., Shaffer, D. B., & Green, R. (1989). *AJ*, **98**, 1195.

Khachikian, E. Y. & Weedman, D. W. (1974). *ApJ*, **192**, 581.

Kinney, A. L., Calzette, D., Bohlin, R. C., et al. (1996). *ApJ*, **467**, 38.

Kleinmann, S. G., Hamilton, D., Keel, W. C., et al. (1988). *ApJ*, **328**, 161.

Klypin, A. A. & Shandarin, S. F. (1983). *MNRAS*, **204**, 891.

Kormendy, J. & Gebhardt, K. (2001). In J. C. Wheeler and H. Martel, editors, *20th Texas Symposium on Relativistic Astrophysics*, volume 586 of *AIP Conf. Proc.*, page 363. Melville: American Institute of Physics.

Kormendy, J. & Richstone, D. (1995). *ARA&A*, **33**, 581.

Koulouridis, E., Plionis, M., Chavushyan, V., et al. (2005). *ApJ*. astro-ph/0509843.

Kukula, M., Dunlop, J. S., McLure, R. J., et al. (2001). *MNRAS*, **326**, 1533.

La Franca, F., Gregorini, L., Cristiani, S., De Ruiter, H., & Owen, F. (1994). *AJ*, **108**, 1548.

La Franca, F., Andreani, P., & Cristiani, S. (1998). *ApJ*, **497**, 529.

Lacy, M., Laurent-Muehleisen, S. A., Ridgway, S. E., et al. (2001). *ApJ*, **551**, L17.

Landman, D. A., Roussel-Dupre, R., & Tanigawa, G. (1982). *ApJ*, **261**, 732.

Lanzetta, K. M., McMahon, R. G., Wolfe, A. M., et al. (1991). *ApJS*, **77**, 1.

Lanzetta, K. M., Bowen, D. V., Tytler, D., & Webb, J. K. (1995). *ApJ*, **442**, 538.

Laor, A. (1998). *ApJ*, **505**, L83.

Laor, A. (2000). *ApJ*, **543**, L111.

Laor, A. (2003). *ApJ*, **590**, 86.

Laurikainen, E. & Salo, H. (1995). *A&A*, **293**, 683.

Lawrence, A. (1991). *MNRAS*, **252**, 586.

Lawrence, A. (2005). *MNRAS*, **363**, 57.

Le Brun, V., Smette, A., Surdej, J., & Claeskens, J.-F. (2000). *A&A*, **363**, 837.

Le Delliou, M., Lacey, C. G., Baugh, C. M., & Morris, S. L. (2005). *MNRAS*. astro-ph/0508186.

Lehnert, M. D. & Becker, R. H. (1998). *A&A*, **332**, 514.

Lehnert, M. D., Heckman, T. M., Chambers, K. C., & Miley, G. K. (1992). *ApJ*, **393**, 68.

Lehnert, M. D., van Breugel, W., Heckman, T. M., & Miley, G. K. (1999). *ApJS*, **124**, 11.

Lloyd, B. D. & Jones, P. A. (2002). *MNRAS*, **331**, 717.

Longair, M. S. (1981). *High Energy Astrophysics*, page 171. Cambridge: Cambridge Univ. Press.

Longair, M. S. (1998). *Galaxy Formation*, chapter 7. A&A Library. Berlin: Springer.

Lowenthal, J. D., Heckman, T. M., Lehnert, M. D., & Elias, J. H. (1995). *ApJ*, **439**, 588.

Lynds, R. & Wills, D. (1972). *ApJ*, **172**, 531.

Madau, P. (2005). In A. Merloni, S. Nayakshin, and R. A. Sunyaev, editors, *Growing Black Holes: Accretion in a Cosmological Context*, ESO Astrophysics Symposia, page 3. Berlin: Springer.

Magliocchetti, M., Maddox, S. J., Hawkins, E., et al. (2004). *MNRAS*, **350**, 1485.

Magorrian, J., Tremaine, S., Richstone, D., et al. (1998). *AJ*, **115**, 2285.

Mainieri, V., Rigopoulou, D., Lehmann, I., et al. (2005). *MNRAS*, **356**, 1571.

Malkan, M. A. (1984). *ApJ*, **287**, 555.

Marconi, A. & Hunt, L. K. (2003). *ApJ*, **589**, L21.

Martínez-Sansigre, A., Rawlings, S., Lacy, M., et al. (2005). *Nature*, **436**, 666.

Martini, P. (2004). In L. C. Ho, editor, *Coevolution of Black Holes and Galaxies*, volume 1 of *Carnegie Observatories Astrophysics Series*, page 170. Cambridge: Cambridge University Press.

Martini, P. & Weinberg, D. H. (2001). *ApJ*, **547**, 12.

Marziani, P., Zamanov, R. K., Sulentic, J. W., & Calvani, M. (2003). *MNRAS*, **345**, 1133.

Matsuda, Y., Yamada, T., Hayashino, T., et al. (2004). *AJ*, **128**, 569.

Matsuda, Y., Yamada, T., Hayashino, T., et al. (2005). *ApJ*, **634**, L125.

Matthews, T. A. & Sandage, A. R. (1963). *ApJ*, **138**, 30.

Matthews, T. A., Morgan, W. W., & Schmidt, M. (1964). *ApJ*, **140**, 35.

McCarthy, P. J. (1993). *ARA&A*, **31**, 639.

McLure, R. J. & Dunlop, J. S. (2001). *MNRAS*, **327**, 199.

McLure, R. J. & Dunlop, J. S. (2004). *MNRAS*, **352**, 1390.

McLure, R. J. & Jarvis, M. J. (2002). *MNRAS*, **337**, 109.

McLure, R. J. & Jarvis, M. J. (2004). *MNRAS*, **353**, L45.

McLure, R. J., Kukula, M. J., Dunlop, J. S., et al. (1999). *MNRAS*, **308**, 377.

McLure, R. J., Jarvis, M. J., Targett, T. A., Dunlop, J. S., & Best, P. N. (2005). *MNRAS*. astro-ph/0510121.

McMahon, R. G., Irwin, M. J., & Maddox, S. J. (2000). *VizieR Online Data Catalog*, **1267**.

Merritt, D. & Ferrarese, L. (2001). *MNRAS*, **320**, L30.

Metcalf, R. B. & Magliocchetti, M. (2005). *MNRAS*. astro-ph/0505194.

Miller, C. J., Nichol, R. C., Gómez, P. L., Hopkins, A. M., & Bernardi, M. (2003). *ApJ*, **597**, 142.

Miller, L., Peacock, J. A., & Mead, A. R. G. (1990). *MNRAS*, **244**, 207.

Miller, P., Rawlings, S., & Saunders, R. (1993). *MNRAS*, **263**, 425.

Miyoshi, M., Moran, J., & Herrnstein, J. (1995). *Nature*, **373**, 127.

Møller, P. (2000). *The ESO Messenger*, **99**, 31.

Møller, P. & Fynbo, J. P. U. (2001). *A&A*, **372**, L57.

Møller, P. & Warren, S. J. (1998). *MNRAS*, **299**, 661.

Møller, P., Warren, S. J., & Fynbo, J. P. U. (1998). *A&A*, **330**, 19.

Møller, P., Warren, S., Fall, S. M., Jakobsen, P., & Fynbo, J. U. (2000). *The ESO Messenger*, **99**, 33.

Møller, P., Warren, S. J., Fall, S. M., Fynbo, J. P. U., & Jakobsen, P. (2002). *ApJ*, **574**, 51.

Møller, P., Fynbo, J. P. U., & Fall, S. M. (2004). *A&A*, **422**, L33.

Monaco, P., Møller, P., Fynbo, J. P. U., et al. (2005). *A&A*, **440**, 799.

Monet, D. B. A., Canzian, B., Dahn, C., et al. (1998). *VizieR Online Data Catalog*, **1252**.

Moretti, A., Campana, S., Lazzati, D., et al. (2003). *ApJ*, **588**, 696.

Mori, M., Umemura, M., & Ferrara, A. (2004). *ApJ*, **613**, L97.

Mullis, C. R., Henry, J. P., Gioia, I. M., et al. (2004). *ApJ*, **617**, 192.

Mushotzky, R. F., Cowie, L. L., Barger, A. J., & Arnaud, K. A. (2000). *Nature*, **404**, 459.

Navarro, J. F., Frenk, C. S., & White, S. D. M. (1997). *ApJ*, **490**, 493.

Nelson, C. H. (2000). *ApJ*, **544**, L91.

Norman, C., Hasinger, G., Giacconi, R., et al. (2002). *ApJ*, **571**, 218.

Ohta, K., Yamada, T., Nakanishi, K., et al. (1996). *Nature*, **382**, 426.

Oke, J. B. (1963). *Nature*, **197**, 1040.

Oke, J. B. & Gunn, J. E. (1983). *ApJ*, **266**, 713.

Omont, A., McMahon, R. G., Cox, P., et al. (1996). *A&A*, **315**, 1.

Oshlack, A. Y. K. N., Webster, R. L., & Whiting, M. T. (2002). *ApJ*, **576**, 81.

Osmer, P. S. (2004). In L. C. Ho, editor, *Coevolution of Black Holes and Galaxies*, volume 1 of *Carnegie Observatories Astrophysics Series*, page 325. Cambridge: Cambridge University Press.

Ouchi, M., Shimasaku, K., & Furusawa, H. (2003). *ApJ*, **582**, 60.

Owen, F. N. & Laing, R. A. (1989). *MNRAS*, **238**, 357.

Padovani, P. (1993). *MNRAS*, **263**, 461.

Page, M. J., Carrera, F. J., Ebrero, J., Stevens, J. A., & Ivison, R. J. (2005). In *The X-ray Universe 2005*. astro-ph/0511747.

Palunas, P., Teplitz, H. I., Francis, P. J., Williger, G. M., & Woodgate, B. E. (2004). *ApJ*, **602**, 545.

Panessa, F. & Bassani, L. (2002). *A&A*, **394**, 435.

Peacock, J. A. (1999). *Cosmological Physics*. Cambridge University Press.

Peng, C. Y., Impey, C. D., Ho, L. C., Barton, E. J., & Rix, H.-W. (2005). *ApJ*. astro-ph/0509155.

Perlmutter, S., Aldering, G. amd Goldhaber, G., et al. (1999). *ApJ*, **517**, 565.

Petitjean, P., Pécontal, E., Valls-Gabaud, D., & Charlot, S. (1996). *Nature*, **380**, 411.

Pettini, M., Smith, L. J., King, D. L., & Hunstead, R. W. (1997). *ApJ*, **486**, 665.

Porciani, C., Magliocchetti, M., & Norberg, P. (2004). *MNRAS*, **355**, 1010.

Press, W. H., Flannery, B. P., Teukolsky, S. A., & Vetterling, W. T. (1989). *Numerical Recipes*. Cambridge University Press.

Prestage, R. M. & Peacock, J. A. (1988). *MNRAS*, **230**, 131.

Pritchet, C. J. (1994). *PASP*, **106**, 1052.

Punsly, B. (1995). *AJ*, **109**, 1555.

Rao, S. M. & Turnshek, D. A. (2000). *ApJS*, **130**, 1.

Rauch, M., Haehnelt, M. G., & Steinmetz, M. (1997). *ApJ*, **481**, 601.

Reuland, M., van Breugel, W., Röttnering, H., et al. (2003). *ApJ*, **592**, 755.

Rhoads, J. E., Malhotra, S., Dey, A., et al. (2000). *ApJ*, **545**, L85.

Richards, G. T., Hall, P. B., Vanden Berk, D. E., et al. (2003). *AJ*, **126**, 1131.

Richards, G. T., Croom, S. M., Anderson, S. F., et al. (2005). *MNRAS*, **360**, 839.

Richstone, D., Ajhar, E. A., Bender, R., et al. (1998). *Nature*, **395**, A14.

Ridgway, S. E., Heckman, T. M., Calzetti, D., & Lehnert, M. (2001). *ApJ*, **550**, 122.

Riess, A. G., Filippenko, A. V., Challis, P., et al. (1998). *ApJ*, **116**, 1009.

Risaliti, G. (2002). *A&A*, **386**, 379.

Risaliti, G., Elvis, M., Fabbiano, G., Baldi, A., & Zezas, A. (2005). *ApJL*. astro-ph/0503351.

Robertson, B., Hernquist, L., Cox, T. J., et al. (2005). *ApJ*. astro-ph/0506038.

Rowan-Robinson, M. (2002). *MNRAS*, **332**, 352.

Rowan-Robinson, M., Broadhurst, T., Oliver, S. J., et al. (1991). *Nature*, **351**, 71.

Russel, D. M., Ellison, S. L., & Benn, C. R. (2005). *MNRAS*. astro-ph/0512210.

Salucci, P., Szuszkiewicz, E., Monaco, P., & Danese, L. (1999). *MNRAS*, **307**, 637.

Sánchez, S. F. & González-Serrano, J. I. (2003). *A&A*, **406**, 435.

Sandage, A. (1961). *ApJ*, **133**, 355.

Sandage, A. R. (1965). *ApJ*, **141**, 1560.

Sargent, W. L. W., Boksenberg, A., & Steidel, C. C. (1988). *ApJS*, **68**, 539.

Savaglio, S., D'Odorico, S., & Møller, P. (1994). *A&A*, **281**, 331.

Schade, D. J., Boyle, B. J., & Letawsky, M. (2000). *MNRAS*, **315**, 498.

Schmidt, G. D., Smith, P. S., Foltz, C. B., & Hines, D. C. (2002). *ApJ*, **578**, L99.

Schmidt, M. (1963). *Nature*, **197**, 1040.

Schmidt, N. L. Z. G. D., Smith, P. S., et al. (2005). *AJ*, **129**, 1212.

Seyfert, C. K. (1943). *ApJ*, **97**, 28.

Shapiro, S. L. (2005). *ApJ*, **620**, 59.

Shaver, P. A. (1984). *A&A*, **136**, L9.

Shields, G. A., Gebhardt, K., Salviander, S., et al. (2003). *ApJ*, **583**, 124.

Simonsen, J. T. & Hannestad, S. (1999). *A&A*, **351**, 1.

Slipher, V. M. (1917). *Lowell Observatory Bulletin*, **3**, 59.

Smith, E. P., Heckman, T. M., Bothun, G. D., Romanishin, W., & Balick, B. (1986). *ApJ*, **306**, 64.

Smith, H. J. & Hoffleit, D. (1963). *Nature*, **198**, 650.

Smith, P. S., Schmidt, G. D., Hines, D. C., & Foltz, C. B. (2003). *ApJ*, **593**, 676.

Smith, R. J., Boyle, B. J., Shanks, T., et al. (1997). In B. J. McLean, D. A. Golombek, J. J. E. Hayes, and E. Payne, editors, *New Horizons from Multi-Wavelength Sky Surveys*, volume 179 of *Proc. IAU Symp.*, page 348. Dordrecht: Kluwer Academic Publishers.

Smith, R. J., Boyle, B. J., & Maddox, S. J. (2000). *MNRAS*, **313**, 252.

Snellen, I. A. G., Lehnert, M. D., Bremer, M. N., & Schilizzi, R. T. (2003). *MNRAS*, **342**, 889.

Somerville, R. S., Primack, J. R., & Faber, S. M. (2001). *MNRAS*, **320**, 504.

Springel, V. & Hernquist, L. (2003). *MNRAS*, **339**, 289.

Springel, V., Di Matteo, T., & Hernquist, L. (2005a). *MNRAS*, **361**, 776.

Springel, V., Di Matteo, T., & Hernquist, L. (2005b). *ApJ*, **620**, L79.

Sramek, R. A. & Weedman, D. W. (1980). *ApJ*, **238**, 435.

Staguhn, J. G., Stern, D., Benford, D. J., et al. (2005). *ApJ*, **629**, 633.

Steidel, C. C., Sargent, W. L., & Dickinson, M. (1991). *AJ*, **101**, 1187.

Steidel, C. C., Adelberger, K. L., Dickinson, M., et al. (1998). *ApJ*, **492**, 428.

Steidel, C. C., Adelberger, K. L., Shapley, A. E., et al. (2000). *ApJ*, **532**, 170.

Stern, D., Djorgovski, S. G., Perley, R. A., et al. (2000). *AJ*, **119**, 1526.

Stern, D., Moran, E. C., Coil, A. L., et al. (2002). *ApJ*, **568**, 71.

Stevens, J. A., Page, M. J., Ivison, R. J., et al. (2005). *MNRAS*, **360**, 610.

Stocke, J. T., Morris, S. L., Weymann, R. J., & Craig, C. B. (1992). *ApJ*, **396**, 487.

Strianand, R., Petitjean, P., Ledoux, C., & Hazard, C. (2002). *MNRAS*, **336**, 753.

Strittmatter, P. A., Hill, P., Pauliny-Toth, I. I. K., Steppe, H., & Witzel, A. (1980). *A&A*, **88**, L12.

Taniguchi, Y. & Shioya, Y. (2000). *ApJ*, **532**, L13.

Tremaine, S., Gebhardt, K., Bender, R., et al. (2002). *ApJ*, **574**, 740.

Treu, T., Malkan, M. A., & Blandford, R. D. (2004). *ApJ*, **615**, L97.

Treu, T., Ellis, R. S., Liao, T. X., & van Dokkum, P. G. (2005). *ApJ*, **622**, L5.

Trimble, V. (1995). *PASP*, **107**, 1133.

Tytler, D. & Fan, X. (1992). *ApJS*, **79**, 1.

Ueda, Y., Akiyama, M., Ohta, K., & Miyaji, T. (2003). *ApJ*, **598**, 886.

Ulrich, M.-H., Maraschi, L., & Urry, C. M. (1997). *ARA&A*, **35**, 445.

Ulvestad, J. S., Antonucci, R. R. J., & Barvainis, R. (2005). *ApJ*, **621**, 123.

Urry, C. M. (2003). In S. Collin, F. Combes, and I. Shlosman, editors, *AGN: From Central Engine to Host Galaxy*, volume 290 of *ASP Conf. Ser.*, page 3. San Fransisco: ASP.

Urry, C. M. (2004). In G. T. Richards and P. B. Hall, editors, *AGN Physics with the Sloan Digital Sky Survey*, volume 311 of *ASP Conf. Ser.*, page 49. San Fransisco: ASP.

Urry, C. M. & Treister, E. (2005). In A. Merloni, S. Nayakshin, and R. A. Sunyaev, editors, *Growing Black Holes: Accretion in a Cosmological Context*, ESO Astrophysics Symposia, page 432. Berlin: Springer.

Urry, M. C. & Padovani, P. (1995). *PASP*, **107**, 803.

Vanden Berk, D. E., Richards, G. T., Baum, A., et al. (2001). *ApJ*, **122**, 549.

Vestergaard, M. (2002). *ApJ*, **571**, 733.

Vilkoviskij, E. Y., Efimov, S. N., Karpova, O. G., & Pavlova, L. A. (1999). *MNRAS*, **309**, 80.

Villar-Martín, M., Vernet, J., di Serego Alighieri, S., et al. (2003). *MNRAS*, **346**, 273.

Volonteri, M., Haardt, F., & Madau, P. (2003). *ApJ*, **582**, 559.

Vreeswijk, P. M., Møller, P., & Fynbo, J. P. U. (2003). *A&A*, **409**, L5.

Wake, D. A., Miller, C. J., Di Matteo, T., et al. (2004). *ApJ*, **610**, L85.

Wandel, A. (1999). *ApJ*, **519**, L39.

Wandel, A., Peterson, B. M., & Malkan, M. A. (1999). *ApJ*, **526**, 579.

Warren, S. J., Hewett, P. C., & Osmer, P. S. (1991). *ApJS*, **76**, 23.

Warren, S. J., Møller, P., Fall, S. M., & Jakobsen, P. (2001). *MNRAS*, **326**, 759.

Waskett, T. J., Eales, S. A., Gear, W. K., et al. (2005). *MNRAS*, **363**, 801.

Weidinger, M., Møller, P., Thomsen, B., Fynbo, J. P. U., & Egholm, M. P. (2002). *A&A*, **391**, 13.

Weidinger, M., Møller, P., & Fynbo, J. P. U. (2004). *Nature*, **430**, 999. (Paper II).

Weidinger, M., Møller, P., Fynbo, J. P. U., & Thomsen, B. (2005). *A&A*, **436**, 825.

Weymann, R. J., Williams, R. E., Peterson, B. M., & Turnshek, D. A. (1979). *ApJ*, **234**, 33.

White, R. L., Becker, R. H., Gregg, M. D., et al. (2000). *ApJS*, **126**, 133.

White, S. D. M., Frenk, C. S., Davis, M., & Efstathiou, G. (1987). *ApJ*, **313**, 505.

Wilkes, B. J. (2000). In A. N. Cox, editor, *Allen's astrophysical quantities*. Berlin: Springer.

Willott, C. J., McLure, R. J., & Jarvis, M. J. (2003). *ApJ*, **587**, L15.

Wilman, R. J., Johnstone, R. M., & Crawford, C. S. (2000). *MNRAS*, **317**, 9.

Wilson, A. S. & Colbert, E. J. M. (1995). *ApJ*, **438**, 62.

Wold, M., Lacy, M., Lilje, P. B., & Serjeant, S. (2000). *MNRAS*, **316**, 267.

Wold, M., Lacy, M., Lilje, P. B., & Serjeant, S. (2001). *MNRAS*, **323**, 231.

Wolter, A., Gioia, I. M., Henry, J. P., & Mullis, C. R. (2005). *A&A*, **444**, 165.

Woo, J.-H. & Urry, C. M. (2002a). *ApJ*, **581**, L5.

Woo, J.-H. & Urry, C. M. (2002b). *ApJ*, **579**, 530.

Wyithe, J. S. B. & Loeb, A. (2002). *ApJ*, **581**, 886.

Yanny, B. & York, D. G. (1992). *ApJ*, **391**, 569.

Yee, H. K. C. & Green, R. F. (1987). *ApJ*, **319**, 28.

Yu, Q. & Tremaine, S. (2002). *MNRAS*, **335**, 965.

Zensus, J. A., Ros, E., Kellermann, K. I., et al. (2002). *AJ*, **124**, 662.

Zheng, W., Overzier, R., Bouwens, R. J., et al. (2005). *ApJ*. astro-ph/0511734.

Zirbel, E. L. & Baum, S. A. (1995). *ApJ*, **448**, 521.

List of publications

Preprints can be obtained at
`http://astro.phys.au.dk/~michaelw/publications.html`

Refereed publications

i. *Deep Ly-alpha imaging of two z=2.04 GRB host galaxy fields*
Fynbo, J. P. U., Møller, P., Thomsen, B., Hjorth, J., Gorosabel, J., Andersen, M. I., Egholm, M. P., Holland, S., Jensen, B. L., Pedersen, H., & **Weidinger, M.** (2002). *A&A*, **388**, 425

ii. *Constraints on* $(\Omega_{\rm m}, \Omega_\Lambda)$ *using distributions of inclination angles for high redshift filaments*
Weidinger, M., Møller, P., Thomsen, B., Fynbo, J. P. U., & Egholm, M. P. (2002). *A&A*, **391**, 13
This paper constitutes Chapter 3

iii. *Absorption Systems in the Spectrum of GRB 021004*
Møller, P., Fynbo, J. P. U., Hjorth, J., Thomsen, B., Egholm, M. P., Andersen, M. I., Gorosabel, J., Holland, S. T., Jakobsson, P., Jensen, B. L., Pedersen, H., Pedersen, K., & **Weidinger, M.** (2002). *A&A*, **396**, L21

iv. *Optical Photometry of GRB 021004: The First Month*
Holland, S. T., **Weidinger, M.**, Fynbo, J. P. U., Gorosabel, J., Hjort, J., Pedersen, K., Andersen, M. I., Augusteijn, T., Castro Cerón, J. M., Castro-Tirado, A., Dahle, H., Egholm, M. P., Jakobsson, P., Jensen, B. L., Levan, A., Méndez, J., Møller, P., Pedersen, H., Pursimo, T., Ruiz-Lapeunte, P., & Thomsen, B. (2003). *AJ*, **125**, 2291

v. *On the Ly*α *emission from gamma-ray burst host galaxies: evidence for low metallicities*
Fynbo, J. P. U., Jakobsson, P., Møller, P., Hjorth, J., Thomsen, B., Holland, S. T., Gorosabel, J., Andersen, M. I., Fruchter, A.S., Ledoux, C., Pedersen, H., Rhoads, J., Tanvir, N., **Weidinger, M.**, & Wijers R. A. M. J. (2003). *A&A*, **406**, L63

vi. *The afterglow and the host galaxy of GRB 011211*
Jakobsson, P., Hjorth, J., Fynbo, J. P. U., Gorosabel, J., Pedersen, K., Burud, I., Levan, A., Fruchter, A., Rhoads, J., Grav, T., Hansen, M. W., Michelsen, R., Andersen, M. I., Jensen, B. L., Pedersen, H., Thomsen, B., **Weidinger, M.**, Bhargavi, S. G., Cowsik, R., & Pandey, S. B. (2003). *A&A*, **408**, 941

vii. *On the Afterglow of the X-Ray Flash of July 23 2003: Photometric evidence for an off-axis Gamma-Ray Burst with an associated Supernova?*
Fynbo, J. P. U., Sollerman, J., Hjorth, J., Grundahl, F., Gorosabel, J., **Weidinger, M.**, Møller, P., Jensen, B. L., Vreeswijk, P. M., Fransson, C., Ramirez-Ruiz, E., Jakobsson, P., Jorgensen, S. F., Vinter, C., Andersen, M. I., Castro Cerón, J. M., Castro-Tirado, A. J. Fruchter, A. S., Greiner, J., Kouveliotou, C., Levan, A., Klose, S., Masetti, N., Pedersen, H., Palazzi, E., Pian, E., Rhoads, J., Rol, E., Sekiguchi, T., Tanvir, N. R., Tristram, P., de Ugarte Postigo, A., Wijers, R. A. M. J., & van den Heuvel, E. (2004). *ApJ*, **609**, 962

viii. *Small-scale variations in the radiating surface of the GRB 011211 jet*
Jakobsson, P., Hjorth, J., Ramirez-Ruiz, E., Kouveliotou, C., Pedersen, K., Fynbo, J. P. U., Gorosabel, J., Watson, D., Jensen, B. L., Grav, T., Hansen, M. W., Michelsen, R., Andersen, M. I., **Weidinger, M.**, & Pedersen, H. (2004). *New Astron.*, **9**, 435

ix. *The Lyman-alpha glow of gas falling into the dark matter halo of a $z = 3$ galaxy*
Weidinger, M., Møller, P., & Fynbo, J. P. U. (2004). *Nature*, **430**, 999
This paper constitutes Chapter 4

x. *The line-of-sight towards GRB 030429 at $z = 2.66$: Probing the matter at stellar, galactic and intergalactic scales*
Jakobsson, P., Hjorth, J., Fynbo, J. P. U., **Weidinger, M.**, Gorosabel, J., Ledoux, C., Watson, D., Bjornsson, B., Gudmundsson, E. H., Wijers, R. A. M. J., Møller, P., Pedersen, K., Sollerman, J., Henden, A. A., Jensen, B. L., Gilmore, A., Kilmartin, P., Levan, A., Castro Cerón, J. M., Castro-Tirado, A. J., Fruchter, A., Kouveliotou, C., Masetti, N., & Tanvir, N. R. (2004). *A&A*, **427**, 785

xi. *The extended Lyman-alpha emission surrounding the $z = 3.04$ radio-quiet QSO1205-30: Primordial infalling gas illuminated by the quasar?*
Weidinger, M., Møller, P., Fynbo, J. P. U., & Thomsen, B. (2005). *A&A*, **436**, 825
This paper constitutes Chapter 5

xii. *Tracing large-scale structure at high redshift with Lyman-α emitters: the effect of peculiar velocities*
Monaco, P., Møller, P., Fynbo, J. P. U., **Weidinger, M.**, Ledoux, C., & Theuns, T. (2005). *A&A*, **440**, 799

Unrefereed publications

i. *The optical afterglow and host galaxy of GRB 000926*
Fynbo, J. P. U., Gorosabel, J., Møller, P., Hjorth, J., Andersen, M. I., Egholm, M. P., Jensen, B. L., Pedersen, H., Thomsen, B., & **Weidinger, M.** (2001). In the proceedings of the conference "Lighthouses of the Universe", Garching 2001 (Springer), p. 187

ii. *Lyα-emission from GRB host galaxies*
Fynbo, J. P. U., Møller, P., Thomsen, B., Hjorth, J., Gorosabel, J., Andersen, M. I., Egholm, M. P., Holland, S. T., Jensen, B. L., Pedersen, H., & **Weidinger, M.** (2002). In the proceedings of the Roma 2002 GRB workshop

iii. *Universets storskala-strukturer*
Weidinger, M. (2003). *Kvant*, **1**, 24

List of Figures

List of Tables

If I make use of the tongues of men and of angels, and have not love, I am like sounding brass, or a loud-tongued bell.

And if I have a prophet's power, and have knowledge of all secret things; and if I have all faith, by which mountains may be moved from their place, but have not love, I am nothing.

And if I give all my goods to the poor, and if I give my body to be burned, but have not love, it is of no profit to me.

Love is never tired of waiting; love is kind; love has no envy; love has no high opinion of itself, love has no pride;

Love's ways are ever fair, it takes no thought for itself; it is not quickly made angry, it takes no account of evil;

It takes no pleasure in wrongdoing, but has joy in what is true;

Love has the power of undergoing all things, having faith in all things, hoping all things.

Though the prophet's word may come to an end, tongues come to nothing, and knowledge have no more value, love has no end.

For our knowledge is only in part, and the prophet's word gives only a part of what is true:

But when that which is complete is come, then that which is in part will be no longer necessary.

When I was a child, I made use of a child's language, I had a child's feelings and a child's thoughts: now that I am a man, I have put away the things of a child.

For now we see things in a glass, darkly; but then face to face: now my knowledge is in part; then it will be complete, even as God's knowledge of me.

But now we still have faith, hope, love, these three; and the greatest of these is love.

Book of 1 Corinthians, chapter 13, verses 1–13